Robust active vibration control of flexible rotor-bearing systems under steady and transient conditions

Mu, Cheng

Award date:
1994

Awarding institution:
University of Bath

ROBUST ACTIVE VIBRATION CONTROL OF FLEXIBLE ROTOR-BEARING SYSTEMS UNDER STEADY AND TRANSIENT CONDITIONS

Submitted by Cheng Mu

for the degree of Ph.D

of the University of Bath

1994

ProQuest LLC
789 East Eisenhower Parkway
P.O. Box 1346
Ann Arbor, MI 48106-1346

ACKNOWLEDGEMENTS

I would like to express my appreciation to Professor C. R. Burrows and Dr. P. S. Keogh for their distinguished guidance and supervision.

I would also like to thank the Committee of Vice-Chancellors and Principals of the University of the United Kingdom for the award of an ORS Scholarship during my study. The financial assistance of the Fluid Power Centre is also acknowledged.

Finally, I wish to thank my wife Su, without whose support, encouragement, patience, and sacrifice this work would have never been completed.

CONTENTS

		Page No.
ABSTRACT		1
NOTATION		2
CHAPTER 1	**INTRODUCTION**	8
1.1	Vibration Problems In Rotating Machinery	8
1.2	Vibration Control In Rotor-Bearing Systems	9
	1.2.1 Passive Control Devices	9
	1.2.2 Active Control Devices	10
	1.2.3 Review Of Magnetic Bearing Control	13
1.3	Justification Of Present Research	16
1.4	Structure Of The Thesis	17
CHAPTER 2	**REVIEW OF ROTOR - BEARING SYSTEM MODELLING**	18
2.1	Introduction	18
2.2	Modelling of Rotors	18
	2.2.1 Modelling Methods	19
	2.2.2 Coordinates And Shape Function Of Finite Element Method	21
	2.2.3 Element Equation Of Motion	24
	2.2.4 Rotor Equation Of Motion	25
2.3	Modelling Of Journal Bearings	26
	2.3.1 Reynolds Equation For Oil Film	26
	2.3.2 Non-linear Oil Film Force	27
	2.3.3 Expression Of Linearilized Oil Film Force	28
2.4	Complete Rotor Bearing System Equations	28

2.5 System Dynamic Analysis 29

2.5.1 Unbalance Response Analysis 30

2.5.2 Stability Analysis 30

The Figures Of Chapter 2 32

CHAPTER 3 REVIEW OF CONTROL STRATEGIES FOR ATTENUATING ROTOR VIBRATION 33

3.1 Introduction 33

3.2 Review of Control Strategies 33

3.2.1 Local Control 34

3.2.2 Decentralized Control 35

3.2.3 Centralized Control 36

3.2.3.1 Linear Quadratic Gaussian Control 36

3.2.3.2 Pole Assignment 37

3.2.3.3 Open Loop Adaptive Control 37

3.3 Some Control Problems 39

3.4 H_∞ Optimization Control 40

3.4.1 Definitions And Objectives 41

3.4.2 The H_∞ Problem Formulation 42

3.4.3 Solution Of General H_∞ Problems In State Space 43

The Figures Of Chapter 3 45

CHAPTER 4 APPLICATION OF H_∞ CONTROL DESIGN TO ROTOR-BEARING SYSTEMS 46

4.1 Introduction 46

4.2 Theoretical Model Of Rotor-Bearing System 46

4.2.1 Model Reduction 47

4.2.2 Analysis Of Controllability And Observability Of The Reduced Order System 50

4.3 Formulation Of The Standard H_∞ Problem 51

4.3.1 Augmented Equations 51

4.3.2 State Space Realisation Of The Augmented System 53

4.4 Controller Design 56

4.4.1 Characteristics Of Control Forces 56

4.4.2 Characteristics of Disturbance Forces 56

4.4.3 Characteristics Of Disturbances Forming D_r 56

4.4.4 Characteristics Of The Shaft Surface Roughness And Electrical Noise 58

4.4.5 Choice Of Weighting Functions 59

4.4.6 Resulting H_∞ Controller 61

The Figures Of Chapter 4 63

CHAPTER 5 CONTROL IMPLEMENTATION ON AN EXPERIMENTAL RIG 68

5.1 Description Of The Experimental System 68

5.2 Details Of The Rotor-Bearing Assembly 68

5.2.1 Flexible Rotor 68

5.2.2 DC Motor And Coupling 68

5.2.3 Oil-Film Bearings 69

5.2.4 Lubrication System 69

5.3 Electromagnetic Bearing Actuators 69

5.3.1 Dynamic Characteristic Of The Control Magnetic actuator 70

5.3.2 Dynamic Characteristic Of The Second Magnetic Actuator 71

5.4 Data Acquisition System 71

5.4.1 Transducers 71

5.4.2 Filter Circuits 72

5.4.3 RTI-815 Interface Board 73

5.4.3.1 Analogue Input / Output Feature 73

5.4.3.2 Time - Related Digital Input / Output Feature 74

5.5 Personal Computer 74

5.6 Transputer Hardware 74

5.6.1 Introduction 74

5.6.2 Structure Of Transputers 75

5.6.3 Structure Of Parallel Computer 75

5.7 Operating System 76

5.8 Software Configuration 77

5.8.1 Data Acquisition Program - RTILINK 78

5.8.2 Digital Control Loop Server Program - DCLSRV 79

5.8.3 Digital Control Loop Monitor Program - DCLMON 79

The Figures Of Chapter 5 80

CHAPTER 6 APPLICATION OF H_∞ CONTROLLER DESIGN PROCEDURE TO EXPERIMENTAL RIG 86

6.1 Introduction 86

6.2 Dynamic Analysis Of The Theoretical Model 86

6.2.1 The System Critical Speeds And Modal Analysis 86

6.2.2 Model Reduction 88

6.3 Meausred Surface Roughness 89

6.4 Analysis And Design Of The H_∞ Controller 90

6.4.1 Choice Of Controller Weighting W_u 91

6.4.2 Controller Design In The Case Of Steady State Response 91

6.4.2.1 Controller Design At Fourth Critical Speed 309 rad/s 91

6.4.2.2 Controller Design At Other Rotational Speeds 93

6.4.2.3 High Reduced Order Model 94

6.4.3 Simulation Of Steady State Responses 95

6.4.4 Controller Design In The Case Of Sudden Mass Loss 96

6.4.5 Transient Responses 97

6.4.6 Effect Of The Surface Roughness On Control Design 97

6.4.7 Effect Of Filters And Measurement Time Delay On Control Design 98

6.4.8 Effect Of Structure Variation On Control Design 98

6.5 Stability Analysis 99

The Figures Of Chapter 6 100

CHAPTER 7 EXPERIMENTAL RESULTS 131

7.1 Brief Description Of Experimental Procedure 131

7.2 Synchronous Control 132

7.2.1 Uncontrolled Response 132

7.2.2 Five Speed H_∞ Controller Case 133

7.2.3 Two Speed H_∞ Controller Case 133

7.2.4 Open-loop Adaptive Controller Case 133

7.2.5 Two Speed H_∞ Controller Designed Without Considering The Rotor Surface Roughness 133

7.2.6 Two Speed H_∞ Controller Based On Inaccurate Model 134

7.2.7 Inaccurate Transducer Position Case 134

7.2.8 Two Speed H_∞ Control With Transducers Removed 135

7.3 Non-Synchronous Control 135

7.3.1 Disturbance Frequency Near The Critical Speeds 135

7.3.2 Disturbance Frequency Below The Critical Speeds 136

7.3.3 Disturbance Frequency Above The Critical Speeds 136

7.4 Transient Control 136

7.4.1 Mass Loss Below Third Critical Speed 137

7.4.2 Mass Loss At Third Critical Speed 137

7.4.3 Mass Loss Between Third And Fourth Critical Speeds 138

7.4.4 Mass Loss At Fourth Critical Speed 138

7.4.5 Mass Loss Above Fourth Critical Speed 139

7.5 Discussion Of Results 139

The Figures Of Chapter 7 140

CHAPTER 8 CONCLUSIONS AND RECOMMENDATIONS 214

REFERENCES 218

APPENDIX A FINITE ELEMENT MATRICES 229

APPENDIX B JOURNAL BEARING STIFFNESS AND DAMPING COEFFICIENTS 233

APPENDIX C WEIGHTING FUNCTION MATRICES 235

ABSTRACT

The H_∞ optimization control strategy has been developed to produce a robust controller for active vibration control of a rotor-bearing system. The system consisted of a flexible rotor, supported by journal bearings, together with a magnetic control actuator and a magnetic disturbance force generator. Real time digital control was realized using transputer hardware. Attenuation of synchronous, non-synchronous, and transient lateral vibration of the system was considered. The emphasis was on a closed loop system that could achieve vibration reduction, robustness in the presence of unwanted disturbances, and avoidance of spillover problems.

The detailed procedure of applying H_∞ control design in rotor-bearing systems was, for the first time, presented and included dynamic analysis of the uncontrolled system, model reduction, evaluation of actuator dynamic characteristics, measurement error, determination of weighting function matrices, formulation of the H_∞ problem and derivation of the controller. Computer simulation was carried out to predict the dynamic characteristic of the controller and responses of the uncontrolled and controlled systems. The theoretical results predicted that the controller had the designed properties.

The control strategy was implemented on an experimental rig and was validated by novel experimental results. Furthermore, the spectra of the rotor surface roughness was included into the control design and this was shown to improve the performance of the closed loop system at lower rotational speeds. The results showed that significant vibration reduction was achieved for both the steady state and transient mass loss cases especially around critical speeds. No spillover instability in the closed loop system was observed. It was also demonstrated that the controller was not sensitive to the variation of the system structure.

NOTATION

A	full order system matrix
A_a, B_{ar}, B_{au} C_{az}, D_{azr}, D_{azu} C_{ay}, D_{ayr}, D_{ayu}	state space matrices of the augmented system
A_c, B_c C_c, D_c	state space matrices of the controller
A_h	high order system matrix in modal space
A_l	reduced order system matrix in modal space
A_f, B_f C_f, D_f	state space matrices of the filter
A_u, B_u C_u, D_u	state space matrices of control force weighting function
A_y, B_y C_y, D_y	state space matrices of measured state weighting function
A_z, B_z C_z, D_z	state space matrices of controlled state weighting function
B_d	full order disturbance input matrix
B_f	control force distribution matrix
B_{hd}	high order disturbance input matrix in modal space
B_{hu}	high order control input matrix in modal space
B_{ld}	reduced order disturbance input matrix in modal space
B_{lu}	reduced order control input matrix in modal space
B_o	journal bearing coefficient
B_u	full order control input matrix
C	damping matrix
C_c	full order control output matrix
C_b	bearing centre
C_j	journal centre

$\boldsymbol{C}_m$	full order measurement output matrix
$\boldsymbol{D}$	disturbance input vector in Laplace space
$\boldsymbol{D}_c$	feedforward matrix from disturbance due to high order modes to controlled output
$\boldsymbol{D}_m$	feedforward matrix from disturbance due to high order modes to measured output
$\boldsymbol{D}_n$	feedforward matrix from disturbance due to surface roughness to measured output
E	Young's modulus
$\boldsymbol{F}$	force vector
F_r	oil film force in direction r
F_t	oil film force in direction t
F_x	oil film force in direction x
F_y	oil film force in direction y
G	shear modulus
$\boldsymbol{G}$	transfer function matrix of the rotor-bearing system
$\boldsymbol{G}_a(s)$	transfer function matrix of the augmented system
$\boldsymbol{G}_c$	controllability gramian matrix
$\boldsymbol{G}_o$	observability gramian matrix
$\boldsymbol{G}_f$	disturbance distribution matrix
$\boldsymbol{G}_{ij}(s)$	partition of transfer function matrix
$\boldsymbol{G}^e$	finite element gyroscopic matrix
$\boldsymbol{G}_r(s)$	transfer function matrix of the reduced order system
$\boldsymbol{H}(s)$	controller transfer function matrix
I	second inertia moment of area
$\boldsymbol{I}$	unit matrix
I_d	diametral moment of inertia per unit length of finite element
$\boldsymbol{K}$	stiffness matrix

K^e	finite element stiffness matrix
L	bearing land length
M	inertia matrix
M_r^e	finite element translational mass matrix
M_t^e	finite element angular mass matrix
N	measurement noise vector in Laplace space
N_m	feedforward matrix from measurement noise to measured output
N_r	translational displacement shape function
N_t	angular displacement shape function
P	modal state vector in Laplace space
P_l	retained modal state vector in Laplace space
P_h	high order modal state vector in Laplace space
Q	global coordinate vector
R	bearing radius
T_g	kinetic energy of finite element due to gyroscopic moment
T_t	finite element kinetic energy
U	control input vector in Laplace space
U^L	left eigenvector matrix
U^R	right eigenvector matrix
U_l^R	partition of right eigenvector matrix relative to retained modes
U_h^R	partition of right eigenvector matrix relative to high order modes
V_o	bias input voltage to magnetic bearing
V_x	input control voltage to magnetic bearing coils in horizontal direction
V_y	input control voltage to magnetic bearing coils in vertical direction
$W_f(s)$	filter transfer function matrix
$W_u(s)$	transfer function matrix of the weighting on control force vector

$\boldsymbol{W}_y(s)$	transfer function matrix of the weighting on measured output vector
$\boldsymbol{W}_z(s)$	transfer function matrix of the weighting on controlled output vector
(X, Y, Z)	fixed coordinate system
$\boldsymbol{X}$	state vector in Laplace space
$\boldsymbol{Y}_f$	filtered measured output vector in Laplace space
$\boldsymbol{Y}_m$	measured output vector in Laplace space
$\boldsymbol{Z}_c$	controlled output vector in Laplace space
$\boldsymbol{Z}_m$	observed output vector in Laplace space
$\boldsymbol{Z}_u$	weighted controlled force vector in Laplace space
$\boldsymbol{Z}_z$	weighted controlled state vector in Laplace space
$\boldsymbol{Z}_y$	weighted measured state vector in Laplace space
c	radial clearance of journal bearing
c_{xx}, c_{xy} c_{yx}, c_{yy}	journal bearing damping coefficients
$\boldsymbol{d}$	disturbance vector due to force acting on the rotor
$\boldsymbol{d}_c$	disturbance vector due to high order modes on controlled output
$\boldsymbol{d}_m$	disturbance vector due to high order modes on measured output
$\boldsymbol{d}_n$	disturbance vector due to measurement noise on measured output
$\boldsymbol{f}$	force vector
$\boldsymbol{f}^e$	forcing vector acting on finite element
i_{+x}, i_{-x}	control current input to magnetic bearing coils in horizontal direction
i_{+y}, i_{-y}	control current input to magnetic bearing coils in vertical direction
j	$(-1)^{½}$
k	shear factor

k_a	power amplifier coefficient
k_i	force-voltage coefficient of magnetic bearing
k_s	stiffness coefficient of magnetic bearing
k_{xx}, k_{xy}, k_{yx}, k_{yy}	journal bearing stiffness coefficients
m	mass per unit length of finite element
p	lubricant film pressure
$\boldsymbol{p}$	modal state vector
$\boldsymbol{p}_l$	retained modal state vector
$\boldsymbol{p}_h$	high order modal state vector
$\boldsymbol{q}$	displacement vector
$\boldsymbol{q}^e$	finite element displacement vector
$q_1,\ldots,q_8$	finite element displacements
$\boldsymbol{r}$	disturbance input vector
s	Laplace transform variable
t	time
$\boldsymbol{u}$	control input vector
$\boldsymbol{v}(\xi,t)$	translational displacement vector of the infinitesimal disc of the finite element
$\boldsymbol{w}(\xi,t)$	angular displacement vector of the infinitesimal disc of the finite element
$\boldsymbol{x}$	state vector
$\boldsymbol{x}_a$	state vector of the augmented system
$\boldsymbol{x}_c$	controller state vector
$\boldsymbol{x}_f$	filter state vector
$\boldsymbol{x}_u$	state vector of control force weighting
$\boldsymbol{x}_y$	state vector of measured state weighting
$\boldsymbol{x}_z$	state vector of controlled state weighting

y_f	filtered measured output vector
y_m	measured output vector
z_c	controlled output vector
z_m	observed output vector
z_u	weighted controlled force vector
z_z	weighted controlled state vector
z_y	weighted measured state vector
Δ	inverse impedance matrix
Λ	flexibility matrix
Φ	transverse shear effect
ε	eccentricity ratio of bearing
ζ_j	j th modal damping coefficient
θ	angular coordinate with respect to the maximum film thickness
$\bar{\sigma}$	singular value
θ_x	rotation angle of infinitesimal disc of the finite element
λ	eigenvalue
μ	lubricant viscosity
ξ	distance from finite element left end
ϕ	angle between load line and line of centres of journal and bearing
$\phi_{\xi x}$	share angle of infinitesimal disc of the finite element
ω_j	j th modal frequency

CHAPTER 1 INTRODUCTION

1.1 Vibration Problems In Rotating Machinery

The application of high speed rotors in modern rotating machinery includes gas turbines, steam turbines, compressors, and centrifuges. Rotor unbalance, which is caused by manufacturing processes, assembly errors, and thermal effects, is a common source for vibration excitation. Under these conditions, the rotor can experience very high vibrational amplitudes, which may lead to large forces being transmitted to the supporting structure and possibly collision between the rotor and stator components, with damaging effect.

Research into rotor dynamic behaviour was started by Rankine [64] in 1869 and more detailed and accurate results were obtained by Jeffcott [39] in 1919. It was shown that there were certain critical speeds at which the rotor vibration could become large. Rotors may be required to pass through several critical speeds or even operate near a critical speed. It was thought that the severe vibrations at these speeds could be avoided as long as some damping force was introduced. However, severe vibrations were later found to occur even when the rotor was running at speeds far away from critical speeds [57]. This initiated research on instability problems in rotor-bearing systems. The vibration control of rotor-bearing systems must therefore take account of attenuation of rotor vibration amplitudes and, in addition, maintain a stable system. This is still a central issue in present research in control of rotor dynamic vibration.

The introduction of journal bearings into systems as supports may cause instability under certain conditions. This phenomenon is called self-excited whirl in which the whirling frequency is usually less than half the rotor running speed. Large vibrations

can be observed even when rotor is well balanced. The problem of finding effective methods to attenuate rotor vibration is now discussed.

1.2 Vibration Control In Rotor-Bearing Systems

1.2.1 Passive Control Devices

Research into vibration control can be traced back to the 1920's when Ormondroyd [59] used 'fixed point' theory to determine the optimum damping so as to reduce the vibration response. Since then, different methods of vibration control have been developed and used in rotor-bearing systems. Proper design of a rotor-bearing system is certainly the simplest way to avoid vibration. The system is designed in such a way that the vibration level remains small by ensuring that rotor critical speeds are not coincident with the operating speed or any other excitation frequency. However, required system performance often conflicts with the rotor dynamic performance. The use only of structured design for vibration control is difficult in modern rotating machinery since rotors may be required to pass through several critical speeds during operation.

The use of passive devices, such as dynamic vibration absorbers and squeeze film dampers provides an alternative way for rotor vibration control. The dynamic vibration absorber consists of an additional mass connected to the main system via a spring and damper. It can reduce the vibration level of the main system at a particular frequency. Squeeze film dampers are used increasingly and extensively in controlling rotor vibrations [14,19,22,35]. An oil film is formed between the outer race of a rolling element bearing (or the bush of a sleeve bearing) and its housing. It is this oil film which generates a damping force acting on the rotor to attenuate the rotor vibration amplitude and the force transmitted to the foundation. Passive devices only dissipate energy and may not be effective at every operating condition, especially when several

modes of vibration are excited. Active techniques of vibration control are therefore increasingly being used in place of passive control.

1.2.2 Active Control Devices

The active vibration control of a rotor-bearing system has been a major subject in the research of rotating machinery for more than two decades. Goodwin [30] introduced a variable stiffness squeeze film damper bearing which enables system critical speeds to be tuned away from the instantaneous running speed, due to its feature of having variable stiffness and damping. Furst [28] used an active support system for a rotor with oil-film bearings to attenuate vibration. The rotor was supported by journal bearings which were mounted via electromagnetic actuators on a foundation plate. Different control strategies were used to determine the control forces, which were applied to the rotor via bearing housings. The improvement of the dynamic behaviour of the rotor was demonstrated.

An adaptive squeeze film bearing was introduced by Burrows [9] in 1984. The oil supply pressure was treated as a controllable element and adjusted so that optimal damping forces could be selected for different operating conditions. Significant reduction of both the maximum rotor response amplitudes and the transmitted forces was achieved. Instead of changing oil supply pressure, variation of clearance and land length of squeeze film bearings provides an alternative means for active control of rotor vibration [53]. The difference between this device and a normal squeeze film damper lies in the profiles of the outer housing and inner ring, which are truncated cones. The radial clearance and land length are adjusted to give the optimal dynamic coefficients of the bearing for variable operating conditions. The possibility of controlling rotor vibration was demonstrated in simulated performance. A squeeze film damper with an electro-rheological fluid [52] is another active control device in which

the film viscosity is changed by the application of an electric field. Thus the support damping capacity can be adjusted continuously to remain at the optimal values for different rotor operating conditions. This has been demonstrated with experimental tests in [52].

Rotor active 'anti-swirl' control methods were developed by Muszynska [55] and a tangentially directed fluid flow against rotation is internally generated or externally injected into the rotor/stator clearance. This will reduce the flow velocity and hence increase the stability threshold. The use of piezoelectric actuators in rotor vibration reduction was examined by Palazzolo *et al* [60]. These devices are formed from stacks of piezoelectric ceramic discs which are connected electrically in parallel. When electrical voltage is applied, the stack expands and the resulting force acts on the rotor through a squirrel cage bearing support.

The development of electro-magnetic bearings provided the means of avoiding problems associated with conventional bearings such as friction and lubrication. Rotors could be suspended by electromagnetic forces without any contact. This basic feature results in the following advantages when compared with conventional bearings:

- No wear, allowing unlimited life of rotating machinery
- No lubrication needed, allowing elimination of pumps, filters, pipings, and fluid contamination
- Greatly reduced thermal losses, allowing much higher speeds than conventional hydrodynamic bearings
- Insensitivity to hostile environments such as vacuum and steam.

The other important inherent feature is that the bearing forces can be applied in a controlled manner. Thus the magnetic bearing can be used as a control actuator as

well as a supporting bearing. This leads to the following applications:

- For attenuating unbalance vibration amplitudes, or for counteracting self-exciting forces due to, for example, other conventional bearings
- For precise control of rotor motion allowing more efficient machinery design, such as closer clearances between fans and stators
- For dynamic identification or condition monitoring by applying test forces

However, some disadvantages also exist in magnetic bearing applications:

- Increased complexity in that microprocessors, sensors and software are added to the system
- Electrical power is required to drive magnetic bearings
- They have reduced load carrying capacity compared with conventional bearings

The idea of suspending a rotor using magnetic forces was used as early as 1964 when Beams [1] studied a high speed centrifuge rotor whose vertical position was maintained by the magnetic field of an axial solenoid. Schweitzer [72,73,74] was among the first researchers to combine modern control theory with magnetic bearings for rotor vibration control. The magnetic bearing was regarded as a control actuator with control current as input and electromagnetic force as output. The rotor was considered as the plant so that the whole system formed a control loop. The relations between electromagnetic force and flux density, number of windings, air gap, and input electrical current was derived. Extensive design research was carried out later.

Imlach *et al* [36] examined the magnetic component design using the optimization method. The bearing consisted of four radial magnets and its optimum parameters

were obtained by solving nonlinear equations. The closed-loop stiffness and load capacity of an industrial magnetic bearing were examined later [37] and the agreement between the predicted and the measured values was demonstrated. Bornstein [7] developed equations to express the maximum dynamic load capacities of magnetic bearings in terms of amplifier size, frequency of excitation, magnetic air-gap, method of force actuation, and geometry factor relating the magnetic area to the inductive area. Maslen *et al* [50] examined load capacity requirements for active bearings supporting a flexible rotor subject to harmonic loading.

1.2.3 Review Of Magnetic Bearing Control

The use of magnetic bearings for automatic rotor balancing is another research area. Magnetic forces acting on a rotor can make its spinning axis correspond with the principal axis of inertia and consequently no reaction force is transmitted through the bearings. Higuchi [32] studied a system composed by a rigid rotor supported vertically by an axial magnetic bearing and two radial magnetic bearings. A digital controller for automatic balancing using an observer was developed and implemented. The effectiveness of using magnetic bearings for automatic balancing was demonstrated by numerical simulation and experiments. Kanemitsu *et al* [42] examined a system consisting of a flexible rotor supported by two radial magnetic bearings and located by a thrust magnetic bearing. Analog and digital compensators were designed by the so-called 'effective coefficient method' and used for real time balancing. The other control scheme used for rotor balancing by magnetic bearings is based on the state-space approach in which output regulator with internal stability concepts was introduced and demonstrated by simulation [41].

Magnetic bearings can also be used to suppress the rotor self-excited vibration caused by journal bearings. Burrows *et al* [16] examined a flexible rotor supported by two

journal bearings and a magnetic actuator. It was shown that instability due to oil whirl at high running speeds may be controlled by the actuator. Keith *et al* [44] designed a digital controller based on the proportional-derivative method, which was used to operate magnetic bearings on a test rig. Williams *et al* [80] compared analog and digital control for reducing rotor vibration by magnetic bearings. Nomami *et al* [58] examined a rotor supported by two ball bearings and two magnetic bearings. Direct output feedback control was applied to the system. Hisatani *et al* [33] discussed several strategies for direct output feedback control design in rotor-magnetic bearing systems and examined the system stability. Schmied [71] described theoretical and test results of the vibrational behaviour of a 6MW pipeline compressor supported on magnetic bearings. Kirk *et al* [45] gave design and test results for a high-speed eight stage centrifugal compressor supported by active magnetic bearings.

Bleuler *et al* [4] studied a system consisting of a rigid rotor supported by two magnetic bearings. The concept of decentralized optimal state feedback was used to design the controller. Salm [68] examined two magnetic bearings to support and control a flexible rotor. The direct-output feedback scheme was applied to the control design. However, it was found that the controller designed using a reduced order system may cause an unstable full order closed loop system. This spillover problem can be solved by adding the constraint condition of co-located actuators and sensors [67]. Lee *et al* [47] used a suboptimal output feedback controller to control unstable or lightly damped vibration with a magnetic bearing. Spillover was prevented using constrained optimization and incorporating the spillover term into the performance index. Chen and Darlow [17] used a magnetic bearing combined with three parallel feedback control loops with velocity and acceleration observers to attenuate vibrations. The measured feedback displacements and estimated velocity were used to provide the stiffness and damping forces. Feedback estimated acceleration was used to create

rotating forces which cancelled the unbalance forces and other external disturbances.

The problems caused by spillover effect in the closed-loop control of rotor bearing systems led Burrows and his colleagues to develop an open-loop strategy [10]. The case of a flexible rotor supported by two journal bearings was examined and a magnetic actuator was used to estimate system characteristics and apply the optimum control forces to minimize synchronous vibration. The control forces were determined without any prior knowledge of the system and significant vibration reduction was achieved [11,12,13,15]. Recently, the work has been extended to use closed-loop feedback control designed based on pole assignment theory. The comparison was made between the open-loop adaptive control and the closed-loop control results [16]. Larsonneur *et al* [46] demonstrated the use of magnetic bearings together with feedforward compensation control to reduce unbalance vibration amplitudes for flexible rotors.

The recent development of H_∞ based control techniques has been brought into the research area of vibration control of rotor-bearing systems. Fujita *et al* [27] carried out H_∞ control design for a magnetic suspension system in which a flexible beam was supported by a hinge at one end and suspended by a electromagnet at the other end. The rig was modelled with two states as a single-input single-output system. It was demonstrated that the designed magnetic suspension system was robustly stable against various parameter changes. Herzog and Bleuler [31] implemented H_∞ control theory to a magnetic bearing used for reducing vibration of milling tools. Their research focused mainly on trade-offs involved in the frequency domain in the controller design. The application of the H_∞ optimization technique to a pair of magnetic bearings used to support and control a flexible rotor was examined by Mu *et al* [54]. The comparison was made between H_∞ and *LQG* controller designs. It was indicated

that a rotor can pass through several critical speeds at low vibration amplitudes by using the H_∞ strategy. It was also shown that the rotor vibration can be reduced significantly and the H_∞ controller does not suffer from modelling uncertainty spillover.

It is seen from the foregoing survey that there are still problems in the vibration control of rotor-bearing systems. It is these problems which resulted in the motivation of the research work in this thesis.

1.3 Justification Of Present Research

The spillover effect arising in closed-loop control systems is due both to measurement error and control signals. Real signals obtained by a controller, which is designed based on a modelled system, are contaminated by noise and may cause the closed-loop system to be unstable. The signal coming from a controller, which is designed based on a reduced order model, acts on the full order system and may result in the instability by excitation of neglected modes. The use of the open-loop adaptive control strategy developed by Burrows [10] avoids the possibility of instability associated with a closed-loop structure and the rotor vibration level is reduced significantly with the full utilization of the magnetic bearings as active elements. However, the work has been restricted to the control of synchronous vibration in rotating machinery. Also, a controller design based on real-time least squares estimation is not robust to system parameter changes. These may be caused by the rotor speed dependent parameters such as unbalance forcing and journal bearing characteristics. The control of both synchronous and transient vibration and avoidance of instability is the general aim of the work in this thesis.

The H_∞ optimization technique is a method for designing a robust controller and the

possibility of overcoming the spillover problems, which are usually caused by modelling uncertainty and measurement disturbance in rotor-bearing systems, is therefore feasible. Furthermore, this closed-loop control method is capable of dealing with both synchronous and transient conditions. So far, little work has been done in robust control design for rotor-bearing systems. Research on using H_∞ techniques for robust control in the rotor-bearing systems is sparse with no experimental results for rotor vibration control existing in the open literature. Therefore the present work will give a detailed insight into the systematic process of applying H_∞ control design in rotor-bearing systems and to validate the control experimentally.

1.4 Structure Of The Thesis

The modelling of flexible rotor-bearing systems is given in Chapter 2. Chapter 3 begins with a survey of control theories that have been applied in rotor-bearing systems and specifies their advantages and disadvantage. Then the design procedure for an H_∞ controller is described in detail and the resulting controller form is expressed. Chapter 4 discusses the theoretical model of the rotor-bearing system under consideration with computer simulation. This includes analysis of critical speeds and modes, model reduction, formulation of a standard equation of H_∞ problem for a rotor-bearing system, off-line design of controllers, and simulation of H_∞ controlled system dynamic response.

Details of the experimental rotor rig are given in Chapter 5 and the data acquisition system and computer hardware/software set-up are described. In Chapter 6, the control strategies are applied to the experimental rig and the simulated results are given. Experimental results are considered in Chapter 7 including the control achieved under both steady state and transient conditions. Conclusions and recommendations for further work are given in Chapter 8.

CHAPTER 2 REVIEW OF ROTOR-BEARING SYSTEM MODELLING

2.1 Introduction

Physical motion of mechanical components such as rotors and bearings can be modelled by mathematical means. The development of computers has enabled engineers to use the models to evaluate designs and predict system performance. Continuous systems have an infinite number of degrees of freedom and their behaviour is described by partial differential equations. However, these may be discretised in order that numerical analysis can be performed computationally. Several numerical methods have been developed to model rotor-bearing systems with a finite number of degrees of freedom. These include the use of:

- Transfer matrices
- Model analysis
- Influence coefficients
- Stiffness coefficients
- Finite elements techniques

The procedure for modelling journal bearing characteristics consists of simplifying the Navier-Stokes equations to the Reynolds equation and solving for lubricant pressure.

Modelling methods are included in this thesis in order that their suitability for control design can be assessed. They are described in outline only since they are available in the open literature.

2.2 Modelling Of Rotors

Usually rotors have rather complicated geometries and some assumptions should be made before any modelling is to be carried out. This is not only to simplify the problems, but also to enable engineers to focus more attention to the main feature of

the system they are interested in. The following assumptions are made in the modelling in this thesis:

- The rotor is symmetric about its axis of rotation
- The rotor material has linear isotropic properties
- The rotor is initially straight
- The axial load is negligible
- The rotor lateral vibration is decoupled from applied torques

2.2.1 Modelling Methods

There are several methods for system modelling. Among them, transfer matrix methods [63] are efficient in evaluating low frequency vibrational modes. The shaft is divided into different segments according to the shaft geometry. The elastic properties of a segment can be expressed by introducing state variables at each end and whose relationship is given by a transfer matrix. The combination of transfer matrices of all segments, together with application of boundary conditions, will form the complete system equations. The main benefit of the method lies in the small memory needed in computer calculation, while the disadvantage is that the higher modes can not be guaranteed to be accurate.

The influence coefficient method [78] provides an alternative way of modelling a rotor system in which the elastic properties of the rotor system are embodied in a flexibility matrix. The element at position (i j) of the matrix is the generalized deflection at the i-th station caused by a unit generalized force exerted at the j-th station. After the flexibility matrix has been obtained, the system dynamic equation is of the form

$$\Lambda(\boldsymbol{M}\ddot{\boldsymbol{q}}) + \Lambda(\boldsymbol{C}\dot{\boldsymbol{q}}) + \boldsymbol{q} = \Lambda \boldsymbol{f} \tag{2.1}$$

where Λ is the flexibility matrix, $\boldsymbol{M}$ is the inertia matrix, $\boldsymbol{C}$ is the damping matrix, $\boldsymbol{q}$ is the displacement vector, and $\boldsymbol{f}$ is the force vector. However, care must be taken in

using this method since the matrix may be ill conditioned, for example, when a free-free rotor is considered.

If, instead of flexibility matrix being introduced, its inverse is formulated, then this matrix is called the stiffness matrix. An element at position (i j) in the matrix is the generalized force required at a station i when a unit generalized deflection occurs at station j. The method is called the stiffness coefficient method and the system dynamic equation can be expressed as:

$$M\ddot{q} + C\dot{q} + Kq = f \tag{2.2}$$

where K is the stiffness matrix. If inversion of K is permissible, the method is basically equivalent to influence coefficient method since $\Lambda=K^{-1}$.

Modal analysis requires system equations to be constructed and then decoupled into individual differential equations each having a single-degree-of-freedom representation. If equation (2.2) is placed into the well known state space form, then

$$\begin{bmatrix} \dot{q} \\ \ddot{q} \end{bmatrix} = \begin{bmatrix} 0 & I \\ -M^{-1}K & -M^{-1}C \end{bmatrix} \begin{bmatrix} q \\ \dot{q} \end{bmatrix} + \begin{bmatrix} 0 \\ M^{-1}f \end{bmatrix} \tag{2.3}$$

Since the system matrix in equation (2.3) is not symmetric, modal analysis requires solution of both left and right eigenvectors. Let the left eigenvectors form the matrix U^{L} and the right eigenvectors form U^{R}. It follows that

$$(U^{L})^{T} \begin{bmatrix} 0 & I \\ -M^{-1}K & -M^{-1}C \end{bmatrix} U^{R}$$

is a diagonal matrix. Therefore, by the coordinate transformation,

$$\begin{bmatrix} q \\ \dot{q} \end{bmatrix} = U^{R} p \tag{2.4}$$

the system equations can be transformed to

$$\dot{p} = \begin{bmatrix} \diagdown & & \\ & \omega_i^2+2j\zeta_i\omega_i & \\ & & \diagdown \end{bmatrix} p + \left(U^L\right)^T \begin{bmatrix} 0 \\ \\ M^{-1}f \end{bmatrix} \qquad (2.5)$$

The finite element technique is a more accurate method of constructing the mathematical system model. Instead of discretising the mass and stiffness at each element end, as in the stiffness coefficient method, the inertia and the stiffness properties of the rotor are formed in a distributed manner. This is the main reason for the relatively high accuracy when compared to the conventional lumped parameter approach. In recent years, the finite element method has been used for rotor dynamics analysis [25,56]. Although the method requires more computer time and storage than other methods, it provides significantly greater accuracy for a given rotor discretization. The construction of the mathematical model that follows is carried out by the finite element method and is based upon Timoshenko beam theory.

2.2.2 Coordinates And Shape Functions Of Finite Element Method

Most flexible rotors are composed of shaft elements and discrete discs. A typical rotor element is illustrated in figure 2.1, together with the coordinate system used to describe the end point displacements. Here (X, Y, Z) is a fixed coordinate system with the Z axis coinciding with the undeformed centreline of the element. The element is considered to be initially straight and is modelled as an eight degree of freedom element system with two translation and two angular displacements at each end point of the element. The cross-section of the element is annular.

Let the element coordinates be written in the vector

$$q^e = \left[q_1,\ q_2,\ q_3,\ q_4,\ q_5,\ q_6,\ q_7,\ q_8\right]^T \qquad (2.6)$$

where q_1,.....,q_4 correspond to the right end, whilst q_5,.....,q_8 correspond to the left end. The translation and angular displacements at a distance ξ from the right end can be described in terms of $\boldsymbol{q}^e$ as

$$v(\xi,t) = \begin{Bmatrix} v_x \\ v_y \end{Bmatrix} = N_t(\xi)\boldsymbol{q}^e(t) \quad , \qquad w(\xi,t) = \begin{Bmatrix} w_x \\ w_y \end{Bmatrix} = N_r(\xi)\boldsymbol{q}^e(t) \tag{2.7}$$

respectively, where

$$\begin{aligned} N_t(\xi) &= \begin{bmatrix} N_{t1} & 0 & 0 & N_{t2} & N_{t3} & 0 & 0 & N_{t4} \\ 0 & N_{t1} & -N_{t2} & 0 & 0 & N_{t3} & -N_{t4} & 0 \end{bmatrix} \\ N_r(\xi) &= \begin{bmatrix} 0 & -N_{r1} & N_{r2} & 0 & 0 & -N_{r3} & N_{r4} & 0 \\ N_{r1} & 0 & 0 & N_{r2} & N_{r3} & 0 & 0 & N_{r4} \end{bmatrix} \end{aligned} \tag{2.8}$$

are the translational and angular displacement shape functions.

In order to derive the above expressions, the deformation including shear effect in the x-z plane is examined. The rotation of the infinitesimal disc of the element can be written as

$$\theta_x = \frac{\partial v_x}{\partial \xi} + \phi_{\xi x} \tag{2.9}$$

where $\partial v_x / \partial \xi$ is the gradient of the neutral axis and $\phi_{\xi x}$ is the shear angle. For static equilibrium,

$$\frac{M_y}{EI} = \frac{\partial^2 v_x}{\partial \xi^2} + \frac{\partial \phi_{\xi x}}{\partial \xi} \quad , \quad F_x = \frac{\partial M_y}{\partial \xi} \quad , \quad \frac{\partial F_x}{\partial \xi} = 0 \tag{2.10}$$

The shear angle is

$$\phi_{\xi x} = \frac{F_x}{kAG} \tag{2.11}$$

Appropriate shape functions can be derived by assuming a cubic displacement along the element into the above equations,

$$v_x = a_0 + a_1\xi + \frac{1}{2}a_2\xi^2 + \frac{1}{6}a_3\xi^3 \tag{2.12}$$

where the constant a_i are determined on substitution of the boundary conditions. For example, for $N_{t1}(\xi)$,

$$\begin{aligned} &N_{t1}(0)= 1 \quad , && N_{t1}(l) = 0, \\ &\left\{\frac{dN_{t1}}{d\xi} + \phi_{\xi x}\right\}_{\xi=0} = 0 \quad , && \left\{\frac{dN_{t1}}{d\xi} + \phi_{\xi x}\right\}_{\xi=l} = 0. \end{aligned} \tag{2.13}$$

The shape functions for the angular displacements, $N_{ri}(\xi)$, can also be derived in the same manner. Both translational and angular shape functions can be written as:

$$\begin{aligned} &N_{ti} = \frac{1}{1+\Phi}\left(\alpha_{ti}+\Phi\beta_{ti}\right) \quad , \quad N_{ri} = \frac{1}{1+\Phi}\left(\alpha_{ri}+\Phi\beta_{ri}\right) \\ &i = 1,2,3,4 \end{aligned} \tag{2.14}$$

$$\begin{aligned} &\alpha_{t1}=1-3l\upsilon^2+2\upsilon^3 \ , \ \alpha_{t2}=l(\upsilon-2\upsilon^2+\upsilon^3) \ , \ \beta_{t1}=1-\upsilon \ , \ \beta_{t2}=\frac{l}{2}(\upsilon-\upsilon^2) \\ &\alpha_{t3}=3\upsilon^2-2\upsilon^3 \ , \quad \alpha_{t4}=\frac{l}{2}(-2\upsilon^2+2\upsilon^3) \ , \ \beta_{t3}=\upsilon \ , \quad \beta_{t4}=\frac{l}{2}(-\upsilon+\upsilon^2) \end{aligned} \tag{2.15}$$

$$\begin{aligned} &\alpha_{r1}=\frac{1}{l}(6\upsilon^2-6\upsilon) \ , \ \alpha_{r2}=1-4\upsilon+3\upsilon^2 \ , \ \beta_{r1}=0 \ , \ \beta_{r2}=1-\upsilon \\ &\alpha_{r3}=\frac{1}{l}(-6\upsilon^2+6\upsilon) \ , \ \alpha_{r4}=3\upsilon^2-2\upsilon \ , \quad \beta_{r3}=0 \ , \ \beta_{r4}=\upsilon \end{aligned} \tag{2.16}$$

where

$$\Phi = \frac{12EI}{kAGl^2} \ , \qquad \upsilon = \frac{\xi}{l} \tag{2.17}$$

2.2.3 Element Equation Of Motion

By examining the rotor element shown in figure 2.1, the differential strain energy of an infinitesimal disc due to bending and shear can be written as

$$dU = \frac{1}{2}EI\left\{v_b''\right\}^T\left\{v_b''\right\}d\xi + \frac{1}{2}kAG\left\{v_s'\right\}^T\left\{v_s'\right\}d\xi \qquad (2.18)$$

where v_b and v_s denote the translations from the bending and shear respectively. Substituting the displacement equations (2.7) into (2.18) and then integrating over the length of the element, the total strain energy for the element is of the form

$$U = \frac{1}{2}\, q^{e\tau}\, K^e\, q^e \qquad (2.19)$$

where K^e is the element stiffness matrix and is of the form

$$K^e = \int_0^l EI\left\{\left[N_{tb}''\right]^T\left[N_{tb}''\right] + \frac{12}{\Phi l^2}\left[N_{ts}'\right]^T\left[N_{ts}'\right]\right\}d\xi \qquad (2.20)$$

The kinetic energy of the infinitesimal disc due to translational and angular mass can be written as

$$dT_t = \frac{1}{2}m(\xi)\dot{v}^T\dot{v}\,d\xi + \frac{1}{2}I_d(\xi)\dot{w}^T\dot{w}\,d\xi \qquad (2.21)$$

where $m(\xi)$ and $I_d(\xi)$ are mass and diametral moment of inertia per unit length respectively. The total kinetic energy is

$$T_t = \frac{1}{2}\, q^{e\tau}\left[M_t^e + M_r^e\right]q^e \qquad (2.22)$$

where the element translational and angular mass matrix are

$$M_t^e = \int_0^l m(\xi)\, N_t^T\, N_t\, d\xi \quad , \quad M_r^e = \int_0^l I_d(\xi)\, N_r^T\, N_r\, d\xi \qquad (2.23)$$

The kinetic energy due to the gyroscopic moments is given by

$$dT_g = \frac{1}{2} I_p(\xi)\Omega w^T \begin{bmatrix} 0 & -1 \\ 1 & 0 \end{bmatrix} \dot{w} d\xi \tag{2.24}$$

and the total kinetic energy is given

$$T_g = \frac{1}{2}\Omega q^{eT} G^e \dot{q}^e \tag{2.25}$$

where the element gyroscopic matrix is

$$G^e = \int_0^l I_p(\xi)\, N_r^T \begin{bmatrix} 0 & -1 \\ 1 & 0 \end{bmatrix} N_r d\xi \tag{2.26}$$

The detailed forms of all above matrices can be found in Appendix A.

By using the Lagrange method, the equation of motion of the element can be expressed by

$$\left(M_t^e + M_r^e\right)\ddot{q}^e - \Omega G^e \dot{q}^e + K^e q^e = f^e \tag{2.27}$$

where f^e is the forcing vector.

2.2.4 Rotor Equation Of Motion

Without considering the supports, the rotor equation can be built up by introducing a new global coordinate system,

$$Q = \left[q_1 \;\; q_2 \;\; \cdots\cdots \;\; q_{4n+4}\right]^T$$

where n is the number of the rotor elements. The new global mass, stiffness, gyroscopic and force matrices can be assembled by using their corresponding element matrices in the element equations. The resulting rotor dynamic equation with damping included can be written as

$$M_s \ddot{Q} + C_s \dot{Q} + K_s Q = F_s \tag{2.28}$$

Components such as impellers, flywheels, which are mounted on the rotor, can be assumed to be rigid discs which are described by mass, transverse moment of inertia and polar moment of inertia. Usually, elements are chosen in such way that the discs are located at their ends. Hence, the equation of the system consisting of flexible shaft and rigid discs can be formed by adding the mass, gyroscopic, and force terms in equation (2.28). The new equation can be written as

$$\left(M_s + \sum_{\text{discs}} M_d\right)\ddot{Q} + \left(C_s + \sum_{\text{discs}} C_d\right)\dot{Q} + K_s Q = F_s + \sum_{\text{discs}} F_d \qquad (2.29)$$

2.3 Modelling Of Journal Bearings

Journal bearings are used to support rotors. The pressure built up in the oil film generates the supporting force. The dynamic characteristics of journal bearings have a great influence on the vibration of rotor systems, both in response to disturbance and in stability of running. Mathematical modelling of journal bearings is based upon hydrodynamic lubrication theory. Some assumptions in the modelling of journal bearings made here are:

- The oil film thickness is much smaller than journal dimensions
- The inertia of oil film is negligible
- The flow in the oil film is laminar
- The viscosity and density of oil are constant throughout the bearing
- The oil is a Newtonian fluid with viscosity independent of shear rate

2.3.1 Reynolds Equation For Oil Film

The geometry of the journal bearing and the coordinate system are shown in figure 2.2. The bearing centre is C_b and the journal centre is displaced to C_j. The attitude line through C_bC_j intersects the film thickness between bearing and journal at its maximum and minimum values. C_s is the journal centre under static load. (X, Y) is a fixed

reference frame with its origin located at the C_b, while (r, s) is a fixed coordinate with some angular difference from the coordinate (X, Y). Another coordinate system (1, 2) rotates with the maximum clearance position when rotor rotates. The Reynolds equation for a journal bearing can be deduced as [34]

$$\frac{1}{R}\frac{\partial}{\partial\theta}\left(\frac{h^3}{R}\frac{\partial p}{\partial\theta}\right) + \frac{\partial}{\partial z}\left(h^3\frac{\partial p}{\partial z}\right) = 12\mu\frac{\partial h}{\partial t} + 6\left(\Omega-2\dot{\phi}\right)\mu\frac{\partial h}{\partial\theta} \qquad (2.30)$$

where the film thickness for a circular bearing is given by

$$h = c\left(1+\varepsilon\cos\theta\right)$$

2.3.2 Non-linear Oil Film Force

For short bearings whose length to diameter ratio is small, reliable results may be obtained by ignoring the first term of the left-hand side of equation (2.30) [34]. In this case, the equation becomes

$$\frac{\partial}{\partial z}\left(h^3\frac{\partial p}{\partial z}\right) = 12\mu\frac{\partial h}{\partial t} + 6\left(\Omega-2\dot{\phi}\right)\mu\frac{\partial h}{\partial\theta} \qquad (2.31)$$

Integration of equation (2.31) subject to the boundary conditions $p = 0$ at $z = 0$ and $z = L$ results in the expression of oil film pressure as

$$p = \frac{3z(z-L)\mu\left(2\dot{\varepsilon}\cos\theta - (\Omega-2\dot{\phi})\varepsilon\sin\theta\right)}{c^2(1+\varepsilon\cos\theta)^3} \qquad (2.32)$$

By integrating equation (2.32) in the positive pressure region, the oil film force in directions 1 and 2 can be derived as

$$F_1 = -\frac{\mu L^3 R}{2c^2}\left(\frac{\pi(1+2\varepsilon^2)l\dot{\varepsilon}}{(1-\varepsilon^2)^{5/2}} - \frac{2(\Omega-2\dot{\phi})\varepsilon^2}{(1-\varepsilon^2)^2}\right)$$

$$F_2 = \frac{\mu L^3 R}{2c^2}\left(\frac{4\varepsilon\dot{\varepsilon}}{(1-\varepsilon^2)^2} - \frac{(\Omega-2\dot{\phi})\pi\varepsilon}{2(1-l\varepsilon^2)^{3/2}}\right) \qquad (2.33)$$

2.3.3 Expression Of Linearised Oil Film Force

It is clear that oil film forces are highly non-linear functions of journal position and velocity. They are usually linearised so that dynamic analysis of a rotor system can be carried out. Suppose that the position under the action of the external static load is C_s, which can be expressed by ε_o and ϕ_o, and the C_jC_s is small compared with C_bC_s. The journal is assumed to have small oscillations about the position C_s. By resolving the oil film forces in directions *r*, *s* and linearizing them about C_s, the oil film forces become

$$\begin{aligned} F_r &= -c_{rr}\dot{r} - k_{rr}r + c_{rs}\dot{s} - k_{rs}s - F_{ro} \\ F_s &= c_{sr}\dot{r} + k_{sr}r - c_{ss}\dot{s} - k_{ss}s + F_{so} \end{aligned} \tag{2.34}$$

The corresponding dynamic force expression in the fixed *X-Y* coordinate system is of the form

$$\begin{aligned} F_x &= -c_{xx}\dot{x} - c_{xy}\dot{y} - k_{xx}x - k_{xy}y + F_{xo} \\ F_y &= -c_{yx}\dot{x} - c_{yy}\dot{y} - k_{yx}x - k_{yy}y + F_{yo} \end{aligned} \tag{2.35}$$

Here both the coefficients and the constants in equation (2.34) are functions of the ε_o and ϕ_o. As long as the static load is known, they can be obtained by solving a nonlinear algebraic equation. Hence all stiffness and damping coefficients can be deduced by substituting ε_o and ϕ_o into the coefficient expressions. The detailed expressions are given in Appendix B.

2.4 Complete Rotor-Bearing System Equations

Having linearised the oil film force, the whole system equation may easily be obtained by simply adding the stiffness and damping matrices due to the oil film force of the bearing into the rotor equation (2.29). Suppose an oil film bearing is mounted on the

rotor at the i-th node position. The stiffness matrix $\boldsymbol{K}_b$ of the bearing has non-zero elements

$$\boldsymbol{K}_b\big(4(i-1)+1\ ,\ 4(i-1)+1\big) = k_{xx} \quad , \quad \boldsymbol{K}_b\big(4(i-1)+1\ ,\ 4(i-1)+2\big) = k_{xy}$$

$$\boldsymbol{K}_b\big(4(i-1)+2\ ,\ 4(i-1)+1\big) = k_{yx} \quad , \quad \boldsymbol{K}_b\big(4(i-1)+2\ ,\ 4(i-1)+2\big) = k_{yy}$$

The damping matrix $\boldsymbol{C}_b$ due to the bearing can be built up in the same way with non-zero elements

$$\boldsymbol{C}_b\big(4(i-1)+1\ ,\ 4(i-1)+1\big) = c_{xx} \quad , \quad \boldsymbol{C}_b\big(4(i-1)+1\ ,\ 4(i-1)+2\big) = c_{xy}$$

$$\boldsymbol{C}_b\big(4(i-1)+2\ ,\ 4(i-1)+1\big) = c_{yx} \quad , \quad \boldsymbol{C}_b\big(4(i-1)+2\ ,\ 4(i-1)+2\big) = c_{yy}$$

The rotor-bearing system equation can be obtained, by adding the stiffness and damping matrices due to oil film bearing to the rotor equation (2.29), as

$$\left(\boldsymbol{M}_s + \sum_{\text{discs}} \boldsymbol{M}_d\right)\ddot{\boldsymbol{Q}} + \left(\boldsymbol{C}_s + \sum_{\text{discs}} \boldsymbol{C}_d + \sum_{\text{bearings}} \boldsymbol{C}_b\right)\dot{\boldsymbol{Q}} + \left(\boldsymbol{K}_s + \sum_{\text{bearings}} \boldsymbol{K}_b\right)\boldsymbol{Q} = \boldsymbol{F}_s + \sum_{\text{discs}} \boldsymbol{F}_d \tag{2.36}$$

The resulting equations of motion for the rotor-bearing system can be re-written in the familiar form as

$$\boldsymbol{M}\ddot{\boldsymbol{Q}} + \boldsymbol{C}\dot{\boldsymbol{Q}} + \boldsymbol{K}\boldsymbol{Q} = \boldsymbol{F} \tag{2.37}$$

The damping matrix $\boldsymbol{C}$ and stiffness matrix $\boldsymbol{K}$ are non-symmetric and are functions of the rotor rotational speed. This is due to the effect of the journal bearings and gyroscopic terms.

2.5 System Dynamic Analysis

The system dynamic analysis can be performed after the system equation (2.37) has

been constructed. The work is usually associated with rotor unbalance response and stability analysis.

2.5.1 Unbalance Response Analysis

If the principal axis of inertia of the rotor does not coincide with the rotor geometric axis, a centrifugal force will be generated when the rotor is rotating about the geometrical axis along the rotor. This force is synchronous with the rotor running speed and causes whirl motion of the rotor, and synchronous vibration in the structure of the rotating machinery through the bearing supports.

The unbalance force on the rotor is of the form

$$\boldsymbol{F} = \boldsymbol{F}_0 e^{j\Omega t} + \bar{\boldsymbol{F}}_0 e^{-j\Omega t} \tag{2.38}$$

where $\bar{\boldsymbol{F}}_0$ is complex unbalance amplitude. The steady response is

$$\boldsymbol{Q} = \boldsymbol{Q}_0 e^{j\Omega t} + \bar{\boldsymbol{Q}}_0 e^{-j\Omega t} \tag{2.39}$$

where

$$\boldsymbol{Q}_0 = \left[\boldsymbol{K} - \Omega^2 \boldsymbol{M} + j\Omega \boldsymbol{C}\right]^{-1} \boldsymbol{F}_0$$

defines elliptic orbits at the rotor element nodes.

2.5.2 Stability Analysis

System instability is another source of rotor vibration. Even if the rotor is perfectly balanced, a small disturbance can lead to severe vibrations for unstable systems. This is sometimes referred to as self-excited vibration.

For stability analysis, the unforced system equation can be written as

$$\boldsymbol{M}\ddot{\boldsymbol{Q}} + \boldsymbol{C}\dot{\boldsymbol{Q}} + \boldsymbol{K}\boldsymbol{Q} = \boldsymbol{0} \tag{2.40}$$

which can be conveniently transferred to the first order form

$$\dot{Z} = \begin{bmatrix} 0 & I \\ -M^{-1}K & -M^{-1}C \end{bmatrix} Z \tag{2.41}$$

where

$$Z = \begin{bmatrix} Q^{T} & \dot{Q}^{T} \end{bmatrix}^{T}$$

Assuming a solution in the form

$$Z = Z_0 e^{\lambda t} \tag{2.42}$$

this leads to the standard eigenvalue problem

$$\left(\lambda I - \begin{bmatrix} 0 & I \\ -M^{-1}K & -M^{-1}C \end{bmatrix} \right) Z_0 = 0 \tag{2.43}$$

System stability can be judged from the real parts of the eigenvalues. If one or more of the real parts is positive, then the system is unstable. Otherwise the system is stable.

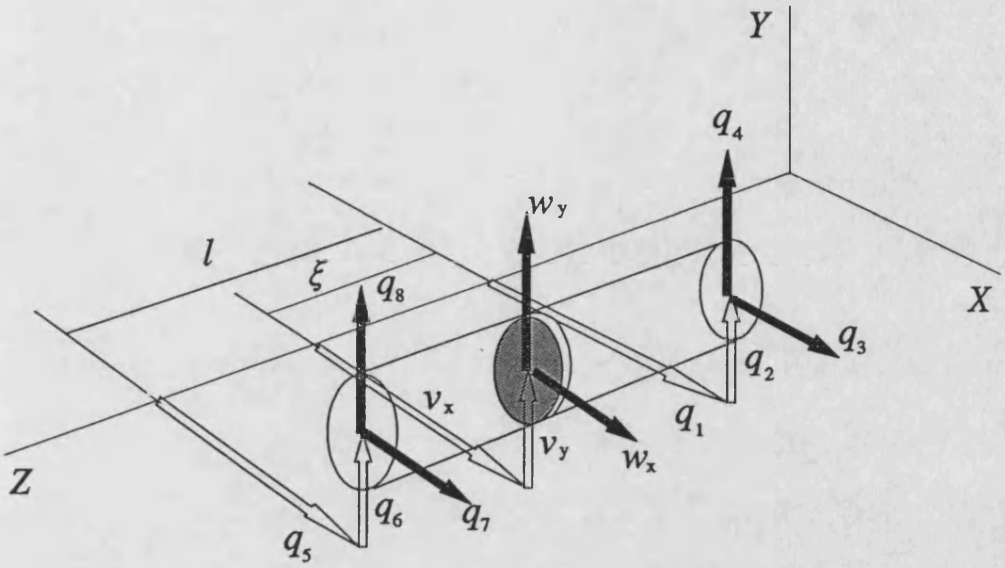

Fig. 2.1 Rotor finite element and coordinates (⇨ signifies linear displacements, ➡ signifies angular displacements)

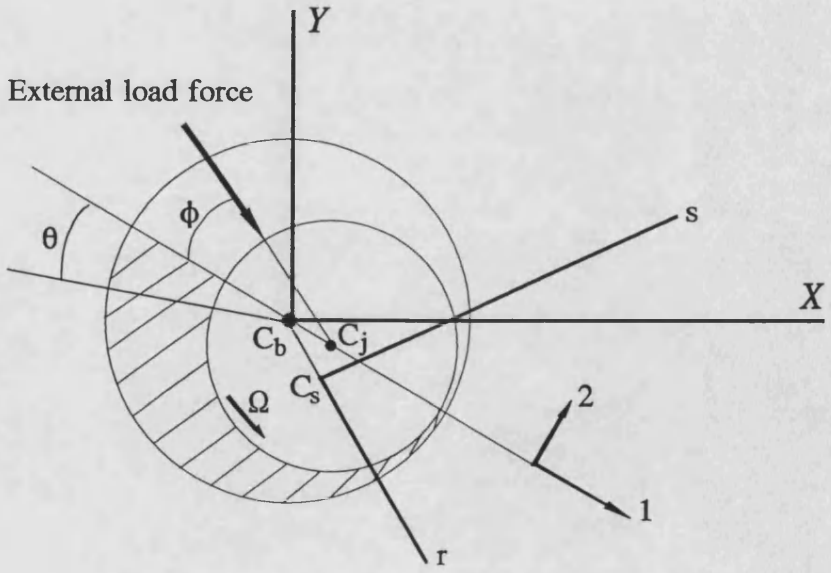

Fig. 2.2 Geometry and coordinate axes of oil-film bearing

CHAPTER 3 REVIEW OF CONTROL STRATEGIES FOR ATTENUATING ROTOR VIBRATION

3.1 Introduction

The development of sophisticated electromagnetic actuators enables control strategies to be implemented for the control of rotor vibration. Usually, introduction of active control to the system focuses attention on the need to develop effective strategies rather than on component hardware design. In rotor-bearing systems, successful implementation of a control strategy is considered after achieving the following criteria:

- Minimisation of rotor vibration amplitudes
- Control forces are within the capability of the actuator
- The system is stable
- The system is robust to imperfection in plant model

This chapter will consider a brief review of the previous work concerned with active control strategies. Then the advantages and disadvantages of different strategies are summarized and the associated problems are detailed. Finally, the H_∞ optimization control design method is introduced.

3.2 Review Of Control Strategies

Different control strategies have been developed and implemented in rotor-bearing systems. They range from the simple local control to more complex centralized control in the categories:

- Local control
- Decentralized control
- Centralized control

3.2.1 Local Control

Suppose that actuators and sensors are collocated and there is no interaction between different positions, i.e. the control signals are obtained directly from the measured signals at the same position. This is known as a local control strategy. There are several control design algorithms for local control. One is damping control which is based upon the theory that there are frequencies at which the vibration amplitude is independent of the system damping constant [21]. These frequencies are usually known as 'fixed points'. The theory was applied to a system consisting of a flexible shaft supported on oil-film bearings for minimizing the synchronous response [22]. The theory was also applied to an 'on-off' adaptive squeeze film damper for rotor vibration control [9]. Good vibration control of a light flexible transmission shaft having an arbitrary unbalance mass distribution was achieved.

In contrast with damping control, stiffness control is carried out by the modification of the system stiffness so as to shift the system natural frequencies. Thus, the system operating speed can always be kept away from the critical speeds so that the system vibration response can be reduced significantly. The effect of changing the support stiffness and thus altering the system critical speeds has been examined by Sandler [69]. In rotor-bearing systems, an adaptive stiffness control strategy by Redmond [65] resulted in avoidance of the shaft critical speeds and a low response level even in the absence of system damping. However, lack of the damping could mean poor robustness of the controller. Therefore, the better alternative is to use combined damping and stiffness control theory. This theory was used by Cunningham [20] to design a squeeze-film damper for a multi-mass flexible rotor. The influence of flexible damped supports on rotor amplitudes and forces transmitted was examined over the speed range encompassing several critical speeds. An investigation of the application of stiffness and damping control to a flexible rotor was also carried out in [43]. The

optimum frequency dependent stiffness and damping coefficients of the system were determined and the overall maximum shaft response amplitude was minimized.

3.2.2 Decentralized Control

A system is assumed to be decomposed into a number of sub-systems as

$$\dot{x}_i = A_i x_i + B_i u_i + R_i , \quad i=1,2,...,p$$

where

$$R_i = \sum_{j=1}^{p} A_{ij} x_j, \quad i=1,2,...,p$$

are interaction terms of each sub-system. The control can be designed based upon the sub-systems with ignored interconnections. The performance index of each sub-system is formulated and the decentralised control design is carried out by optimizing each index as if the sub-systems are decoupled. When the sub-systems are coupled together, the interactions act as perturbations which may worsen each sub-system performance index. Finally, the resulting controller should be applied to the overall system so that the stability of the overall closed-loop system can be examined.

A decentralized optimal state feedback control was derived for a magnetic rotor-bearing system by Bleuler [4]. The rotor was modelled as being rigid on two magnetic bearing supports. It was indicated that a reduction in complexity of the problem can be included without significant loss in system performance. More detailed work was given later in [5]. The theory was also applied to the vibration control of an active rotor isolation system [48]. It was demonstrated by analytical and simulation work that the system can be decomposed into four sub-systems with the symmetrical pattern of interactions. The Linear Quadratic (*LQ*) control methods were then utilized to design the control for each sub-systems in a decentralized manner. It was shown that the resulting controller had vibration isolation characteristics and also maintained the overall system stability.

3.2.3 Centralized Control

Differing from both local and decentralized controls, the centralized control system is not required to be decomposed and the control design is based on the overall system. The most commonly used methods are Linear Quadratic Gaussian (*LQG*) control, pole assignment, and open loop adaptive control.

3.2.3.1 Linear Quadratic Gaussian Control

LQG control is a strategy which can lead to a stabilizing linear controller. The problem is formulated from the system equations

$$\begin{aligned} \dot{\boldsymbol{x}} &= \boldsymbol{A}\boldsymbol{x} + \boldsymbol{B}\boldsymbol{u} + \boldsymbol{w}_{\mathrm{u}} \\ \boldsymbol{y} &= \boldsymbol{C}\boldsymbol{x} + \boldsymbol{w}_{\mathrm{y}} \end{aligned} \tag{3.1}$$

where $\boldsymbol{w}_{\mathrm{u}}$ and $\boldsymbol{w}_{\mathrm{y}}$ are random white noise disturbances. The quadratic performance index to be minimized is defined by

$$J = \frac{1}{2}\int_0^{\infty} (\boldsymbol{x}^{\mathrm{T}}\boldsymbol{Q}\boldsymbol{x} + \boldsymbol{u}^{\mathrm{T}}\boldsymbol{R}\boldsymbol{u})\,dt \tag{3.2}$$

where $\boldsymbol{Q}$ and $\boldsymbol{R}$ are two matrices chosen by the controller designer. By solving the Riccati equation, the control force can be expressed from the system states as

$$\boldsymbol{u} = -\boldsymbol{H}\boldsymbol{x} \tag{3.3}$$

However, it is difficult to implement full state feedback control even with a rigid rotor. In practical applications, only a few of the states can be measured. Therefore, observers have to be introduced to estimate the complete set of states. Another way is to use the direct output feedback method in which the performance index is of the form

$$J = \frac{1}{2}\int_0^{\infty} (\boldsymbol{y}^{\mathrm{T}}\boldsymbol{Q}_{\mathrm{y}}\boldsymbol{y} + \boldsymbol{u}^{\mathrm{T}}\boldsymbol{R}\boldsymbol{u})\,dt \tag{3.4}$$

The objective of the closed loop control is to find a feedback gain matrix $\boldsymbol{H}_{\mathrm{y}}$ such that

$$u = -H_y\, y \tag{3.5}$$

where the performance index is minimized and the closed loop system

$$\dot{x} = (A - BH_yC)x \tag{3.6}$$

has designed characteristics. The method was used in a rotor-bearing system by Salm [68] to calculate the state feedback matrix. Then the approximative optimal direct output feedback control was obtained by using the pseudo-inverse method.

3.2.3.2 Pole Assignment

The system is described by equation (3.1) and the state feedback gain matrix H is calculated in such a way that the poles of the closed loop system, i.e. the eigenvalues of the matrix $A-BH$, are located at desired positions. Similarly, the output feedback gain matrix H_y can be determined according to the position of the desired closed loop poles, i.e. the eigenvalues of matrix $A-BH_yC$.

In the state feedback case, an observer can be used to estimate the unmeasured states under the condition that system is observable. In the output feedback case, the gain matrix can be obtained either by approximative methods or by solving a set of linear algebraic equations. The method was used to design a output feedback controller in a system consisting of rotor, oil film bearings, and a magnetic bearing [76]. The rotor vibration level was brought down by the control.

3.2.3.3 Open Loop Adaptive Control

This approach was developed by Burrows *et al* [8]. The system equation is of the form

$$M\ddot{q} + C\dot{q} + Kq = f \tag{3.7}$$

which can be expressed in the frequency domain as

$$\left(-\omega^2 \boldsymbol{M} + \boldsymbol{K} + j\omega \boldsymbol{C}\right)\boldsymbol{Q}(j\omega) = \boldsymbol{F}(j\omega) \tag{3.8}$$

By introducing the inverse impedance matrix

$$\Delta(j\omega) = \left(-\omega^2 \boldsymbol{M} + \boldsymbol{K} + j\omega \boldsymbol{C}\right)^{-1} \tag{3.9}$$

it follows that

$$\boldsymbol{Q}(j\omega) = \Delta(j\omega)\boldsymbol{F}(j\omega) \tag{3.10}$$

The synchronous rotor response due to unbalance force $\boldsymbol{F}_0(j\omega)$ is

$$\boldsymbol{Q}_0(j\omega) = \Delta(j\omega)\boldsymbol{F}_0(j\omega) \tag{3.11}$$

When control forces $\boldsymbol{U}$ are included, the controlled response can be expressed as

$$\boldsymbol{Q}_c(j\omega) = \boldsymbol{Q}_0(j\omega) - \boldsymbol{R}(j\omega)\boldsymbol{U}(j\omega) \tag{3.12}$$

where $\boldsymbol{R}$ is a matrix containing the columns of the inverse impedance matrix corresponding to the control force variables. This equation can be rearranged as

$$\boldsymbol{Q}_0(j\omega) = \boldsymbol{R}(j\omega)\boldsymbol{U}(j\omega) + \boldsymbol{Q}_c(j\omega) \tag{3.13}$$

If the structural parameters of the system and the out-of-balance responses are known, either by measurement or by calculation from an estimation, the equation can be considered to be a linear stochastic equation with the unknown parameter vector $\boldsymbol{U}$ and the error term $\boldsymbol{Q}_c$. Therefore the least-squares approach can be applied to estimate the control force vector $\boldsymbol{U}$ so as to minimize the controlled response $\boldsymbol{Q}_c$.

The approach was applied to a system consisting of flexible rotor supported on two oil-film bearings. A magnetic bearing actuator was employed to supply control force. The optimum control force was determined without any prior knowledge of the bearing or rotor characteristics or the distribution of out-of-balance. As the result, the synchronous vibration of the rotor was attenuated significantly by the method [13,15].

3.3 Some Control Problems

Although the above control strategies have been utilized in rotor-bearing system applications, neither of them is completely satisfactory in control. The local control method is easy to use and the spillover problem can be avoided because the condition of collocated actuators and sensors is certainly satisfied [67]. However, local control is equivalent to a passive spring and damper with variable stiffness and damping coefficients. Thus, the potential of active control is not fully utilised. Compared with local control, decentralized control behaves more satisfactorily in the sense of efficiency. The method makes the control design easier when compared with centralized control methods. However, the full potential of the controller is still in doubt. Of more importance, the controller design is based upon sub-systems, which ignore interconnections, and it is not possible to guarantee system stability.

The *LQG* method is a well known centralised approach to feedback control design and is widely used. In the method, the uncertainty is modelled as a white noise Gaussian process added as an extra input to the system. Unfortunately, this is not true with parameter uncertainty. Therefore, it can not cope directly with model uncertainties and may result in a design which is not robust. Research has shown that its stability margins can be arbitrarily small [23]. Furthermore, the assumption of white noise process disturbances is not the case for rotor-bearing system forcing.

The pole assignment method is an easy way to design a feedback controller. As with the *LQG* method, it can not deal with the problem of model uncertainty. Because model reduction techniques have to be used in most applications, the controller designed by the pole assignment method based upon the reduced order system may cause severe spillover problems when applied to the full order system.

The open loop adaptive control is very effective in attenuating the vibration of rotor-bearing systems. The control can be carried out without any prior knowledge of the system characteristics and the possibility of the instability can be avoided. However, the work has been restricted to the control of synchronous vibrations. It can not cope with transient vibrations due to, for example, sudden imbalance of blade loss or the rotor running up and down quickly in speed. However, the method has been adapted in a closed loop procedure for transient vibration control [3]. Transient behaviours of a rigid rotor supported by magnetic bearings after the loss of a blade was also examined by Viggiano using both decentral and central control method [79].

The previously mentioned problems raise the question of using a more effective control strategy which is robust, can deal with both synchronous and transient vibrations, and can avoid spillover problems. The H_∞ control approach is now discussed.

3.4 H_∞ Optimization Control

In the 1960s, considerable research was carried out for optimal control, which resulted in the well-known state space *LQG* approach to feedback design. The method can be used to design a controller in multivariable systems. However, it can not deal with the problem of model plant uncertainty. Since the 1980's, a major development in feedback control design has centred on H_∞ optimization and has become more popular in control design. The work originated from the study of Zames [81] and can be seen as a protracted return to the ideas and principles developed by Bode in the 1940s. The theory was developed in the frequency domain [26] and has now been successfully extended to state space form [24], which is easier in practical applications.

3.4.1 Definitions And Objectives

The central issue in the H_∞ control design is the introduction of the *infinity norm* of a transfer function matrix as a measure of gain. Consider a linear system in state space form

$$\begin{aligned} \dot{\boldsymbol{x}} &= \boldsymbol{A}\boldsymbol{x} + \boldsymbol{B}\boldsymbol{u} \\ \boldsymbol{y} &= \boldsymbol{C}\boldsymbol{x} + \boldsymbol{D}\boldsymbol{u} \end{aligned} \tag{3.14}$$

where $\boldsymbol{u}$ is a vector of inputs, $\boldsymbol{y}$ is the vector of outputs, and $\boldsymbol{x}$ is the state vector. An equivalent expression in the Laplace domain is

$$\boldsymbol{Y}(s) = \boldsymbol{G}(s)\boldsymbol{U}(s) \tag{3.15}$$

where the transfer function matrix $\boldsymbol{G}(s)$ relating the input and output vectors is given by

$$\boldsymbol{G}(s) = \boldsymbol{C}(s\boldsymbol{I} - \boldsymbol{A})^{-1}\boldsymbol{B} + \boldsymbol{D} \tag{3.16}$$

$\boldsymbol{G}$ is a real rational matrix, i.e. its elements are rational functions of s with real coefficients. It is said to be stable if all of its elements have no poles in the closed right-half complex plane, $\mathrm{Re}(s) > 0$, and proper if all of its elements are finite at $s=\infty$. The H_∞ norm of the transfer matrix is defined as the maximum over all real ω of the largest singular value of $\boldsymbol{G}(j\omega)$:

$$\|\boldsymbol{G}\|_\infty = \sup_{\omega} \bar{\sigma}(\boldsymbol{G}(j\omega)) \tag{3.17}$$

where ω is system vibration frequency. The H_∞ norm can, equivalently, be written as

$$\|\boldsymbol{G}\|_\infty = \sup_{\boldsymbol{u}\neq\boldsymbol{0}} \frac{\|\boldsymbol{y}\|_2}{\|\boldsymbol{u}\|_2} \tag{3.18}$$

which is related to notional input and output signal energies

$$\|u\|_2 = \left(\int_{-\infty}^{\infty} u^T(t)u(t)dt \right)^{1/2}, \quad \|y\|_2 = \left(\int_{-\infty}^{\infty} y^T(t)y(t)dt \right)^{1/2} \tag{3.19}$$

provided that they exist. Thus, the H_∞ norm also provides an upper bound on the output to input energy ratio over all possible finite energy input signals. Physically, it provides the worst-case gain between the input and output and, therefore, minimization of the H_∞ norm is equivalent to minimizing the square root of the maximum energy gain from system input to output.

3.4.2 The H_∞ Problem Formulation

A standard configuration used in H_∞ literature is shown in figure 3.1. The state space representation is

$$\begin{aligned} \dot{x} &= Ax + B_1 w + B_2 u \\ z &= C_1 x + D_{11} w + D_{12} u \\ y &= C_2 x + D_{21} w + D_{22} u \end{aligned} \tag{3.20}$$

Here, the vector w is regarded as an input due to modelling uncertainty, physical disturbances, and noise, whilst vector u is control input. The two output equations represent measured states y together with states to be controlled z, which may include errors, process outputs and control inputs. The transfer function relationship between inputs and outputs must be of the form

$$\begin{bmatrix} z \\ y \end{bmatrix} = \begin{bmatrix} G_{11}(s) & G_{12}(s) \\ G_{21}(s) & G_{22}(s) \end{bmatrix} \begin{bmatrix} w \\ u \end{bmatrix} \tag{3.21}$$

where

$$\begin{bmatrix} G_{11}(s) & G_{12}(s) \\ G_{21}(s) & G_{22}(s) \end{bmatrix} = \begin{bmatrix} D_{11} & D_{12} \\ D_{21} & D_{22} \end{bmatrix} + \begin{bmatrix} C_1 \\ C_2 \end{bmatrix} (sI - A)^{-1} \begin{bmatrix} B_1 & B_2 \end{bmatrix} \tag{3.22}$$

For a linear controller, $u = H(s)y$, the closed-loop transfer function from w to z can be expressed as

$$\mathcal{F}(G,H) = G_{11} + G_{12}H(I - G_{22}H)^{-1}G_{21} \tag{3.23}$$

The 'H_∞ control problem' is to find the controller $H(s)$ such that

$$\| G_{11} + G_{12}H(I - G_{22}H)^{-1} G_{21} \|_\infty \tag{3.24}$$

is minimised under the constraint that the system is stable, i.e. to reduce the signal energy transfer from the input to the control states.

3.4.3 Solution of general H_∞ problems in state space

Solving the H_∞ problem is equivalent to finding the solution of a minimax optimization problem. The original solution procedure was carried out in the frequency domain. It involved steps such as factorization of functions, converting the standard problem into a model-matching problem, which can be further reduced to a Nehari problem, minimal realization of functions in state space, solving the Lyapunov equations etc [26]. In a mathematical sense, the procedure solved the problem. Unfortunately, the complexity associated with computation and the lack in the explanation associated with physical meaning made it very difficult to obtain a solution. The recent developments in state space formulation for H_∞ control have shown that the problem can be reduced to the solution of algebraic Riccati equations and has similarities with the *LQG* theory [24]. In fact, the *LQG* problem can be regarded as a special case of H_∞ problems.

The system equation for standard H_∞ problems is denoted by equation (3.20). By a technique given in [29], the system can be transformed to the one with the conditions

$$D_{11} = 0 \quad , \quad D_{22} = 0$$

$$D_{12}^{\top}\left[C_1 \;\; D_{12}\right] = \left[\, 0 \;\; I \,\right] \quad , \quad \begin{bmatrix} B_1 \\ D_{21} \end{bmatrix} D_{21}^{\top} = \begin{bmatrix} 0 \\ I \end{bmatrix} \tag{3.25}$$

Therefore the equation of the standard problem can, without loss of generality, be represented as

$$\begin{aligned} \dot{x} &= Ax + B_1 w + B_2 u \\ z &= C_1 x + D_{12} u \\ y &= C_2 x + D_{21} w \end{aligned} \tag{3.26}$$

The controller is of the form

$$\begin{aligned} \dot{x}_c &= A_c x_c + B_c y \\ u &= C_c x_c + D_c y \end{aligned} \tag{3.27}$$

where

$$\begin{aligned} A_c &= A + \gamma^{-2}(B_1 B_1^{\top} - B_2 B_2^{\top}) X_\infty - (I - \gamma^{-2} Y_\infty X_\infty)^{-1} Y_\infty C_2^{\top} C_2 \\ B_c &= (I - \gamma^{-2} Y_\infty X_\infty)^{-1} Y_\infty C_2^{\top} \\ C_c &= -B_2^{\top} X_\infty \\ D_c &= 0 \end{aligned} \tag{3.28}$$

in which X_∞ and Y_∞ are the symmetric positive solutions of the algebraic Riccati equations

$$\begin{aligned} A^{\top} X_\infty + X_\infty A + X_\infty(\gamma^{-2} B_1 B_1^{\top} - B_2 B_2^{\top}) X_\infty + C_1^{\top} C_1 &= 0 \\ A Y_\infty + Y_\infty A^{\top} + Y_\infty(\gamma^{-2} C_1^{\top} C_1 - C_2^{\top} C_2) Y_\infty + B_1 B_1^{\top} &= 0 \end{aligned} \tag{3.29}$$

The controller transfer function is of the form

$$H(s) = C_c(sI - A_c)^{-1}B_c + D_c \tag{3.30}$$

If the condition

$$\rho(X_\infty Y_\infty)<\gamma^2 \tag{3.31}$$

holds, where $\rho(X_\infty Y_\infty)$ denotes the square of largest eigenvalue of the relative matrix $X_\infty Y_\infty$, the H_∞ norm of the transfer function form w to z will satisfy

$$\|G_{11} + G_{12}H(I-G_{22}H)^{-1}G_{21})\|_\infty < \gamma \tag{3.32}$$

It is obvious that the H_∞ control is equivalent to the *LQG* control if $\gamma\rightarrow\infty$. The calculation of the H_∞ controller is an iterative procedure which starts from some initial values of γ. The optimal H_∞ solution is associated with the minimal value of γ which makes the relation (3.32) remain true, i.e. the least upper bound.

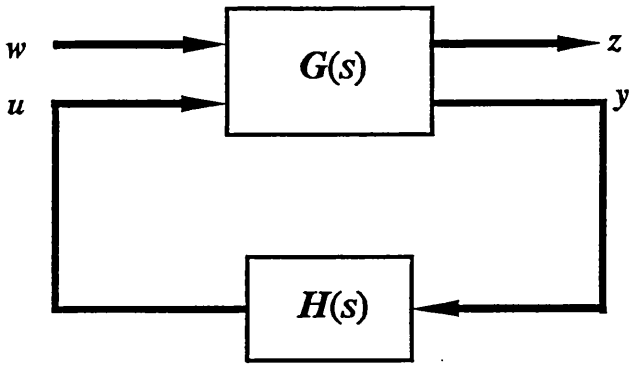

Fig. 3.1 The block diagram of a standard H_∞ control problem

CHAPTER 4 APPLICATION OF H_∞ CONTROL DESIGN TO ROTOR-BEARING SYSTEMS

4.1 Introduction

In this chapter, the characteristics of a general rotor-bearing system are analyzed. The work considers model reduction of the full order system and system controllability and observability. The formulation of a standard H_∞ problem is then carried out. The process of the formulation includes characteristic analysis of system input disturbances, choice of weighting functions, and formation of an augmented model of a system consisting of the rotor-bearing system and weighting function matrices. Application of the design process to an experimental rig is considered in Chapter 6.

4.2 Theoretical Model Of Rotor-Bearing System

The equation of motion for lateral vibration of a passive rotor-bearing system modelled with finite elements has been considered in Chapter 2. If actuators are also included in the system for control purposes (figure 4.1), the equation of the motion may be written as

$$\boldsymbol{M}\ddot{\boldsymbol{Q}} + \boldsymbol{C}(\Omega)\dot{\boldsymbol{Q}} + \boldsymbol{K}(\Omega)\boldsymbol{Q} = \boldsymbol{B}_f\boldsymbol{u} + \boldsymbol{G}_f\boldsymbol{d} \qquad (4.1)$$

where $\boldsymbol{Q}$ is the vector of generalised coordinates, $\boldsymbol{u}$ is the dimensionless control force vector scaled to have maximum amplitude of unity, and $\boldsymbol{d}$ is the vector of physical disturbance forces acting on the rotor. Suppose that n elements have been used to model the rotor. According to Chapter 2, the dimensions of the mass, damping, and stiffness matrices $\boldsymbol{M}$, $\boldsymbol{C}$, $\boldsymbol{K}$ will be n_d x n_d, where n_d=4n+4. $\boldsymbol{G}_f$ will have dimensions $n_d \times \frac{1}{2}n_d$ since disturbances generally act laterally at each node point. If there are n_a actuators, each of which can apply forces in two directions, then $\boldsymbol{B}_f$ will have dimensions $n_d \times 2n_a$

The state space representation follows from the transformation

$$x = \begin{bmatrix} Q \\ \dot{Q} \end{bmatrix} \tag{4.2}$$

and is of the form

$$\dot{x} = Ax + B_d d + B_u u \tag{4.3}$$

where

$$A = \begin{bmatrix} 0 & I \\ -M^{-1}K & -M^{-1}C \end{bmatrix}_{(2n_d \times 2n_d)}$$

$$B_d = \begin{bmatrix} 0 \\ G_f \end{bmatrix}_{(2n_d \times \frac{1}{2}n_d)} , \qquad B_u = \begin{bmatrix} 0 \\ B_f \end{bmatrix}_{(2n_d \times 2n_u)} \tag{4.4}$$

Usually, the states to be controlled and states to be measured are not the same. Suppose that they can be defined respectively from the state vector by

$$z_c = C_c x \quad , \qquad z_m = C_m x \tag{4.5}$$

C_c has dimensions $n_c \times 2n_d$, where n_c is determined by the number of the states required to be controlled. C_m has dimensions $n_m \times 2n_d$, where n_m is the number of measured states.

4.2.1 Model Reduction

Typically, the modelled system will have a large number of generalised coordinates (and states). It is difficult therefore to design a controller based directly on this system. To overcome the problem, model reduction techniques are introduced. The first step in model reduction is to solve the eigenvalue problem for the system (section 2.5). Then the states of the system are transformed into modal coordinates by

$$x = U^R p$$

where U^R is the right eigenvector matrix. If the moduli of the eigenvalues imaginary parts are ordered in ascending frequency and the modal vector is partitioned into low and high frequency states by

$$p = \begin{bmatrix} p_l \\ \cdots \\ p_h \end{bmatrix} \quad \begin{matrix} \text{- low frequency modes} \\ \\ \text{- high frequency modes} \end{matrix} \tag{4.6}$$

then equation (4.3) yields the system

$$\begin{bmatrix} \dot{p}_l \\ \cdots \\ \dot{p}_h \end{bmatrix} = (U^L)^T A\, U^R \begin{bmatrix} p_l \\ \cdots \\ p_h \end{bmatrix} + (U^L)^T B_d d + (U^L)^T B_u u \tag{4.7}$$

where U^L is the left eigenvector matrix. From Chapter 2, $(U^L)^T A U^R$ is a diagonal matrix. With appropriate partitioning, the modal form of the state equation is

$$\begin{aligned} \dot{p}_l &= A_l p_l + B_{ld} d + B_{lu} u \\ \dot{p}_h &= A_h p_h + B_{hd} d + B_{hu} u \\ z_c &= C_c x \quad , \qquad z_m = C_m x \\ x &= U_l^R p_l + U_h^R p_h \end{aligned} \tag{4.8}$$

where A_l and A_h are diagonal. The representation of the model in the frequency domain is

$$\begin{aligned} P_l &= (sI - A_l)^{-1} B_{ld} D + (sI - A_l)^{-1} B_{lu} U \\ P_h &= (sI - A_h)^{-1} B_{hd} D + (sI - A_h)^{-1} B_{hu} U \\ Z_c &= C_c X \quad , \qquad Z_m = C_m X \\ X &= U_l^R P_l + U_h^R P_h \end{aligned} \tag{4.9}$$

which is shown in figure 4.2. The system can be expressed in a standard way with

$$X = G_{lu}(s)U + D_r$$
$$Z_c = C_c X \quad , \qquad Z_m = C_m X \tag{4.10}$$

where

$$D_r = G_{ld}(s)D + G_{hd}(s)D + G_{hu}(s)U$$
$$G_{lu}(s) = U_l^R(sI - A_l)^{-1}B_{lu}$$
$$G_{ld}(s) = U_l^R(sI - A_l)^{-1}B_{ld}$$
$$G_{hd}(s) = U_h^R(sI - A_h)^{-1}B_{hd}$$
$$G_{hu}(s) = U_h^R(sI - A_h)^{-1}B_{hu}$$

which is shown in figure 4.3.

The full order system (4.8) has been converted to a reduced order system $G_{lu}(s)$. The input to the reduced order system is control signal U only. The disturbance D_r is composed of three terms. The first is $G_{ld}(s)D$, which contains the response of the retained lower frequency modes due to the physical disturbances in D. The second term $G_{hd}(s)D$ contains the response of the higher frequency modes due to the physical disturbances in D. The final term $G_{hu}(s)U$ contains the response of the higher frequency modes due to the control forces in U. The retained modes in the reduced order system will be determined by certain criteria. They should be controllable and observable and the desired characteristics of the full order system should remain in the reduced order system. It is also advisable that the achievable frequency bandwidth of the controller should cover the frequency range of the reduced order system.

It is emphasized here that the controller design will be based on a reduced order system, where the neglected high frequency mode effects have been included in the disturbance terms. In many control design procedures, high frequency disturbance terms are ignored. However, controllers designed in this way may cause a spillover

problem in the closed-loop system. Hence, those disturbance terms due to the effects of high frequency modes should remain so that a controller can be designed for robustness and the elimination of spillover problems.

4.2.2 Analysis Of Controllability And Observability Of The Reduced Order System

It is impossible to control and observe all modes of the full order system with a limited number of actuators and transducers. Therefore model reduction techniques have to be carried out to eliminate all uncontrollable and observable modes from the reduced order system. The reduced order system in state space is derived from equation (4.8) as

$$\begin{aligned} \dot{p}_l &= A_l p_l + B_{ld} d + B_{lu} u \\ z_m &= C_m U_l^R p_l + C_m U_h^R p_h \end{aligned} \tag{4.11}$$

The controllability and observability of the reduced order system can be analyzed by calculating the controllability gramian matrix [40]

$$G_c = \int_0^\infty e^{\tau A_l} B_{lu} B_{lu}^T e^{\tau A_l^T} d\tau \tag{4.12}$$

and the observability gramian matrix

$$G_o = \int_0^\infty e^{\tau A_l} (C_m U_l^R)^T (C_m U_l^R) e^{\tau A_l^T} d\tau \tag{4.13}$$

A system is said to be controllable and observable if and only if the gramian matrices are positive definite. Since the matrices are symmetric, their eigenvalues are real. Moreover, they are positive definite if and only if every eigenvalue is positive. Therefore the eigenvalues of G_c and G_o may be used to assess system controllability and observability. Physically, a non-controllable mode will occur when all actuators coincide with node points in that mode. A non-observable mode will occur when all measurement transducers are at the node points.

4.3 Formulation Of The Standard H_∞ Problem

The closed-loop system with H_∞ controller to be designed can be obtained from the open-loop system expressed by equation (4.10). It is noted that errors due to shaft surface roughness and/or electrical noise in the rotor-bearing system have not yet been included in the measurement states $\boldsymbol{Z}_m$. When a controller is also included, the closed-loop system can be represented by

$$\begin{aligned} \boldsymbol{X} &= \boldsymbol{G}_{lu}(s)\boldsymbol{U} + \boldsymbol{D}_r \\ \boldsymbol{Z}_c &= \boldsymbol{C}_c\boldsymbol{X} \quad , \qquad \boldsymbol{Z}_m = \boldsymbol{C}_m\boldsymbol{X} \\ \boldsymbol{Y}_m &= \boldsymbol{Z}_m + \boldsymbol{N} \\ \boldsymbol{Y}_f &= \boldsymbol{W}_{fm}(s)\boldsymbol{Y}_m \\ \boldsymbol{U} &= \boldsymbol{H}(s)\boldsymbol{Y}_f \end{aligned} \tag{4.14}$$

Here $\boldsymbol{N}$ contains the errors due to shaft surface roughness and electrical noise, which must be added to the measurement states $\boldsymbol{Z}_m$. It follows that $\boldsymbol{Y}_m$ represents the measurement states as picked up by the measurement transducers. In any practical implementation of a control system, the measured signals $\boldsymbol{Y}_m$ will also be conditioned by transducer characteristics, amplifier and filters before entering the controller. The matrix $\boldsymbol{W}_{fm}(s)$ represents this conditioning and $\boldsymbol{Y}_f$ contains the signals representing the measurement states that enter the controller $\boldsymbol{H}(s)$.

4.3.1 Augmented Equations

Weighting function matrices $\boldsymbol{W}_u(s)$, $\boldsymbol{W}_z(s)$, $\boldsymbol{W}_y(s)$ are introduced to allow flexibility in the controller design. These operate on the control signals $\boldsymbol{U}$, the control states $\boldsymbol{Z}_c$, and the measured signals $\boldsymbol{Y}_m$, respectively. The augmented closed-loop system is then of the form

$$
\begin{aligned}
&X = G_{lu}(s)U + D_r \\
&Z_c = C_c X \quad , \qquad Z_m = C_m X \\
&Y_m = Z_m + N \\
&Y_f = W_{fm}(s)Y_m \\
&U = H(s)Y_f \\
&Z_u = W_u(s)U \quad , \qquad Z_z = W_z(s)Z_c \quad , \qquad Z_y = W_y(s)Y_m
\end{aligned}
\tag{4.15}
$$

which is shown in figure 4.4. It is noted that there are transfer function matrices relating input disturbances D_r and N to control signals U, control states Z_c, and contaminated measurement states Y_m, in the form

$$
U = T_u \begin{bmatrix} D_r \\ N \end{bmatrix} \quad , \quad Z_c = T_z \begin{bmatrix} D_r \\ N \end{bmatrix} \quad , \quad Y_m = T_y \begin{bmatrix} D_r \\ N \end{bmatrix} \tag{4.16}
$$

The matrices are given by

$$
T_u = \begin{bmatrix} T_{ud} & T_{un} \end{bmatrix} \quad , \qquad T_z = \begin{bmatrix} T_{zd} & T_{zn} \end{bmatrix} \quad , \qquad T_y = \begin{bmatrix} T_{yd} & T_{yn} \end{bmatrix} \tag{4.17}
$$

where

$$
\begin{aligned}
&T_{ud} = (I - HW_{fm}C_m G_{lu})^{-1} HW_{fm}C_m \\
&T_{un} = (I - HW_{fm}C_m G_{lu})^{-1} HW_{fm} \\
&T_{zd} = C_c(G_{lu}T_{ud} + I) \quad , \quad T_{zn} = C_c G_{lu} T_{un} \\
&T_{yd} = C_m(G_{lu}T_{ud} + I) \quad , \quad T_{yn} = C_m G_{lu} T_{un} + I
\end{aligned}
$$

The H_∞ controller design is then the solution obtained by minimization of the H_∞ norm

$$
\left\| \begin{matrix} W_u T_u \\ W_z T_z \\ W_y T_y \end{matrix} \right\|_\infty \tag{4.18}
$$

Clearly, the choice of weighting function matrices has a significant influence on the

controller design. These must be considered with regard for the vibration reduction required, the avoidance of spillover effects and the capabilities of the control actuators. Guidelines for the weighting function selection are detailed in section 4.4.

4.3.2 State Space Realisation Of The Augmented System

The system analysis in the frequency domain mentioned above is very useful for aiding the choice of weighting function matrices. However, it is very difficult to solve the H_∞ problem in the frequency domain. In contrast, the solution can be easily obtained in the state space domain. From equations (4.8) and (4.14), the reduced order equation of the rotor-bearing system in state space is of the form

$$\begin{aligned} \dot{\boldsymbol{p}}_l &= \boldsymbol{A}_l \boldsymbol{p}_l + \boldsymbol{B}_{ld} \boldsymbol{d} + \boldsymbol{B}_{lu} \boldsymbol{u} \\ \boldsymbol{z}_c &= \boldsymbol{C}_{cl} \boldsymbol{p}_l + \boldsymbol{C}_{ch} \boldsymbol{p}_h \\ \boldsymbol{y}_m &= \boldsymbol{C}_{ml} \boldsymbol{p}_l + \boldsymbol{C}_{mh} \boldsymbol{p}_h + \boldsymbol{n} \end{aligned} \tag{4.19}$$

where

$$\boldsymbol{C}_{cl} = \boldsymbol{C}_c \boldsymbol{U}_l^R \quad , \qquad \boldsymbol{C}_{ml} = \boldsymbol{C}_m \boldsymbol{U}_l^R$$

$$\boldsymbol{C}_{ch} = \boldsymbol{C}_c \boldsymbol{U}_h^R \quad , \qquad \boldsymbol{C}_{mh} = \boldsymbol{C}_m \boldsymbol{U}_h^R$$

and $\boldsymbol{n}$ is a vector of shaft surface roughness and electrical noise time domain signals appropriate to the measurement locations. It is noted that terms $\boldsymbol{C}_{ch}\,\boldsymbol{p}_h$ and $\boldsymbol{C}_{mh}\,\boldsymbol{p}_h$ can not describe the disturbances acting on the measured states accurately due to the uncertainty of the high frequency modes. Furthermore, in any finite element analysis, the dimension of $\boldsymbol{p}_h$ will be large making it computationally inefficient to include the high frequency modes in the system equations. However, the dimensions of the controlled and measured states are likely to be much smaller.

An alternative form of (4.19) is now derived to reduce the computational problems incurred on retaining $\boldsymbol{p}_h$. Let $\boldsymbol{D}_c$ be a diagonal matrix with dimensions $n_c \times n_c$. Let each non-zero element correspond to the maximum value of each control state

variable. It follows that

$$\boldsymbol{C}_{ch}\,\boldsymbol{p}_h = \boldsymbol{D}_c\boldsymbol{d}_c$$

where $\| \boldsymbol{d}_c \| \leq 1$ and $\boldsymbol{d}_c$ represents any time variation of the control states due to high frequency modes. A similar procedure may be used to define a $n_m \times n_m$ diagonal matrix $\boldsymbol{D}_m$ for the measurement states:

$$\boldsymbol{C}_{mh}\,\boldsymbol{p}_h = \boldsymbol{D}_m\boldsymbol{d}_m$$

where $\| \boldsymbol{d}_m \| \leq 1$. Also for the shaft roughness and electrical noise

$$\boldsymbol{n} = \boldsymbol{D}_n\boldsymbol{d}_n$$

where $\boldsymbol{D}_n$ is an $n_m \times n_m$ diagonal matrix and $\| \boldsymbol{d}_n \| \leq 1$.

It now follows that equation (4.19) may be replaced by

$$\begin{aligned} \dot{\boldsymbol{p}}_l &= \boldsymbol{A}_l\boldsymbol{p}_l + \boldsymbol{B}_{ld}\boldsymbol{d} + \boldsymbol{B}_{lu}\boldsymbol{u} \\ \boldsymbol{z}_c &= \boldsymbol{C}_{cl}\boldsymbol{p}_l + \boldsymbol{D}_c\boldsymbol{d}_c \\ \boldsymbol{y}_m &= \boldsymbol{C}_{ml}\boldsymbol{p}_l + \boldsymbol{D}_m\boldsymbol{d}_m + \boldsymbol{D}_n\boldsymbol{d}_n \end{aligned} \qquad (4.20)$$

It is remarked that exact forms of the $\boldsymbol{D}_c$, $\boldsymbol{D}_m$, $\boldsymbol{D}_n$ matrices and $\boldsymbol{d}_c$, $\boldsymbol{d}_m$, $\boldsymbol{d}_n$ vectors are not required in an H_∞ controller design. It need only be recognised that they represent the uncertain modelling and measurement parameters in the system.

The state space equations of three weighting function matrices $\boldsymbol{W}_u$, $\boldsymbol{W}_z$, and $\boldsymbol{W}_y$ are

$$\begin{aligned} \dot{\boldsymbol{x}}_u &= \boldsymbol{A}_u\boldsymbol{x}_u + \boldsymbol{B}_u\boldsymbol{u} \\ \boldsymbol{z}_u &= \boldsymbol{C}_u\boldsymbol{x}_u + \boldsymbol{D}_u\boldsymbol{u} \end{aligned} \qquad (4.21)$$

$$\begin{aligned} \dot{\boldsymbol{x}}_z &= \boldsymbol{A}_z\boldsymbol{x}_z + \boldsymbol{B}_z\boldsymbol{z}_c \\ \boldsymbol{z}_z &= \boldsymbol{C}_z\boldsymbol{x}_z + \boldsymbol{D}_z\boldsymbol{z}_c \end{aligned} \qquad (4.22)$$

$$\dot{x}_y = A_y x_y + B_y y_m$$
$$z_y = C_y x_y + D_y y_m \tag{4.23}$$

The equations of the filter are

$$\dot{x}_f = A_f x_f + B_f y_m$$
$$y_f = C_f x_f + D_f y_m \tag{4.24}$$

Hence, the equations of the augmented system are

$$\dot{x}_a = A_a x_a + B_{ar} r + B_{au} u$$
$$z = C_{az} x_a + D_{azr} r + D_{azu} u \tag{4.25}$$
$$y_f = C_{ay} x_a + D_{ayr} r + D_{ayu} u$$

where

$$x_a = \left[p_l^T \; x_u^T \; x_z^T \; x_y^T \; x_f^T\right]^T$$
$$z = \left[z_u^T \; z_z^T \; z_y^T\right]^T$$
$$r = \left[d^T, \; d_c^T, \; d_m^T, \; d_n^T\right]^T$$

$$A_a = \begin{bmatrix} A_l & 0 & 0 & 0 & 0 \\ 0 & A_u & 0 & 0 & 0 \\ B_z C_{cl} & 0 & A_z & 0 & 0 \\ B_y C_{ml} & 0 & 0 & A_y & 0 \\ B_f C_{ml} & 0 & 0 & 0 & A_f \end{bmatrix} \quad B_{ar} = \begin{bmatrix} B_{ld} & 0 & 0 & 0 \\ 0 & 0 & 0 & 0 \\ 0 & B_z D_c & 0 & 0 \\ 0 & 0 & B_y D_m & B_y D_n \\ 0 & 0 & B_f D_c & B_f D_n \end{bmatrix} \quad B_{au} = \begin{bmatrix} B_{lu} \\ B_u \\ 0 \\ 0 \\ 0 \end{bmatrix}$$

$$C_{az} = \begin{bmatrix} 0 & C_u & 0 & 0 & 0 \\ D_z C_{cl} & 0 & C_z & 0 & 0 \\ D_y C_{ml} & 0 & 0 & C_y & 0 \end{bmatrix} \quad D_{azr} = \begin{bmatrix} 0 & 0 & 0 & 0 \\ 0 & D_z D_c & 0 & 0 \\ 0 & 0 & D_y D_m & D_y D_n \end{bmatrix} \quad D_{azu} = \begin{bmatrix} D_u \\ 0 \\ 0 \end{bmatrix}$$

$$C_{ay} = \begin{bmatrix} D_f C_{ml} & 0 & 0 & 0 & C_f \end{bmatrix} \qquad D_{ayr} = \begin{bmatrix} 0 & 0 & D_f D_m & D_f D_n \end{bmatrix} \qquad D_{ayu} = \begin{bmatrix} 0 \end{bmatrix}$$

This is the state space formulation of the H_∞ problem.

4.4 Controller Design

The most important detail in the H_∞ control design is the choice of weighting function matrices so that the resulting controller can make the closed-loop system achieve required characteristics. The choice depends mainly on the characteristics of the actuators, robustness requirements, characteristics of input disturbances and performance requirements.

4.4.1 Characteristics Of Control Forces

A magnetic bearing has low pass characteristic between output forces and input voltages. Cut-off frequencies depend on the bearing design parameters and power amplifier coefficients. The control forces will therefore be the series combination of the controller design and the magnetic bearing characteristics.

4.4.2 Characteristics Of Disturbance Forces

Within the scope of this thesis, three types of disturbance forces will be considered

(a) Steady synchronous forcing due to unbalance.

(b) Steady non-synchronous forcing due to external excitation.

(c) Sudden forcing due to mass loss.

In case (a) the forcing is at a single frequency ($\omega = \Omega$) with an amplitude proportional to Ω^2. In case (b) the forcing is also at a single frequency ($\omega = \omega_s$, $\omega_s \neq \Omega$) with a fixed amplitude. Case (c) corresponds to unbalance forcing with a step change in amplitude.

4.4.3 Characteristics Of Disturbances Forming D_r

According to equation (4.10), as stated in section 4.2.1, the full order system

disturbance terms in $\boldsymbol{D}_r$ are dependent on the direct forcing terms in $\boldsymbol{D}$ and the control forces in $\boldsymbol{U}$. Specifically the terms involved are

$\boldsymbol{G}_{ld}(s)\boldsymbol{D}$ - excitation of low frequency modes by direct forces

$\boldsymbol{G}_{hd}(s)\boldsymbol{D}$ - excitation of high frequency modes by direct forces

$\boldsymbol{G}_{hu}(s)\boldsymbol{U}$ - excitation of high frequency modes by control forces

The degree to which $\boldsymbol{D}$ influences $\boldsymbol{D}_r$ depends on the type of disturbance force and transfer function matrices $\boldsymbol{G}_{ld}(s)$, $\boldsymbol{G}_{hd}(s)$ and $\boldsymbol{G}_{hu}(s)$.

In the case of steady synchronous unbalance forcing, the system response will be synchronous and large around critical speeds. Since the low frequency modes are within the running speed range, significant contributions from $\boldsymbol{G}_{ld}(s)\boldsymbol{D}$ must be expected. However, if the high frequency modes are well away from the maximum running speed then the contributions from $\boldsymbol{G}_{hd}(s)\boldsymbol{D}$ will be small.

A similar argument may be applied to the case of steady non-synchronous forcing. The excitation occurs when the forcing frequency is in the domain of the higher frequency modes in which case the $\boldsymbol{G}_{hd}(s)\boldsymbol{D}$ term may give rise to a significant system response.

The case of a sudden change in unbalance condition will cause all modes to be excited simultaneously. To see this, let f_x and f_y be the unbalance force components in a rotor plane due to an mass eccentricity m_e that results after $t = 0$. Then

$$\begin{bmatrix} f_x \\ f_y \end{bmatrix} = m_e \Omega^2 \begin{bmatrix} \cos\Omega t \\ \sin\Omega t \end{bmatrix}, \qquad t \geq 0 \tag{4.26}$$

In the Laplace transform domain

$$\begin{bmatrix} F_x(s) \\ F_y(s) \end{bmatrix} = \frac{m_e \Omega^2}{(s^2+\Omega^2)} \begin{bmatrix} s \\ \Omega \end{bmatrix} \tag{4.27}$$

The poles at $s = \pm j\Omega$ give rise to mode excitations. The proximity of $s = \pm j\Omega$ to the system poles or eigenvalues determines the levels to which the modes are excited. The running speed dependence is obvious and large responses will occur if mass loss occurs at or near to critical speeds.

The final term contributing to the disturbance $\boldsymbol{D}_r$ is the control force excitation of the high frequency modes. The controller design could ensure that this term is minimised, thus avoiding controller spillover. If this is not the case then the controller may cause the rotor to respond unnecessarily. In other words, since the modelled high frequency modes are considered to be uncertain, it is not feasible to control these modes in the physical system. One of the consequences of this is that disturbance forces that cause significant responses of high frequency modes will only be partially compensated for (through the low frequency modes).

4.4.4 Characteristics Of The Shaft Surface Roughness And Electrical Noise

Consider shaft roughness n_k appropriate to the k th transducer position. This may be specified by the Fourier decomposition

$$n_k = \sum_1 n_{kl} e^{jl\theta} \tag{4.28}$$

where θ is a circumferential coordinate around the shaft. When the rotor rotates at speed Ω, n_k is of the time dependent form

$$n_k = \sum_1 n_{kl} e^{jl(\Omega t+\phi_{kl})} \tag{4.29}$$

where ϕ_{kl} is a phase angle. It is apparent that the amplitudes of the surface roughness harmonic components will remain the same whatever the rotational speed is. However, in the frequency domain, the components are at frequencies that are multiples of Ω. As the rotor speed increases, these components sweep through the frequency range in a manner shown in figure 4.5. Therefore, if the maximum rotational speed is known, the spectrum of n_k over the whole frequency range can be identified and bounded by an enveloping curve.

It is to be noted that one option is to eliminate the surface roughness from the measurement signals by subtracting off 'slow roll' measurement signals. However, each controller implementation would require tuning. The alternative approach taken in this thesis is to incorporate the roughness into the controller design through an enveloping spectrum. In this way, rotor manufacturing tolerances may be incorporated and different controller implementations should not require any tuning.

Electrical noise will also contaminate the measurement signals. The spectrum of any noise will be speed independent and will include high frequency components. When combined with the surface roughness spectrum, a complete enveloping spectrum can be defined for $N(j\omega)$.

4.4.5 Choice Of Weighting Functions

W_u - W_u should reflect the frequency response characteristics of the system magnetic actuators and ensure that the maximum control forces are within the limits of their capabilities. The weighting should also ensure that the controller does not excite the neglected high frequency modes. The maximum singular value of the weighting function inverse will then have a characteristic similar to the magnetic bearings characteristics. It should also have a low value in the

frequency range of the neglected high order modes. Figure 4.6 shows the anticipated variation of maximum singular value of the weighting function matrix with frequency.

W_z - This weighting function matrix modifies the controlled output Z_c. It should be chosen to have a maximum singular value that is large in the frequency range in which vibrations are required to be attenuated, and small otherwise. However, it is argued that a weighting function with a low pass characteristic or even constant weighting can also be chosen. The low pass characteristic means that more importance to vibration reduction at low frequencies is assigned, while the constant weighting simply means that the vibration control is regarded as being equally important at all frequencies. Furthermore, choice of either low pass or constant weighting function will reduce the order of the augmented system compared with a band pass weighting. These choices can be seen in figure 4.7.

W_y - This weighting function matrix is related to the contaminated measured output $Y_m = Z_m + N$. In terms of any vector norm, it follows that

$$| \|Y_m\| - \|N\| | \leq \|Z_m\| \leq \|Y_m\| + \|N\| \qquad (4.30)$$

Ideally, $Z_m = 0$ in the controlled system. However, the controller utilises the Y_m states and it is not possible to achieve perfect control. For example, it follows from (4.31) that

(a) $\|Y_m\| = 0$ implies $\|Z_m\| = \|N\|$

(b) $\|Y_m\| = \|N\|$ implies $0 \leq \|Z_m\| \leq 2\|N\|$

Provided the error term N is within acceptable bounds, either of the above constraints may be chosen. For this thesis only case (b) is considered. An enveloping bound on N is shown in figure 4.8 covering both shaft surface

roughness and electrical noise. Ideally, in order that $\|Y_m\| = \|N\|$, the maximum singular value of W_y should have an inverse characteristic similar in shape to the enveloping bound on N. However, it is now recognised that a conflict may arise with the objectives of the controller weighting function matrix W_u. This was defined to limit the controller ability of exciting neglected high frequency modes. Therefore, it is accepted that high frequency mode signals may be present in the measured states Y_m if excited by other external forcing (eg. mass loss). Now

$$\|Y_m\| = \|Y_{mh} + N\| \leq \|Y_{mh}\| + \|N\| \qquad (4.31)$$

where Y_{mh} represents possible high frequency mode signals. The spectrum of $\|Y_{mh}\|$ is therefore added to $\| N \|$ so that the maximum singular value of W_y is chosen to have an inverse characteristic similar in shape to an enveloping bound on $\| Y_{mh}\| + \| N \|$ (figure 4.8).

4.4.6 Resulting H_∞ Controller

After the suitable choice of weighting functions, equation (4.25) can be solved to obtain the H_∞ controller. However, it is noted that equation (4.25) has a solution only if some controllability and observability conditions are held. Furthermore, the matrix A_c of the controller will have the same dimensions as matrix A_a of augmented system (4.25). This may result in a high order controller and if no further model reduction is done, may leave the problem either unsolvable or very difficult to apply in practice. Therefore, model reduction must be performed on the augmented equation (4.25) so that unobservable/uncontrollable states in the system can be removed and control law complexity reduced to meet practical requirements.

The balanced truncated model reduction method [51] was used in the augmented

system, in which an n th order full order system

$$\boldsymbol{G}_a(s) = \boldsymbol{C}_a(s\boldsymbol{I} - \boldsymbol{A}_a)^{-1}\boldsymbol{B}_a + \boldsymbol{D}_a \tag{4.32}$$

can be approximated by a k th order reduced model

$$\boldsymbol{G}_r(s) = \boldsymbol{C}_r(s\boldsymbol{I} - \boldsymbol{A}_r)^{-1}\boldsymbol{B}_r + \boldsymbol{D}_r \tag{4.33}$$

such that

$$\left\|\boldsymbol{G}_a(j\omega) - \boldsymbol{G}_r(j\omega)\right\|_\infty \le 2\sum_{i=k+1}^{n} g_i \tag{4.34}$$

where g_i are square roots of the eigenvalues of $\boldsymbol{G}_a(s)$. Then the resultant reduced order controllable/observable equation can be performed by the same procedure described in Chapter 3 and the H_∞ controller can be represented in state space form by

$$\begin{aligned} \dot{\boldsymbol{x}}_c &= \boldsymbol{A}_c\boldsymbol{x}_c + \boldsymbol{B}_c\boldsymbol{y}_f \\ \boldsymbol{u} &= \boldsymbol{C}_c\boldsymbol{x}_c + \boldsymbol{D}_c\boldsymbol{y}_f \end{aligned} \tag{4.35}$$

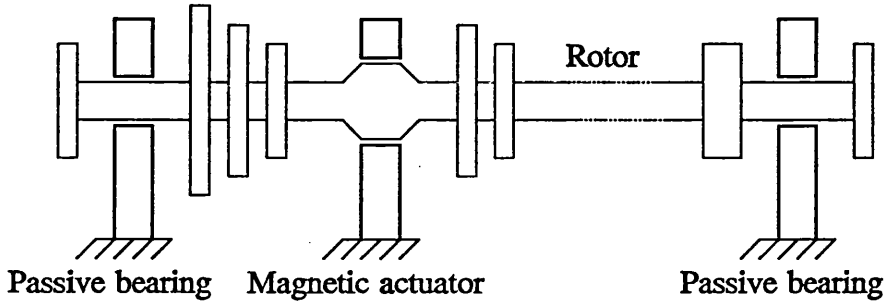

(a) Rotor system with bearings and actuators

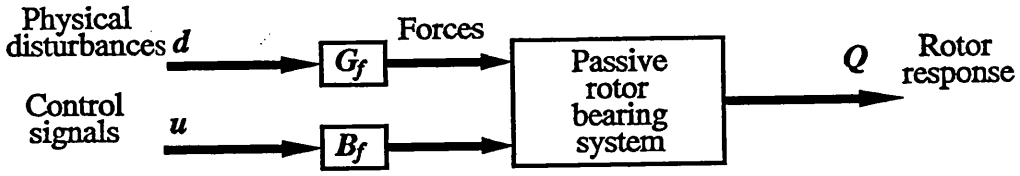

(b) Block diagram of a rotor system with control and disturbance forces

Fig. 4.1 Rotor dynamic control

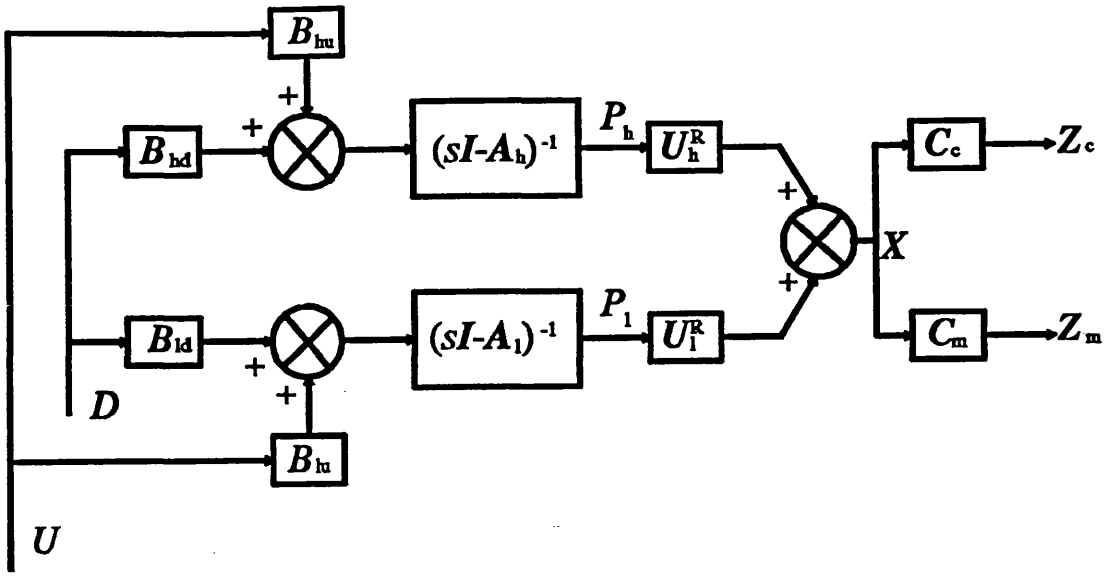

Fig. 4.2 Block diagram of the full order system

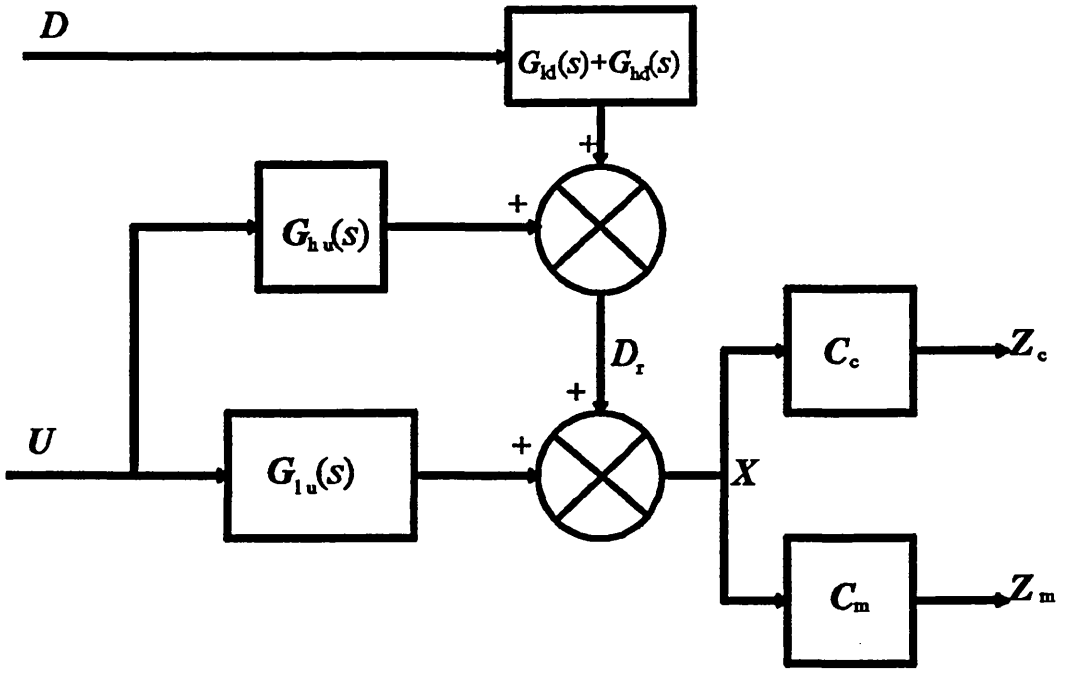

Fig. 4.3 Block diagram of the full order system with low and high frequency mode partitioning

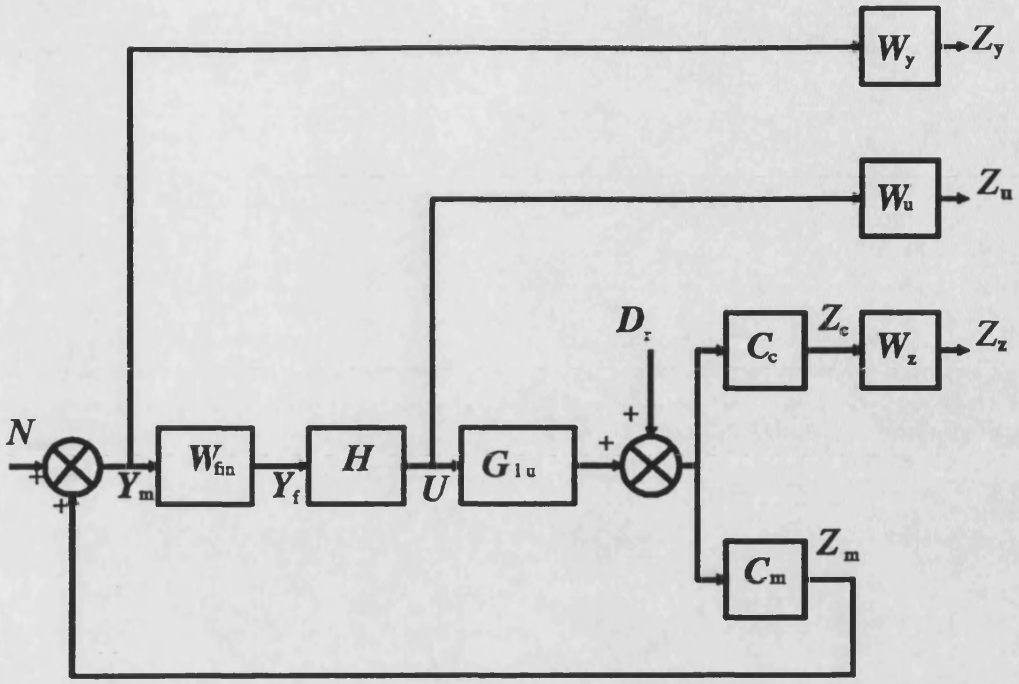

Fig. 4.4 Block diagram of the augmented closed loop system

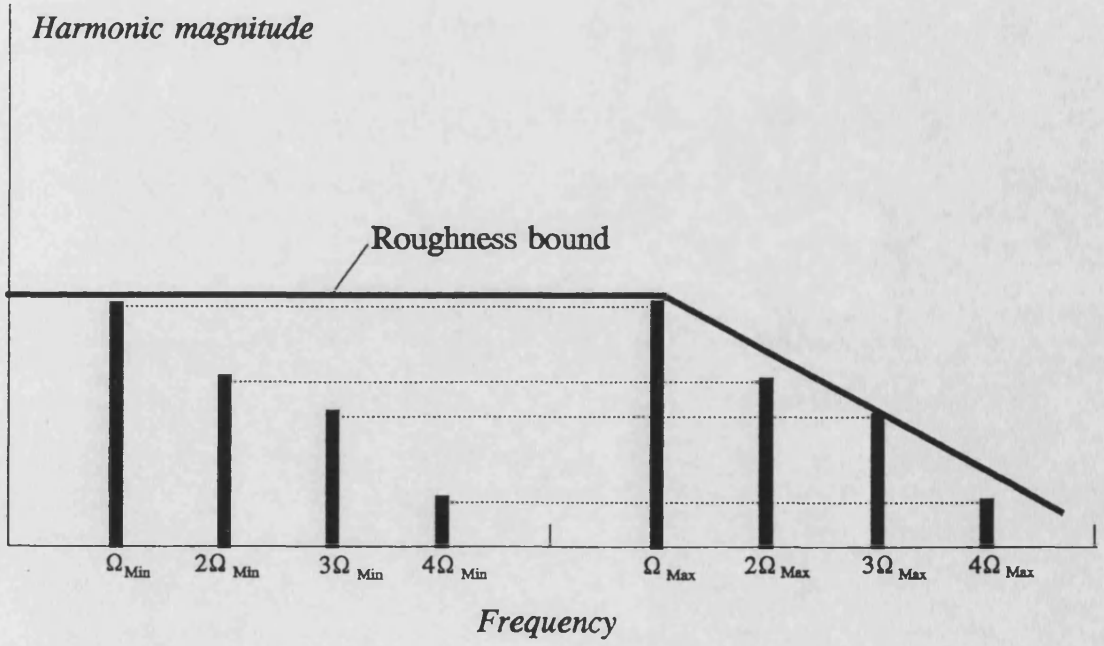

Fig. 4.5 Shaft surface roughness signal component variation with rotational speed / frequency

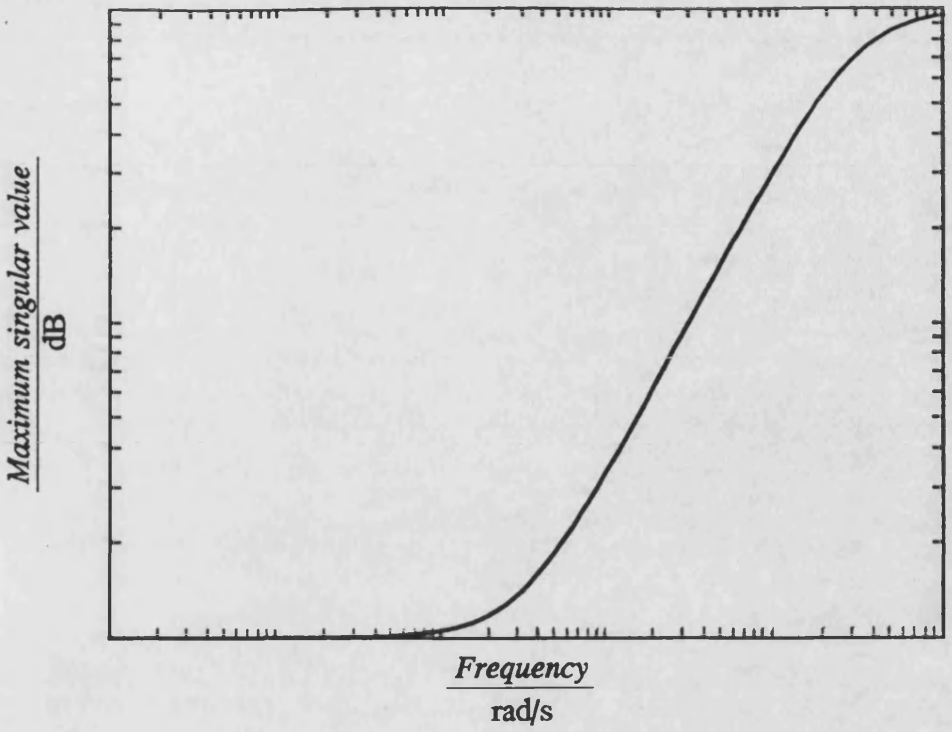

Fig. 4.6 General form of weighting function W_u

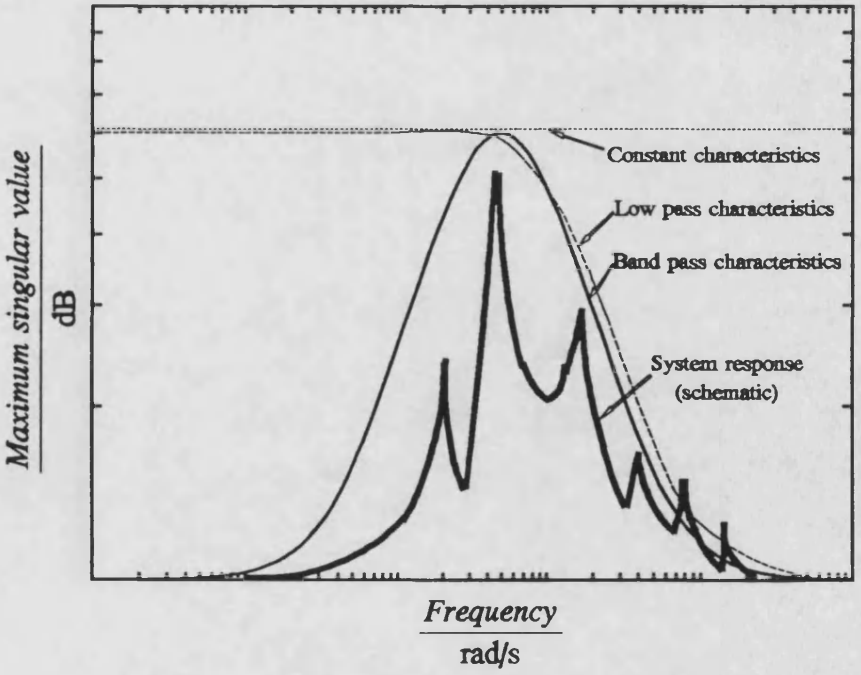

Fig. 4.7 General forms of weighting function W_z

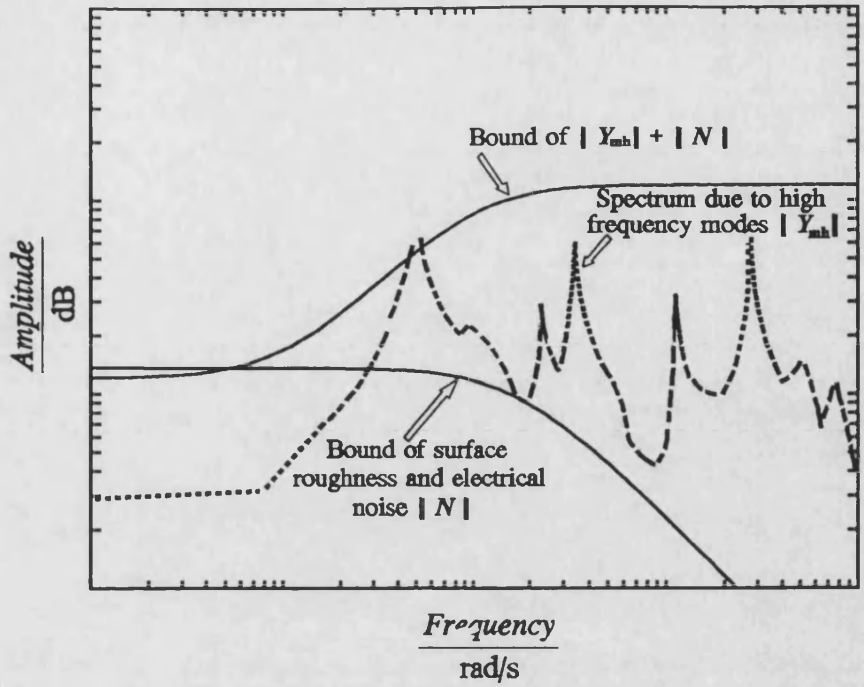

(a) Enveloping bounds of surface roughness, noise and high frequency modes

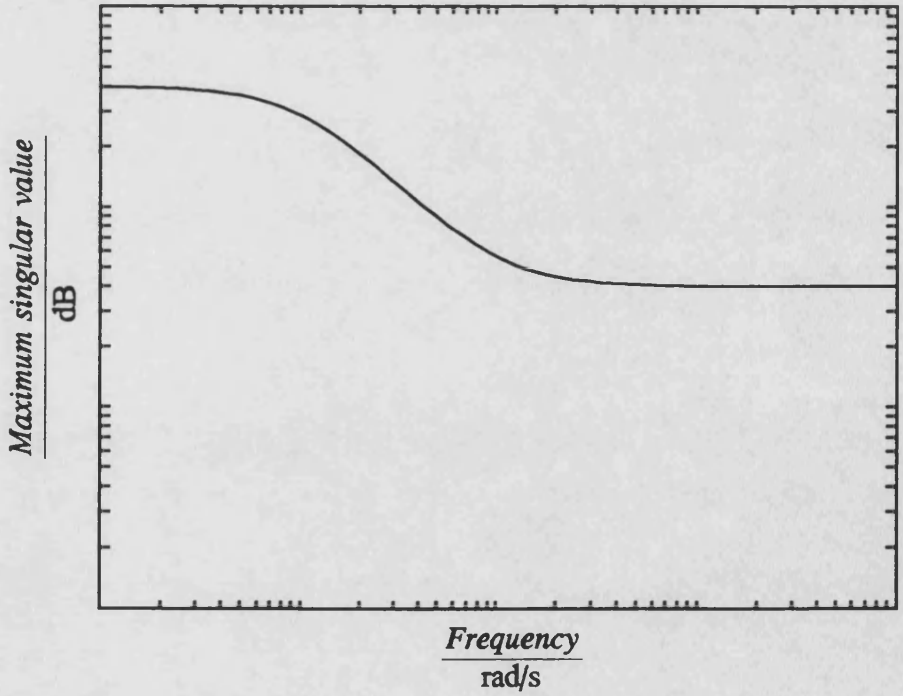

(b) General form of weighting function W_y

Fig. 4.8 Enveloping bounds and measurement state weighting function characteristic

CHAPTER 5 CONTROL IMPLEMENTATION ON AN EXPERIMENTAL RIG

5.1 Description Of The Experimental System

The real-time implementation of the control strategies was carried out on the rig shown in figure 5.1. The rotor is of an industrial size and supported by oil-film bearings. It has the capability of running above its first flexural critical speed and therefore can be regarded as a flexible rotor. The presence of the end mounted disks means that gyroscopic moments are important. Two electromagnetic actuators were used to supply control and disturbance forces.

5.2 Details Of The Rotor-Bearing Assembly

5.2.1 Flexible Rotor

The rotor consisted of a mild steel shaft and two steel disks mounted at each end of the shaft with ETP bushes. The shaft diameter and nominal length were 100 mm and 2385 mm respectively, while the disk diameter and thickness were 406 mm and 90 mm respectively. There were eight equally spaced holes on each face of the disks for the purpose of rotor balancing and introducing known unbalance into the system.

5.2.2 DC Motor And Coupling

The rotor was driven by a 25 kW variable speed DC motor through a stub shaft via a 1:1.89 step-up flexible tooth belt drive. The motor speed range was 0 to 3000 rev/min (314 rad/s). Thus the maximum running speed of the rotor was 5670 rev/min (594 rad/s). A regenerative braking system was introduced for the variable speed drive so as to provide a means of decelerating the rotor. A universal coupling was used to link the stub and main shafts so that no lateral forces from the stub shaft could be transferred to the main shaft.

5.2.3 Oil-Film Bearings

Two oil film bearings were mounted near the two end disks and used to support the rotor. Each bearing consisted of a housing and two brass bushes having 35 mm land length. A 10 mm circumferential groove was left between the two bushes so that oil could be fed into it from a supply hole on top of the bearing. The bushes were designed to give the nominal diametral clearance of 0.25 mm. Thermocouples were attached to the end face of each bush for monitoring the bearing oil-film temperatures.

5.2.4 Lubrication System

Tellus oil T15 was used as lubricant. The lubrication system is shown in figure 5.2. A perplex shield arrangement was supplied to collect and drain oil to a small tank. A level switch was appended to the tank to ensure that the oil pump would force oil up to the header oil tank. A ten micron filter was fitted immediately after the pump. The high mounted header tank resulted in 0.4 bar supply pressure at the journal bearing housing.

5.3 Electromagnetic Bearing Actuators

Two electromagnetic actuators were used to apply forces to the rotor. The control actuator was located at a position to guarantee that the rotor system was controllable. The second actuator was located in a similar off-centre position and was used to apply disturbance forces. Both actuators consisted of a magnet unit, a rotor sleeve, and an emergency bearing. The magnet units had eight poles with coils on each of them. The coils of each pole-pair were connected together and consequently produced a configuration of four U-shaped magnets (figure 5.3). When electrical current passed through the coils, magnetic flux was generated and closed by a ferromagnetic ring on

the rotor sleeve. Emergency bearings were fixed within the actuator housings to limit the motion of rotor and avoid contact between the magnets and sleeves. The gap between the magnet pole face and the sleeve was 1.2 mm. Between the emergency bearing and the sleeve the gap was 1.0 mm.

Each actuator had a power amplifier. The applied voltage of both amplifiers was 310 V. For the control amplifier, the range of input control voltage and maximum output current of each channel was ± 10 V and 2.5 A respectively, while, for the second amplifier, these were ± 50 V and 25 A respectively.

5.3.1 Dynamic Characteristic Of The Control Magnetic Actuator

An input-output system consisting of magnetic actuators and power amplifiers is, strictly speaking, a non-linear system. The power amplifier was designed in such a way that control currents, i_{+x}, i_{-x}, i_{+y}, i_{-y}, and input control voltage U_x and U_y had the following linearized relation in the working range:

$$i_{+x} = k_a(V_o + V_x) \quad , \qquad i_{-x} = k_a(V_o - V_x)$$

$$i_{+y} = k_a(V_o + V_y) \quad , \qquad i_{-y} = k_a(V_o - V_y)$$

where V_o is the bias input voltage which was equal to the maximum possible value of the input control voltage V_x or V_y. The actuator characteristics can be linearized using premagnetization and differential currents in opposite faced pairs of magnets [73]. Therefore the overall linearized relation between input control voltages and output magnetic forces were

$$F_x = k_i V_x + k_s x$$

$$F_y = k_i V_y + k_s y$$

where k_i and k_s are force-voltage and stiffness coefficients, which had values

approximately 225 N/V and 1740 N/mm respectively. x and y are rotor displacements at the position of the actuator.

The characteristic of the actuator-amplifier system is shown in frequency domain in figure 5.4 . It is indicated that the system is similar to low pass filter with cut off frequency 150 rad/s. Consequently, the maximum force amplitude of 1200 N can be delivered by the actuator below this frequency, while the amplitude reduces by 20dB per decade at frequencies above 150 rad/s.

5.3.2 Dynamic Characteristic Of The Second Magnetic Actuator

The dynamic characteristics of the second magnetic actuator are similar to the control actuator. The actuator and power amplifier were designed in such a way that the maximum force the actuator could deliver was 1000 N. However, this maximum force can be applied up to 314 rad/s, compared with the control actuator force of 700 N at frequency 314 rad/s. This is expressed in figure 5.5.

The second magnetic actuator was used only as a disturbance force generator. The excitation frequency and amplitude of force could be adjusted to supply either a non-synchronous excitation, or simulated noise with high frequency components.

5.4 Data Acquisition System

5.4.1 Transducers

Six eddy current transducers were used to measure the shaft displacement. Their effective measurement range was from 0.48 mm to 4.8 mm. Signals with frequency up to 10 kHz (62.8×10^3 rad/s) could be detected by the transducers. The transducers were mounted horizontally and vertically at three locations, including the control actuator position.

An incremental encoder was connected to the shaft at the driven end of the rotor. TTL compatible pulses of 1/rev and 256/rev were provided by the encoder. These pulse signals entered an interface board for initiating the A/D conversion and supplying the rotor speed measurement.

5.4.2 Filter Circuits

In real time control systems, physical variables measured are continuous-time signals, which should be converted into digital form by a A/D convertor in order that control process can be carried out digitally in computers. The conversion is performed at the sampling time. Computers interpret the signals as a sequence of digital numbers, process them according to an algorithm, and give a new sequence of digital numbers as a output. The output numbers can be converted to analog signals by a D/A convertor, which can be used to drive control actuators. A problem is then raised that sampled signals may be contaminated by high frequency noises. Thus, filters are needed to prevent signal contamination.

Filter circuits were placed between the displacement transducers and the A/D convertor. They were used to avoid the possibility of aliasing corrupting results of the measurements. If signals with maximum frequency f_{max} are required to be measured, the sampling frequency f_s must be at least twice of f_{max}. The frequency $f_s/2$ is refereed as Nyquist rate. A component above this frequency y_a may appear as a aliased image y_a' in low frequency range shown in figure 5.6. This will result in a spurious component which does not actually exist in the real signals. If the controller acts on this false component, the performance of the closed-loop system may worsen. Therefore a filter was added immediately before A/D convertor.

The diagram of the filter circuitry is shown in figure 5.7. The filter actually consisted of two parts. The first part had high pass characteristics, while the second part had low pass characteristics. As a whole, the filter had band pass characteristics with frequency bandwidth from 10 to 2513 rad/s as shown in figure 5.8. It then can be used to block the DC and alias components. The form of W_{fm} (from equation (4.14)) is given in Appendix C.

5.4.3 RTI-815 Interface Board

The RTI-815 board is a multi-function data acquisition card which can be plugged in a personal computer so as to provide a real-time direct interface between the analog signals in real world and digital signals in computer. It is a 12-bit A/D and D/A convertor and has the feature of analog I/O, digital I/O, and timer-counter pulse I/O.

5.4.3.1 Analogue Input / Output Feature

The board contained a 12-bit analog-to-digital convertor with conversion speed between 25 μs to 30 μs. It had 16 channel single ended analog inputs or, alternatively, 8 channel differential analog inputs. By choosing different configuration of the board, the input voltage could be set at ranges of 0 to +10 V, -5 to +5 V, and -10 to +10 V. A on-board amplifier with several gain selection was included and could be used to condition low-level analog input signals so that accurate measurement can be obtained. The 12 bit (4096) counts provided a LSB (least significant bit) 4.88 mV when in the ±10 V range. There were two modes for data acquisition. The first was the collect mode for single input and the second was the scan mode for multiple channel input. The scan mode, with automatic wrap around when the last channel conversion was finished, was performed to convert analog signals to digital form, channel by channel sequentially, together with the direct memory access (DMA) circuitry of the board. This mode was used in the project.

The board also contained two independent 12-bit digital-to-analog convertors with settling time 20 μs for full-scale step changes. These two output channels could be set individually to a voltage within the range of 0 to +10 V or -10 to +10 V. The 12 bit (4096) resolution provided a LSB 4.88 mV when in the ±10 V range, and 2.44 mV when in the 0 to +10 V range.

5.4.3.2 Time - Related Digital Input / Output Feature

A 16-bit counter/timer chip was included in the board which could be used to measure the rotational speed of the rotor. The 256/rev TTL signals from the encoder was linked to the input part of the chip. The frequency measurement range was 0 to 100 kHz (628×10^3 rad/s).

5.5 Personal Computer

An IBM AT-compatible computer (Opus V) was used as a frame to hold the RTI-815 interface board. The speed of the computer CPU was 12 MHz with turbo mode on, and 8 MHz with turbo mode off. The 8 MHz speed option was applied since the RTI-815 board could work only in the non-turbo mode. The PC was used to act as a mainframe for performing data acquisition and direct communication with the transputer.

5.6 Transputer Hardware

5.6.1 Introduction

For rotor bearing systems with high rotational speed, a fast processor capability is essential for implementing real-time control strategies. This requirement may be feasible on a very expensive single processor computer. Alternatively, a relatively low cost multiprocessor computer called a transputer can be used to achieve satisfactory results. A transputer is both a computer on a chip and a silicon component like a

transistor. It has conventional CPU, links, on-chip RAM etc, similar to a computer. However, each one of them can be treated as a component and they may be connected together by on-board links to form a parallel computer. This leads to faster calculation and communication than is available with conventional computers.

5.6.2 Structure Of Transputers

Inmos T800 transputers constituted the main part of the parallel computer for the project. The Inmos T800 is a processor consisting of a 32-bit CPU, a 64-bit floating point unit (FPU), 4KB of fast on-chip RAM, an external memory interface, four serial links, and internal timers. The block diagram of a T800 transputer is shown in figure 5.9. The FPU provides single and double length operations for floating point arithmetic. The on-chip RAM provides a maximum data rate of 80 Mbytes/s with access from both the processor and links. A DMA block transfer mechanism was used to transfer messages between memory and other transputers via the links which have a maximum operating speed of 20 Mbits/s. The external memory interface used multiplexed data and address lines and provided a data rate of up to 26.6 Mbytes/s. The internal processor speed could be generated by a 5 MHz external clock and, hence, the CPU clock speed could be scaled up to 25 MHz.

5.6.3 Structure Of Parallel Computer

The parallel computer hardware for the project consisted of nine transputer boards which were hosted by a rack made up of the following processing boards:

1) Six Inmos T800 boards to supply the main computational power.
2) One I/O board to provide input-output capability.
3) One link topology configuration board to configure the topology of all the boards.
4) One graphics board to provide high resolution graphics.

The communication between the T800 processing boards was achieved via the four links on each transputer. A unique number was assigned to each transputer rack. The four links were generally referred to as link 0 to link 3. The interconnection of all the transputer rack is shown in figure 5.10.

A total of four transputers were used for the project. The transputer connected to the PC executed a control server program and a user monitor program executed on a second transputer. The third one was used to create high resolution graphics and the fourth ran system network management software and text input/output.

5.7 Operating System

An operating system developed in 1986, called Helios Parallel Operating System, was used in the parallel computer. The idea of the system was based upon the Client-Server model with inter-processor communication handled transparently by the system kernel.

According to the communication methods used, programming philosophy can be categorised into four types in applications in follows:

1) Single processor programs. Helios contains libraries for FORTRAN, C, and Posix (UNIX functions which provide a transparent interface to the operating system facilities).

2) Multiprocessor task force. The Component Distribution Language (CDL) can be utilised to define parallel task components which can be then loaded and executed by Helios with defined logical interconnected communication via pipe streams.

3) Distributed servers. Helios can be used to run a number of servers distributed around a processor network. The server accepts requests from clients, then performs the requested service, and finally sends back a reply.

4) Stand-alone programs. Some transputers can be booted with Helios stand alone run-time programs that use the links directly without Helios being loaded. This was required if the processor had limited memory or full control of some transputers was needed.

5.8 Software Configuration

The software for on-line control executed on the transputers under Helios Parallel Operating System to execute the control process. The general arrangement of the control system is shown in figure 5.11. In the project, the control law had the state space form

$$\dot{x}_c = A_c x_c + B_c y$$

$$u = C_c x_c + D_c y$$

It can be diagonalised by the eigenvector matrix transformation

$$x_c = V q_c$$

where V is the eigenvector matrix for A_c. This leads to

$$\dot{q}_c = A_q q_c + B_q y$$

$$u = C_q q_c + D_q y$$

where

$$A_q = V^{-1} A_c V \quad , \quad B_q = V^{-1} B_c \quad , \quad C_q = C_c V \quad , \quad D_q = D_c$$

and A_q is a diagonal matrix.

This continuous form the controller can be converted to digital form with the bilinear transform the Laplace transform variable

$$s = \frac{2(1-z^{-1})}{T_s(1+z^{-1})}$$

to give

$$q_{c_{k+1}} = A_d q_{c_k} + B_d(y_k + y_{k+1})$$

$$u_{k+1} = C_d q_{c_{k+1}} + D_d y_{k+1}$$

where

$$A_d = \left(\frac{2}{T_s}I - A_q\right)^{-1}\left(\frac{2}{T_s}I + A_q\right), \qquad B_d = \left(\frac{2}{T_s}I - A_q\right)^{-1} B_q$$

$$C_d = C_q, \qquad D_d = D_q$$

In practice, the above matrices may be multiplied by a set of fixed scaling factors which map the ADC and DAC values to standard units. This is more efficient than scaling the input/output variables for every sample.

After discretzation, the control process could be executed on the computer. The control software consisted of three bits: RTILINK, DCLSRV, and DCLMON.

5.8.1 Data Acquisition Program - RTILINK

This program was executed on the PC to handle analogue data input/output and the data transfer to/from transputers. It carried out following steps:

```
while(Mode != Exit)
{       Check frequency counter
        Input data from transputer link
        Set analogue outputs
        Read analogue inputs
        Output data to transputer link      }
```

5.8.2 Digital Control Loop Server Program - DCLSRV

This server program ran on the transputer as a controller. It was used to set control parameters and collect data. The server was implemented as a number of cooperating processes:

1) Timer process which was programmed to generate a software interrupt at regular intervals;

2) Control process which was programmed to wait for timer interrupt, get inputs from the PC, check trip limit, calculate control output, and send output to the PC;

3) Communication process which could update or inspect the shared data while the control process was waiting for the timer interrupt;

4) Event process which performed fast data logging and could transfer data concurrently with the control calculation.

5.8.3 Digital Control Loop Monitor Program - DCLMON

This program ran on the transputer and a shell with built-in commands for input/output of coefficient matrices, conduction of the DCLSEV server, data logging, data saving, and data plotting.

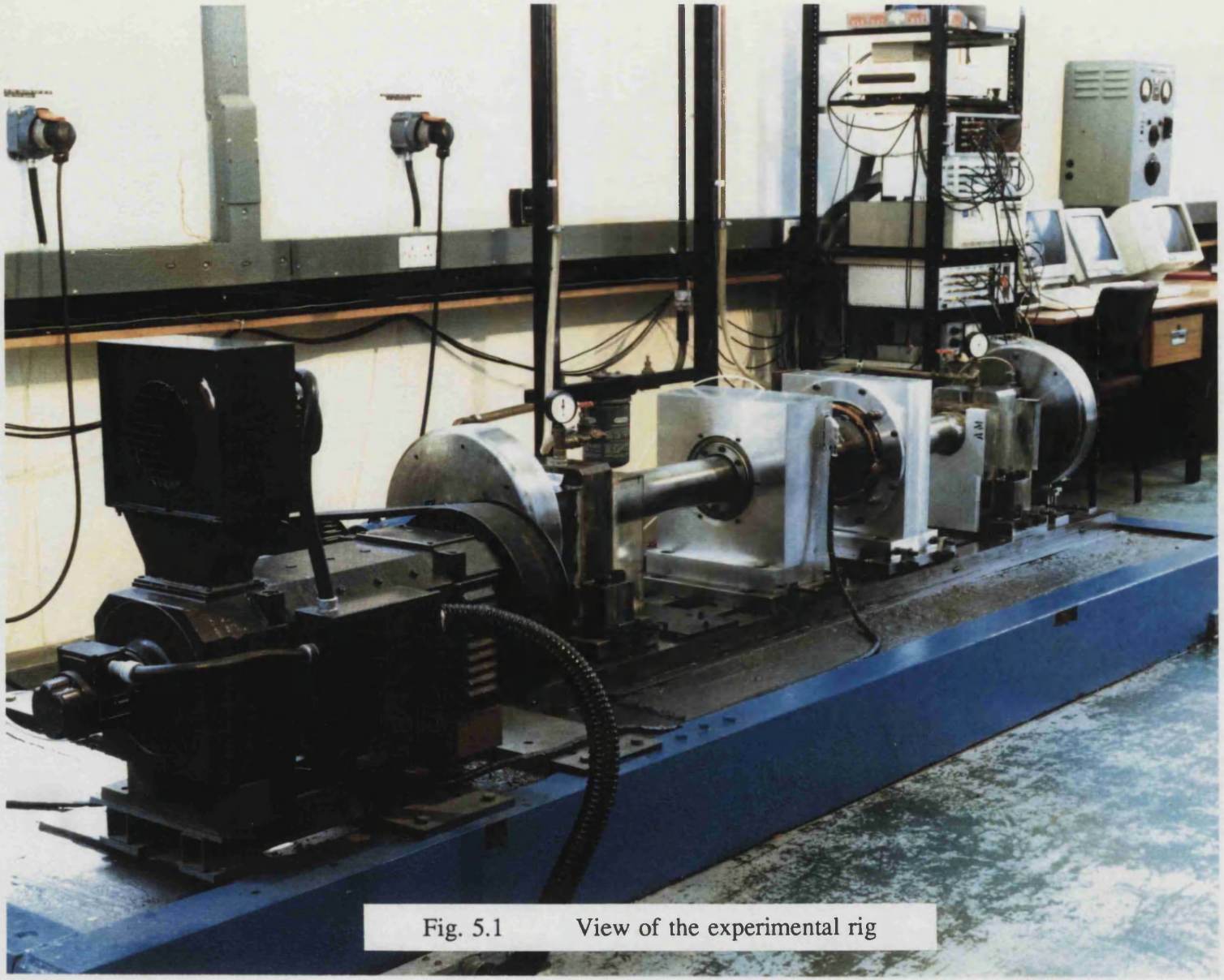

Fig. 5.1 View of the experimental rig

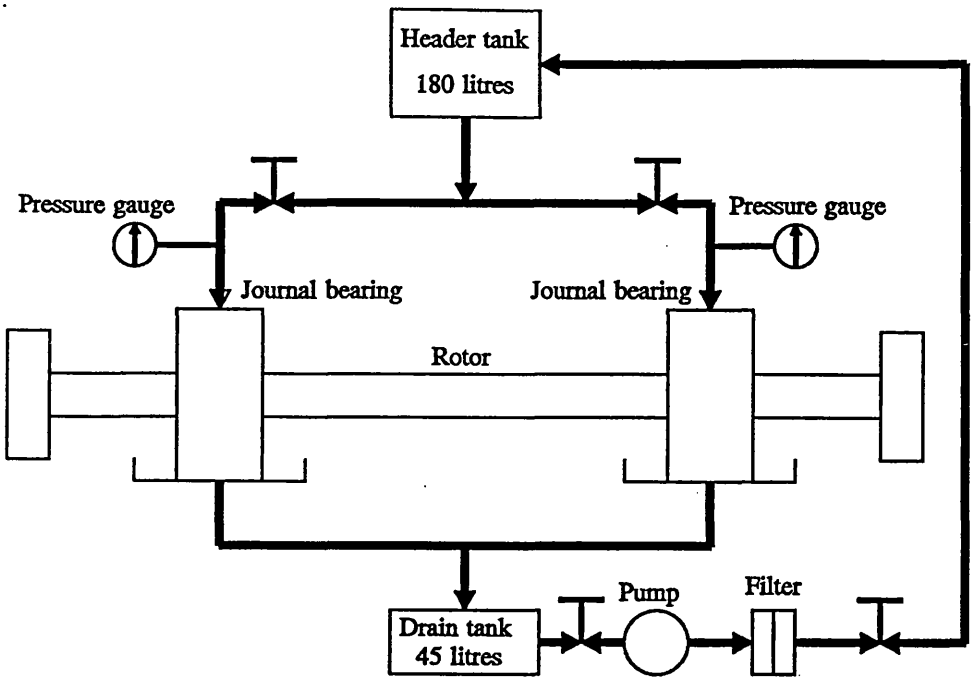

Fig. 5.2 Journal bearing lubrication system

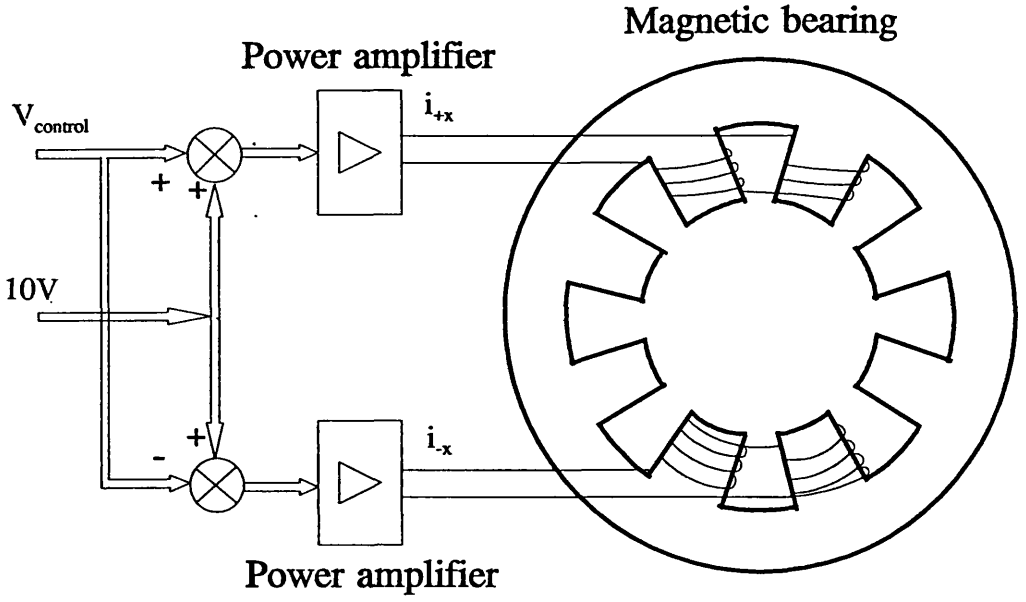

Fig. 5.3 Magnetic bearing configuration with current and voltage connection

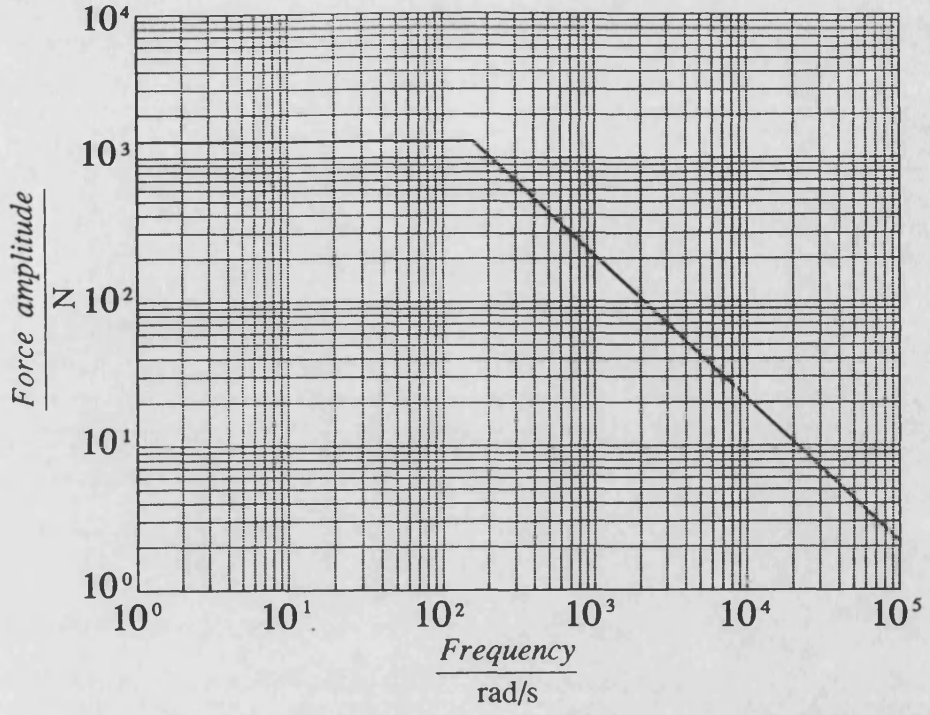

Fig. 5.4 Variation of the maximum output force amplitude of control actuator with frequency

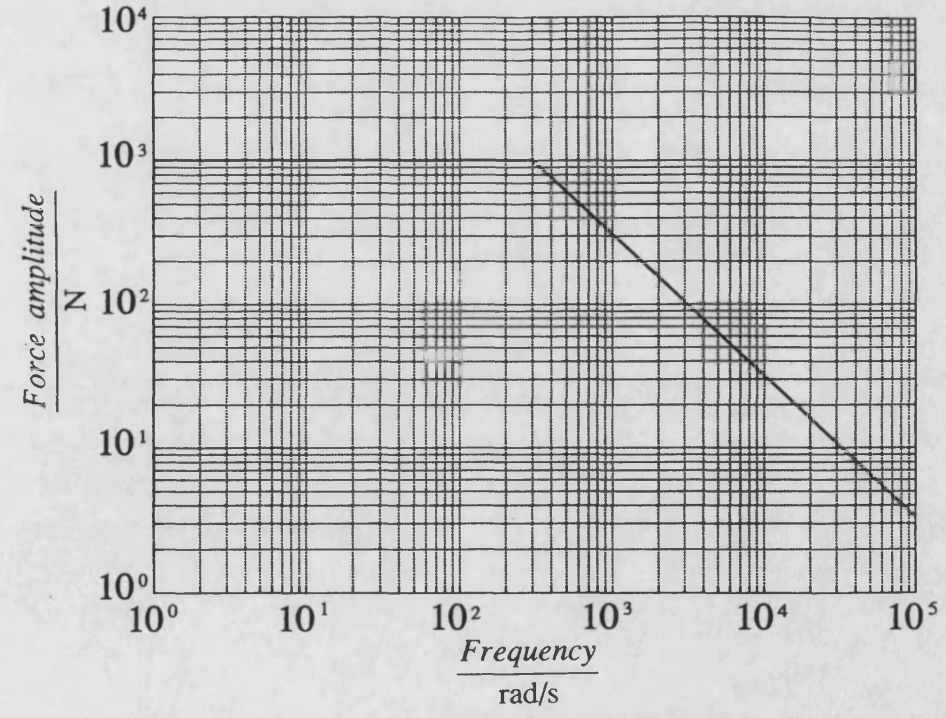

Fig. 5.5 Variation of the maximum output force amplitude of disturbance actuator with frequency

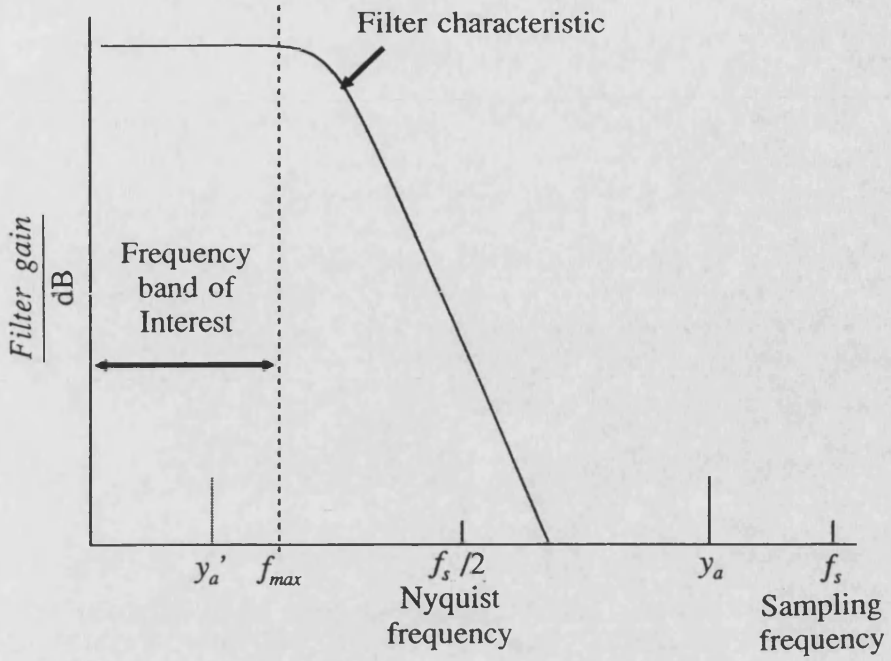

Fig. 5.6 Principle of anti-alias filter

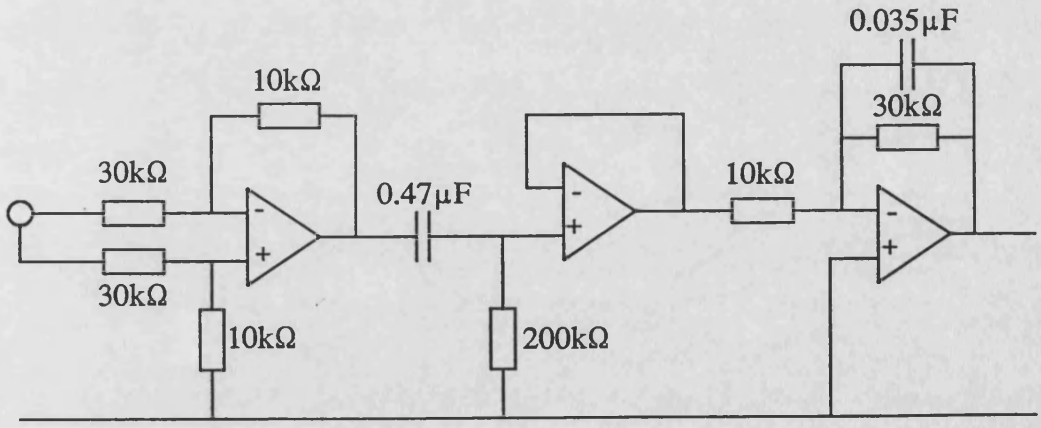

Fig. 5.7 Filter circuit for A/D converter

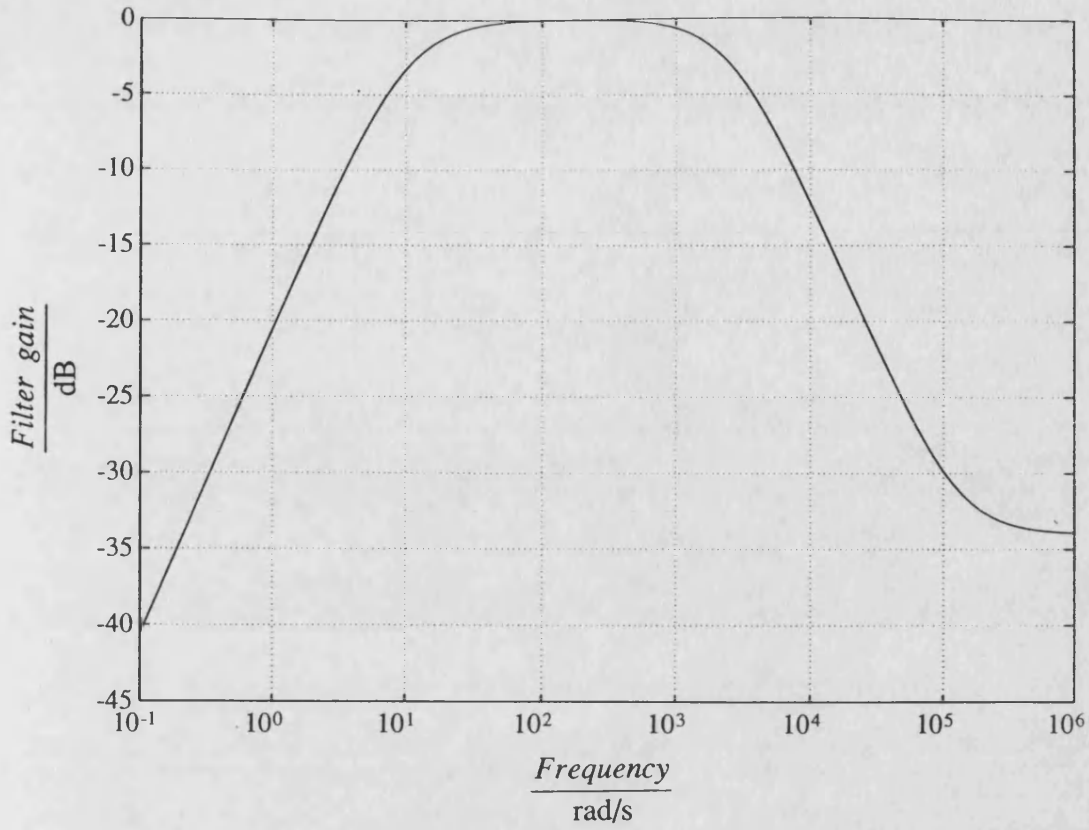

Fig. 5.8 Filter band pass characteristic

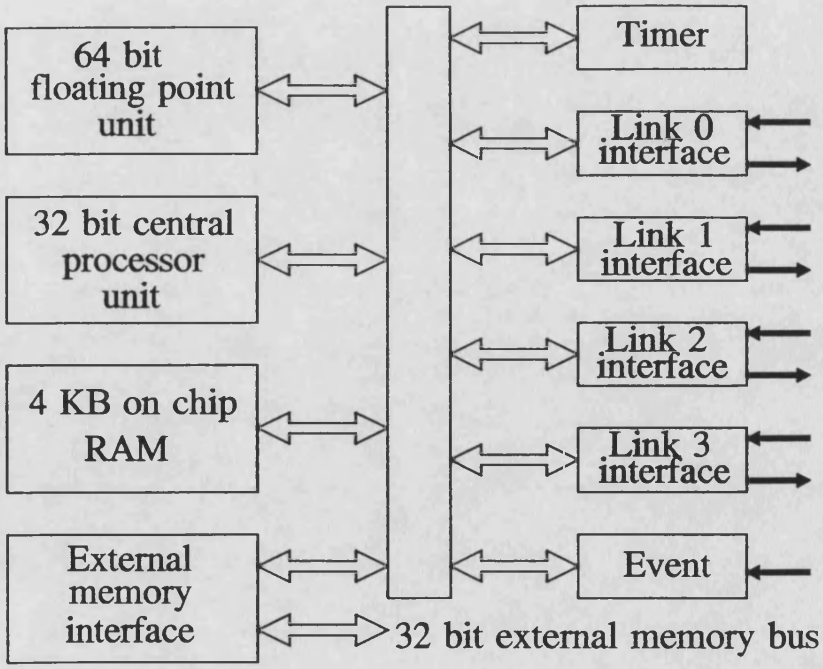

Fig. 5.9 Block diagram of T800 transputer

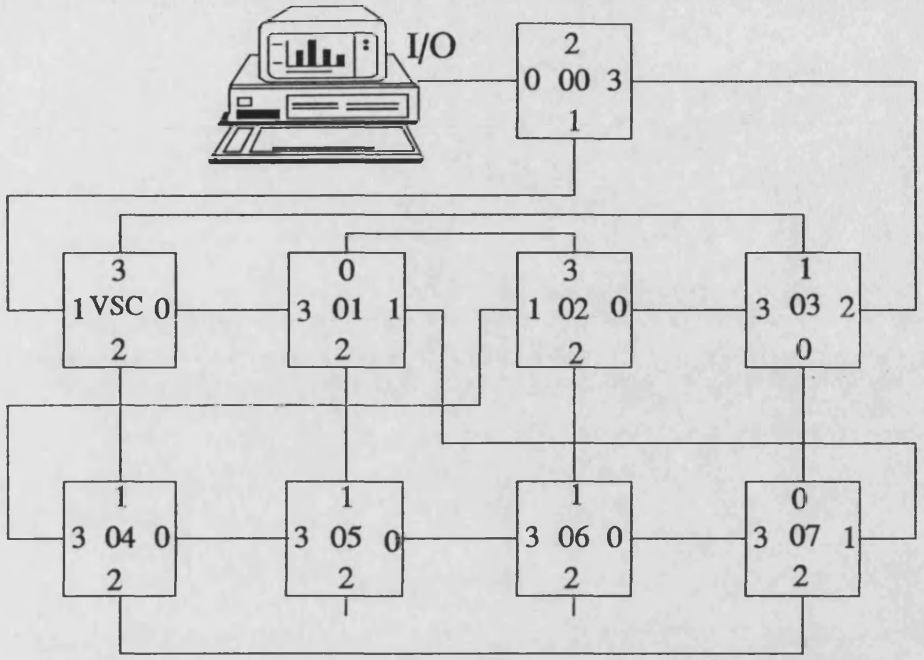

Fig. 5.10 Interconnection of transputers (VSC = Video System Controller)

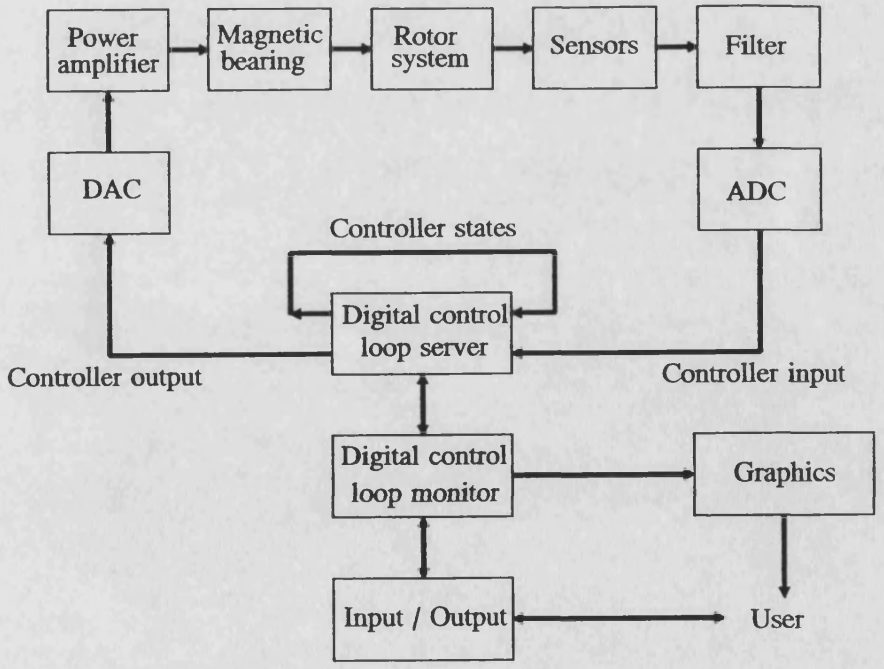

Fig. 5.11 Control scheme block diagram

CHAPTER 6 APPLICATION OF H_∞ CONTROLLER DESIGN PROCEDURE TO EXPERIMENTAL RIG

6.1 Introduction

In this chapter, a model of the experimental rig described in Chapter 5 is analyzed. The analysis follows the procedure described in Chapter 4 and the characteristics of the full order and reduced order open loop systems are obtained by computer simulation. The surface roughness signals were obtained by measurement and digital signal processing. The general forms of the H_∞ controller weighting function matrices are then chosen based on these results. After forming the standard H_∞ equation, the controller is derived. Characteristics of the controller and the closed loop system are then analyzed in different situations and vibration reduction capability is evaluated theoretically.

6.2 Dynamic Analysis Of The Theoretical Model

The equation of the rotor-bearing system can be written in the form of equation (4.1). In order to model the rotor-bearing system accurately, 11 finite elements were chosen as a division of the rotor (figure 6.1). Thus the mass, damping, and stiffness matrices $\boldsymbol{M}$, $\boldsymbol{C}$, $\boldsymbol{K}$ of the equation (4.1) have dimensions 48×48. $\boldsymbol{B}_f$ and $\boldsymbol{G}_f$ have dimensions 48×24 and 48×2 respectively. Therefore, in the state space equations (4.3) and (4.6), matrices $\boldsymbol{A}$, $\boldsymbol{B}_d$ and $\boldsymbol{B}_u$ have dimensions 96×96, 96×24 and 96×2 respectively. Figure 6.1 also shows the measurement states (n_m = 6 displacements) and the control states (n_c = 16 displacements and velocities). Thus $\boldsymbol{C}_c$ has dimensions 16x96 and $\boldsymbol{C}_m$ has dimensions 6x96.

6.2.1 The System Critical Speeds And Modal Analysis

The first and second natural frequencies of the free-free rotor were calculated without

the 2nd magnetic bearing sleeve to be 290 rad/s and 906 rad/s. These compare with the measured natural frequencies of 301 rad/s and 919 rad/s [2] and demonstrate that the theoretical model of the system without bearings is accurate up to a frequency around 950 rad/s with error around 3%. When gyroscopic effects and oil-film bearings are introduced, the system matrices are a function of the rotational speed and, consequently, the eigenvalues of the rotor-bearing system are also functions of the rotational speed.

The variation of the imaginary part of the eigenvalues with the rotational speed is shown in the Campbell diagram of figure 6.2. Intersections of the synchronous excitation line $\omega = \Omega$ and lines of imaginary part of the eigenvalues indicate approximate critical speeds of the system. They are 228, 249, 271, 309, 467, 559, 630, and 809 rad/s respectively. The divergence of the eigenvalues with speed shows the effect of gyroscopic moment and oil-film bearings on the system.

Mode shapes corresponding to the lower critical speeds are shown in figure 6.3. The first two represent nearly rigid body modes, whilst the third and fourth represent the first order rotor flexural modes, which are split due to gyroscopic coupling and bearing asymmetry. The fifth represent the split of second order rotor flexural modes. It is indicated that the oil-film bearing positions are close to the nodes of the first order rotor flexural mode shapes.

The variation of eigenvalues with the rotational speed in the complex plane is shown in figure 6.4. It is indicated that the system becomes unstable as the rotational speed increases beyond 588 rad/s. This is caused by the oil-film bearings and the frequencies of the unstable modes are below half of the rotor rotational speed. This is related to oil whirl instability.

The rotor-bearing system is multi-input, multi-output by nature and may be represented by a transfer function matrix $\boldsymbol{G}(s)$. The generalised frequency response for such a system may be obtained in terms of the maximum singular value of $\boldsymbol{G}(s)$ (denoted by $\bar{\sigma}(\boldsymbol{G}(j\omega))$ in section 3.4.1). It is also noted that $\bar{\sigma}(\boldsymbol{G}(j\omega))$ will be speed dependent. Figure 6.5 shows the generalised frequency responses over a frequency range 0 - 1000 rad/s and for a range of rotational speeds 0 - 346 rad/s. These show that only two modes around the frequency 300 rad/s are lightly damped. This is due to the fact that the bearings are close to the nodes of the rotor first and second flexural modes. The damping contribution from the bearings to the third and fourth critical speed modes (271 rad/s, 309 rad/s) is therefore small.

6.2.2 Model Reduction

The reduced order system can be obtained by truncating the full order system at a frequency just above the frequencies of the lightly damped modes. Since the system response over the frequency range 0 - 1000 rad/s is due mainly to the lightly damped modes, a reduced model chosen in this way retains most of the desired characteristics of the full order system.

The characteristics of the reduced order system, which retains the first four modes (four conjugate pair of eigenvalues/vectors), are evident from the maximum singular value plot in figure 6.6. Comparison with figure 6.5 shows that the reduced order system has the same characteristics as those of the full order system for frequencies 0 - 346 rad/s and eliminates all resonance effect above this frequency range.

For the reduced order system with 4 retained modes (4 conjugate pairs of system eigenvalues/vectors), eigenvalues of the controllability and observability gramians of the system at rotational speed 309 rad/s are

2.49×10^{-3}; 3.25×10^{-3}; 0.83; 1.15; 162; 163; 189; 190

and

2.78×10^{-8}; 3.30×10^{-8}; 3.47×10^{-8}; 4.19×10^{-8}; 7.89×10^{-8}; 7.90×10^{-8}; 1.80×10^{-7}; 1.81×10^{-7}

respectively. The first four correspond to the rigid body modes, whilst the second four correspond to the split first order rotor flexural modes. It is indicated that the modes in the reduced order system can be controlled and observed.

For a reduced order system including the split second order rotor flexural modes (i.e. 6 retained modes), eigenvalues of controllability and observability gramians relating to the extra modes are

0.178; 0.219; 3.28; 4.87

and

1.23×10^{-10}; 1.87×10^{-10}; 1.26×10^{-9}; 1.56×10^{-9}

respectively. These values indicate that, although the extra modes are still controllable and observable, they are less so than the lightly damped first flexural modes. Since these modes are also well damped and the control force required by the actuator is not very large around these frequencies, the reduced order system was chosen to retain the first four modes only.

6.3 Measured Surface Roughness

Six displacement transducers (figure 6.1) were used to measure rotor vibration. However, these also detected surface roughness. At slow rotational speeds, dynamic motion of the rotor will be negligible and the transducer signals will almost entirely be due to the roughness. Figure 6.7 shows the transducer displacement measurements at a rotational speed of 21 rad/s. The time base covers approximately two shaft revolutions. Figure 6.8 shows the corresponding discretised frequency spectra of the measured displacement signals. For the particular rig or rotor, it is seen that harmonics higher that 5th order are not significant. The importance of obtaining the frequency

spectra of the roughness signals was detailed in section 4.4.4 and figure 4.5. Suppose that the maximum rotational speed is 3300 rev/min (346 rad/s). Figure 6.9 shows how the set of roughness spectra shift in frequency with this rotational speed change. A bounding curve has also been drawn to encompass the spectra. In some cases this bound is clearly conservative, but when included in the controller design there should be no complication arising due to measurement spillover.

6.4 Analysis And Design Of The H_∞ Controller

Ideally, for a rotor-bearing system with rotational speed dependent coefficients, the controller should be designed at every rotational speed. Practically, this is not possible because a large amount of computer memory and calculation is needed. To compromise, a step change controller can be used. The rotational speed range is divided into several sub-ranges. A controller designed at one specific speed within each range can then be applied when the rotational speed remains in this range. When the speed moves into another range, the controller can be switched. In this way, less computer memory and calculation are required. Therefore, the better approach is to design a controller with a minimum number of the ranges whilst retaining the required closed loop system performance characteristics.

As remarked in Chapter 4, three types of forcing were considered:

(a) Steady synchronous forcing due to unbalance.

(b) Steady non-synchronous forcing due to external excitation.

(c) Sudden forcing due to mass loss.

Controllers were designed for each case and the differences in the designs will be explained in the following sections. The differences arise in the choice of weighting function matrices $\boldsymbol{W}_u$, $\boldsymbol{W}_z$, $\boldsymbol{W}_y$ as outlined in section 4.4.4. For reference, the different forms of the weightings are specified in Appendix C.

6.4.1 Choice Of Controller Weighting W_u

In fact the first weighting function W_u did not vary between force types. The frequency characteristic of the control magnetic bearing was similar to a first order low pass filter with cut-off frequency 150 rad/s (figure 5.4). The chosen weighting function maximum singular value therefore had the form of the high pass characteristic shown in figure 6.10. The break point frequency of its inverse was 150 rad/s, the same as that of the magnetic bearing controller. The characteristic also limited the ability of the controller to excite neglected high frequency modes. Since the third and fourth modes varied only slightly with rotational speed the weightings W_u was not varied with speed.

6.4.2 Controller Design In The Case Of Steady State Response

Controllers were designed at rotational speeds 100, 150, 200, 250, 309 rad/s to cover speed ranges 0-125, 125-175, 175-225, 225-275, 275-350 rad/s respectively. The last speed 309 rad/s was chosen to correspond with the fourth critical speed where large responses are expected.

6.4.2.1 Controller Design At Fourth Critical Speed 309 rad/s

This speed is considered in the first instance since the critical speed around 309 rad/s will involve large amplitude rotor vibration. Options in the choices of W_z and W_y are studied with regard to their influence on the controller performance.

The full order system was transformed into the reduced order system with four retained modes. The weighting W_y was chosen to have the maximum singular value

low pass characteristic of figure 6.11. A break point was chosen at 1000 rad/s. The aim of W_y is to reduce measurement states Y_m down to the level of the roughness bound in figure 6.9, but to allow the high frequency modes to be evident in these states above 350 rad/s. The frequency characteristic of the magnetic bearing means that control capability is greatly reduced above 350 rad/s.

Three choices of W_z were considered with maximum singular values having band pass, low pass, and constant characteristics as shown in figure 6.12. They were chosen to be effective in achieving attenuation of rotor vibration around the critical speeds of 271 rad/s and 309 rad/s (see figure 6.5).

The controller was obtained using the procedure in the section 4.4. For the three forms of W_z, the maximum singular values of the controllers are plotted in figure 6.13. It is clear that the controllers all have low pass characteristics and, hence, can filter out high frequency mode effects in the full order closed loop system. It is also seen that there are no large differences between the controller designs. To see this the lightly damped third and fourth modes of the full order system at speed 309 rad/s had open loop eigenvalues -1.9 ± j271, -3.36 ± j309. The controller shifted these as follows:

W_z band pass: -28 ± j252, -60 ± j293
W_z low pass: -26 ± j261, -106 ± j330
W_z constant: -30 ± j262, -98 ± j316

respectively. However, the controllers have different number of states:

W_z band pass: 12
W_z low pass: 12
W_z constant: 10

It is seen that no loss of controller performance occurs when lowest order controller

(W_z constant) is selected. Table 6.1 presents some eigenvalues (with their imaginary parts ≤ 1500 rad/s) of the open and closed loop system at 309 rad/s.

Table. 6.1 Some eigenvalues of the open and closed loop system at 309 rad/s

Open loop	Closed loop	Closed loop	Closed loop
	W_z band pass	W_z low pass	W_z constant
-42.3 ± j264	-36.7 ± j245	-731 ± j237	-315 ± j214
-33.2 ± j244	-28.0 ± j252	-32.1 ± j242	-31.8 ± j243
-1.90 ± j269	-60.3 ± j293	-25.8 ± j261	-29.8 ± j262
-3.40 ± j309	-217 ± j381	-106 ± j330	-97.8 ± j316
-57.3 ± j504	-127 ± j385	-126 ± j387	-1075 ± j356
-194.1 ± j867	-57.3 ± j467	-714 ± j485	-122 ± j388
-158.0 ± j943	-59.0 ± j507	-57.9 ± j505	-57.2 ± j502
	-192 ± j865	-194 ± j872	-188 ± j872
	-153 ± j941	-155 ± j944	-155 ± j945

6.4.2.2 Controller Design At Other Rotational Speed

At low rotational speed, surface roughness has an increasingly important effect on the measurement of the rotor displacement states. This is reflected in the measurement state weighting W_y. As in the 309 rad/s design, W_y had a low pass characteristic. The magnitude of this characteristic increased with speed in the manner shown in figure 6.14. The weighting W_z was, based on the experiences of the design at 309 rad/s, chosen to have a constant maximum singular value that shifted the lightly damped

third and fourth modes of the full order system as follows:

	open loop	closed loop
100 rad/s	-0.78 ± j282	-63 ± j294
	-1.15 ± j295	-67 ± j311
150 rad/s	-0.97 ± j279	-65 ± j243
	-1.60 ± j298	-100 ± j332
200 rad/s	-1.20 ± j276	-47 ± j248
	-2.10 ± j301	-117 ± j339
250 rad/s	-1.40 ± j273	-36 ± j256
	-2.60 ± j305	-89 ± j314

The maximum singular values of W_z are indicated in figure 6.15 for each case. The maximum singular values of the resulting controllers are shown in figure 6.16. Again the controllers have low pass characteristics where values increase with rotational speed.

6.4.2.3 Higher Reduced Order Model

Consider the controller design at 309 rad/s. If higher modes are required to be controlled, they should also be included in the reduced order system. If the fifth and sixth modes corresponding to open-loop system eigenvalues -57 ± j504 and -194 ± j867 are included, the maximum singular value of the controller designed, based on this model and with the same weightings as in section 6.4.1.1, is shown in figure 6.17. The eigenvalues of the open-loop system -57 ± j504 and -194 ± j867 were shifted to

-63 ± j508 and -203 ± j835 respectively by the controller. It is obvious that the magnetic controller actuator can not do much about the higher frequency modes due to the inherent low pass characteristics. This confirms that it is sufficient to retain only the first four modes in the reduced order system.

6.4.3 Simulation Of Steady State Responses

The series of the controllers designed at the rotational speeds 100, 150, 200, 250, 309 rad/s were used to simulate control of the rotor-bearing system in the speed ranges 0-125, 125-175, 175-225, 225-275, 275-350 rad/s respectively. This is referred to overall as a five speed controller. The synchronous unbalance responses of the controlled system are shown in figure 6.18 in which the vibration amplitudes are at the positions of stations 1, 5, 12 of figure 6.1. The unbalance was a nominal 5 g mass on the non-driven end disk at a radius of 200 mm. The uncontrolled responses are also shown in figure 6.18. It is seen that the vibration levels of the system are reduced significantly by the five speed controller. The controlled system experiences both low level and smooth responses, especially around the critical speeds.

Instead of using the five speed controller as above, only the two controllers designed at 100 rad/s and 309 rad/s were used. Switching between controller occurred at speed 250 rad/s and overall it is referred to as a two speed controller. Figures 6.19 shows the controlled and uncontrolled synchronous responses and comparison with the five speed controller results indicates that the vibration reduction is not affected significantly when the two speed controller is used. The reasons for this are:

1) The 309 rad/s controller was designed when the disturbance $\boldsymbol{D}_r$ was a maximum at fourth critical speed, ie, in the worst case. Hence, it should cover the other cases.

2) The dynamic characteristics of the system on which the control design was based varied little in the speed range 0-250 rad/s. Any small variations can always be compensated by a controller designed for robustness. The reason the 100 rad/s controller was applied was for coping with the effect of the dominant surface roughness at low rotational speeds. This effect becomes relatively smaller when the rotational speed increases.

6.4.4 Controller Design In The Case Of Sudden Mass Loss

Suddenly applied forcing on rotor-bearing systems due to, for example, mass loss can cause large rotor vibration amplitudes. It may also excite many modes simultaneously and the system may take a long time to settle down from one steady state condition to the other. For the system under consideration the fourth critical speed (309 rad/s) is an important reference case to examine.

The weighting function W_u remained the same as in the steady state case. W_z was chosen to have a maximum singular value to be constant and twice as large as that in steady state case to reflect the fact that transient responses may include overshoot. The low pass characteristic of W_y was increased accordingly. Both the maximum singular values of W_y and W_z are shown in figure 6.20. The characteristic of the resultant controller is shown in figure 6.21. It is clear that the maximum singular value of the controller (and hence control force) are larger than in the steady state case, but the high frequency uncertain modes are still filtered out by the controller.

6.4.5 Transient Responses

The controller designed at the fourth critical speed 309 rad/s, but for transient vibration control, was implemented numerically in the full order rotor-bearing system model. The transient responses of the controlled system in the time domain when the rotational speed was 290 and 309 rad/s are shown in figures 6.22 and 6.23. These responses were caused by a nominal mass loss of 20 g on the non-driven end disk at a radius of 200 mm. The vibration amplitudes at the stations 1, 5, 12 (figure 6.1) are plotted together with the responses of uncontrolled system. It is seen that the vibration levels of the controlled system are reduced significantly by the controller. The settling time of the controlled system from one steady state condition to another is much less than that of the uncontrolled system (around 0.1s from 0.5s). Furthermore, the large jumps in the responses of the uncontrolled system are nearly eliminated by the controller.

6.4.6 Effect Of The Surface Roughness On Control Design

The effects of the shaft surface roughness was included in the control designs previously mentioned. Consider now the controller designed at the rotational speed 100 rad/s. Suppose that all conditions are the same as in the section 6.4.1.2 except that no surface roughness term is included, i.e. $n=0$ in equation (4.23). The maximum singular value of the resultant controller is shown in figure 6.24 and is larger than that of the controller including the roughness. This may result in large control forces being applied even when the displacements are contributed mainly by the surface roughness. The controller acting on these false (vibration) displacement signals may degrade the performance of the closed loop system.

The procedure may be repeated for controller design at rotational speed 309 rad/s, without consideration of the roughness. The maximum singular value of the controller is shown in figure 6.25 together with the controller of 6.4.1.1 including roughness. The differences are small since the displacements are due mainly to rotor vibration and the roughness error is therefore small. The effect of the surface roughness must be taken into account in the control design, especially in a control design for use at low rotational speeds.

6.4.7 Effect Of Filters And Measurement Time Delay On Control Design

If the transfer function matrix W_{fm} (Appendix C) due to the measurement filter and time delay is ignored, the same control design procedure as in the section 6.4.1.1 will lead to a controller characteristic shown in figure 6.26. The phases of the transfer function from x-direction displacement to x-direction control force at the control magnetic actuator position are plotted for the cases with and without the W_{fm} matrix in figure 6.27. It is seen that phase differences of around 180° may occur. If the controller with consideration of the filter effect stabilizes the closed-loop system, the other controller with the 180° phase lag will certainly result in an unstable closed loop system.

6.4.8 Effect of Structure Variation On Control Design

The same control design procedure as in section 6.4.1 was carried out at 309 rad/s, but the model on which the control design was based had the second actuator sleeve removed from the shaft (figure 6.28). To the system with the second sleeve included, this system could be regarded as inaccurate. The controller can be regarded as a one designed when model error occurred. The third and fourth theoretical critical speeds

of the system without the second sleeve were 279 and 322 rad/s. Comparison with 271 and 309 rad/s in the system with the second sleeve indicates the extent of this modelling error. Figure 6.29 shows the maximum singular values of the controllers which were designed on the model with and without the second sleeve . The results indicate that the small variation of the system structure leads to a correspondingly small change in the controller.

6.5 Stability Considerations

The stability of a closed loop system can be examined by checking its eigenvalues. Consider the controller of section 6.4.1.1 designed at 309 rad/s. The two lightly damped eigenvalues of the open loop system are shifted in the complex plane at the rotational speed 309 rad/s as specified in section 6.4.1.1. At the rotational speed 588 rad/s, where open loop system instability occurs, unstable eigenvalues are

$$+0.02 \pm j304$$

It is noted that the imaginary part of the eigenvalue is about half of the rotational speed and this is due to oil whirl in the journal bearings. When the controller was implemented, however, the closed loop system was stabilised. The eigenvalue with the smallest stability margin was

$$-1.70 \pm j284$$

It has therefore been shown that the implementation of the controller can not only reduces vibration levels, but also increases stability margins, although the later effect is too small to be of any real benefit.

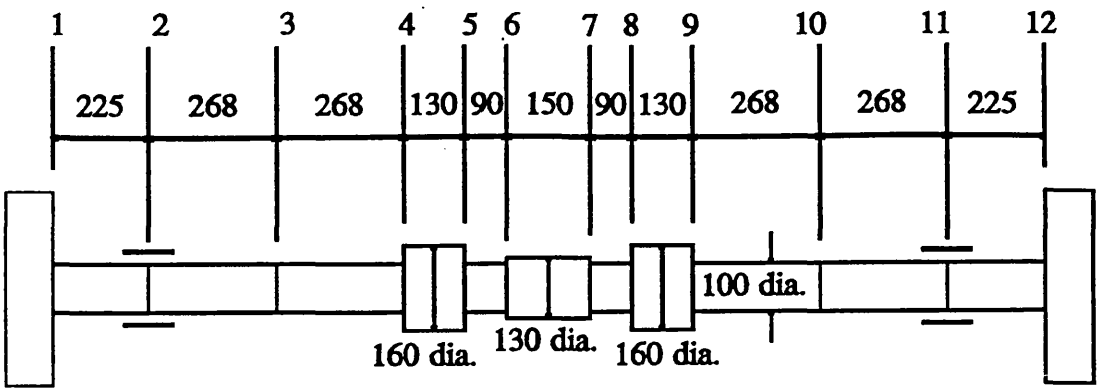

(a) Finite element discretisation

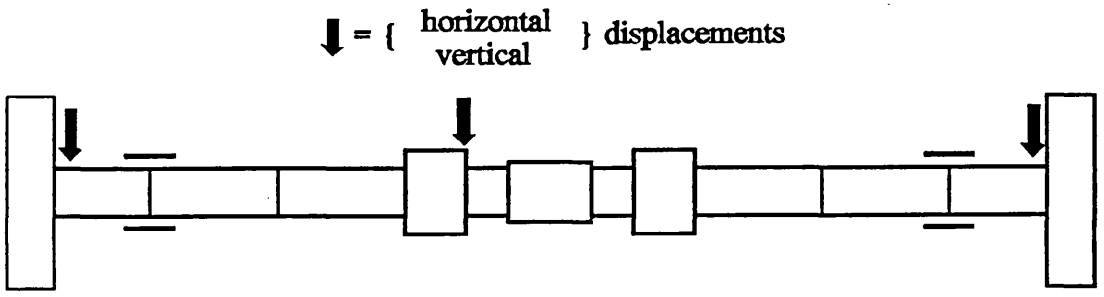

(b) Measurement states

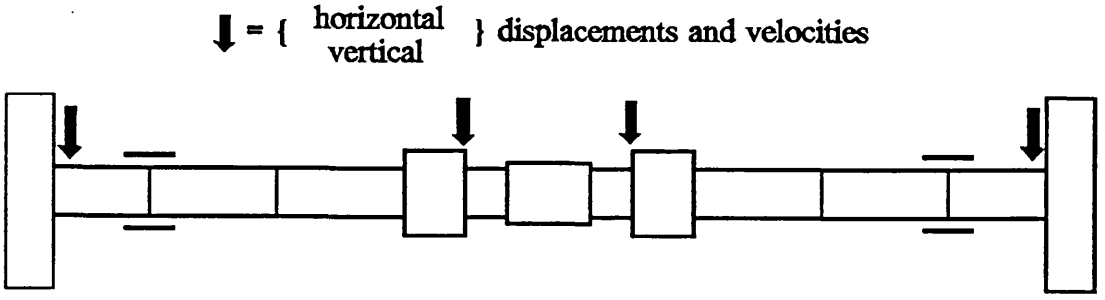

(c) Control states

Fig. 6.1 Finite element discretisation of the experimental rotor (all dimensions in mm)

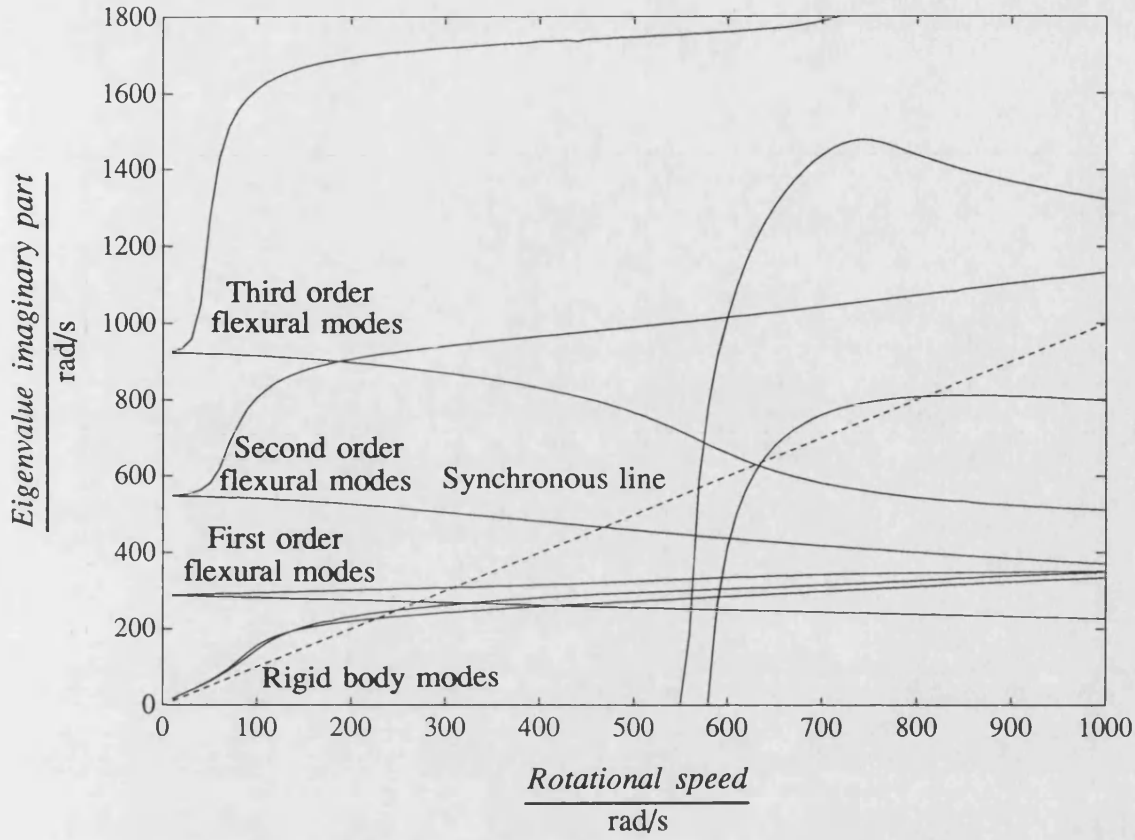

Fig. 6.2 Variation of rotor-bearing system natural frequencies with rotational speed

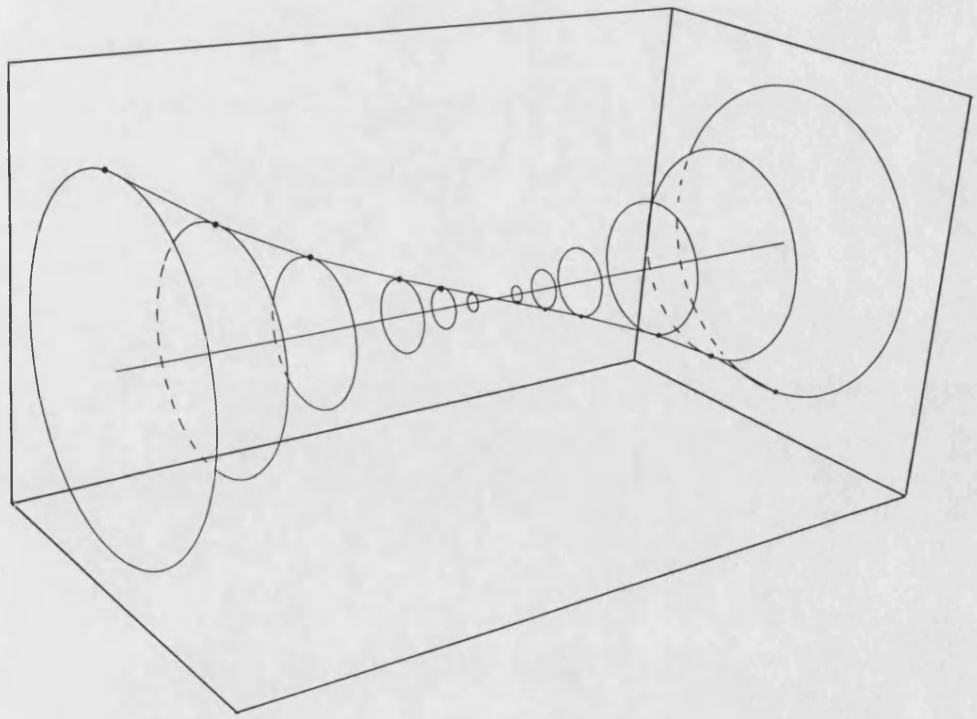

Mode shape at first critical speed (228 rad/s)

Fig. 6.3 Mode shapes at critical speeds

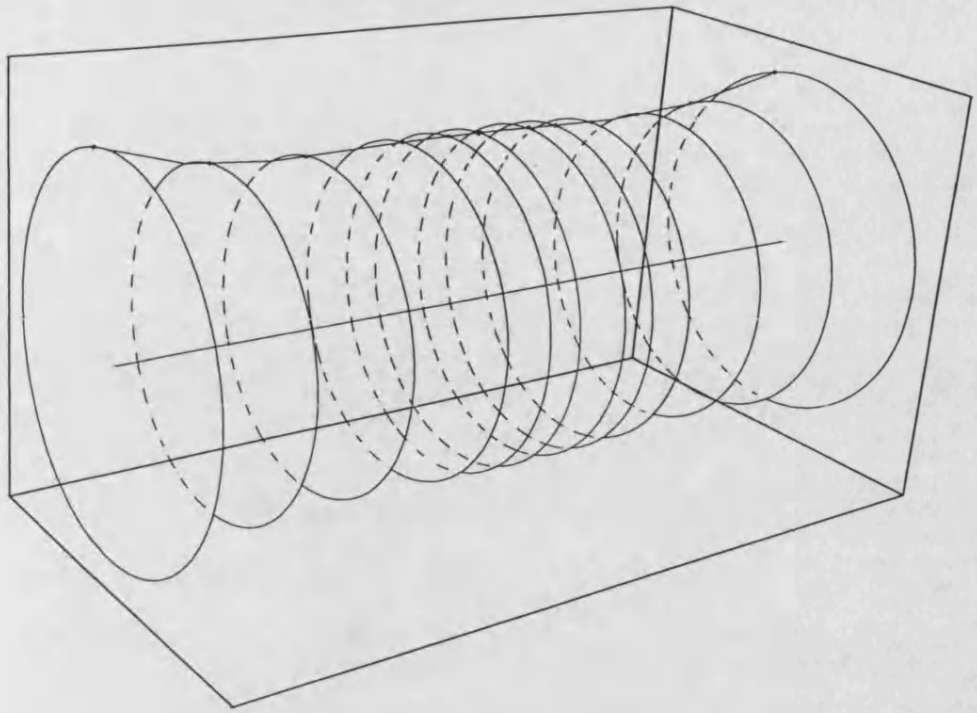

Mode shape at second critical speed (249 rad/s)

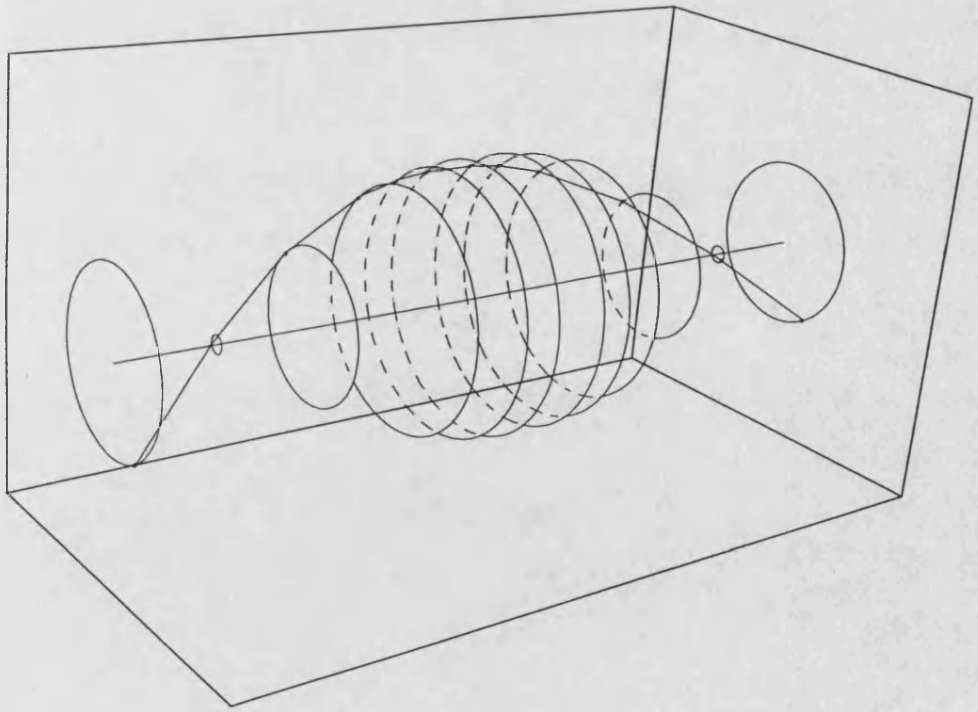

Mode shape in at third critical speed (271 rad/s)

Fig. 6.3 (continued)

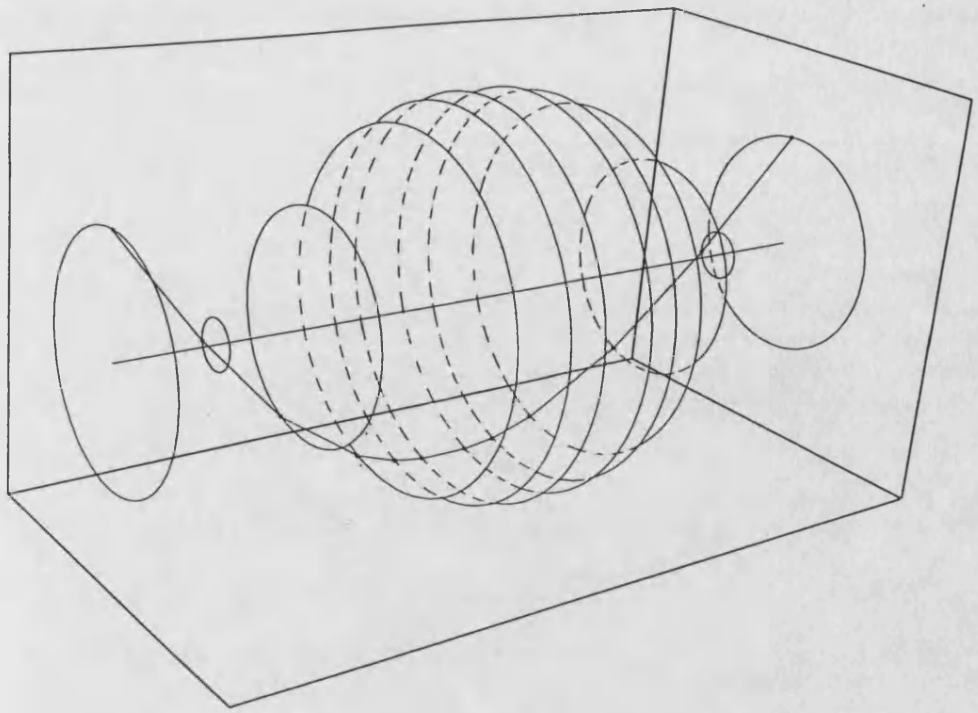

Mode shape at fourth critical speed (309 rad/s)

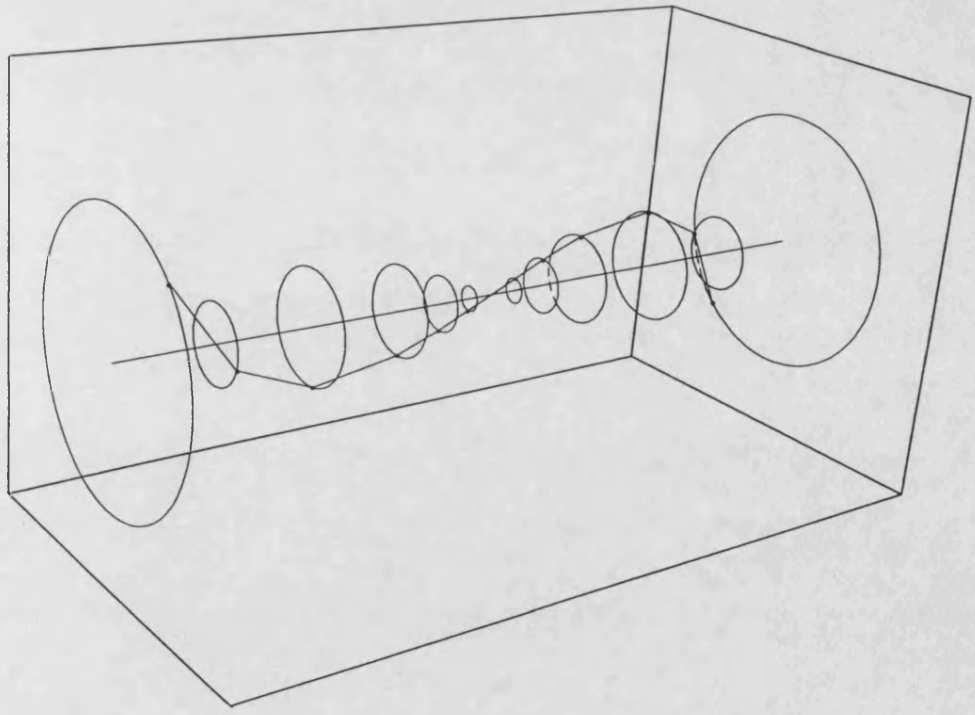

Mode shape at fifth critical speed (467 rad/s)

Fig. 6.3 (continued)

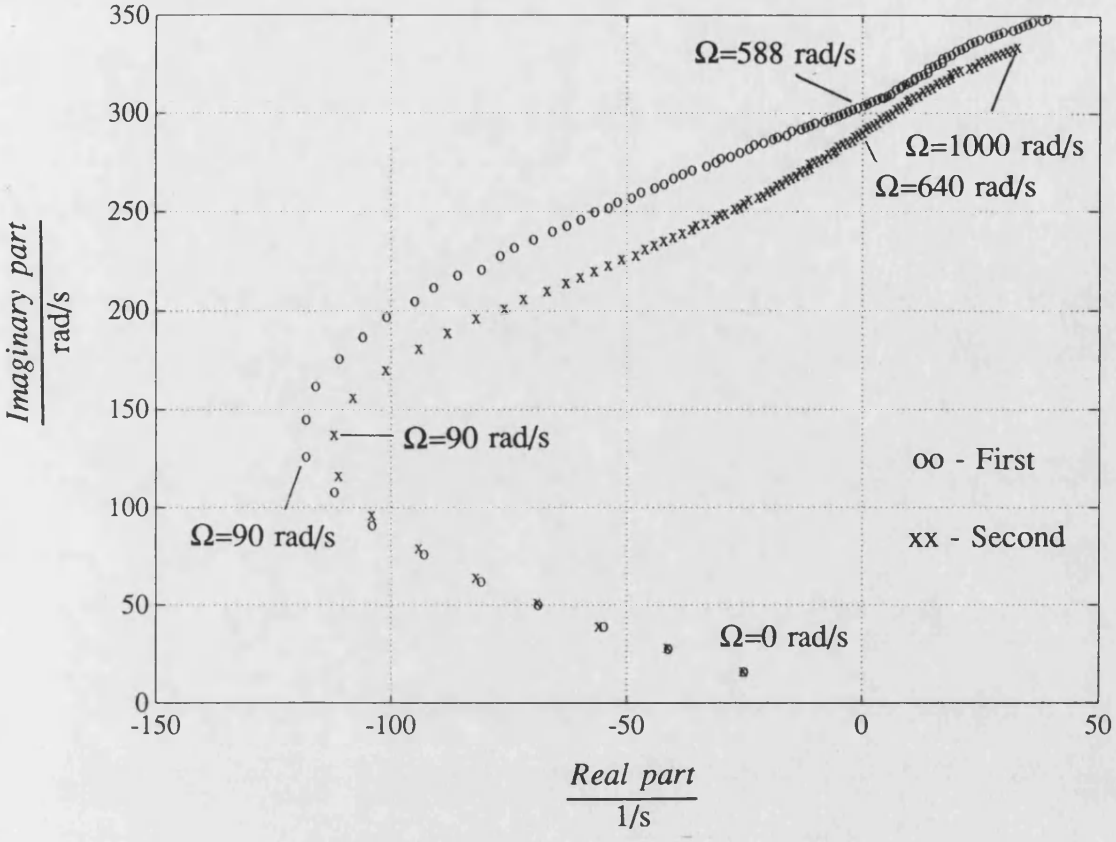

Fig. 6.4a Variation of the eigenvalues of first and second modes in complex plane

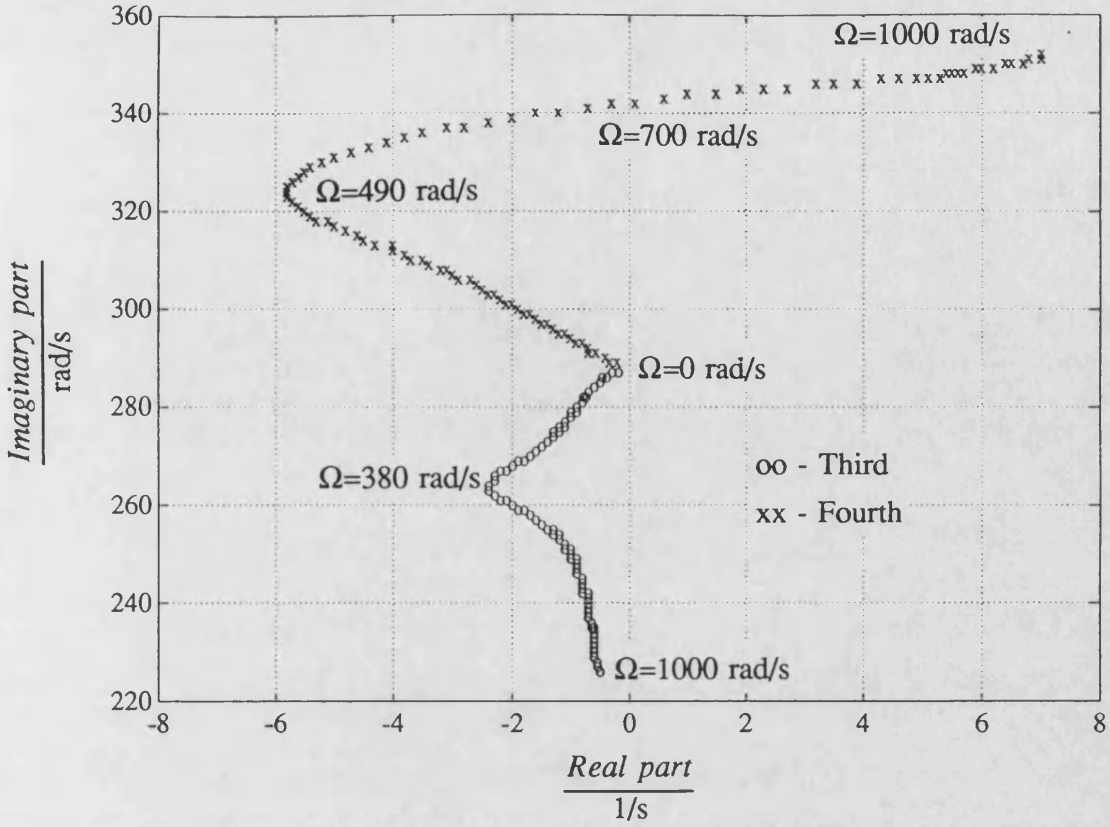

Fig. 6.4b Variation of the eigenvalues of third and fourth modes in complex plane

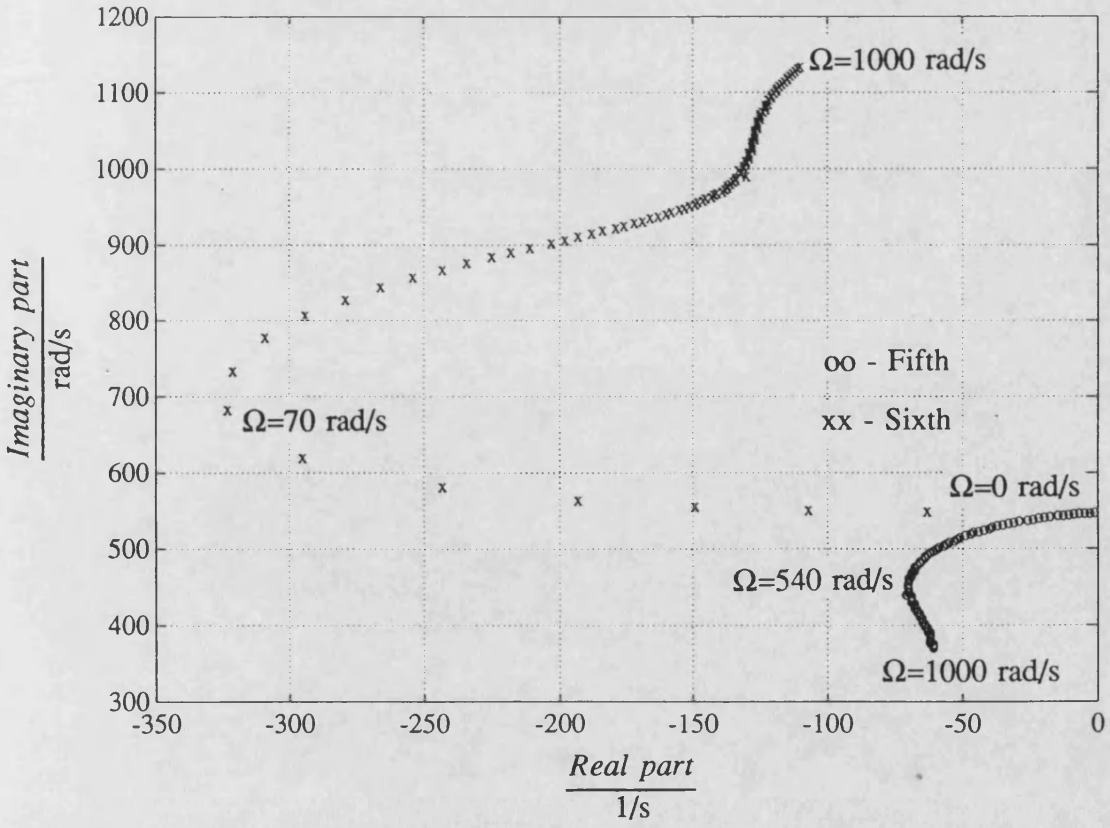

Fig. 6.4c Variation of the eigenvalues of fifth and sixth modes in complex plane

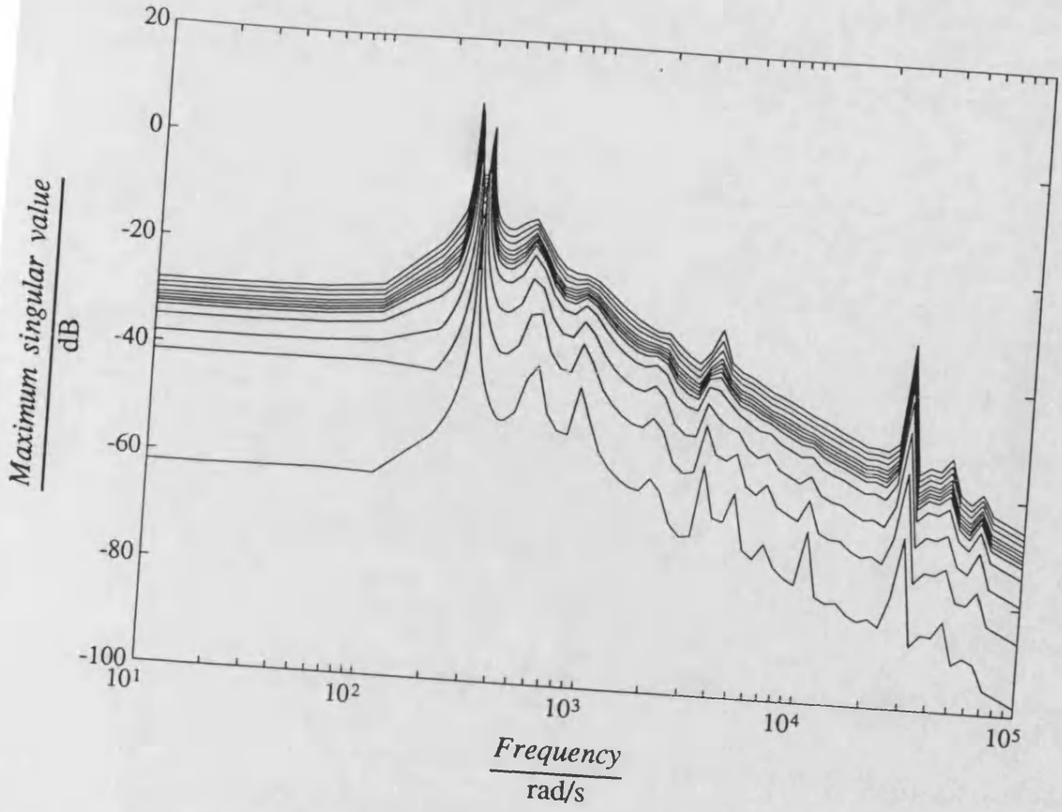

(a) All speeds

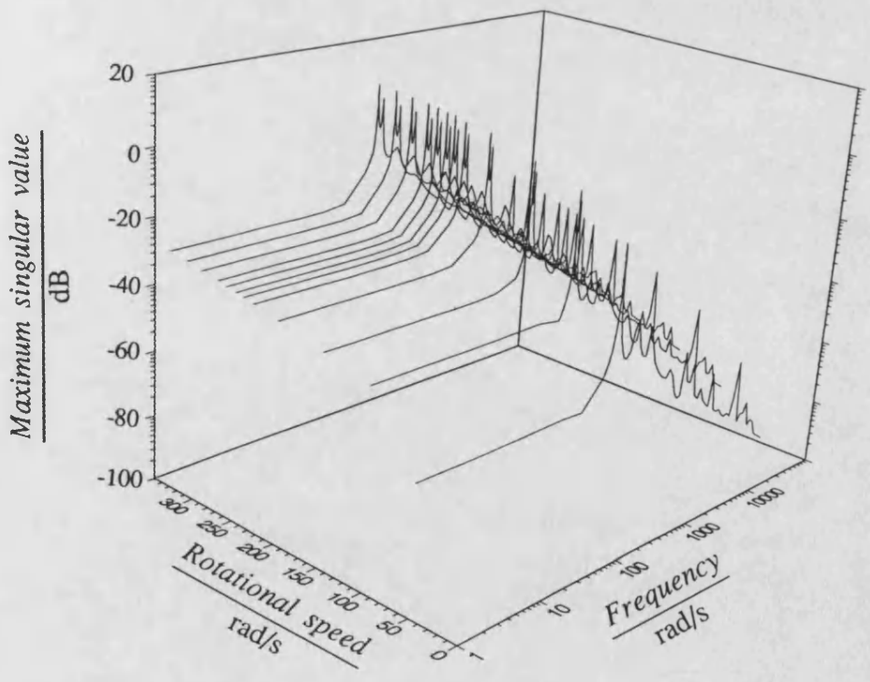

(b) Showing speed variation

Fig. 6.5 Full order system variation of maximum singular value with frequency and rotational speed

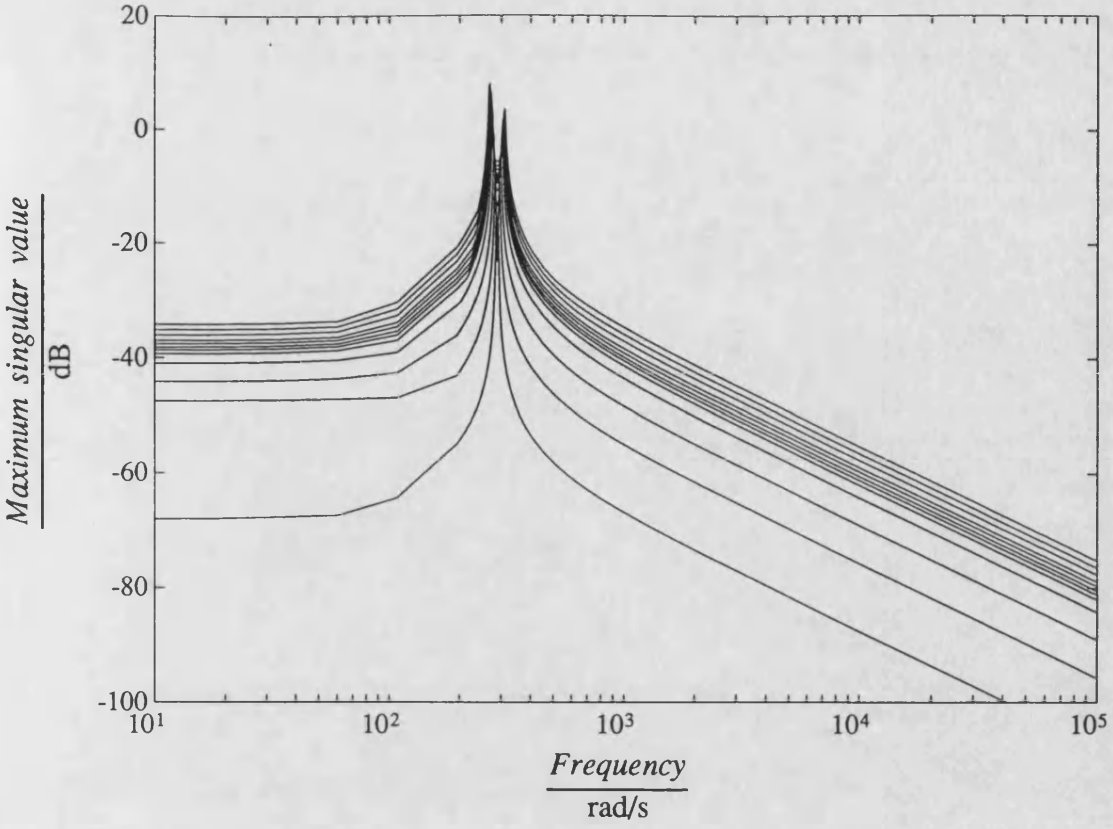

(a) All speeds

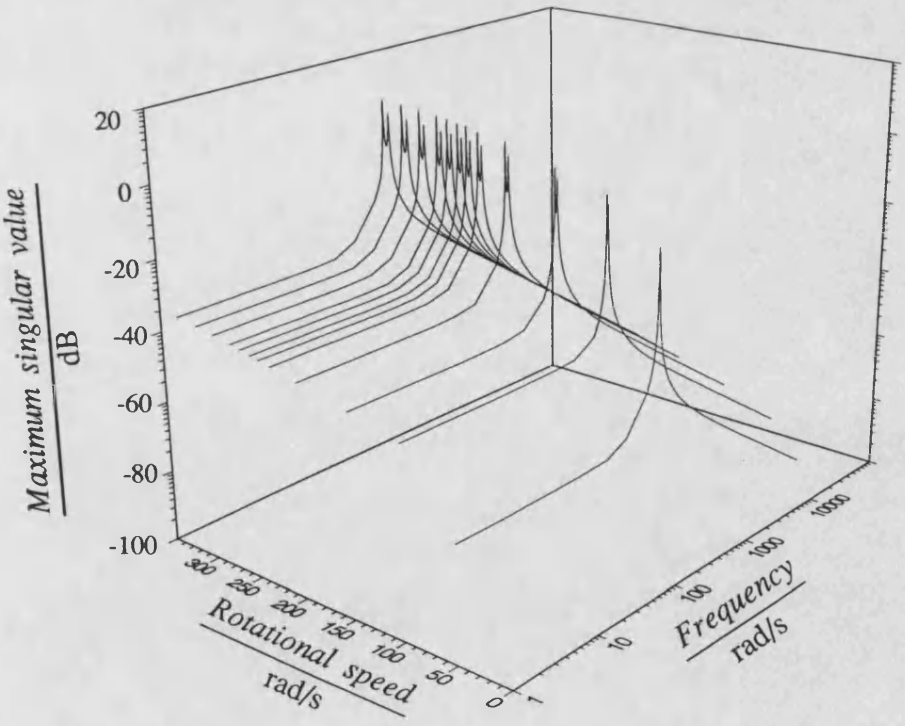

(b) Showing speed variation

Fig. 6.6 Reduced order system variation of maximum singular value with frequency and rotational speed

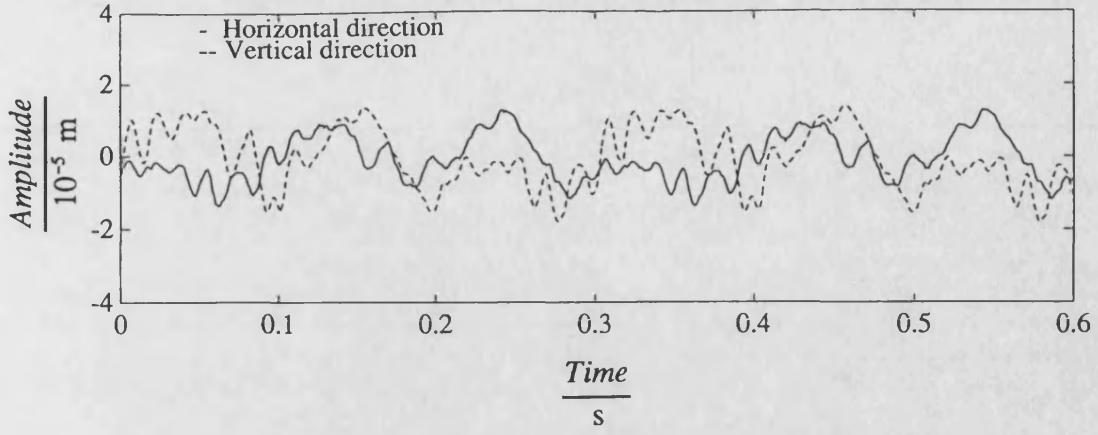

(a) Driven end transducers

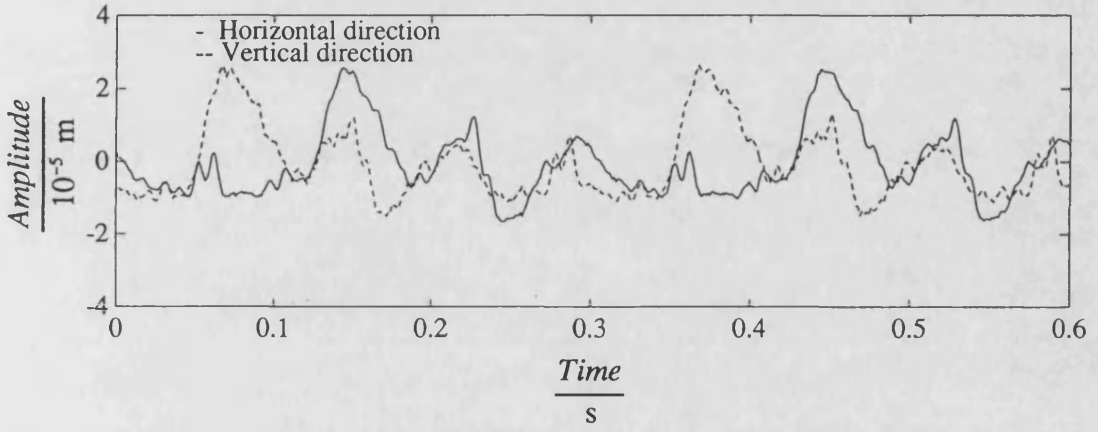

(b) Actuator position transducers

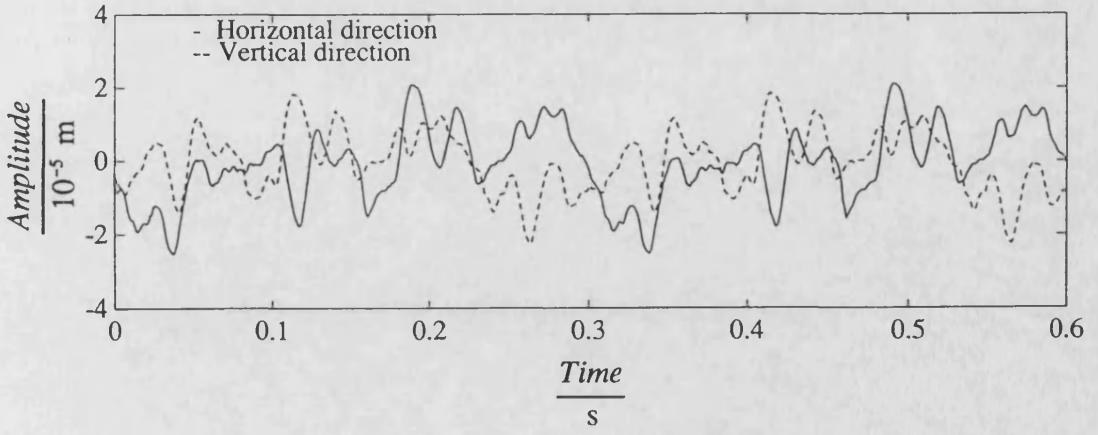

(c) Non-driven end transducers

Fig. 6.7 Displacements measured by transducers at rotational speed 21 rad/s

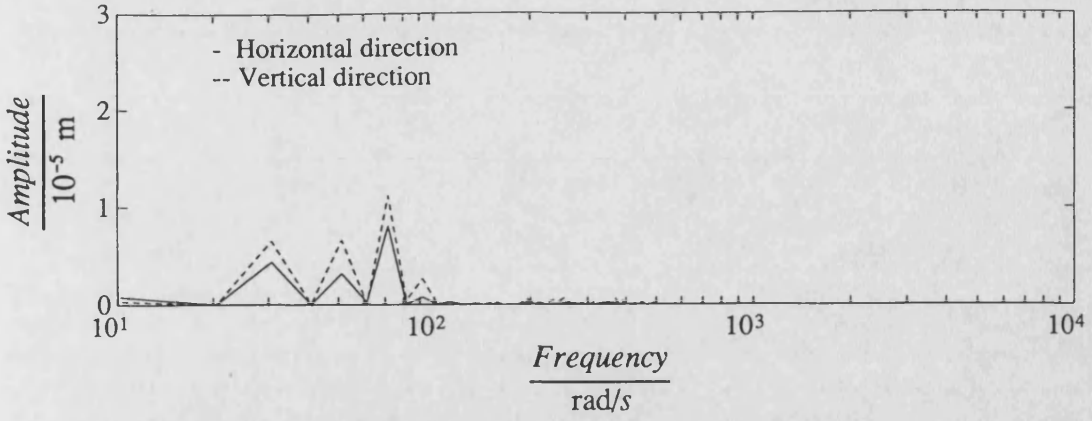

(a) Driven end transducers

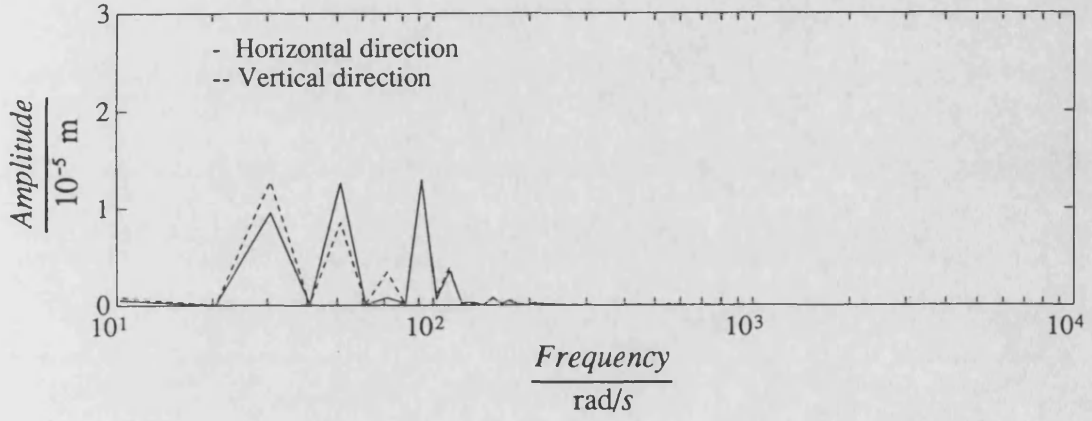

(b) Actuator position transducers

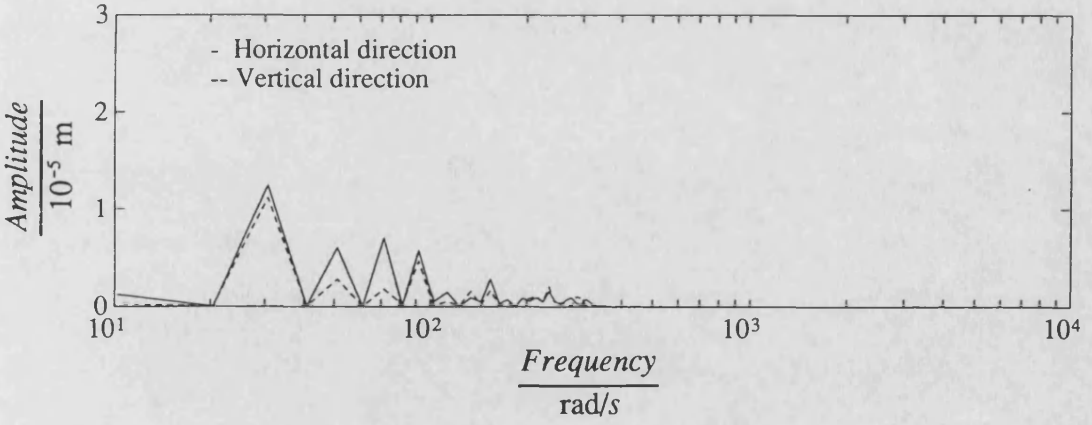

(c) Non-driven end transducers

Fig. 6.8 Frequency spectra of measured displacement signals at rotational speed 21 rad/s

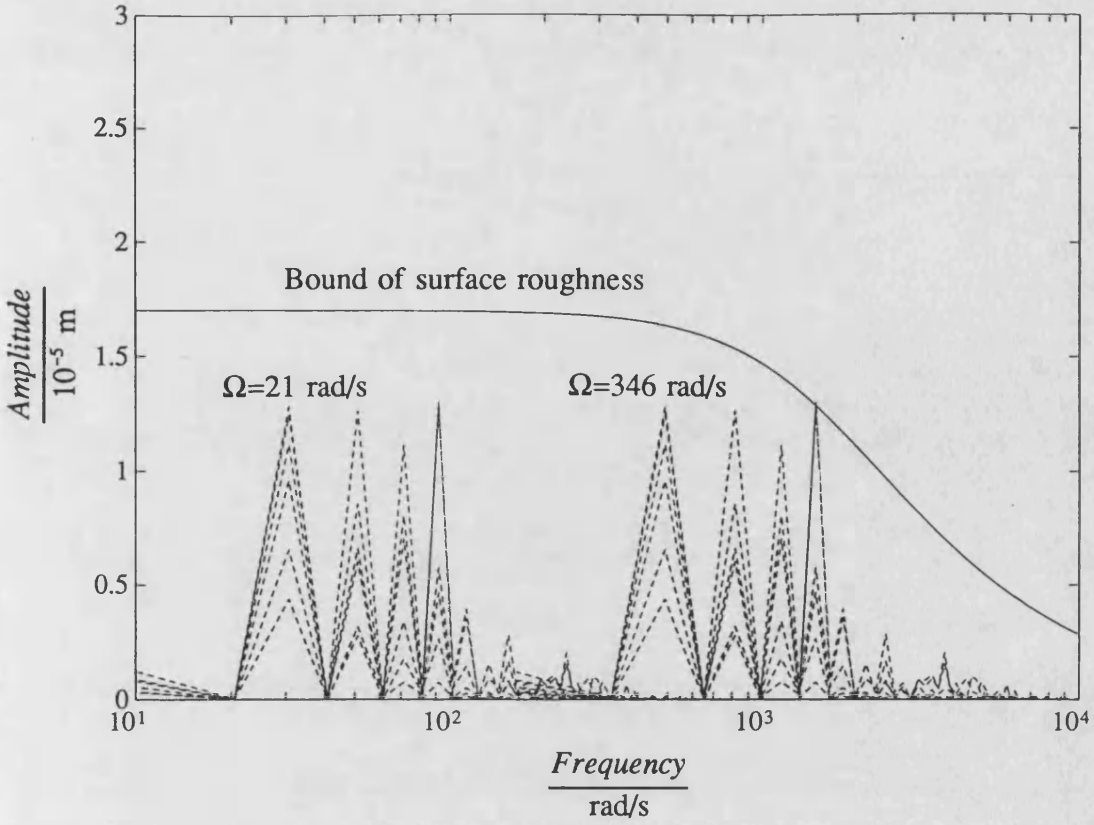

Fig. 6.9 Bound of surface roughness signals

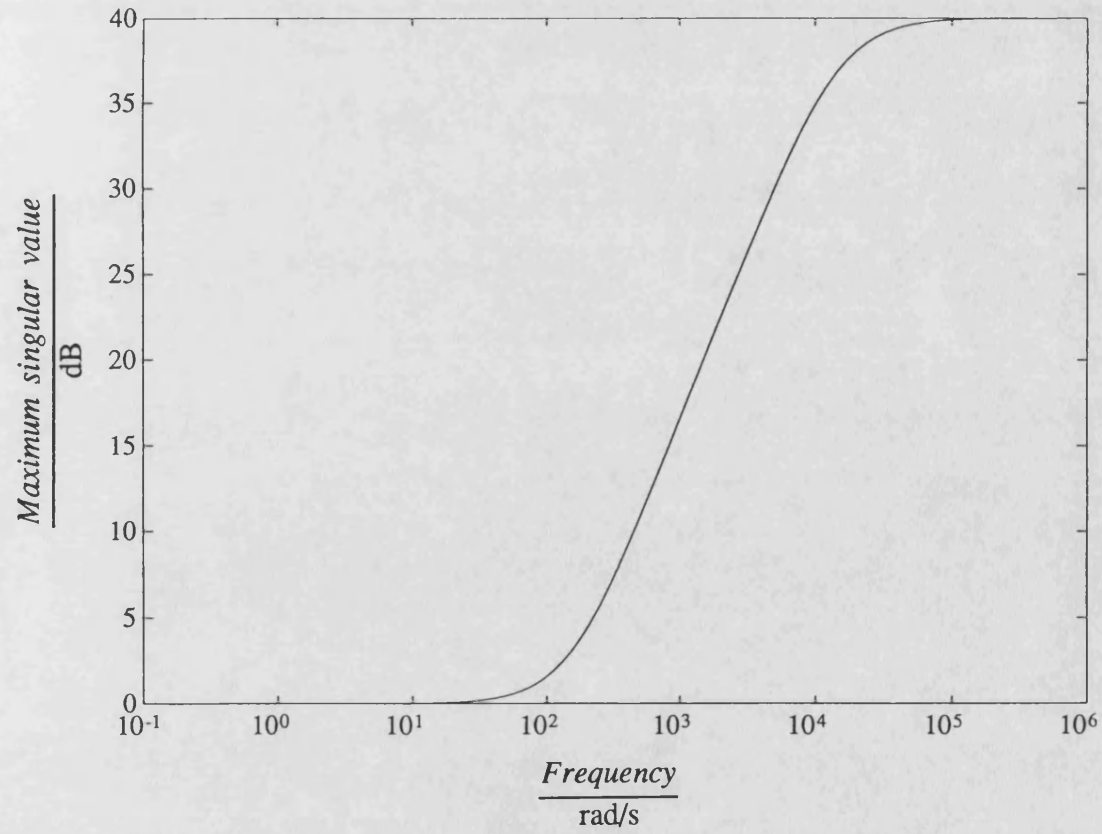

Fig. 6.10 Weighting function W_u when controller designed at fourth critical speed 309 rad/s

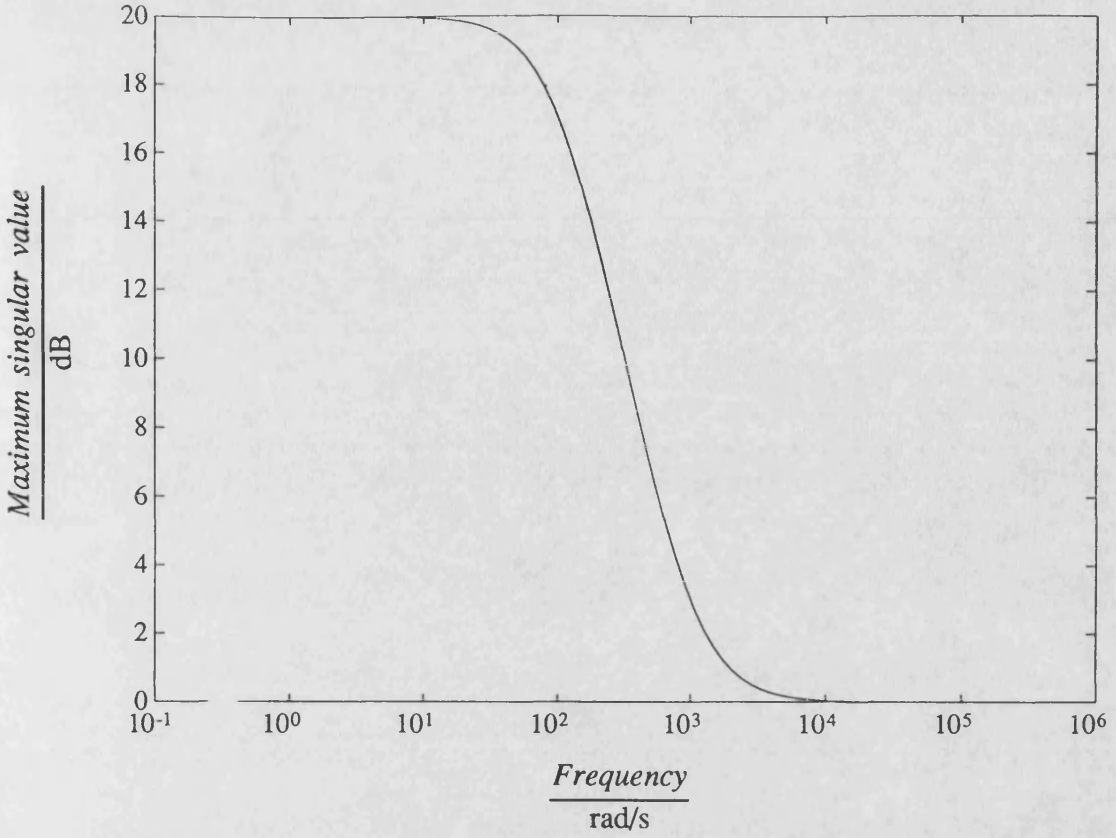

Fig. 6.11 Weighting function W_y when controller designed at fourth critical speed 309 rad/s

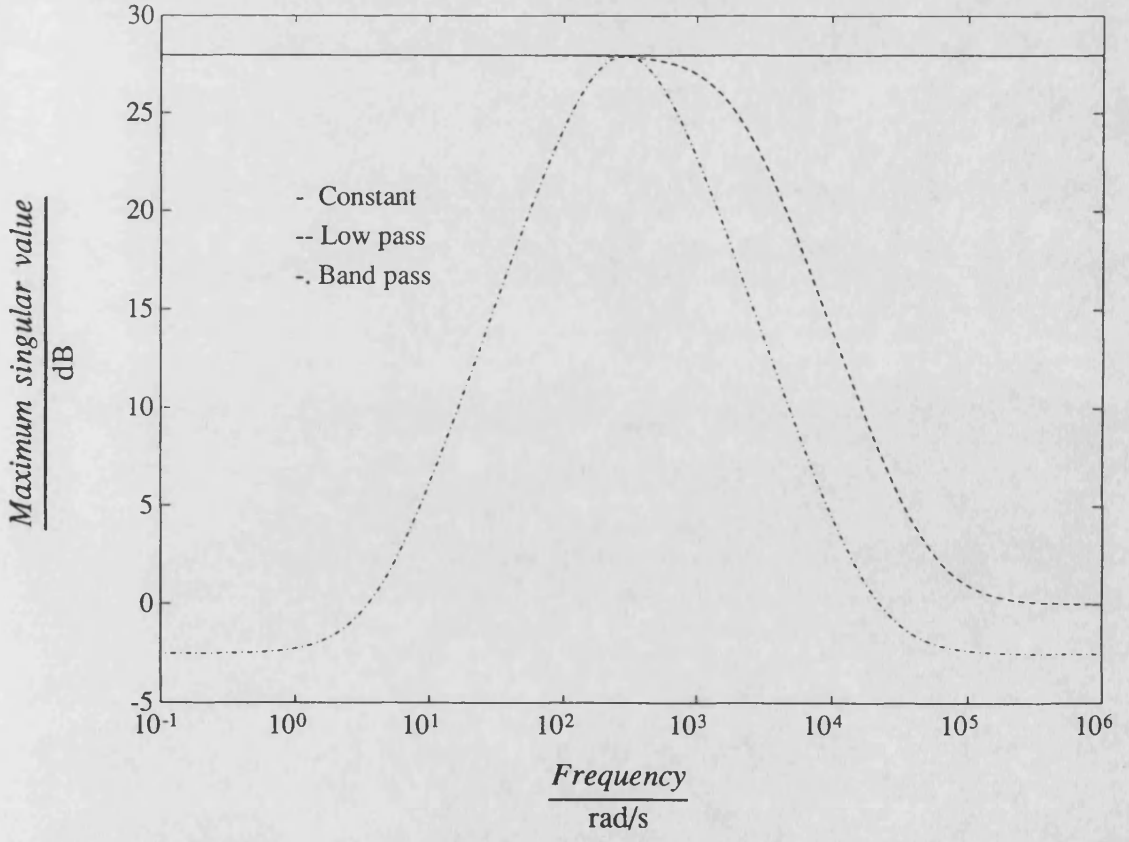

Fig. 6.12 Weighting function W_z when controller designed at fourth critical speed 309 rad/s

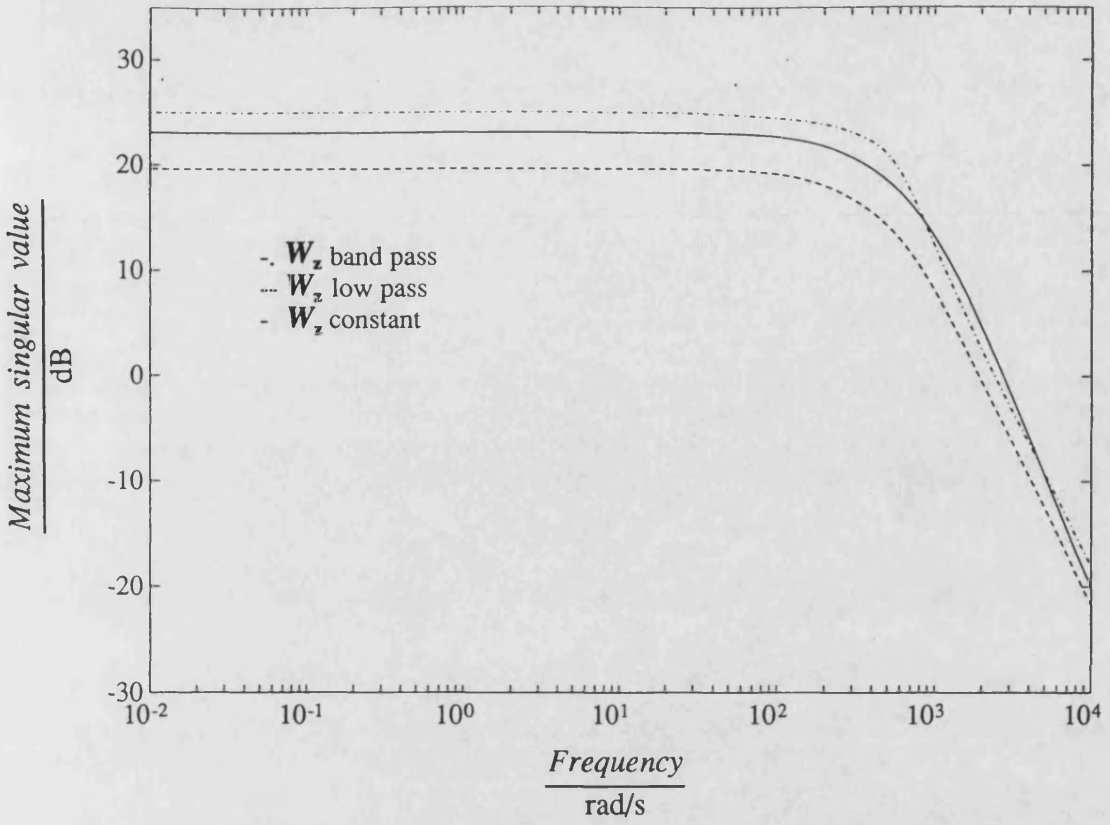

Fig. 6.13 Maximum singular value of the controllers designed at fourth critical speed 309 rad/s

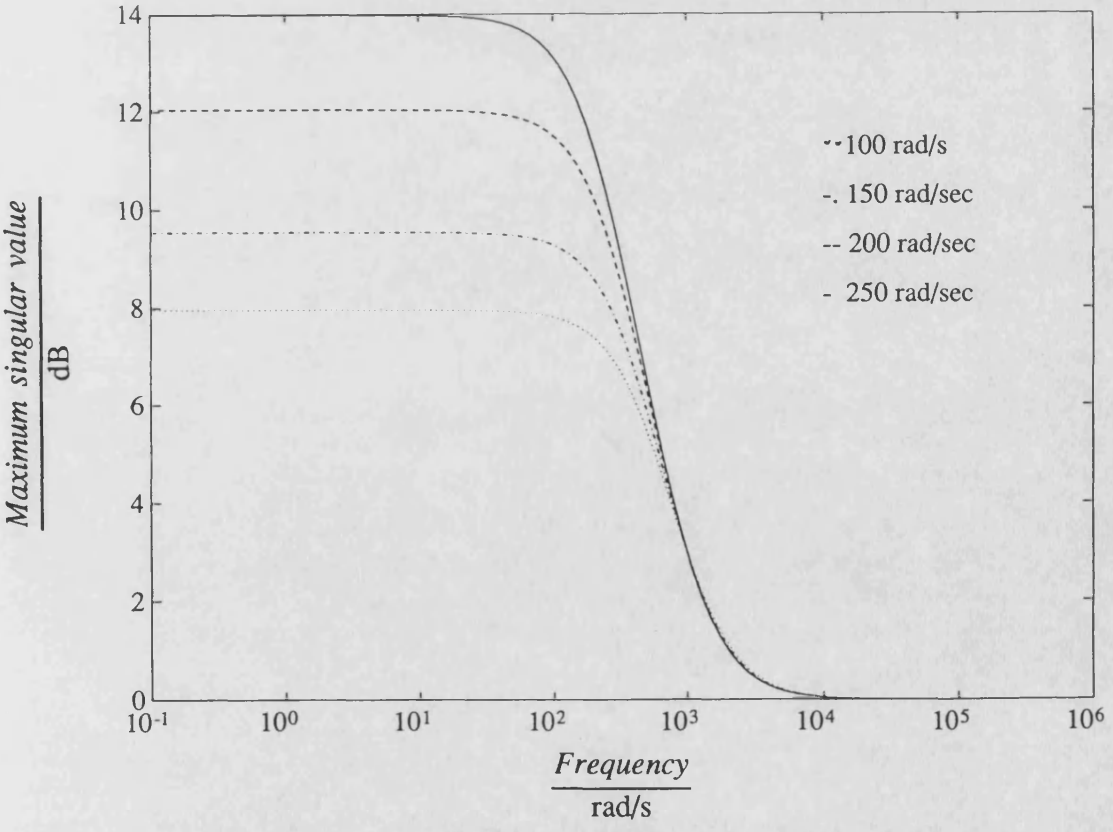

Fig. 6.14 Weighting functions W_y when controller designed at speeds 100, 150, 200, 250 rad/s

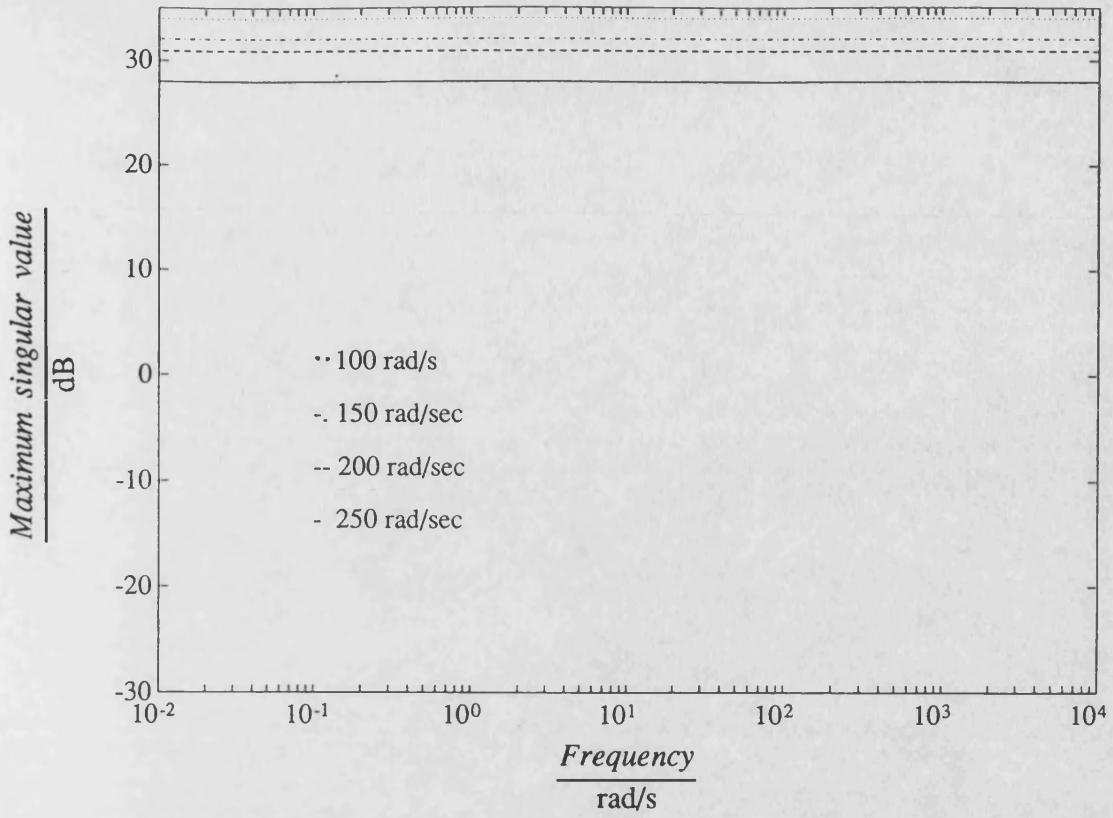

Fig. 6.15 Weighting function W_z when controller designed at speeds 100, 150, 200, 250 rad/s

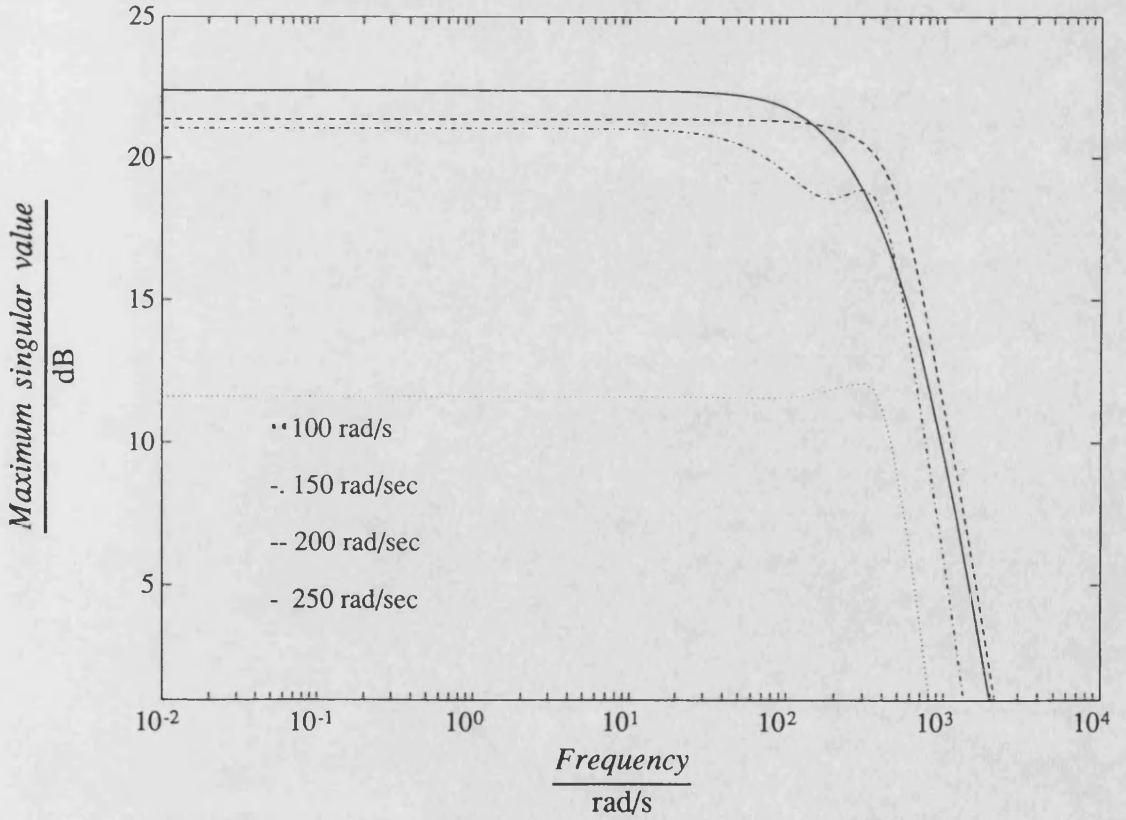

Fig. 6.16 Maximum singular value of the controllers designed at speed 100, 150, 200 250 rad/s

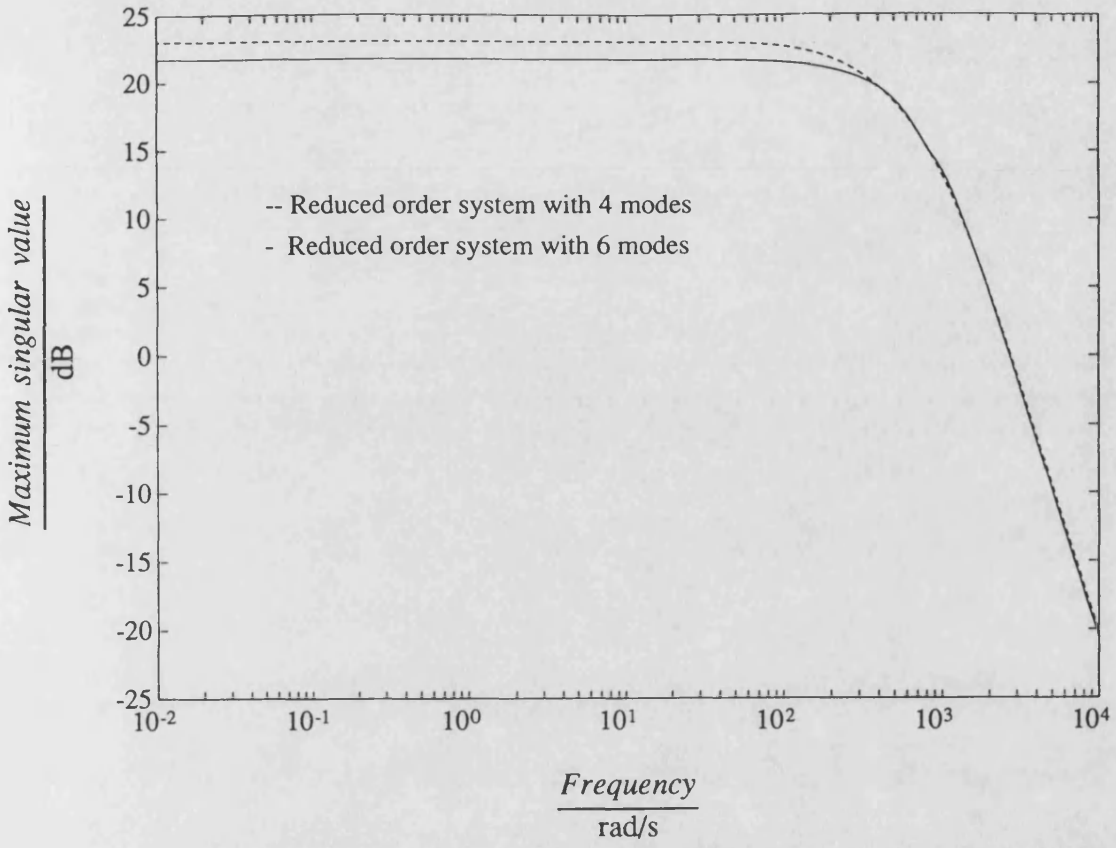

Fig. 6.17 Maximum singular value of the controllers designed with extra high frequency modes

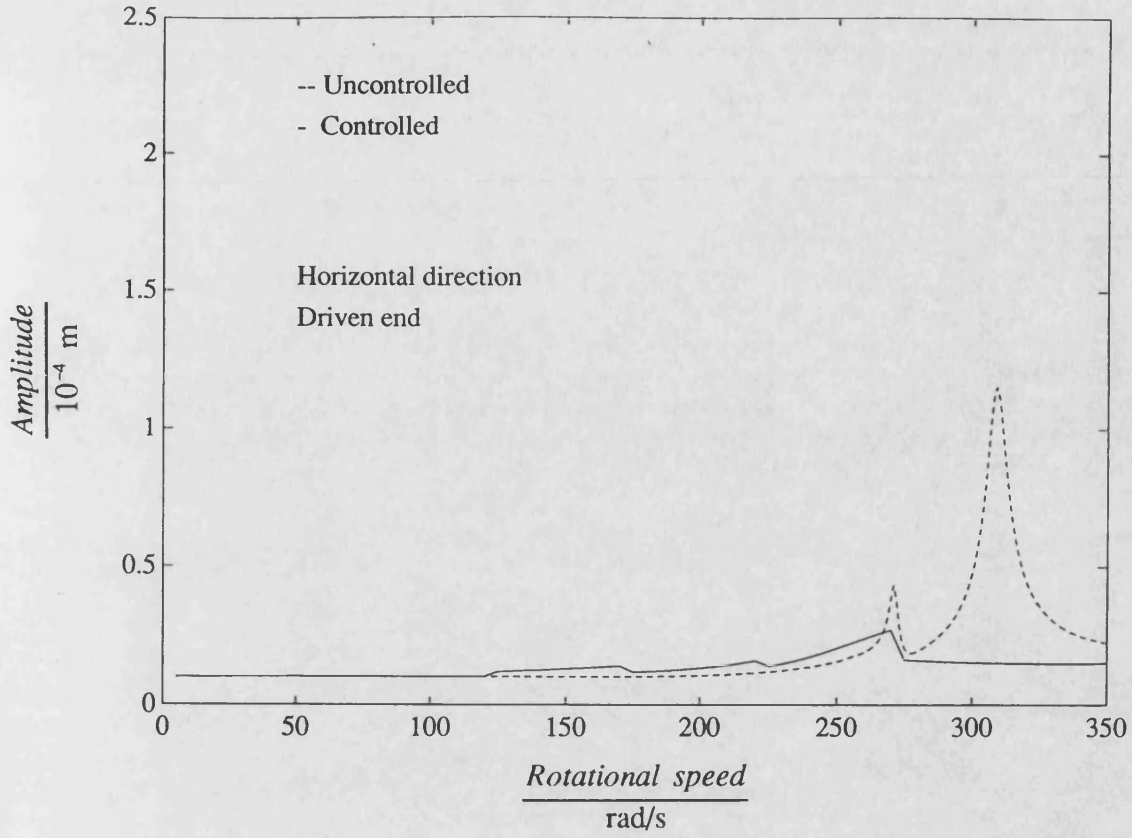

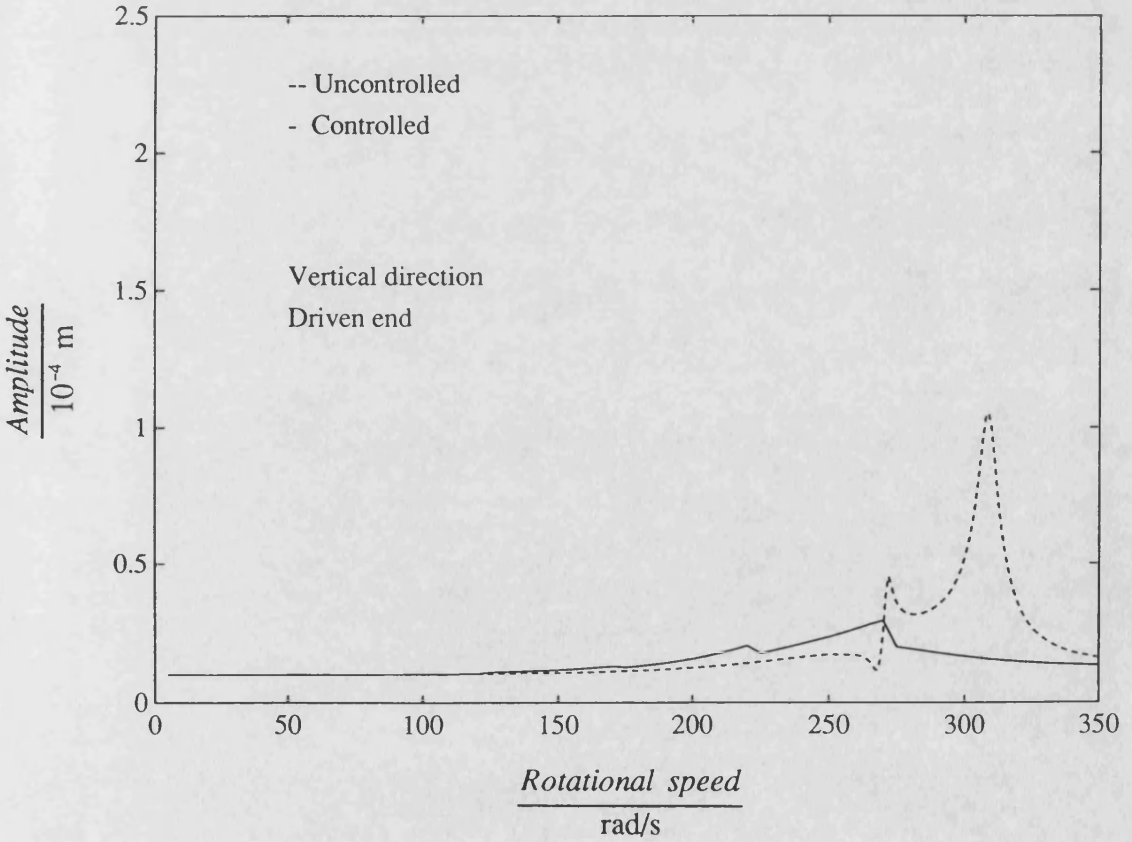

Fig. 6.18 Theoretical synchronous response of five speed controlled system

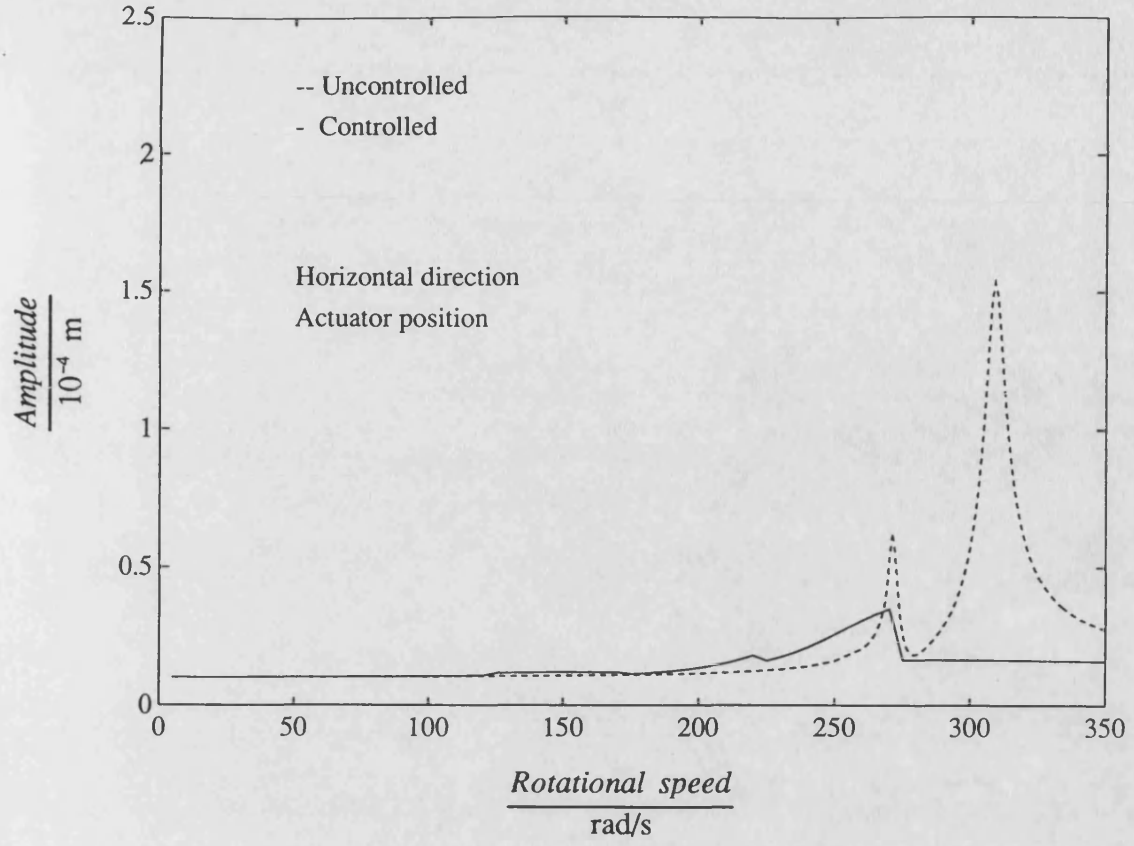

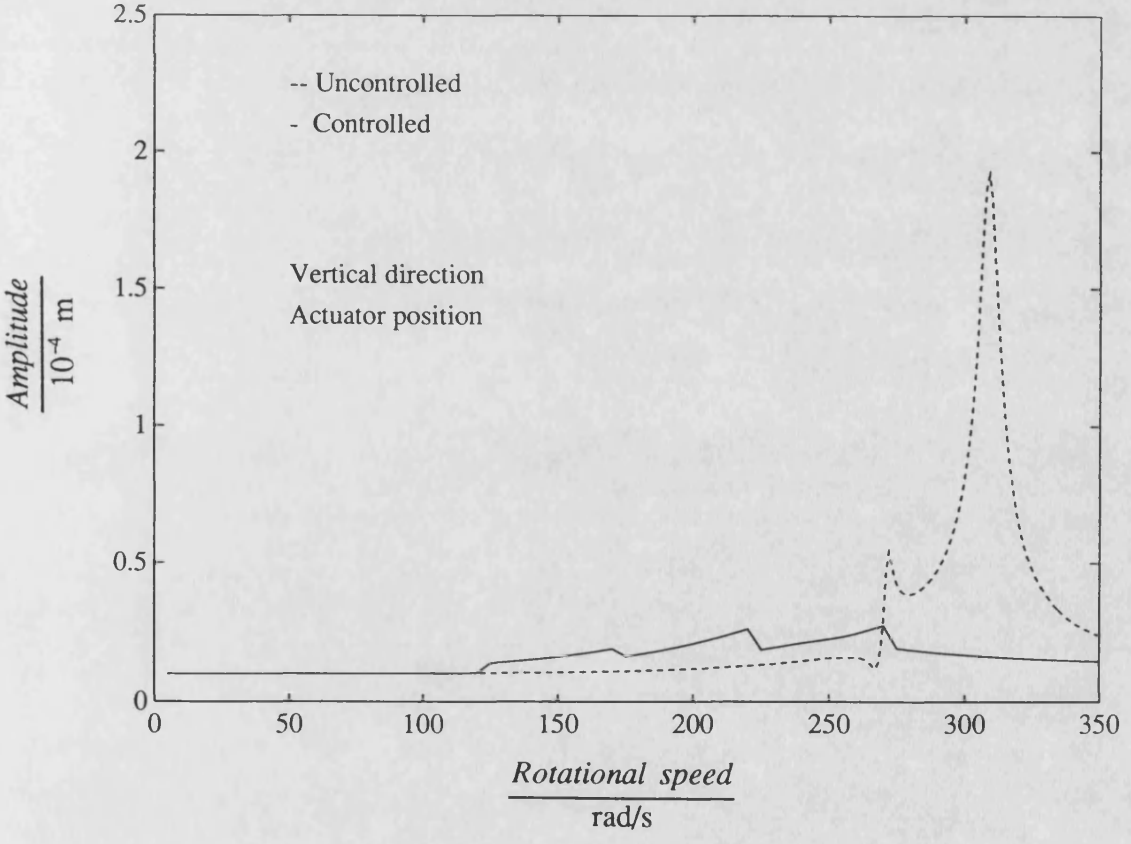

Fig. 6.18 (continued)

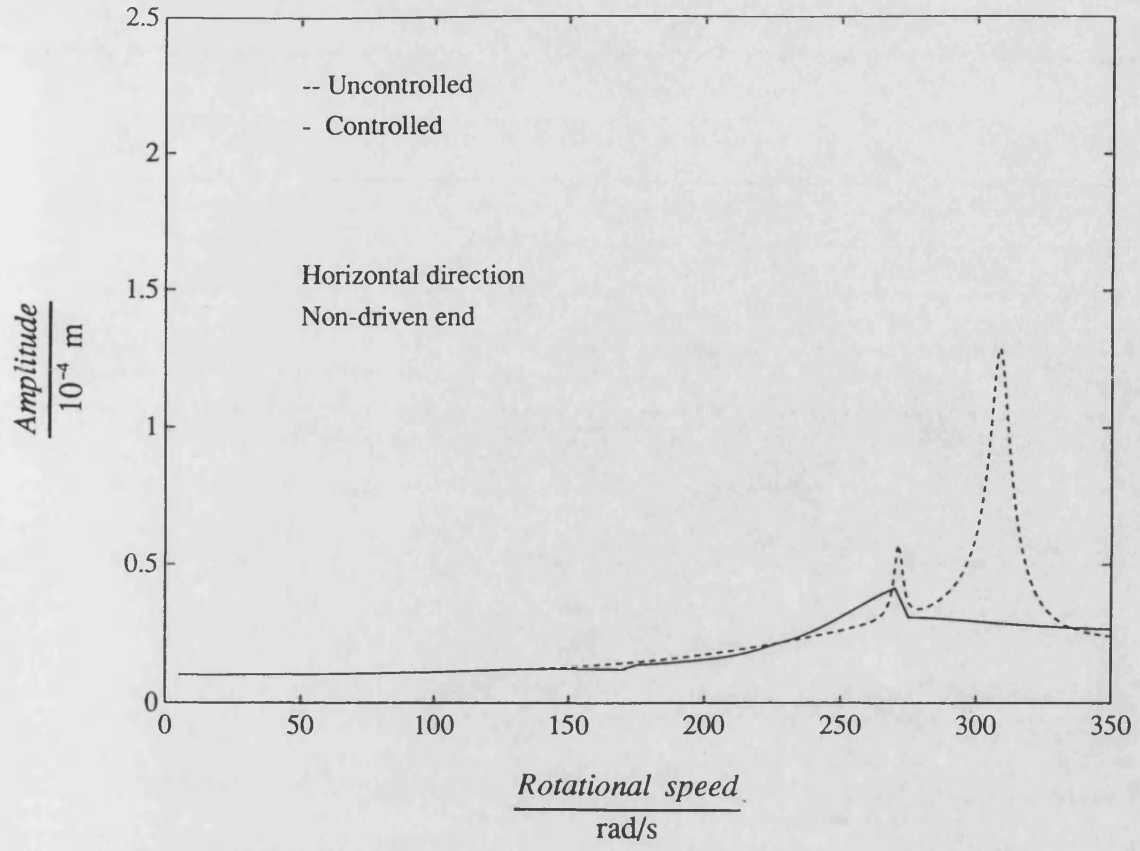

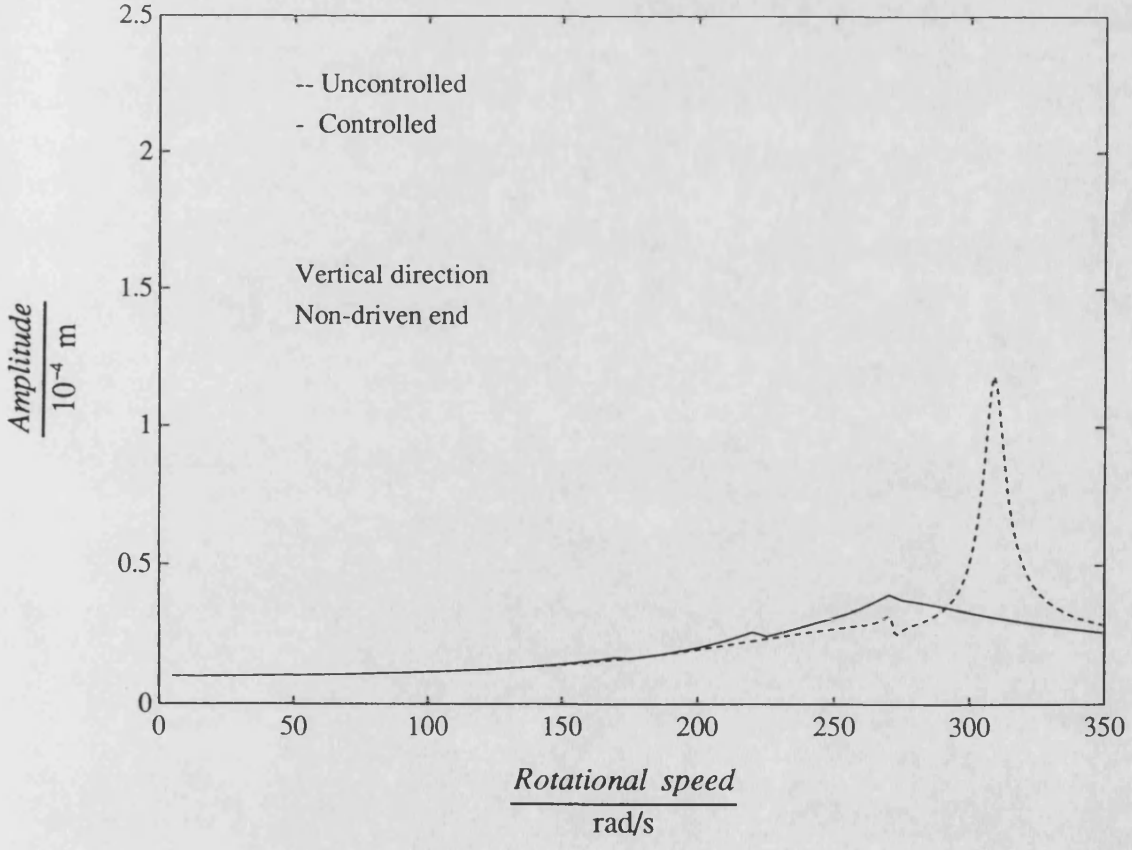

Fig. 6.18 (continued)

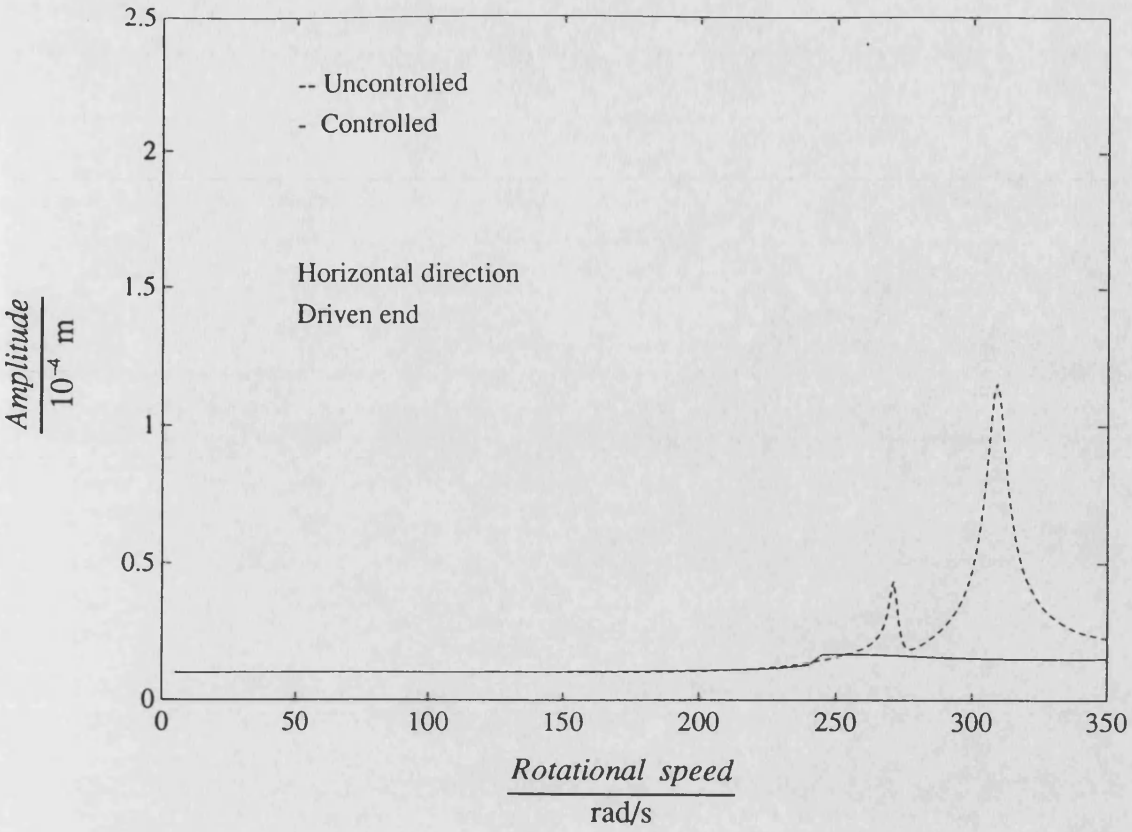

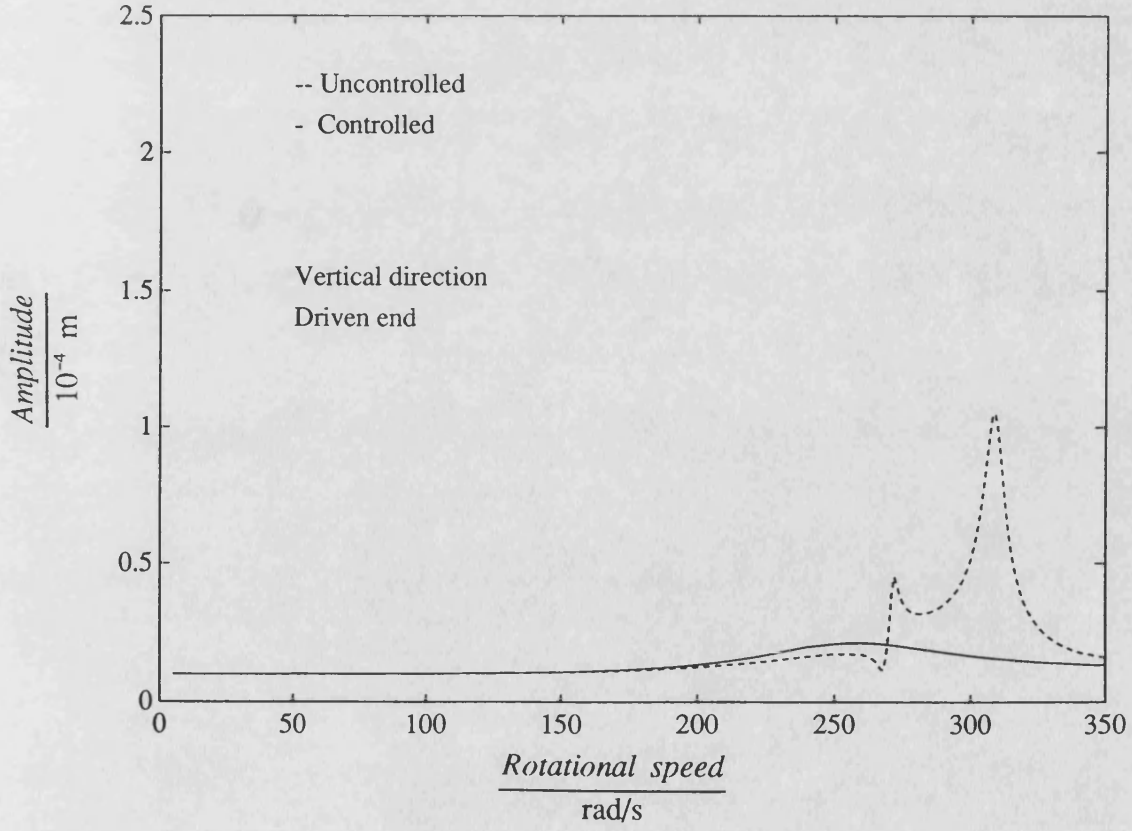

Fig. 6.19 Theoretical synchronous response of two speed controlled system

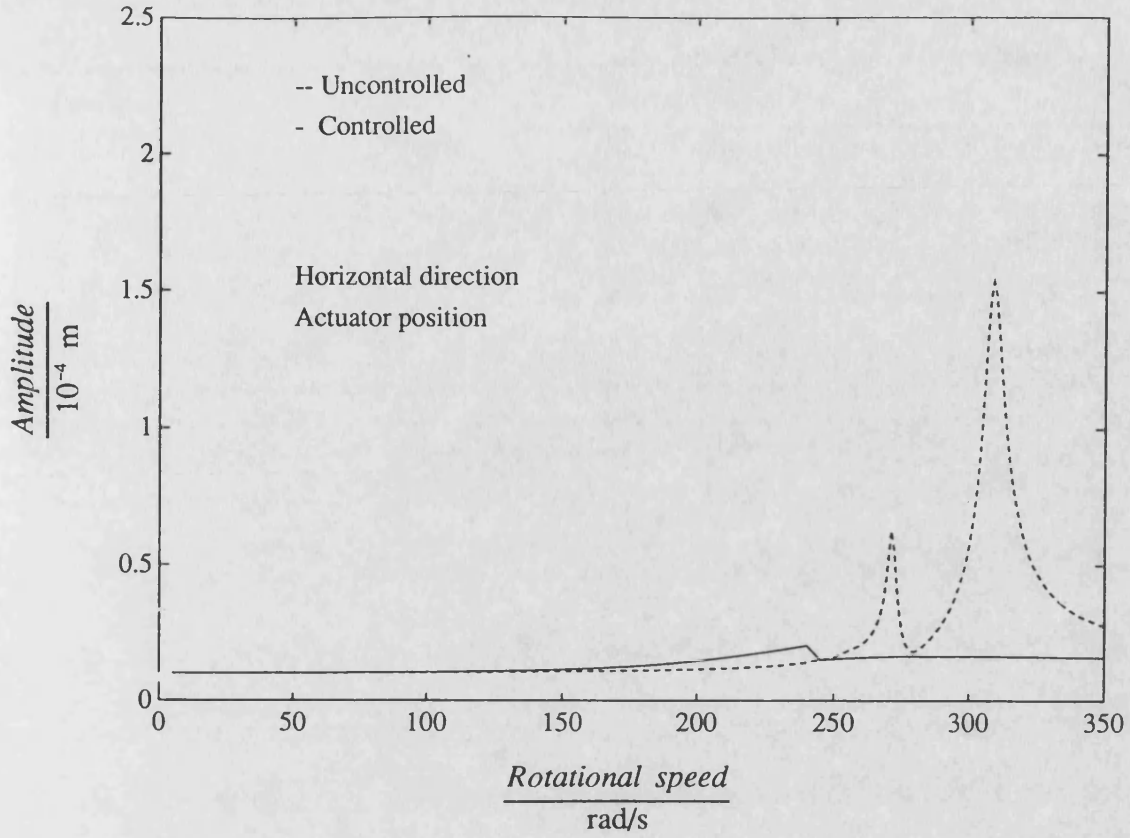

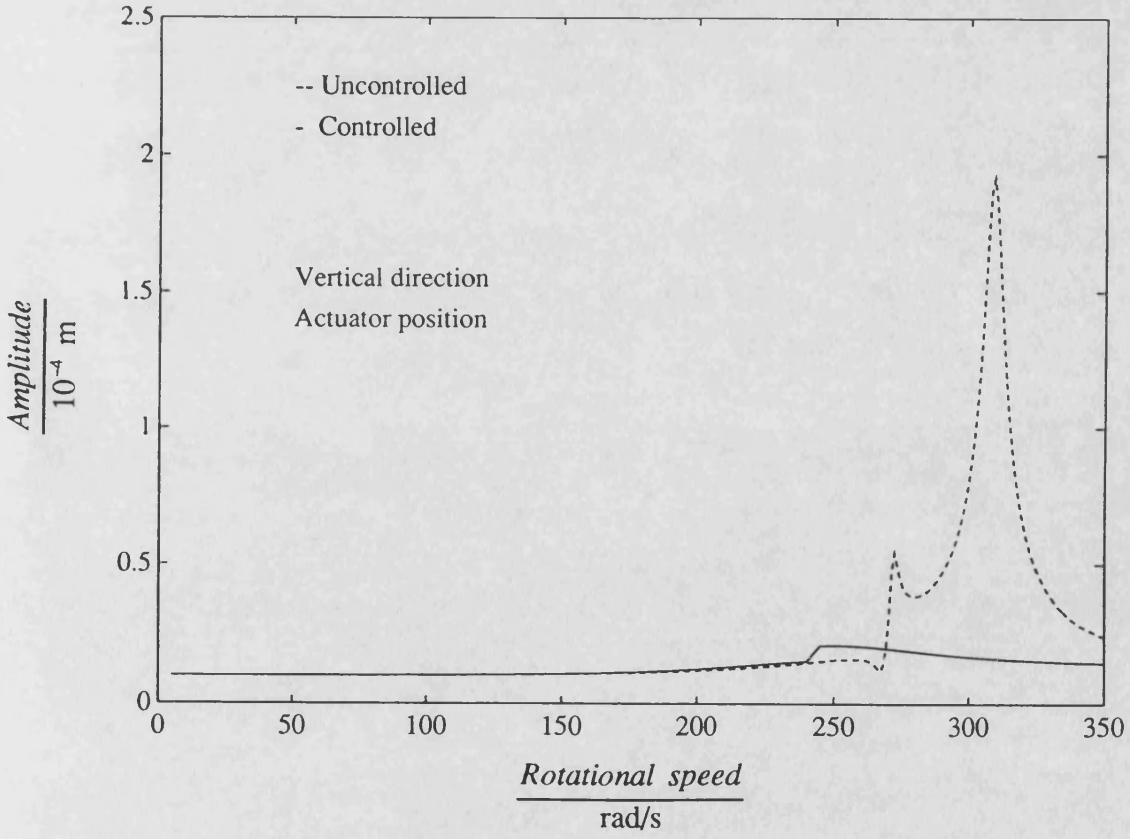

Fig. 6.19 (continued)

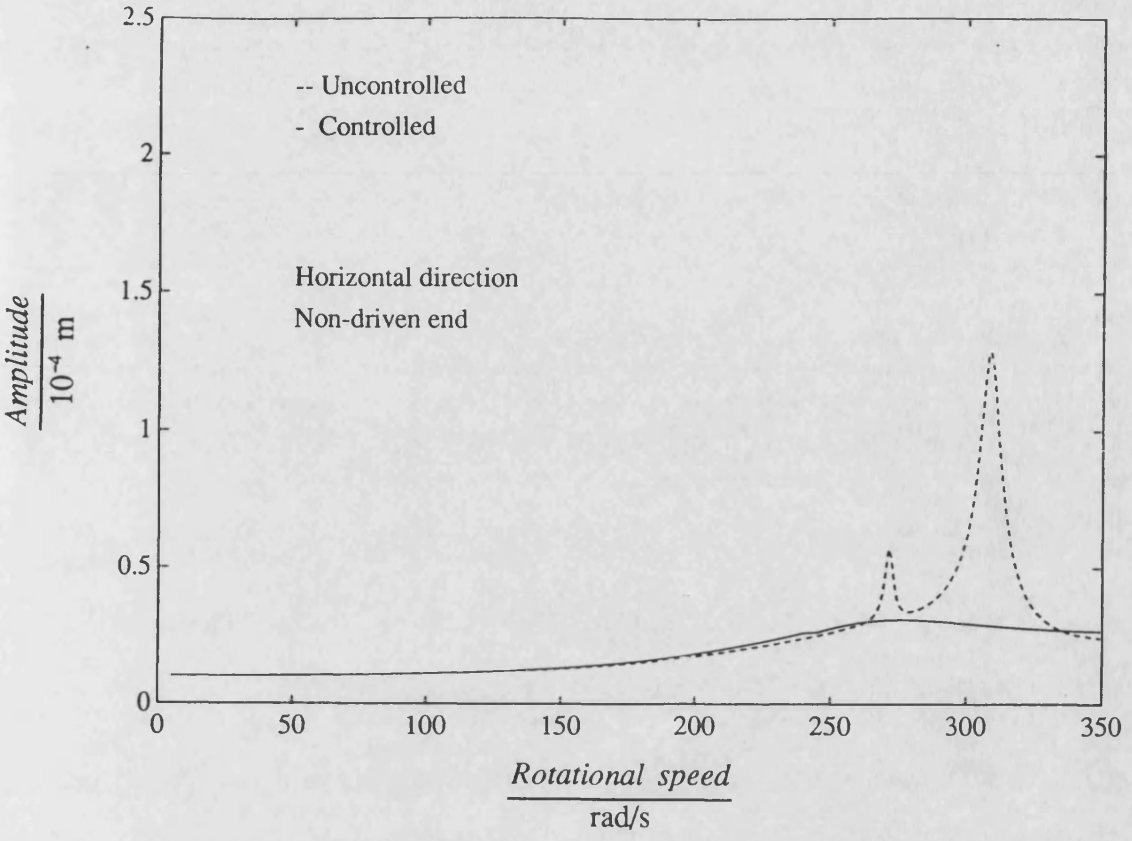

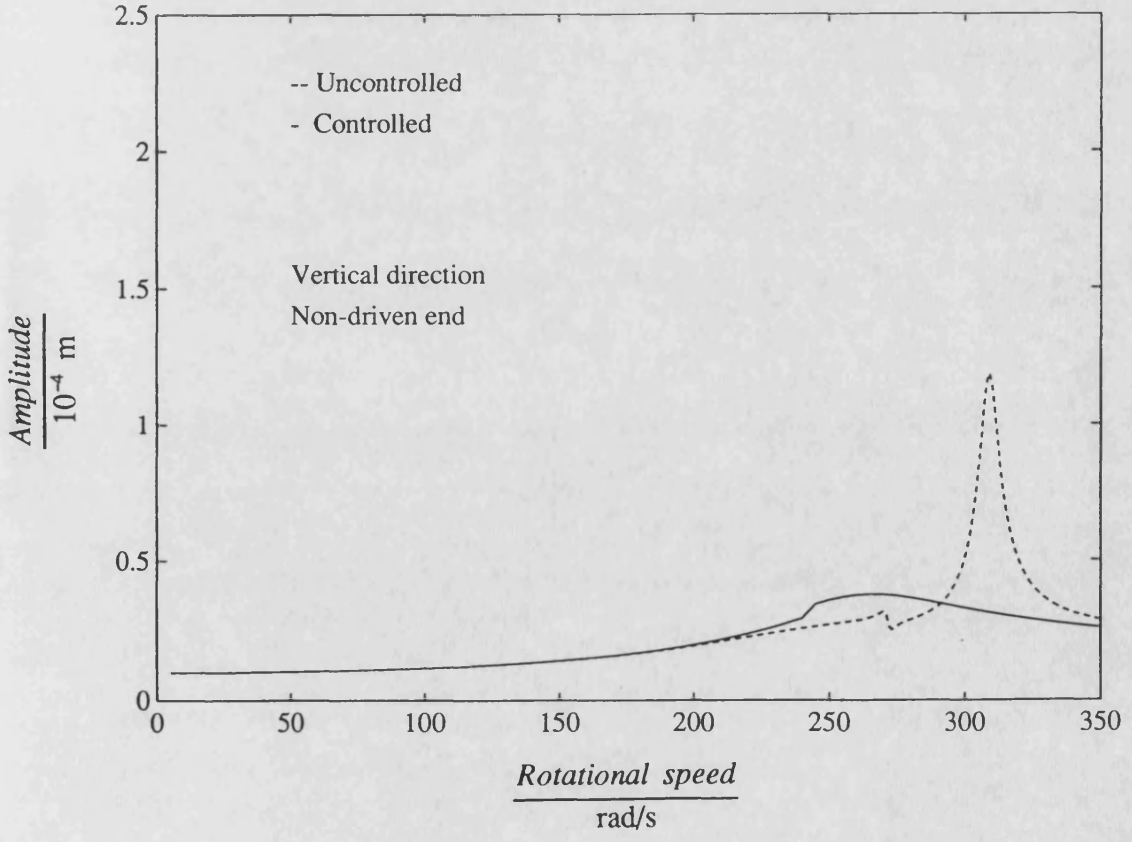

Fig. 6.19 (continued)

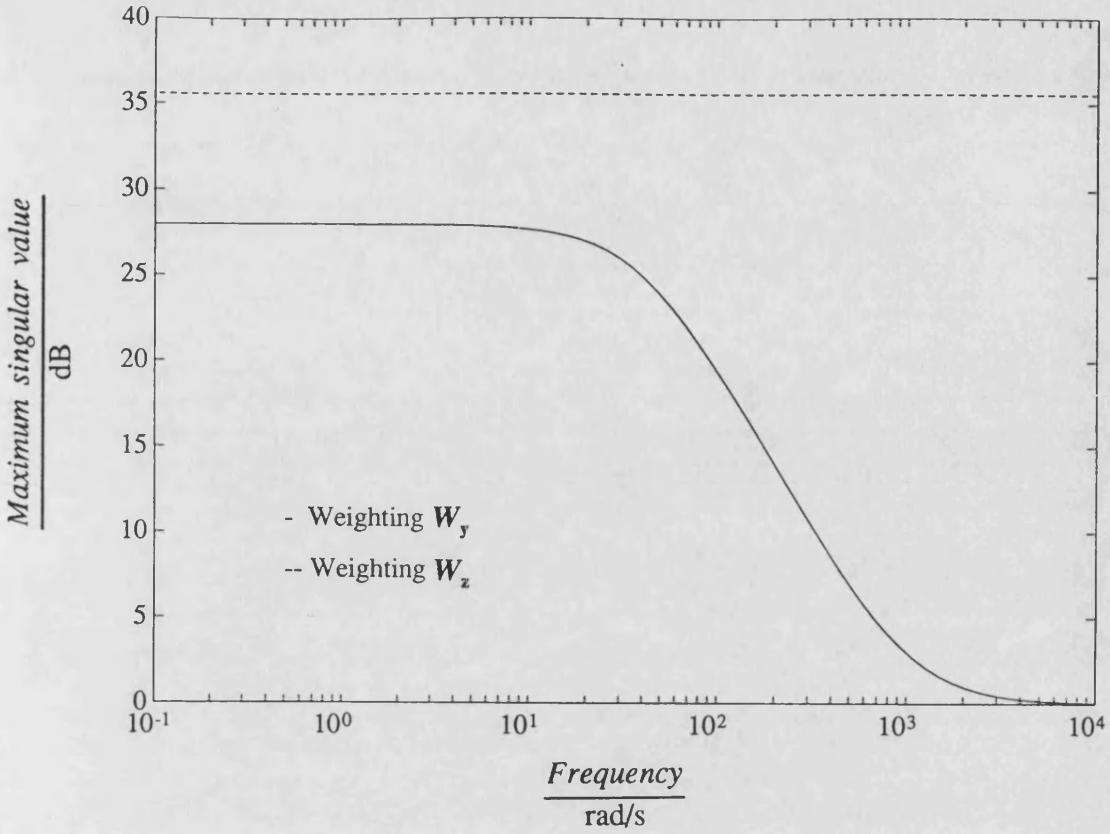

Fig. 6.20 Weighting function W_y and W_z when controller designed for transient response case, Ω=309 rad/s

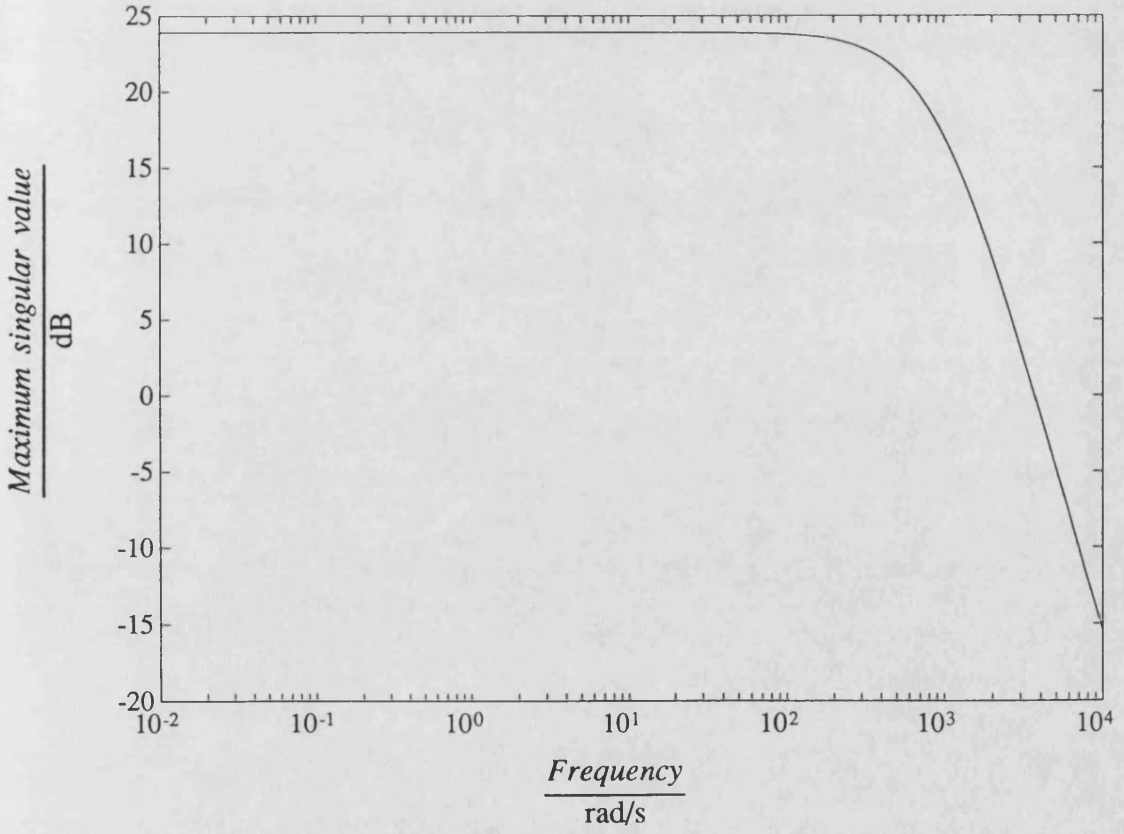

Fig. 6.21 Maximum singular value of the controller designed for transient response case, Ω=309 rad/s

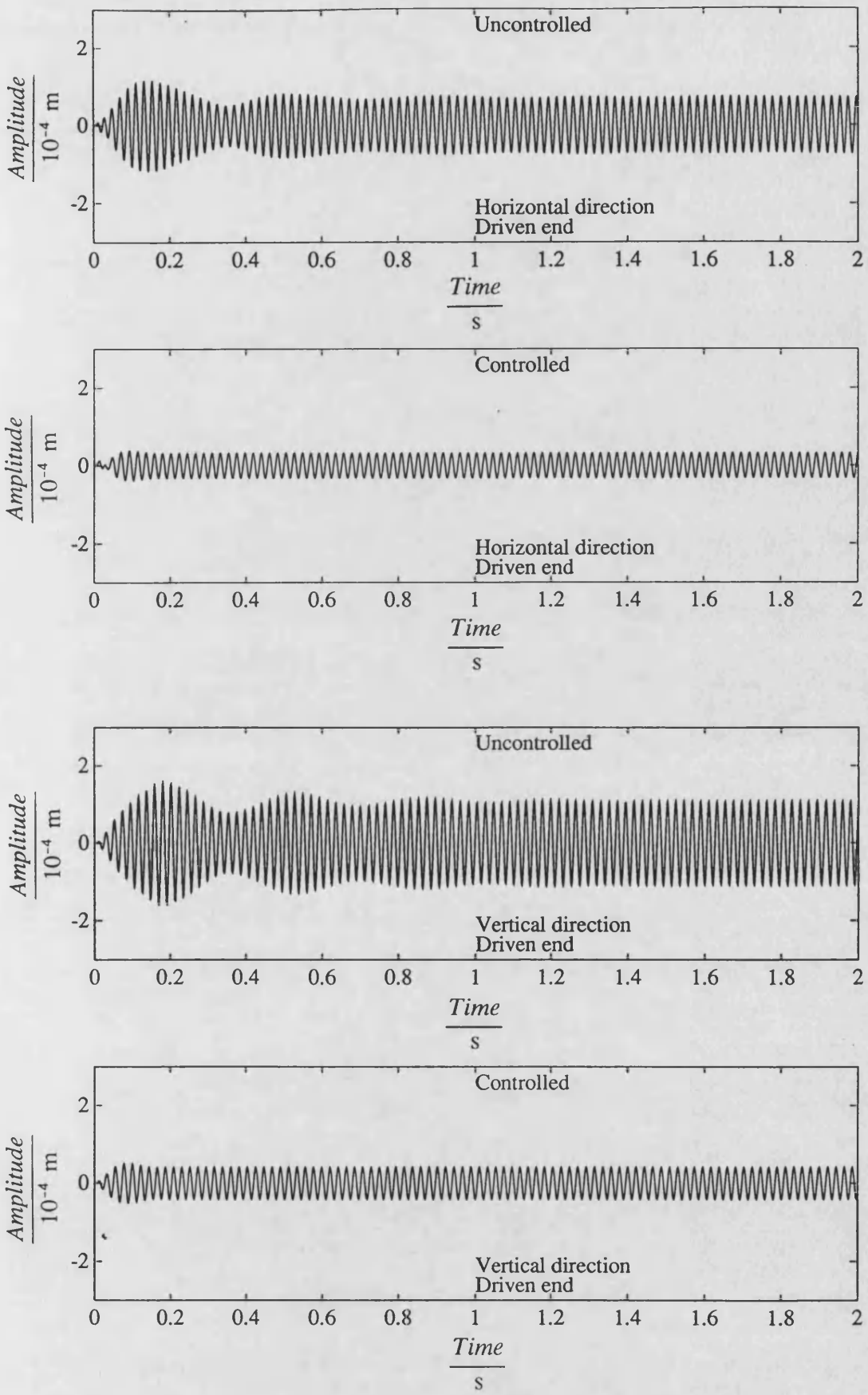

Fig. 6.22 Theoretical transient response of controlled system at speed 290 rad/s, mass loss at t=0

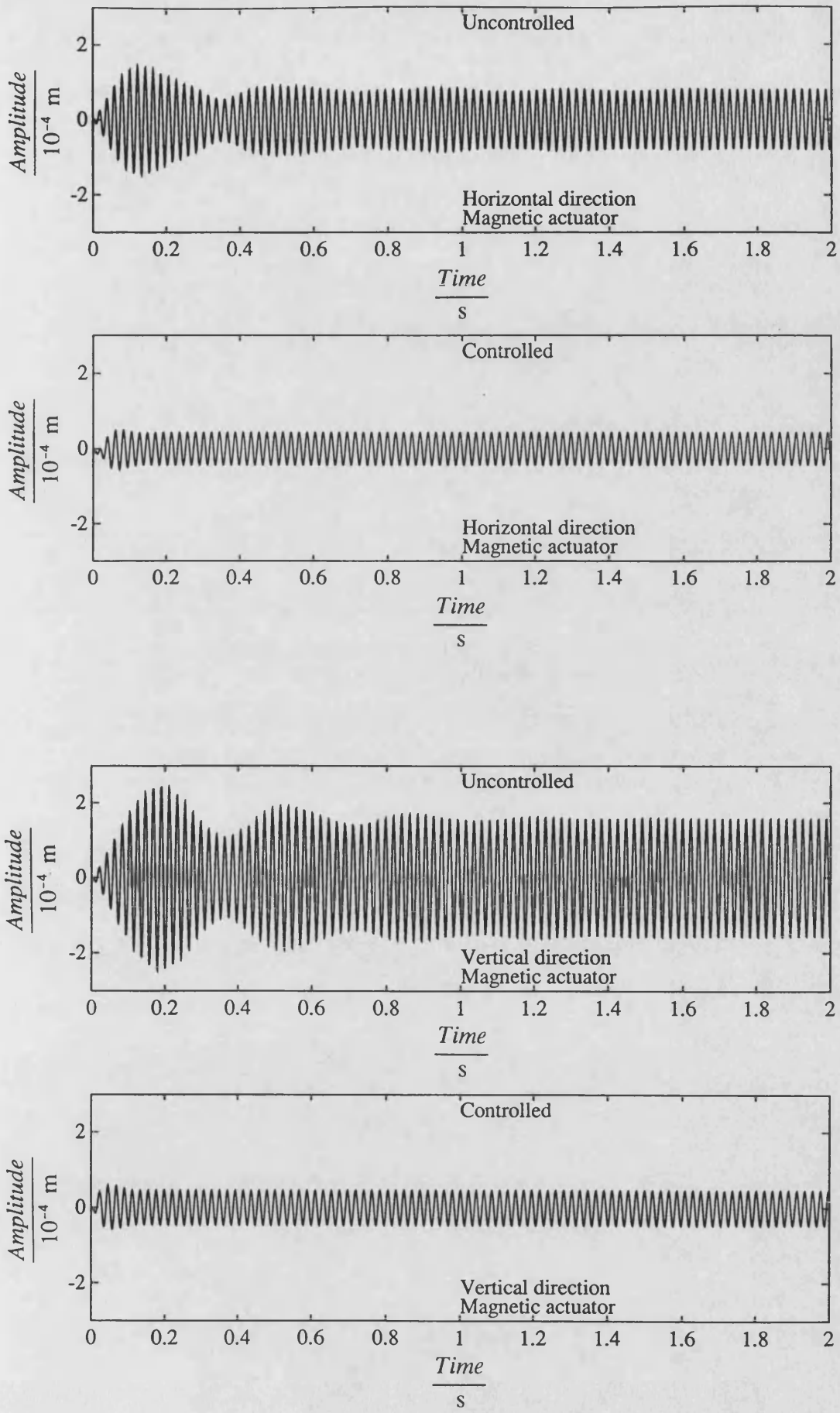

Fig. 6.22 (continued)

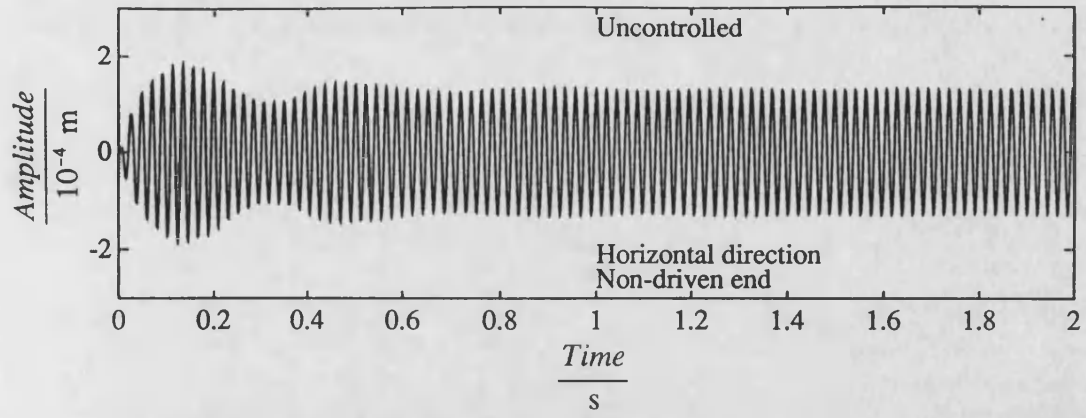

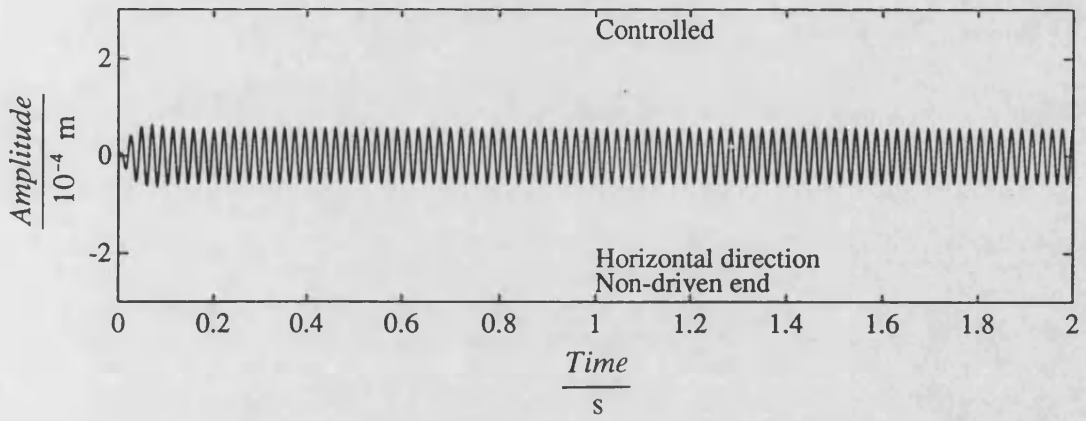

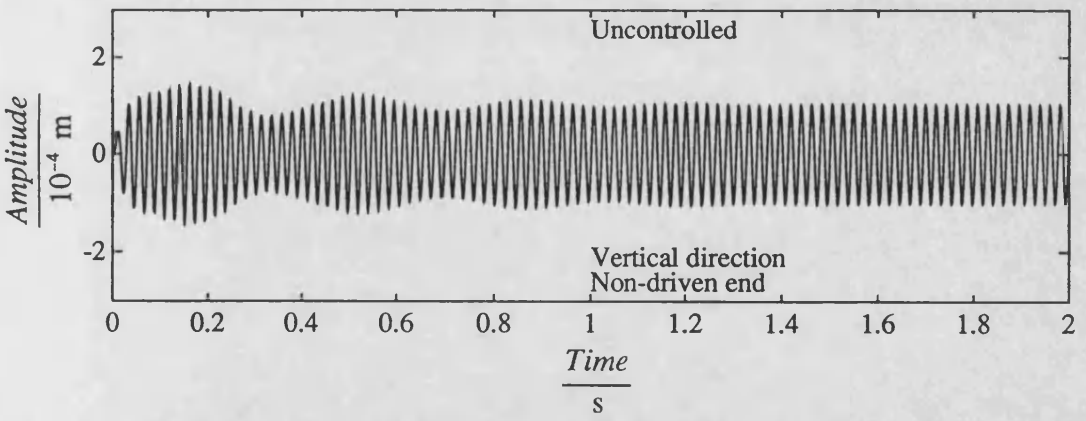

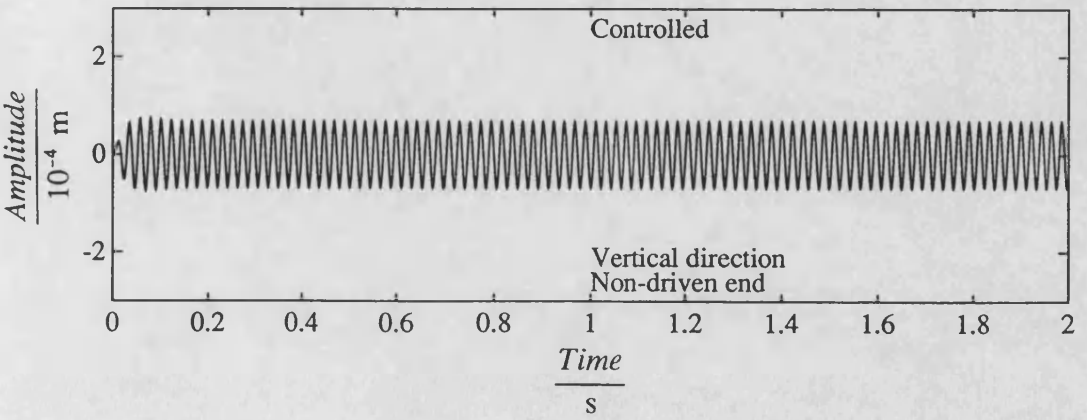

Fig. 6.22 (continued)

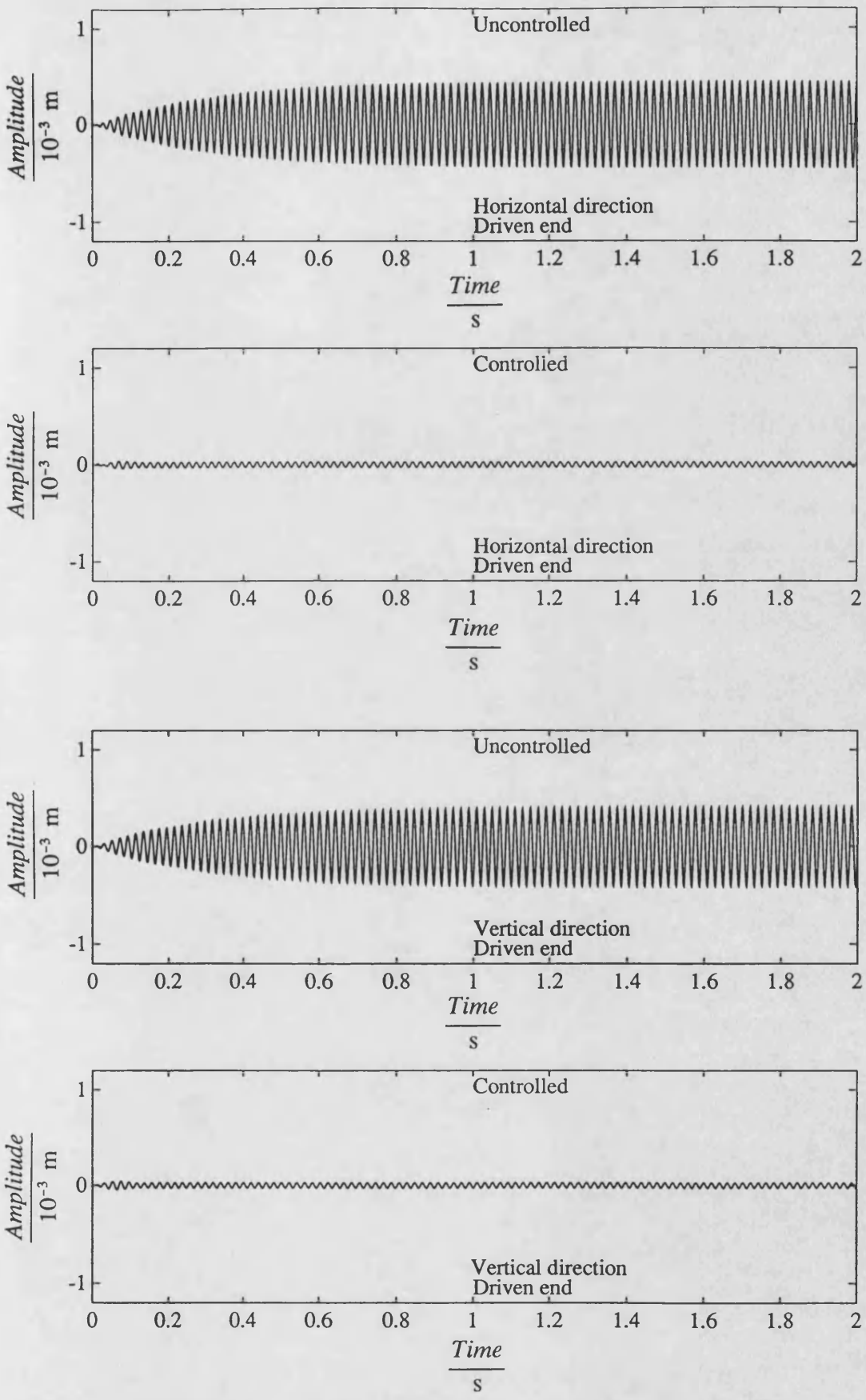

Fig. 6.23 Theoretical transient response of controlled system at speed 309 rad/s, mass loss at t=0

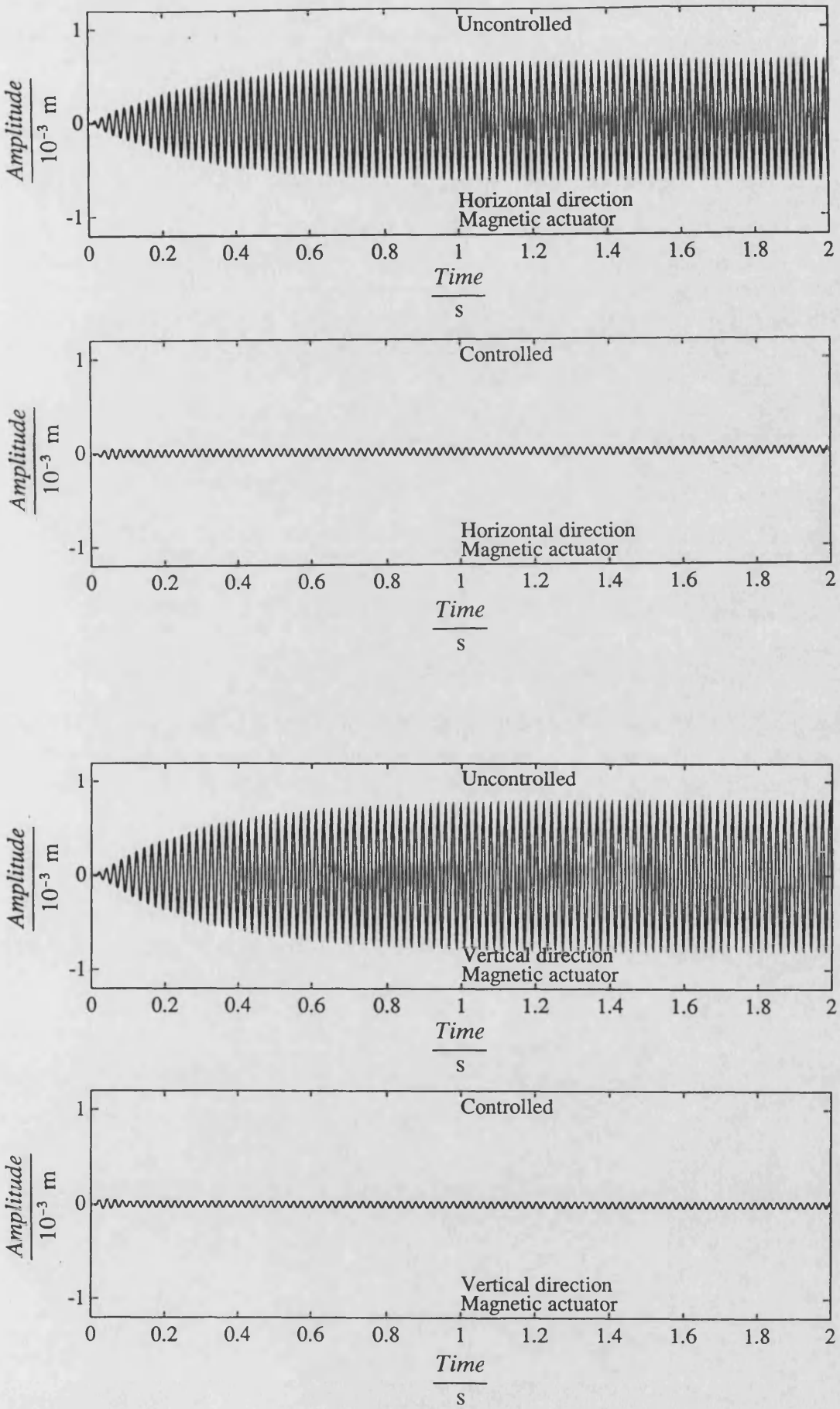

Fig. 6.23 (continued)

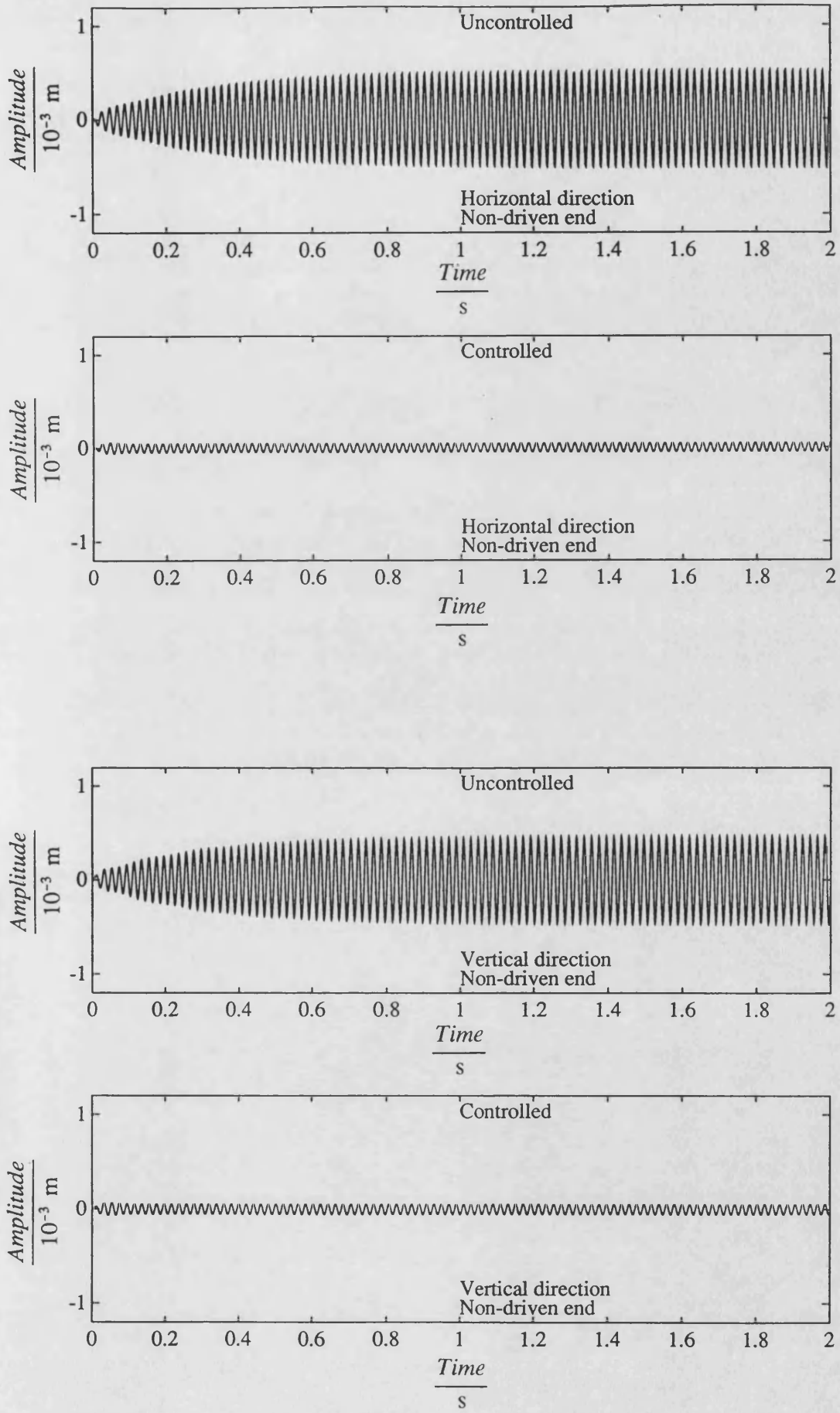

Fig. 6.23 (continued)

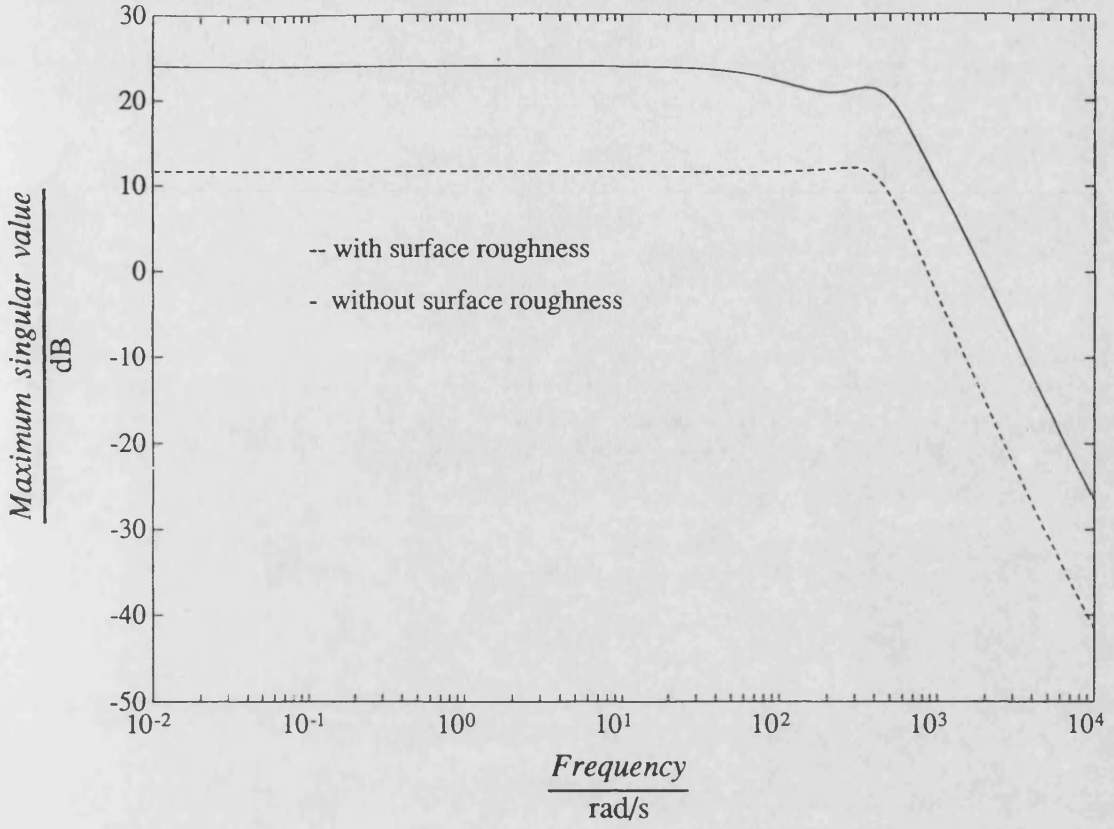

Fig. 6.24 Controller designs with and without surface roughness, Ω=100 rad/s

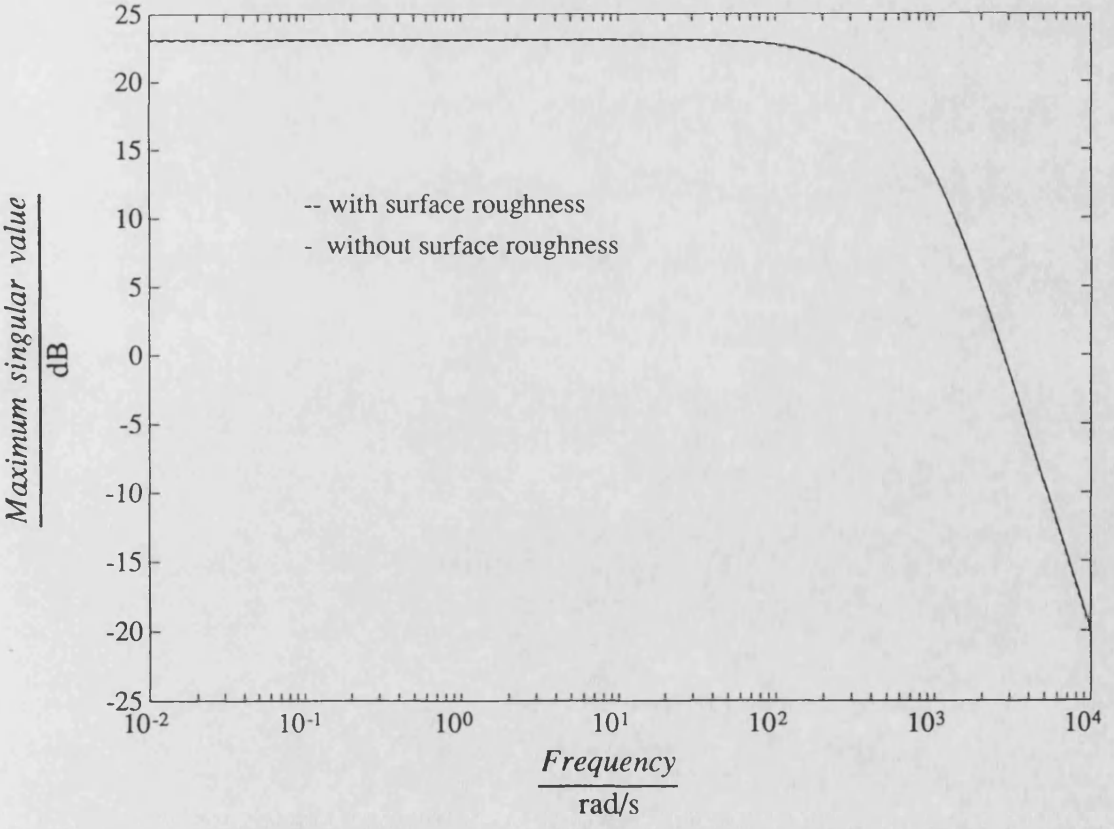

Fig. 6.25 Controller designs with and without surface roughness, Ω=309 rad/s

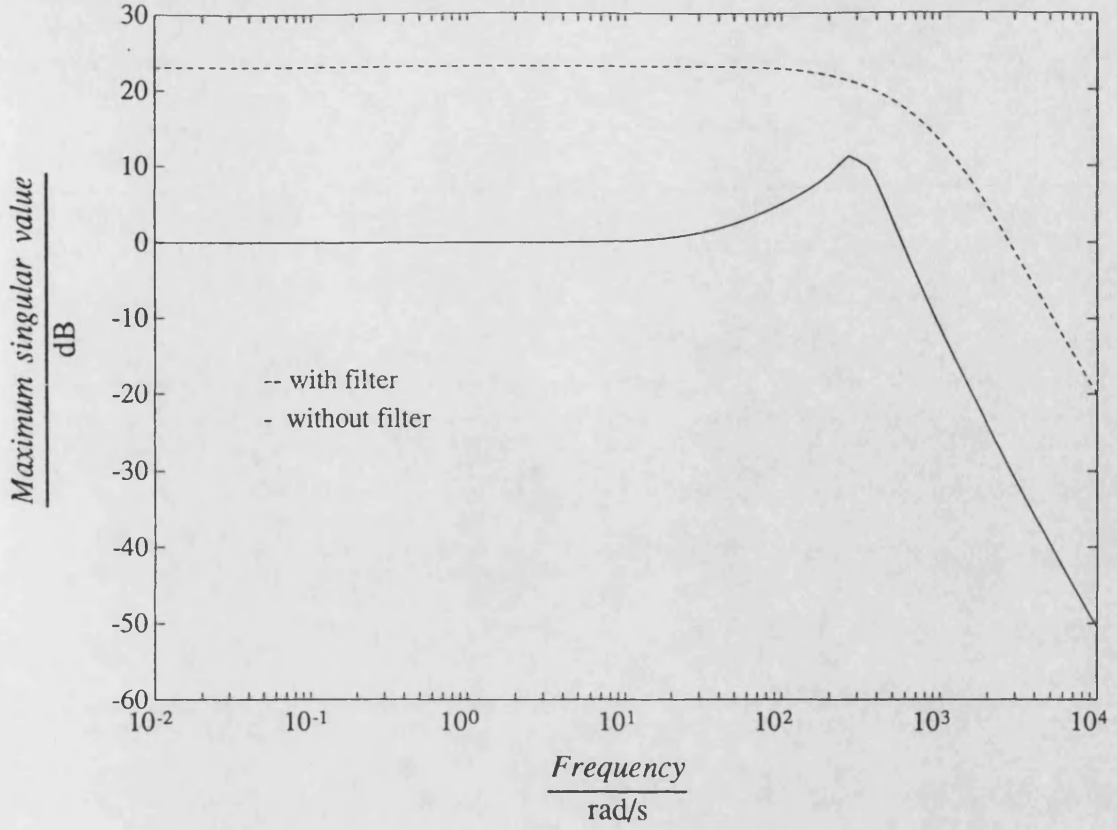

Fig. 6.26 Maximum singular value of the controller with and without measurement filter, Ω=309 rad/s

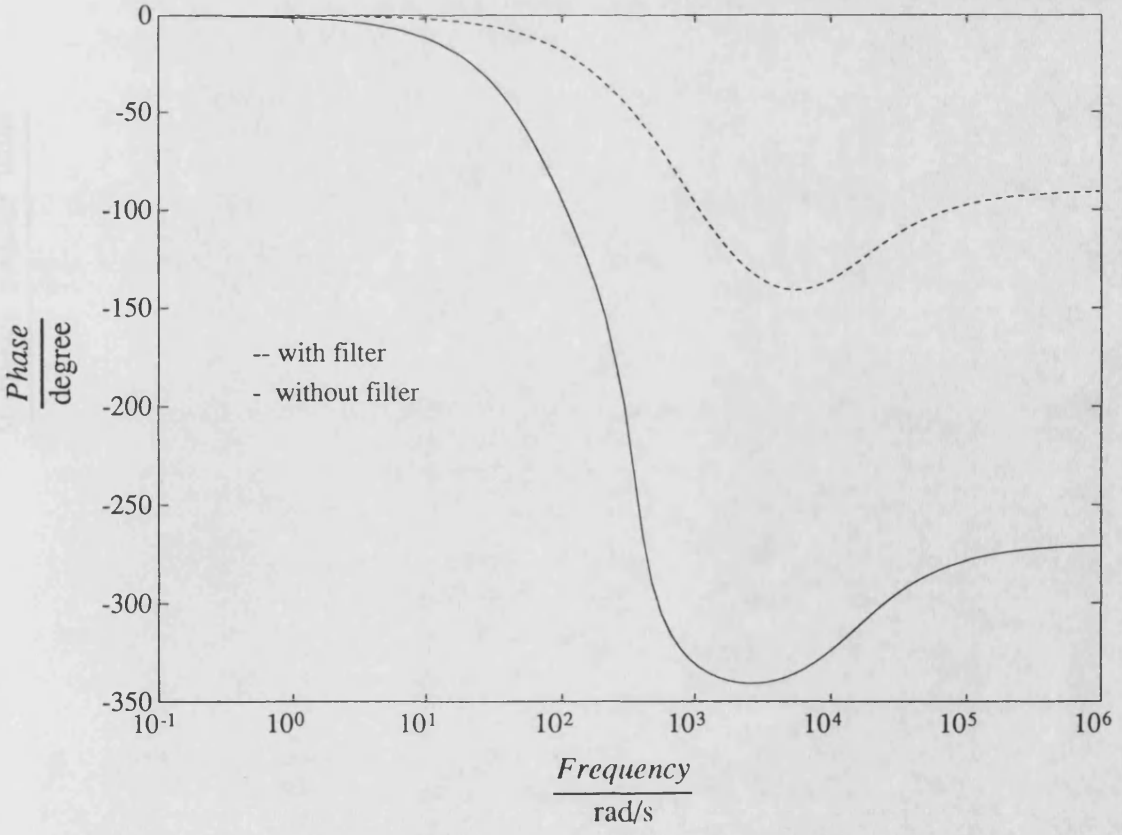

Fig. 6.27 Phase shift of the controller with and without measurement filter, Ω=309 rad/s

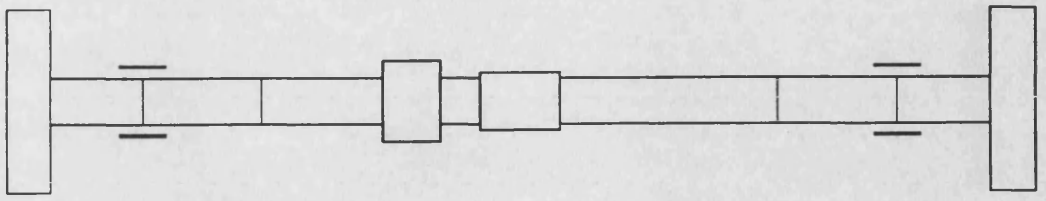

Fig. 6.28 Rotor without second actuator sleeve

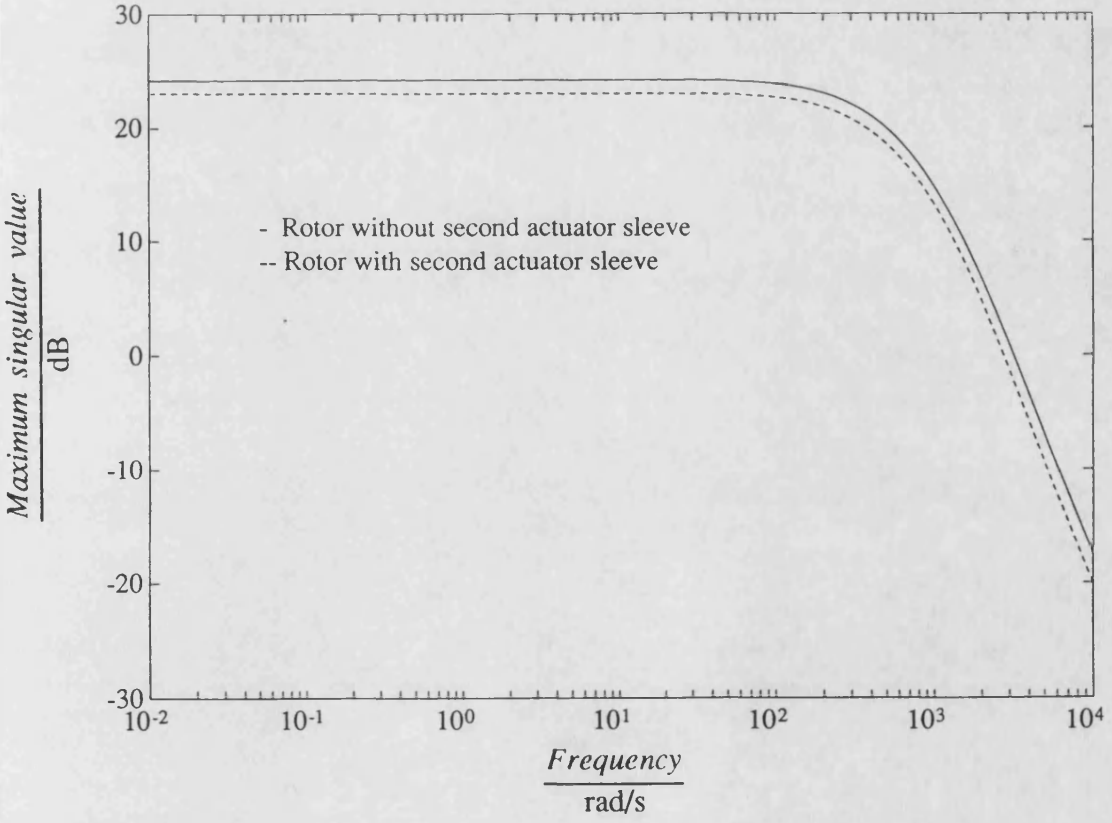

Fig. 6.29 Maximum singular value of the controller with and without second actuator sleeve, Ω=309 rad/s

CHAPTER 7 EXPERIMENTAL RESULTS

The implementation of the H_∞ controller designs from Chapter 6 to the experimental rig leads to the results of this chapter. The controller was tested for attenuation of rotor synchronous response, non-synchronous response, and transient response due to mass loss. The rotor responses of the uncontrolled and controlled system were measured for each case. Comparisons were then made to evaluate the effectiveness of the controllers for vibration reduction. The rotor speed was varied over the range 0 - 3300 rev/min (346 rad/s) so that it could pass the third and fourth critical speeds.

7.1 Brief Description Of Experimental Procedure

Firstly, the rotor was balanced to a level to enable it pass the critical speeds in the uncontrolled state. The synchronous rotor unbalance responses in both horizontal and vertical directions for the uncontrolled system were measured at the six displacement transducer positions. A series of tests were then carried out for the controlled case. Rotor synchronous responses were obtained for the following controller implementations:

(a) Five speed H_∞ control (section 6.4.2)

(b) Two speed H_∞ control (section 6.4.2)

(c) Open-loop adaptive control

(d) Two speed H_∞ control design without considering rotor surface roughness

(e) Two speed H_∞ control design based on inaccurate model

(f) Two speed H_∞ control with transducer positions changed

(g) Two speed H_∞ control with transducers removed

Secondly, non-synchronous response tests were conducted on the rig. Starting with the uncontrolled rotor, a disturbance force from the second magnetic actuator was applied to the rotor. The frequency of the disturbance was varied so that the rotor was excited by a combination of non-synchronous disturbance force and synchronous unbalance. The rotor was more finely balanced than in the synchronous response tests so that it could pass safely through the critical speeds when the disturbance force frequency coincided with rotor critical speeds. The rotor responses for both uncontrolled and controlled systems were measured. The open loop adaptive control was not implemented since it was designed specifically for synchronous control only.

Finally, transient response tests were conducted on the rig. A mass was attached to the non-driven end rotor disk using a simple tie on technique. Before a test, the rotor condition was such that it was better balanced with the tied on mass than without the tied on mass. A test was conducted by running the rotor up to a selected running speed. The tied on mass was then removed using a cable operated blade mechanism (figure 7.1). The rotor responses for the uncontrolled and controlled system were measured in the time domain.

7.2 Synchronous Control

7.2.1 Uncontrolled Response

The rotor responses of the uncontrolled system were measured at different rotational speeds and the results are shown in figure 7.2. The responses show the two critical speeds at 270 rad/s and 305 rad/s, first rotor flexural mode split by bearing asymmetry. The rigid body critical speeds do not appear in the responses since these modes are highly damped. These results are consistent with the theoretical results in Chapter 6.

7.2.2 Five Speed H_∞ Controller Case

The controllers designed at the rotational speeds 100, 150, 200, 250, 309 rad/s were implemented for each of the speed ranges mentioned in Chapter 6 and the response results are shown in figure 7.2. Significant vibration reduction is achieved, especially around the critical speeds. The maximum amplitude of the rotor response was reduced from 0.23 mm for the uncontrolled system to 0.04 mm for the controlled system. The two critical speed peaks of the uncontrolled system are totally suppressed and the resulting controlled responses are flat over the complete rotational speed range.

7.2.3 Two Speed H_∞ Controller Case

The two controllers designed at speeds 100 and 309 rad/s were used on the system in the speed ranges 0 - 250 rad/s and 250 - 345 rad/s respectively and the results are shown in figure 7.3, with the uncontrolled responses. The results show that the controller can achieve nearly the same vibration reduction as that achieved by the five speed controller.

7.2.4 Open-loop Adaptive Controller Case

For the purpose of comparison, the open-loop adaptive control strategy described in Chapter 3 was implemented and the results are shown in figure 7.4. The rotor vibration levels over the rotational speed range are reduced significantly. By comparing the results shown in figures 7.3 and 7.4, it is seen that the H_∞ controller can achieve similar vibration attenuation as the open-loop adaptive controller.

7.2.5 Two Speed H_∞ Controller Designed Without Considering The Rotor Surface Roughness

The controller that was obtained without taking the surface roughness into account in the design was implemented and the results are shown in figure 7.5. These indicate

that the response amplitudes without considering the roughness effect are larger than those of the uncontrolled system in the low speed range below 150 rad/s where the roughness has a relatively larger influence on the measurements. In contrast, consideration of the roughness effect in the control design results in a controller which decreases the vibration levels almost uniformly over the complete speed range (figure 7.3).

7.2.6 Two Speed H_∞ Controller Based On Inaccurate Model

The controller in this section was designed based on a rotor model in which the second magnetic actuator sleeve attached to the shaft was removed from the original model. This resulted in the two measured critical speeds being changed from 270 rad/s and 305 rad/s to 277 rad/s and 315 rad/s respectively. The controller can therefore be regarded as the one designed when model error exists. The controller was implemented and the results obtained are shown in figure 7.6. Slight differences appear between these results and those shown in figure 7.3. This demonstrates that the controller is robust to the small changes in the system structure.

7.2.7 Inaccurate Sensor Position Case

Here the two speed H_∞ controller was used in the test. The position of the two displacement transducers at the rotor non-driven end was moved approximately 10 cm towards the journal bearing direction (figure 7.7). This is equivalent to designing a controller when certain transducer positions are not accurately known. The results are shown in figure 7.8. Since the transducer positions at the non-driven end were changed, comparison with non-driven end responses shown in figure 7.3 can not be made. However, comparison can be made at both driven end position and the control magnetic actuator position. It can be seen that the reduction of the uncontrolled responses remains significant and no large differences exist. This demonstrates that

the controller is not sensitive to perturbations of the position of a pair of transducers.

7.2.8 Two Speed H_∞ Control With Transducers Removed

The test procedure was same as that of section 7.2.2 except that the non-driven end horizontal transducer signal was removed from the system. This simulates a failed transducer. The rotor responses are shown in figure 7.9. No large differences exist when compared with all transducer working normally (figure 7.2). Similar results were also obtained when the pair of transducers at the non-driven end were removed (figure 7.10). Therefore, it can be concluded that the H_∞ controller is not sensitive to transducer failure.

7.3 Non-Synchronous Control

The amplitude of the input voltage to the second actuator amplifier was set in such a way that the maximum amplitude of the rotor always remained within safe limits, particularly when the disturbance frequency was coincident with the rotor critical speeds. Since the system response was non-synchronous, the maximum amplitude of each transducer measurement was recorded at each running speed. The two speed controller was implemented in the non-synchronous case.

7.3.1 Disturbance Frequency Near The Critical Speeds

The disturbance frequency was set to 48 Hz (302 rad/s) and the force was applied in the horizontal direction. The maximum amplitudes of the rotor response at the three transducer positions are shown in figure 7.11 for both uncontrolled and two speed H_∞ controlled conditions. The response of the uncontrolled system shows large amplitudes around and above the critical speeds. The maximum amplitude of the rotor response was reduced from 0.22 mm for the uncontrolled system to 0.06 mm for the controlled system. Similar results were obtained when the force was applied in the vertical

direction (figure 7.12). It is noted that the response of the controlled system is slightly worse than that of the uncontrolled system below the critical speeds at the rotor non-driven end position. However, the controller has a clear beneficial effect overall for vibration reduction.

7.3.2 Disturbance Frequency Below The Critical Speeds

The test was carried out for the disturbance frequency set to 40 Hz (251 rad/s) . The maximum amplitudes of the rotor are shown in figure 7.13 for both uncontrolled and two speed H_∞ controlled conditions. The response of the uncontrolled system has two amplitude peaks at the critical speeds. The maximum amplitude of the rotor response was reduced by the controller from 0.16 mm to 0.06 mm. Similar results were also obtained when the disturbance force was applied in vertical direction (figure 7.14).

7.3.3 Disturbance Frequency Above The Critical Speeds

The frequency of the disturbance force was set to 60 Hz (377 rad/s). This force could be viewed as a high frequency disturbance. The vibration amplitudes are shown in figure 7.15. The maximum vibration level was brought down by the two speed H_∞ controller from 0.13 mm to 0.06 mm. Similar results were observed when the disturbance force was applied to the rotor in vertical direction. These are shown in figure 7.16.

7.4 Transient Control

Sudden mass loss causes a step change in the rotor balance condition resulting in transient rotor vibration. Twenty transient response tests were carried out including the rotational speeds of 262, 270, 278, 283, 288, 293, 301, 305, 309, 314 rad/s for uncontrolled and controlled cases respectively. The controller designed at 309 rad/s for the transient case was used (section 6.4.4). Speed 262 rad/s is below the third

critical speed, speed 270 rad/s coincides with the third critical speed, speeds 278 - 301 rad/s are between the third and fourth critical speeds, speed 305 rad/s coincides with fourth critical speed, and speeds 309 and 314 rad/s are above the fourth critical speed. The shaft surface roughness signals are subtracted from the time history responses in all cases.

7.4.1 Mass Loss Below Third Critical Speed

The measured responses of the rotor for both uncontrolled and controlled cases at speed 262 rad/s are shown in figure 7.17. An unbalance mass of 42 g was added to the non-driven end disk of the well balanced rotor. A similar mass was tied on 180° further round and it was removed with the blade mechanism (figure 7.1). It is seen that the transient responses of the uncontrolled system experience overshoot. The settling time from one steady state condition before mass loss to another after mass loss is about 0.6 s. For the controlled system, however, no overshoot occurs and the settling time is below 0.1 s. Since the vibration amplitudes of the uncontrolled system are not very large, the effectiveness of the controller does not appear to be significant, especially at the two end positions of the rotor. However, the overall vibration level was brought down from 0.15 mm to 0.05 mm by the controller after the mass loss.

7.4.2 Mass Loss At Third Critical Speed

The attached mass of 42 g was removed at the speed 270 rad/s and the transient response results are shown in figure 7.18 for the uncontrolled and controlled systems. The uncontrolled rotor experiences larger vibration levels before and after the mass loss when compared with the 262 rad/s case. The maximum amplitude of the uncontrolled system was 0.08 mm before the mass loss and 0.2 mm after mass loss. For the controlled system, however, these amplitudes are below 0.06 mm. Furthermore, the controller suppresses the large overshoot experienced by the

uncontrolled system. The controller can respond to the sudden unbalance change with a settling time of around 0.1 s.

7.4.3 Mass Loss Between Third And Fourth Critical Speeds

The mass loss tests were conducted at the speed 278, 283, and 288 rad/s respectively and the unbalance mass was 42 g. The transient response results are shown in figures 7.19, 7.20, and 7.21 for the uncontrolled and controlled systems respectively. The maximum amplitude of the uncontrolled system was 0.23 mm for the 278 rad/s case, 0.27 mm for the 283 rad/s case, and 0.4 mm for the 288 rad/s case. For the controlled system, however, these amplitudes are below 0.08 mm, 0.075 mm, and 0.1 mm respectively. Furthermore, the controller suppresses the overshoot experienced by the uncontrolled system. The controller can respond to the sudden unbalance change with a settling time below 0.1 s for all three cases.

For safety reasons, an unbalance mass of 16 g was used when mass loss occurred at speed 293, 301 rad/s. The transient response results are shown in figures 7.22 and 7.23 for the uncontrolled and controlled systems respectively. The maximum amplitude of the uncontrolled system was 0.2 mm for the 293 rad/s case, and 0.4 mm for the 301 rad/s case. These amplitudes were reduced to 0.04 mm and 0.05 mm by applying the controller.

7.4.4 Mass Loss At Fourth Critical Speed

It is noted that the rotor could not pass through the fourth critical speed with an unbalance mass of 16 g. Therefore, an unbalance mass of 7 g was used when mass loss occurred at speed 305 rad/s. The transient responses for the uncontrolled and controlled systems are shown in figure 7.24. It is indicated that the uncontrolled maximum amplitude was 0.1 mm before the mass loss and 0.25 mm after mass loss.

When the controller was implemented, the maximum amplitude was below 0.02 mm both before and after mass loss. The controller can cope with the sudden unbalance change with a settling time below 0.1 s.

7.4.5 Mass Loss Above Fourth Critical Speed

The attached mass of 7 g was used when mass loss occurred at speeds 309 and 314 rad/s. The transient responses for the uncontrolled and controlled system are shown in figures 7.25 and 7.26. The uncontrolled maximum amplitude was 0.08 mm before the mass loss and 0.2 mm after mass loss for the 309 rad/s case, and 0.05 mm and 0.16 mm for the 314 rad/s case. When the controller was implemented, the maximum amplitudes were below 0.04 mm before and after mass loss. The controller suppressed transient vibration in such a way that the transient period was reduced below 0.1 s for the controlled system.

7.5 Discussion Of Results

The results demonstrate that the H_∞ controller is effective in the vibration attenuation of rotor-bearing systems. In the tests, no spillover phenomenon was observed when the H_∞ controller was implemented. The controller was designed to ensure a stable closed loop system.

The H_∞ controller was insensitive to the variation of rotational speed. Since the variation of speed causes a change of system parameters, the H_∞ controller is robust to the system structure change. This conclusion was further demonstrated with the implementation of a controller which was designed when model error existed.

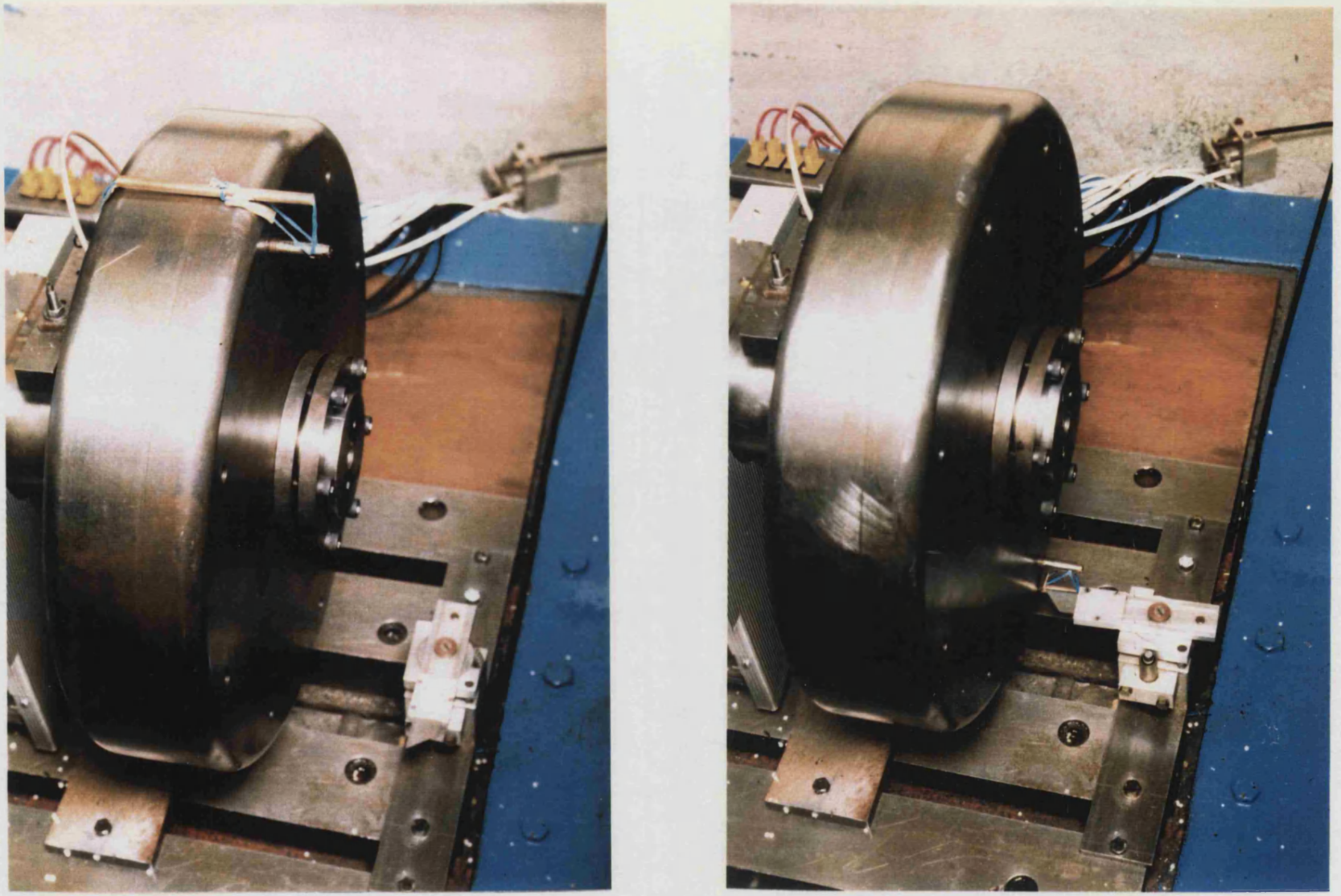

Fig. 7.1 Attached mass and cable operated blade mechanism

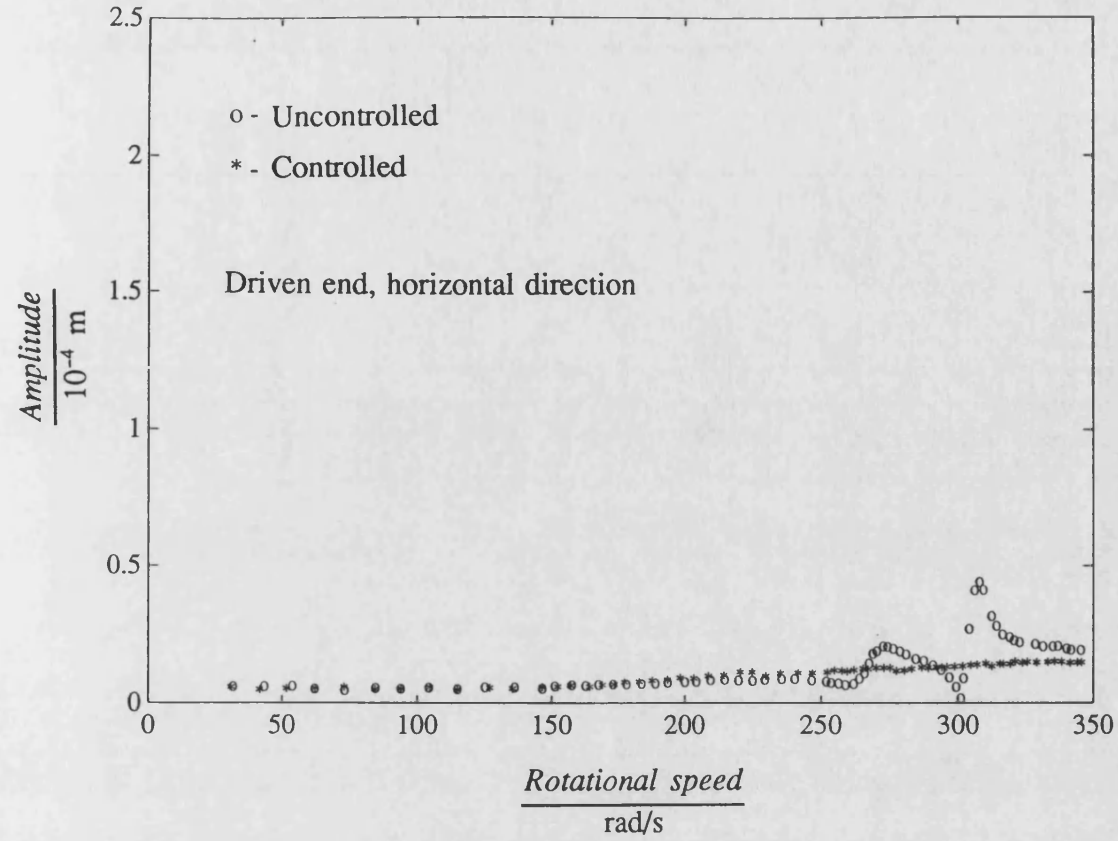

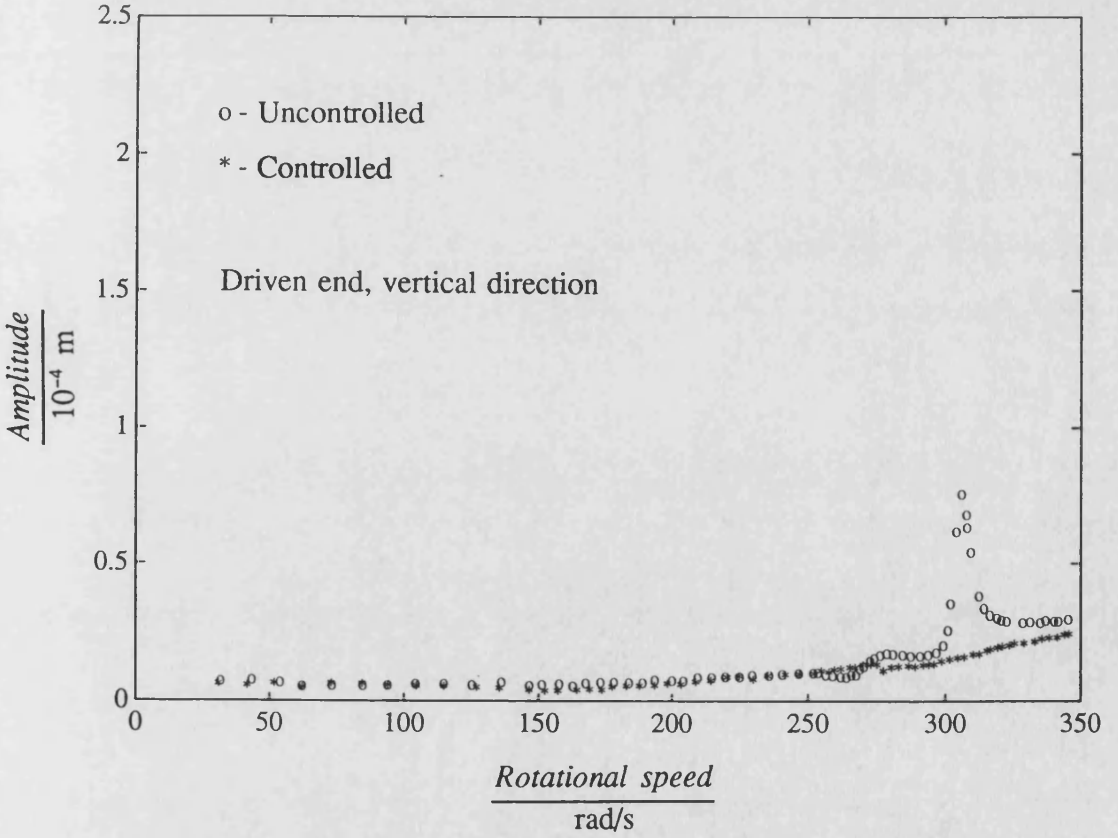

Fig. 7.2 Comparison of uncontrolled and five speed H_∞ controlled measured synchronous responses

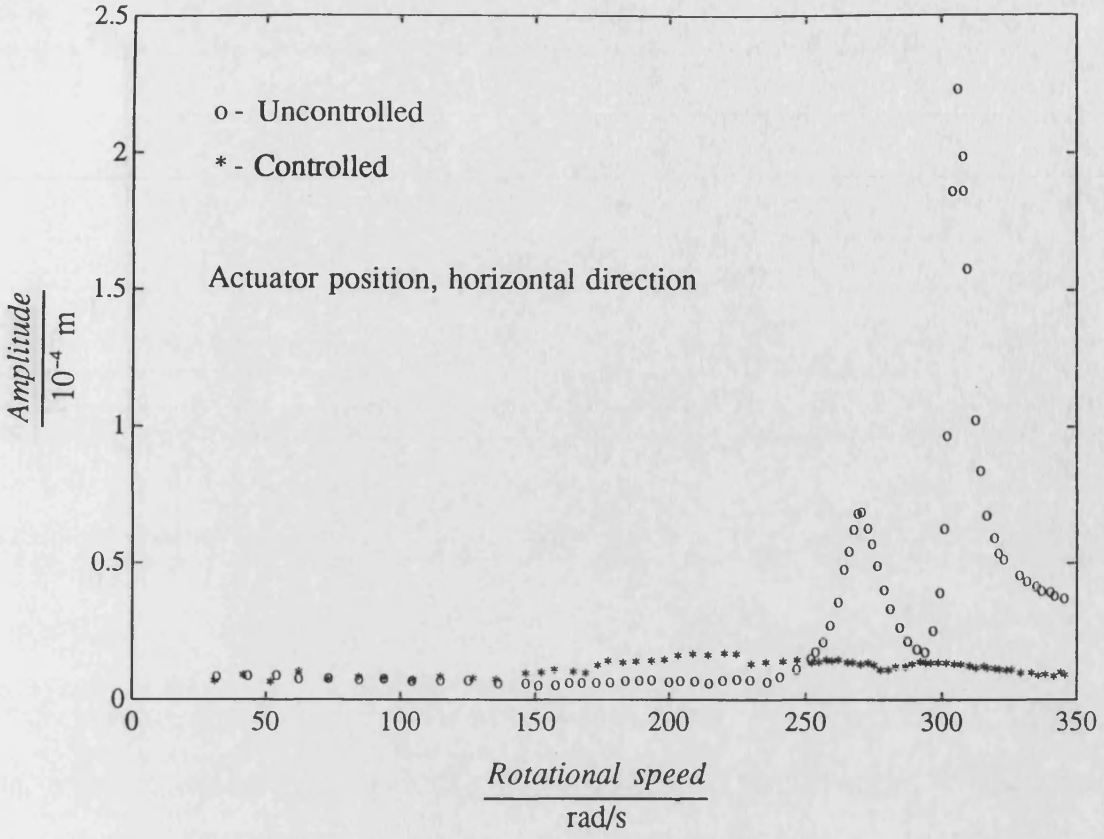

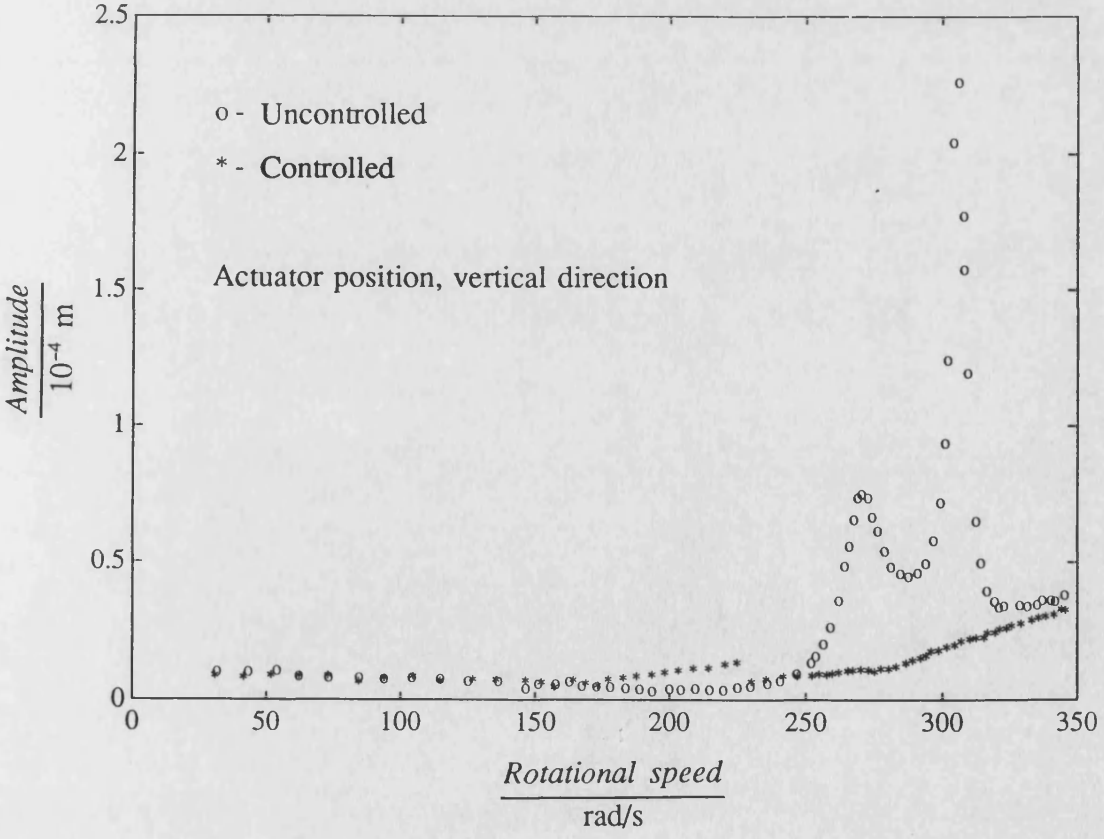

Fig. 7.2 (continued)

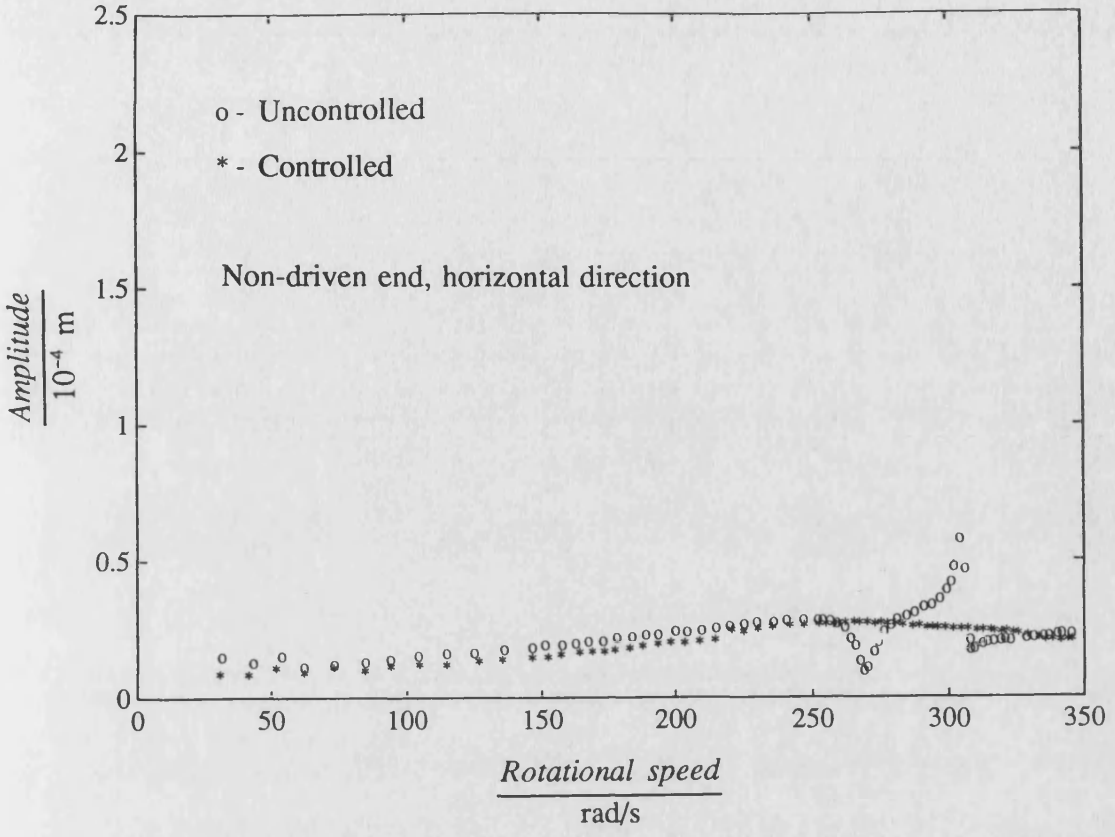

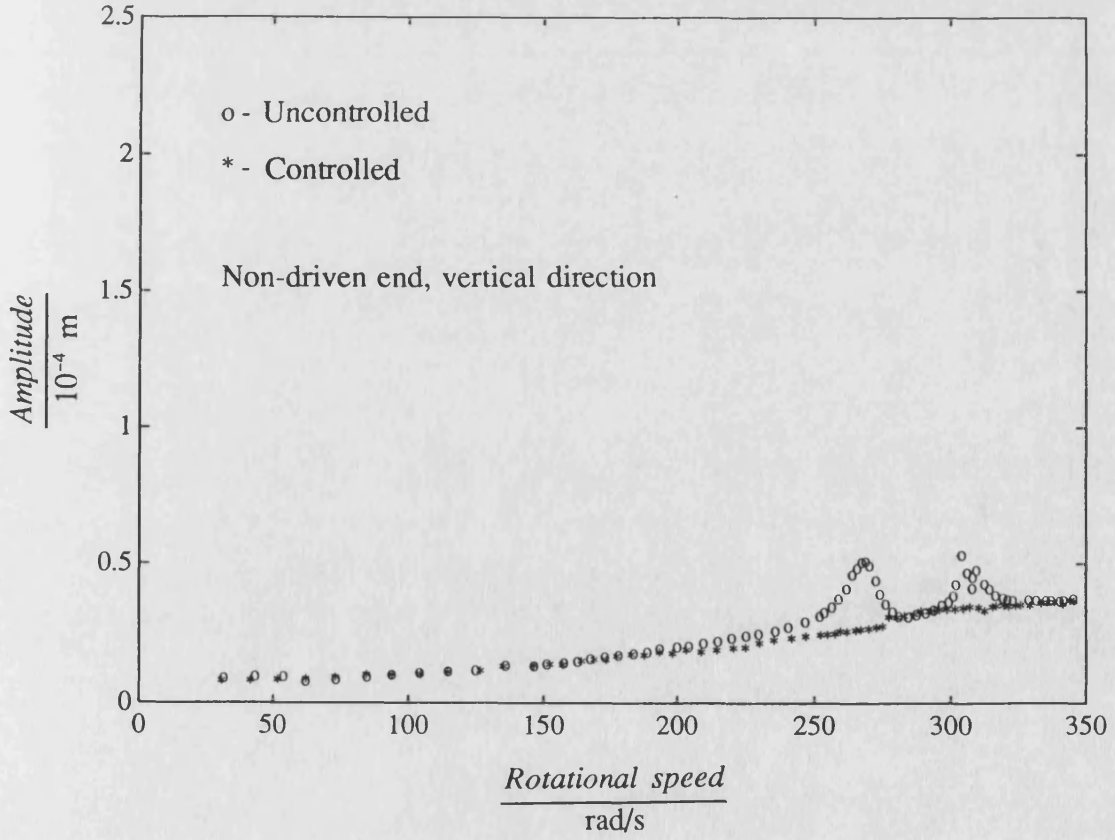

Fig. 7.2 (continued)

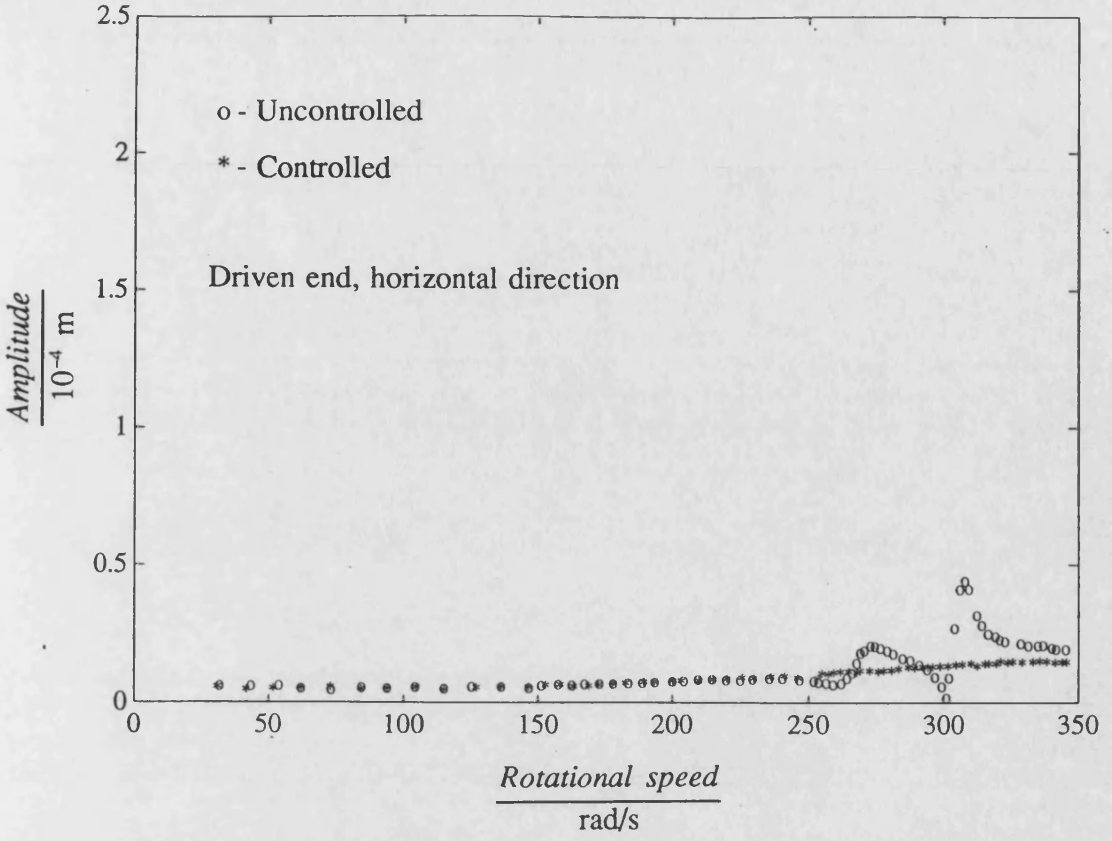

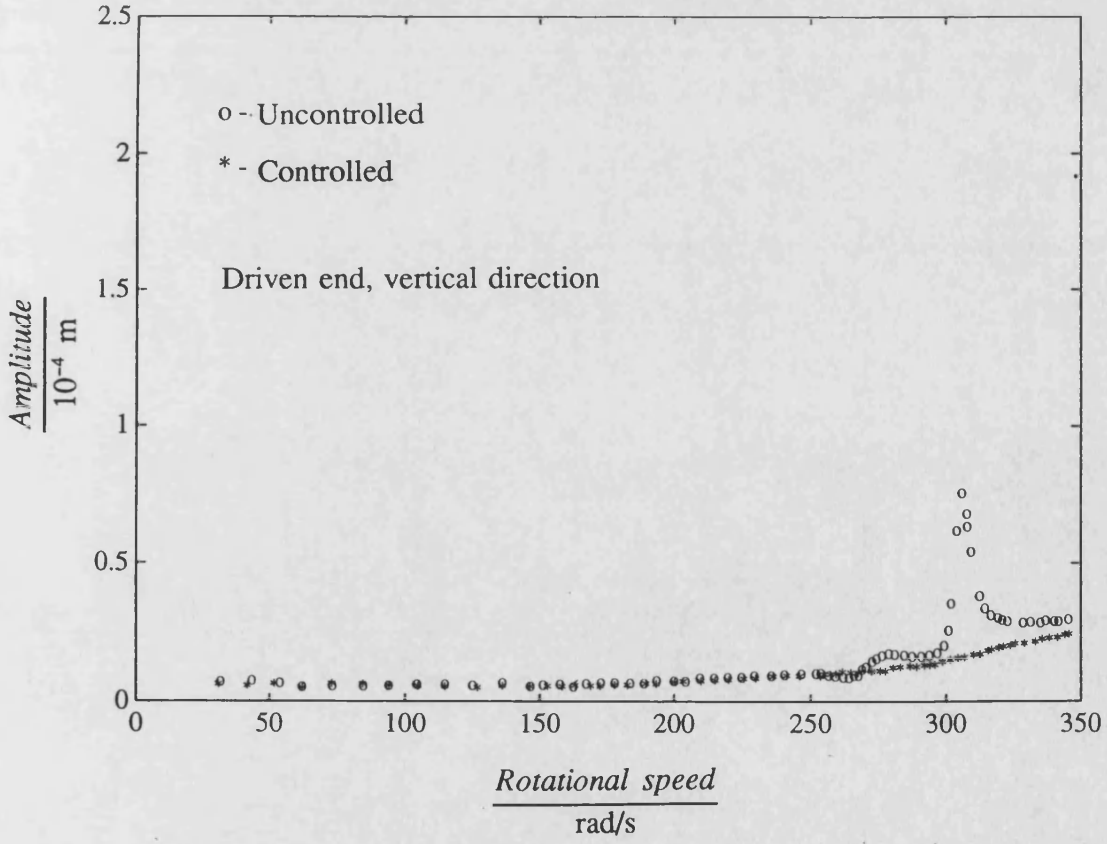

Fig. 7.3 Comparison of uncontrolled and two speed H_∞ controlled measured synchronous responses

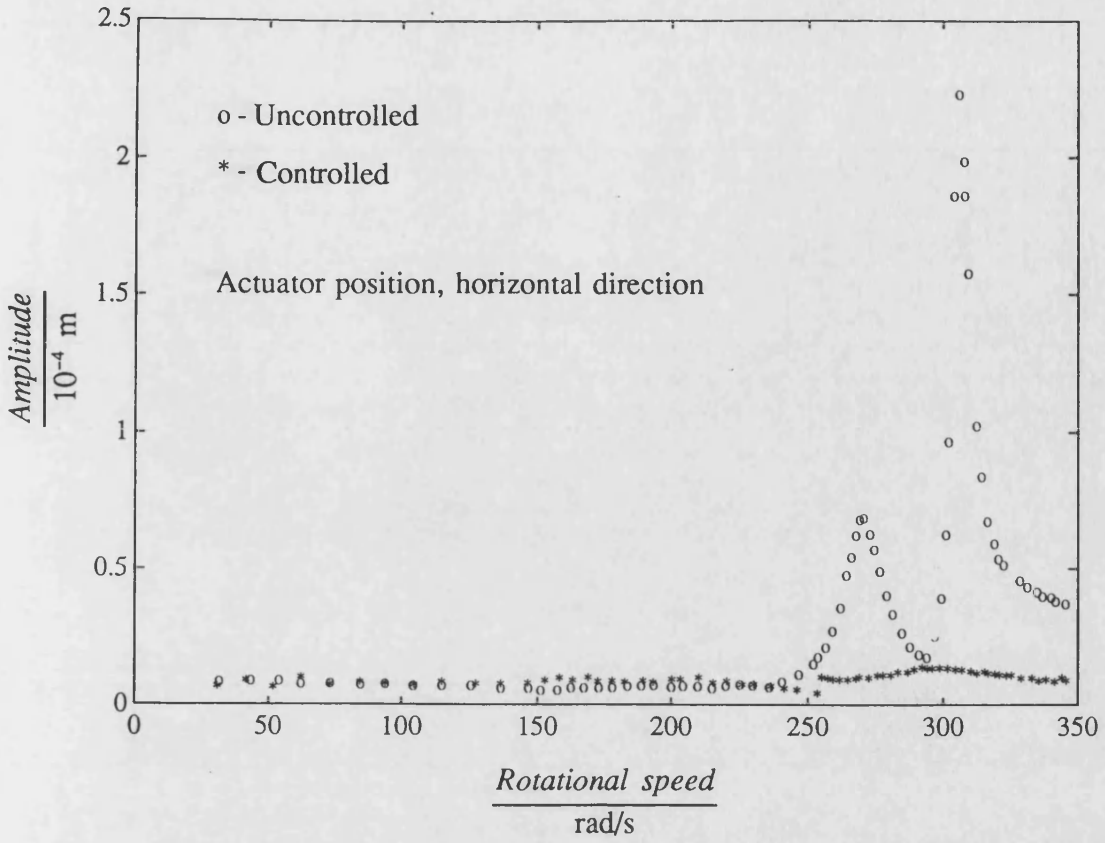

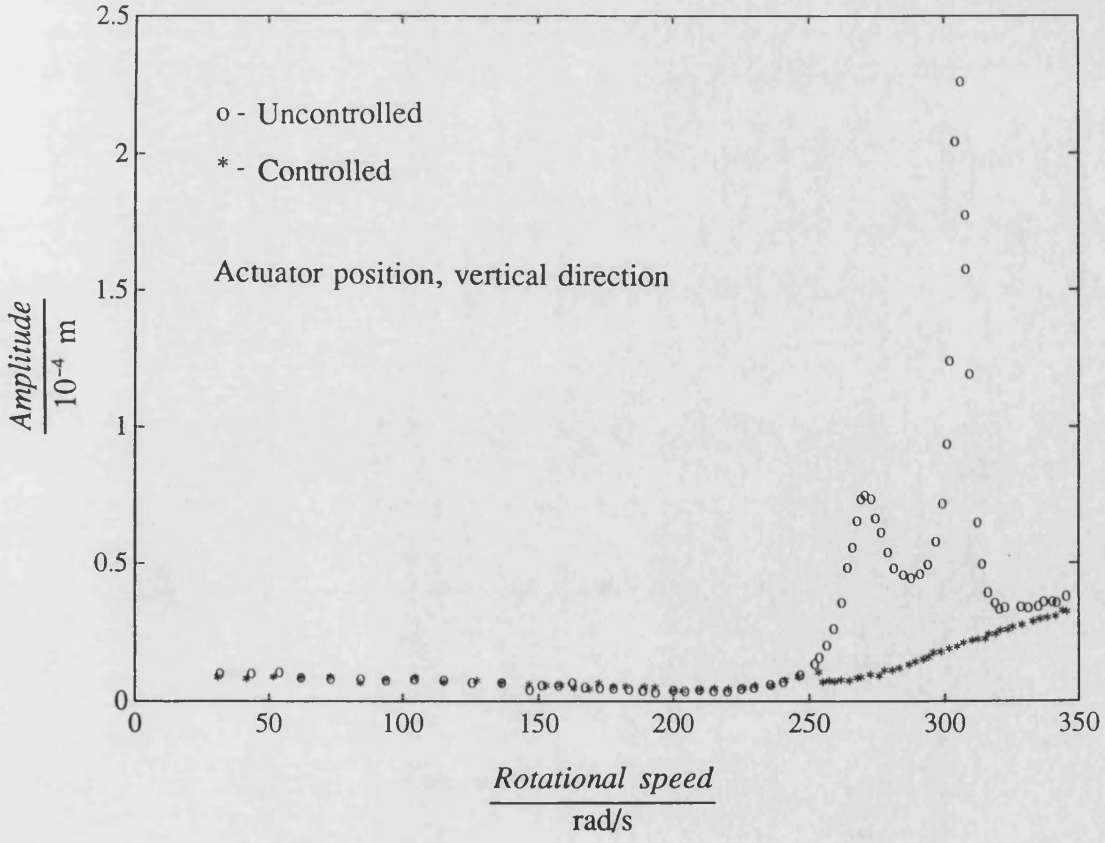

Fig. 7.3 (continued)

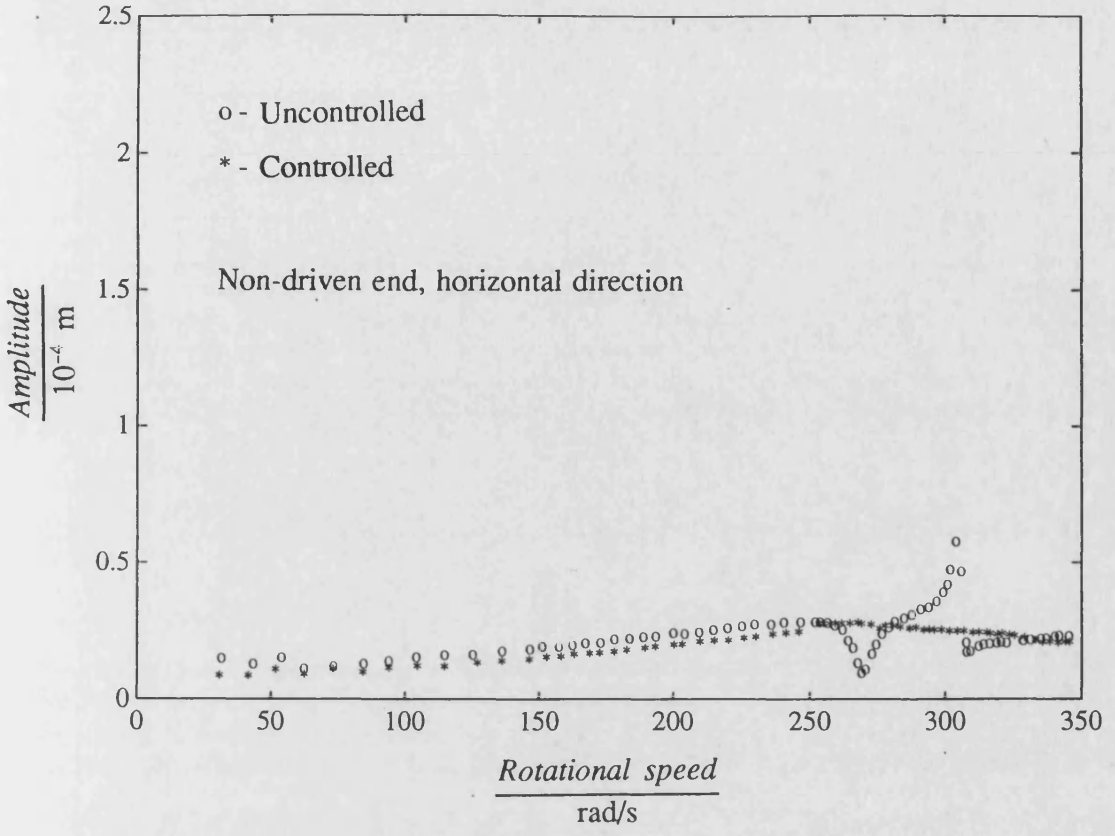

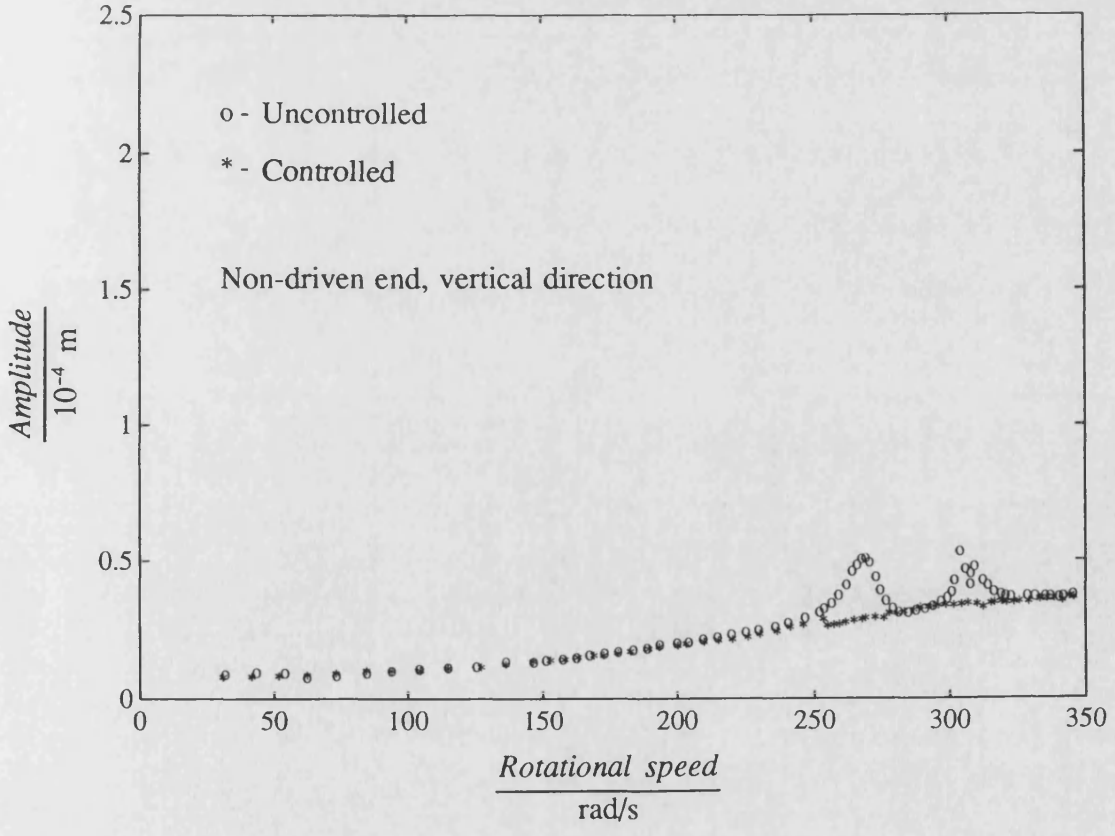

Fig. 7.3 (continued)

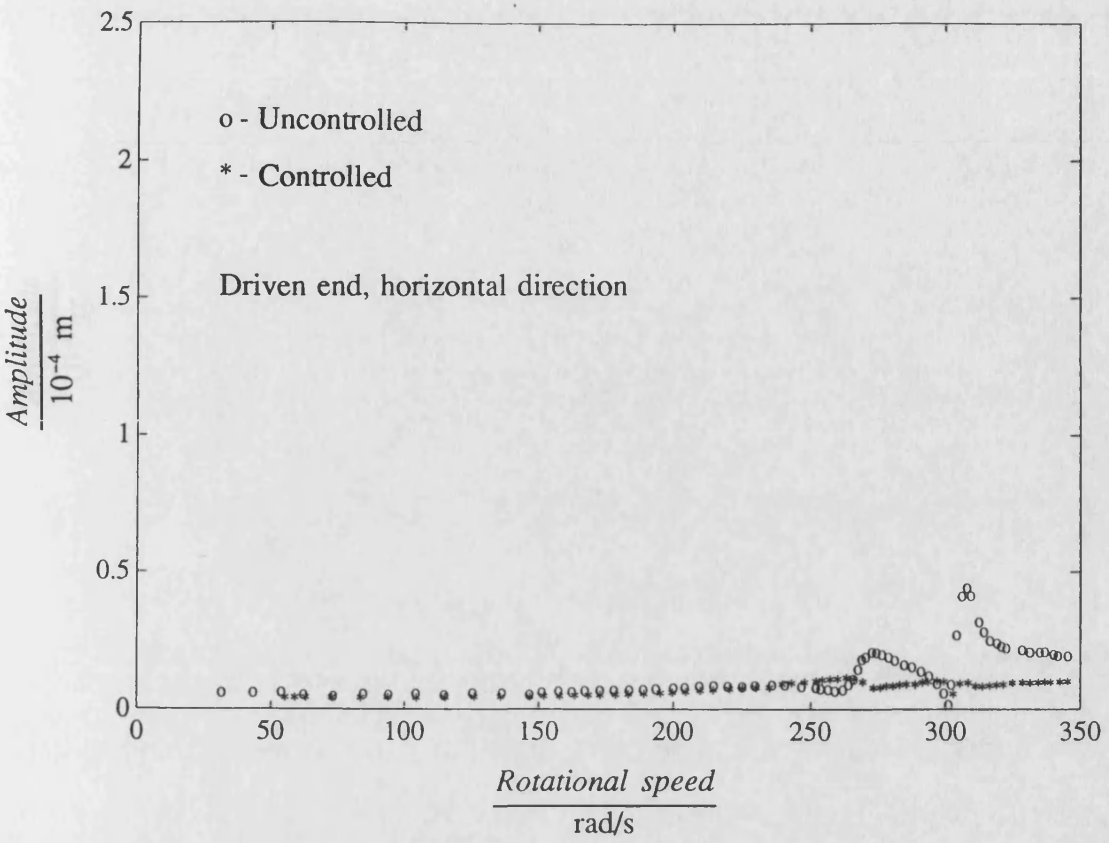

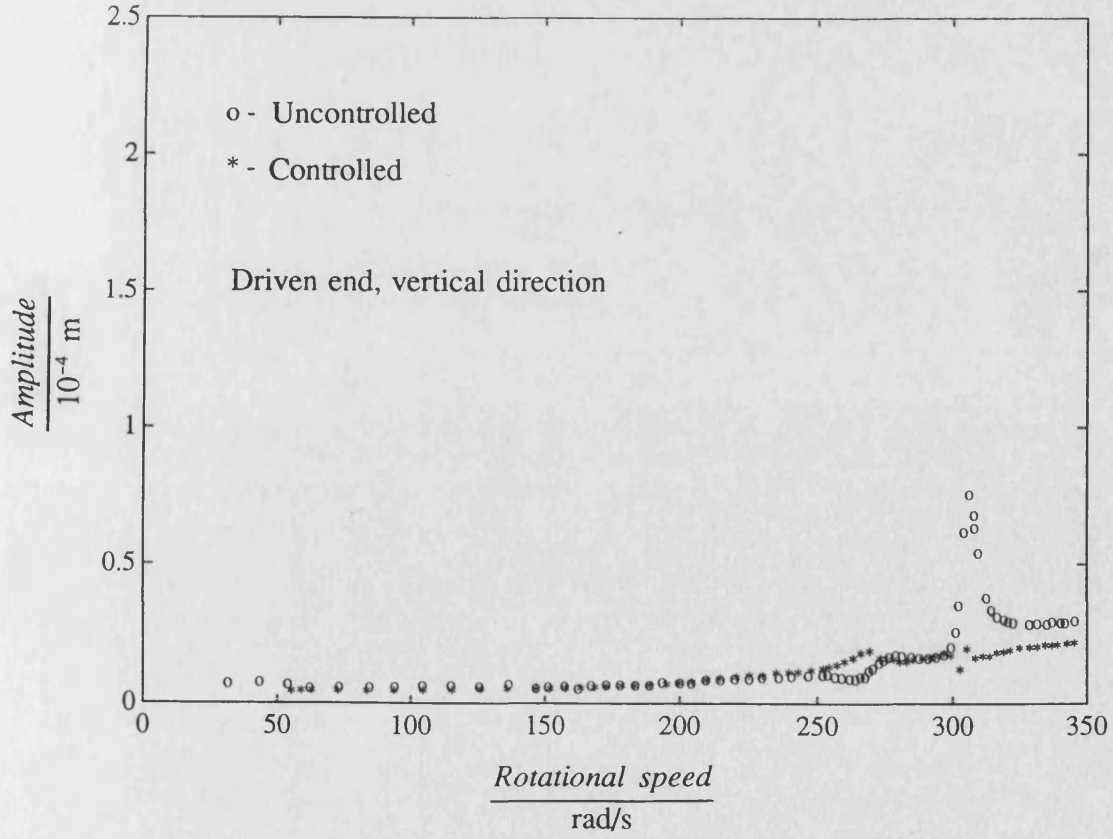

Fig. 7.4 Comparison of uncontrolled and open loop adaptive controlled measured synchronous responses

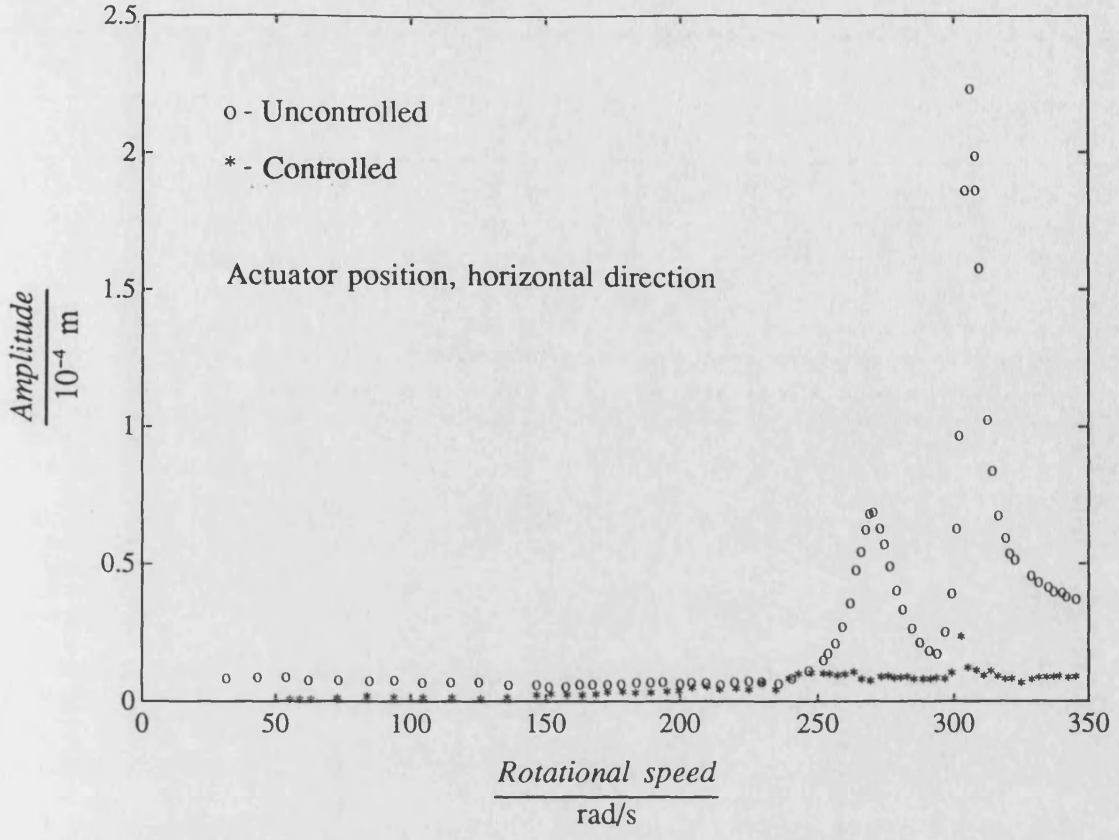

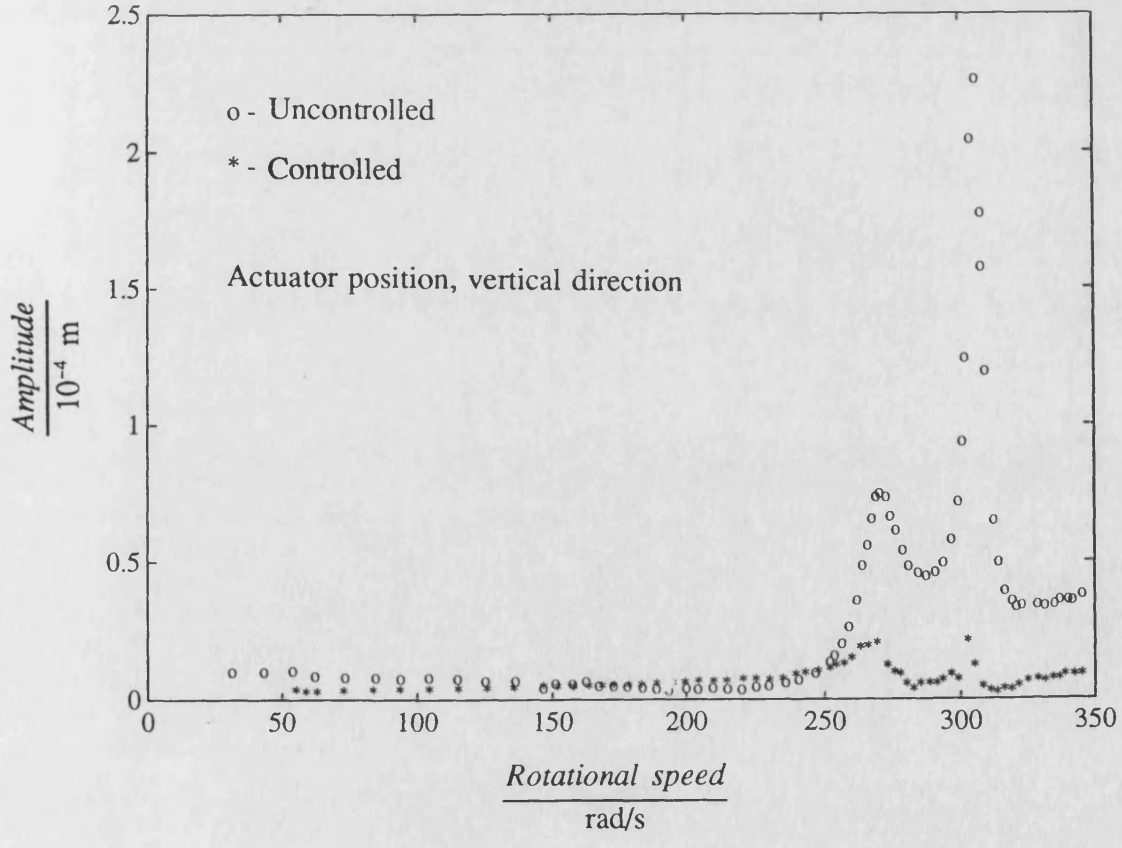

Fig. 7.4 (continued)

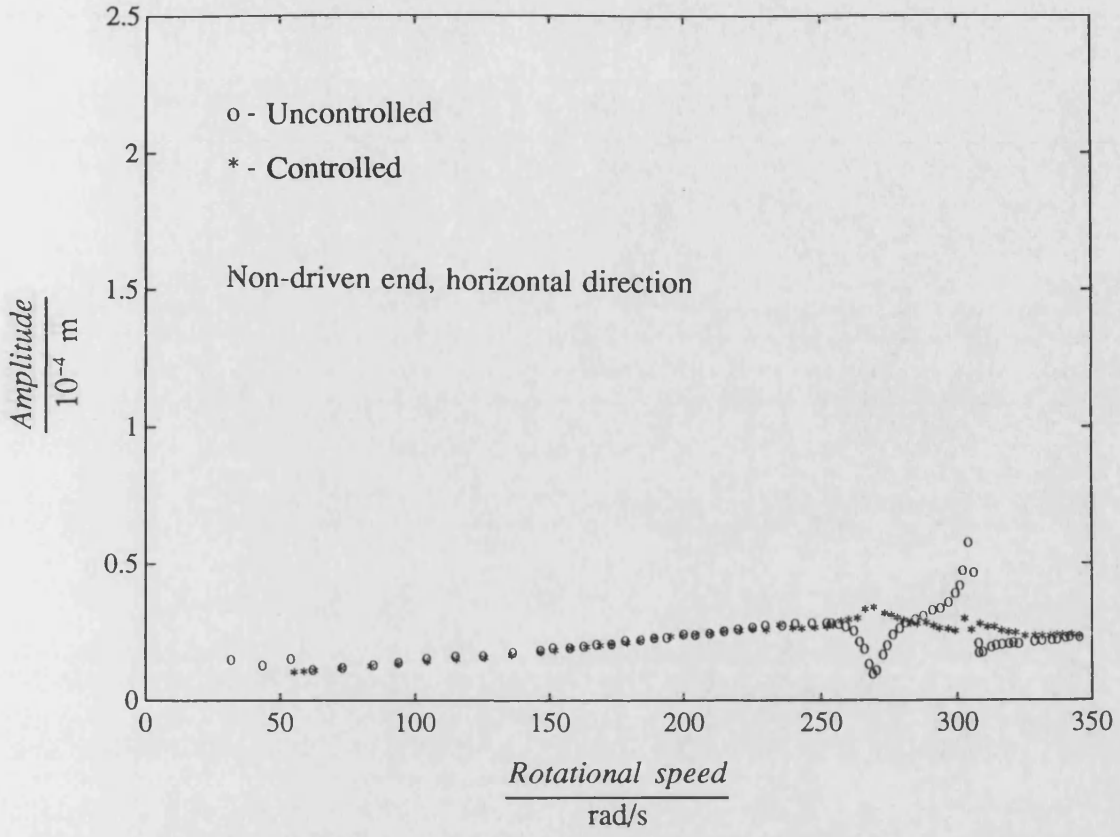

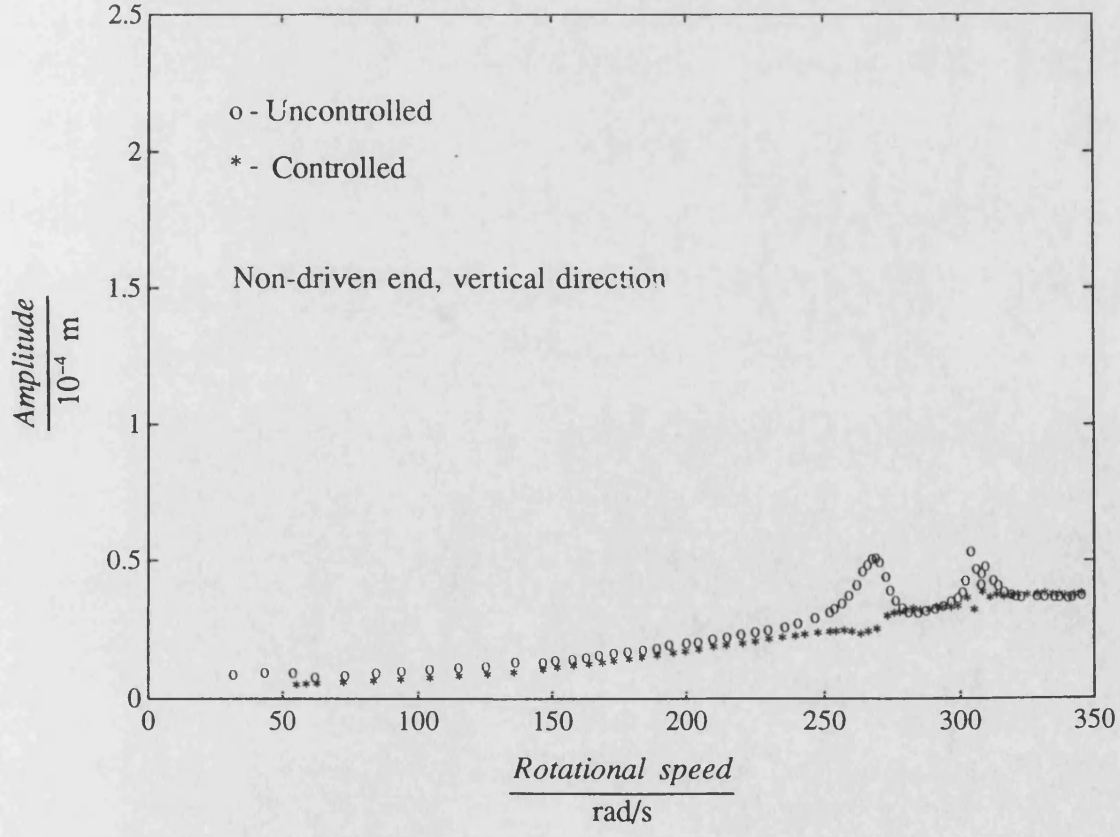

Fig. 7.4 (continued)

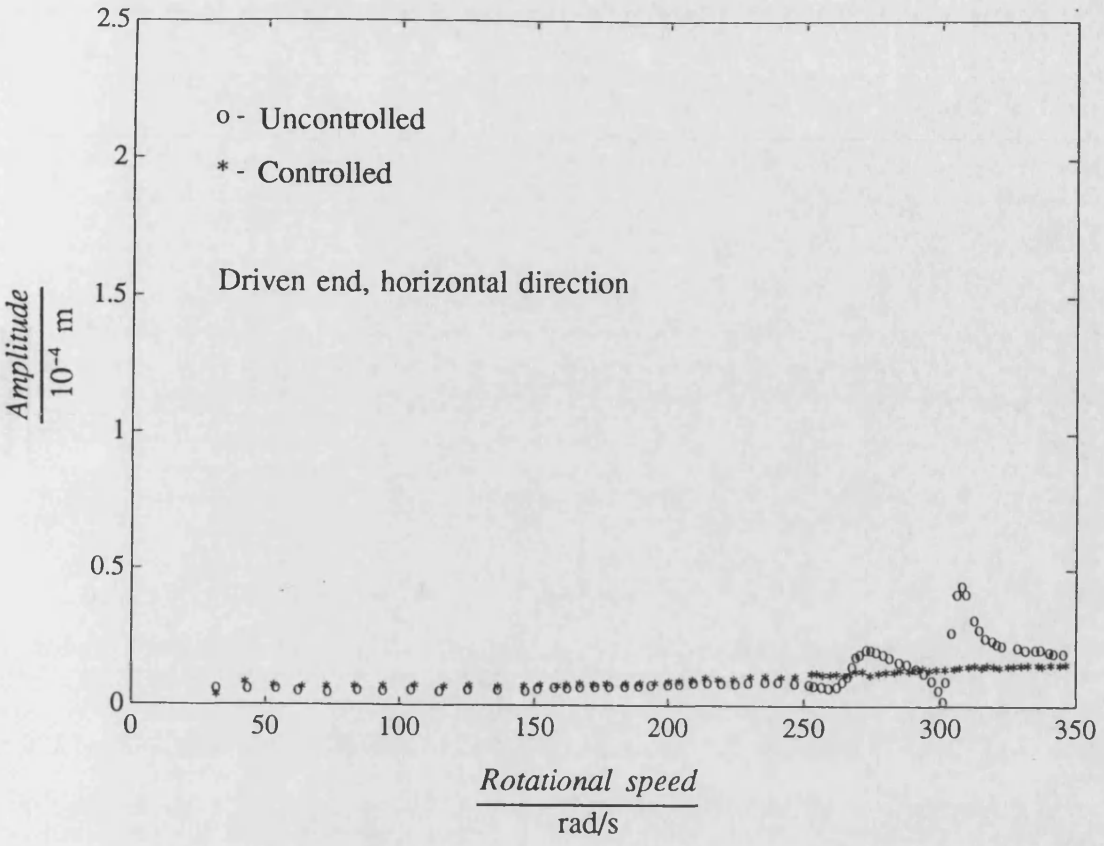

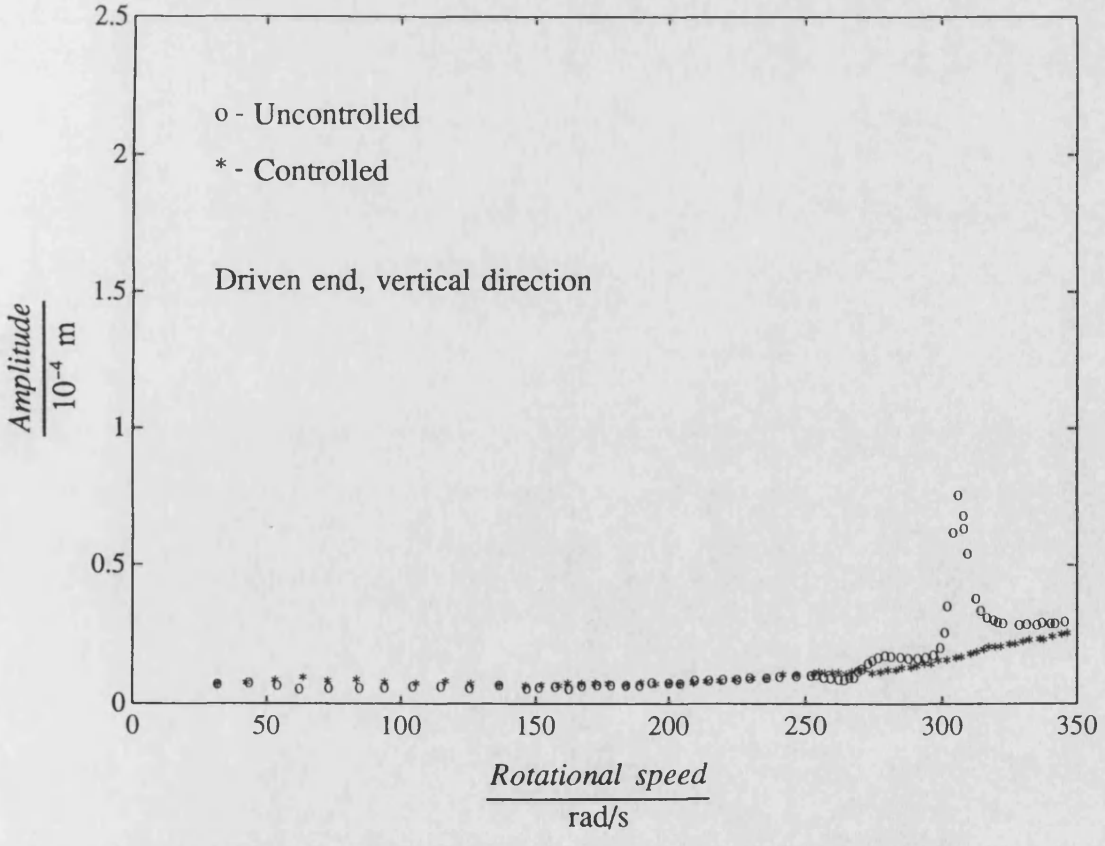

Fig. 7.5 Two speed H_∞ controlled measured synchronous responses without surface roughness included in the design

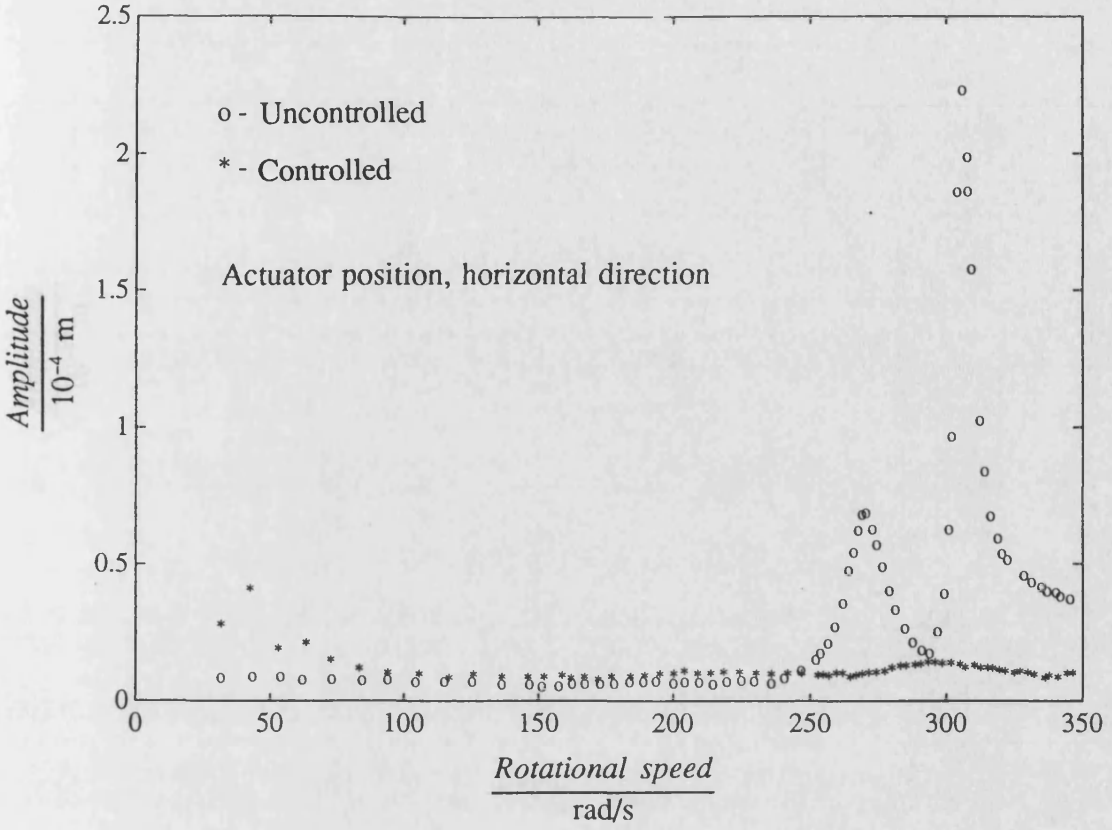

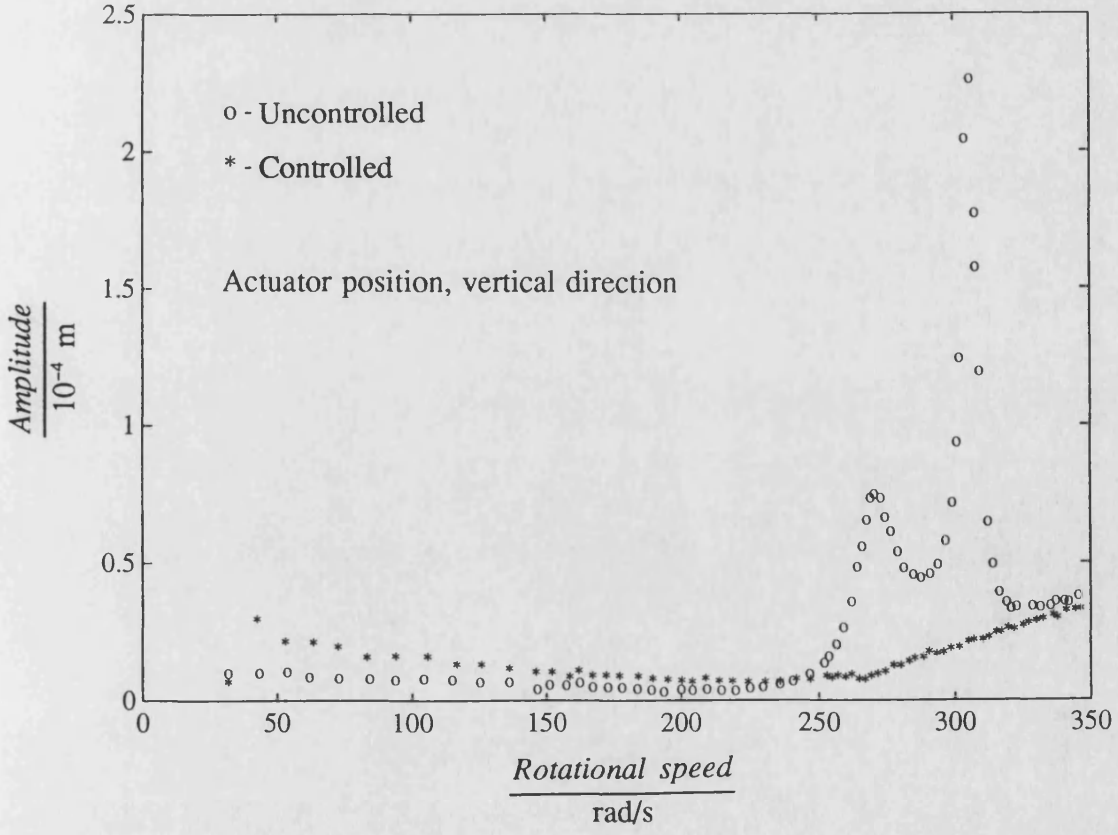

Fig. 7.5 (continued)

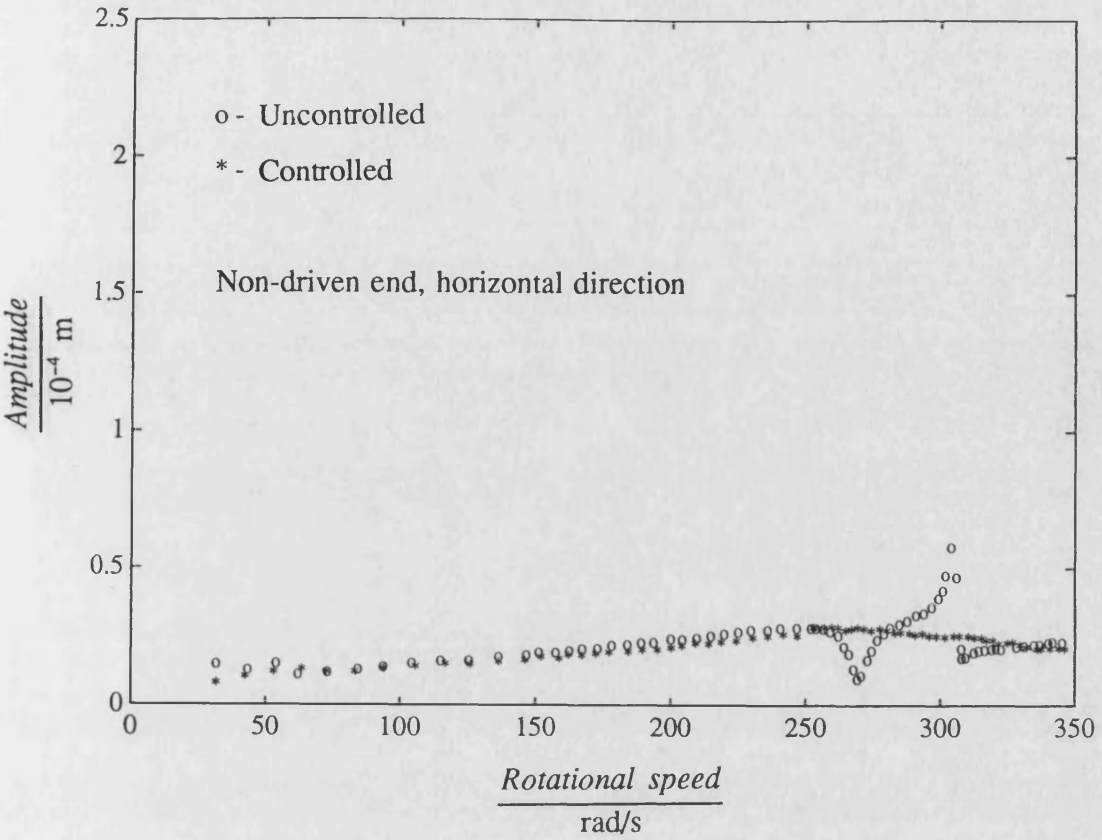

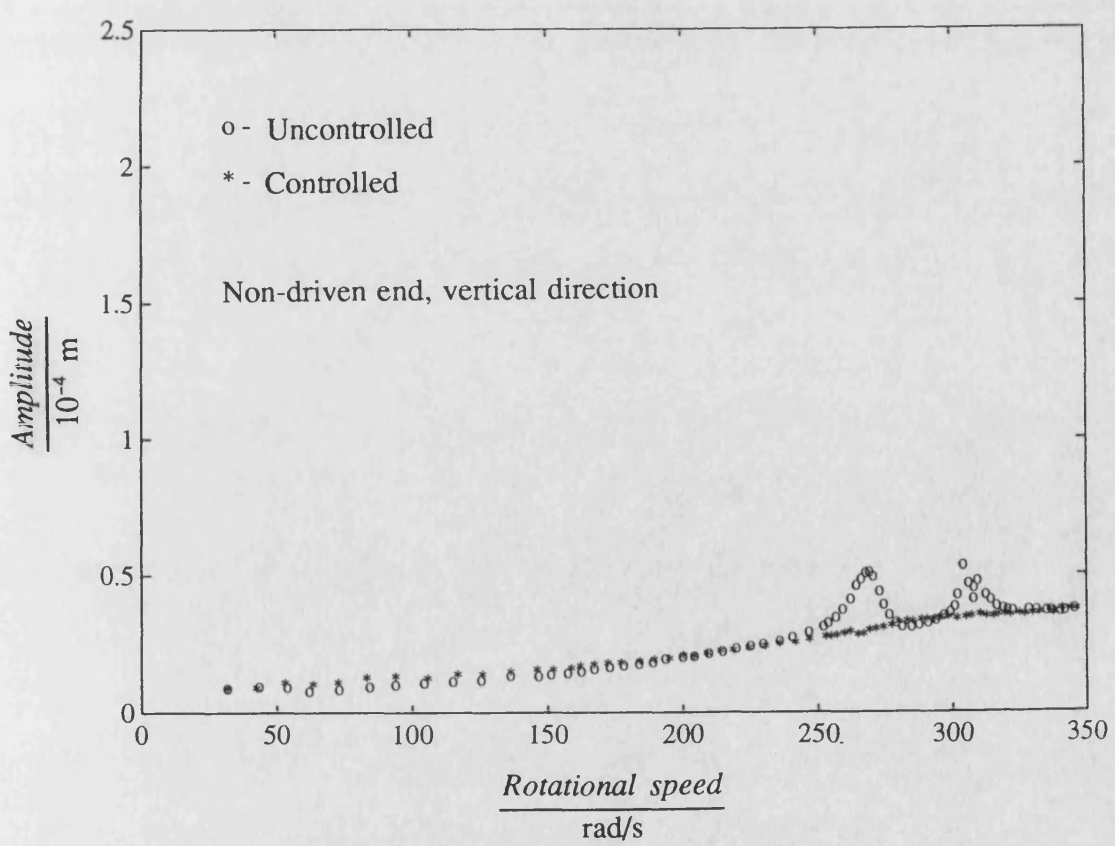

Fig. 7.5 (continued)

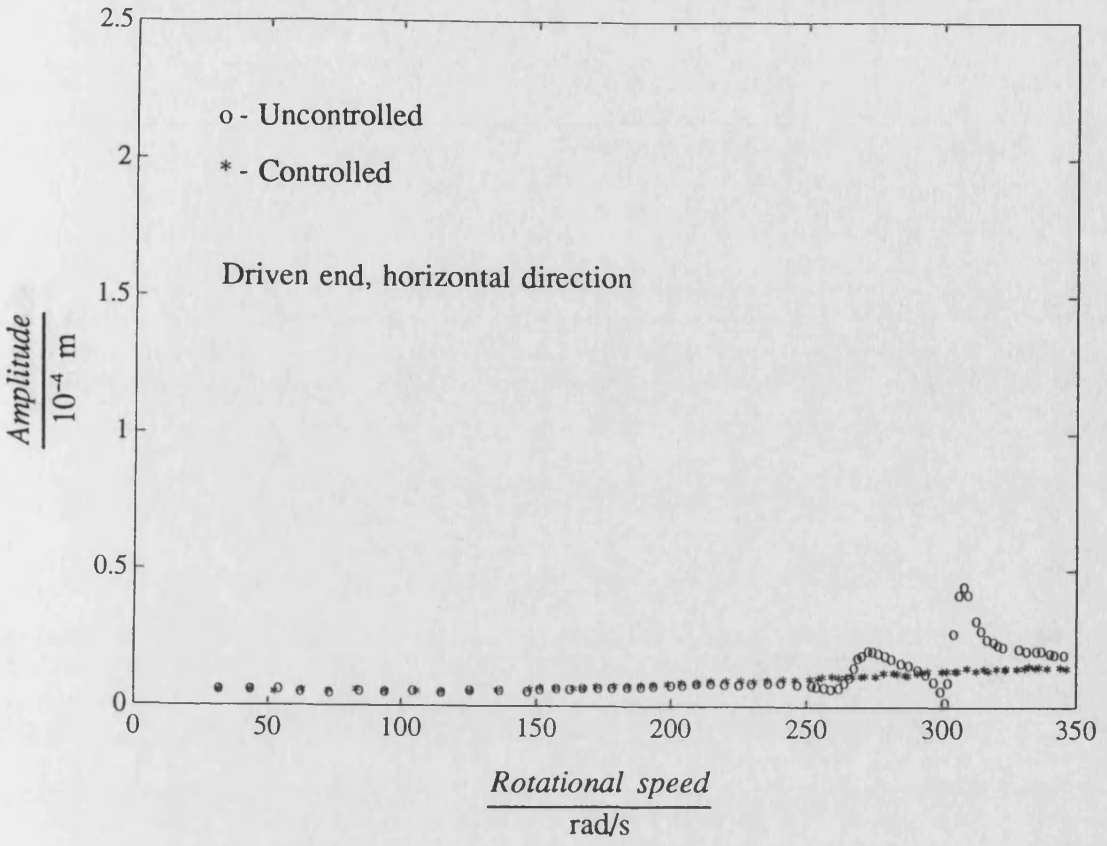

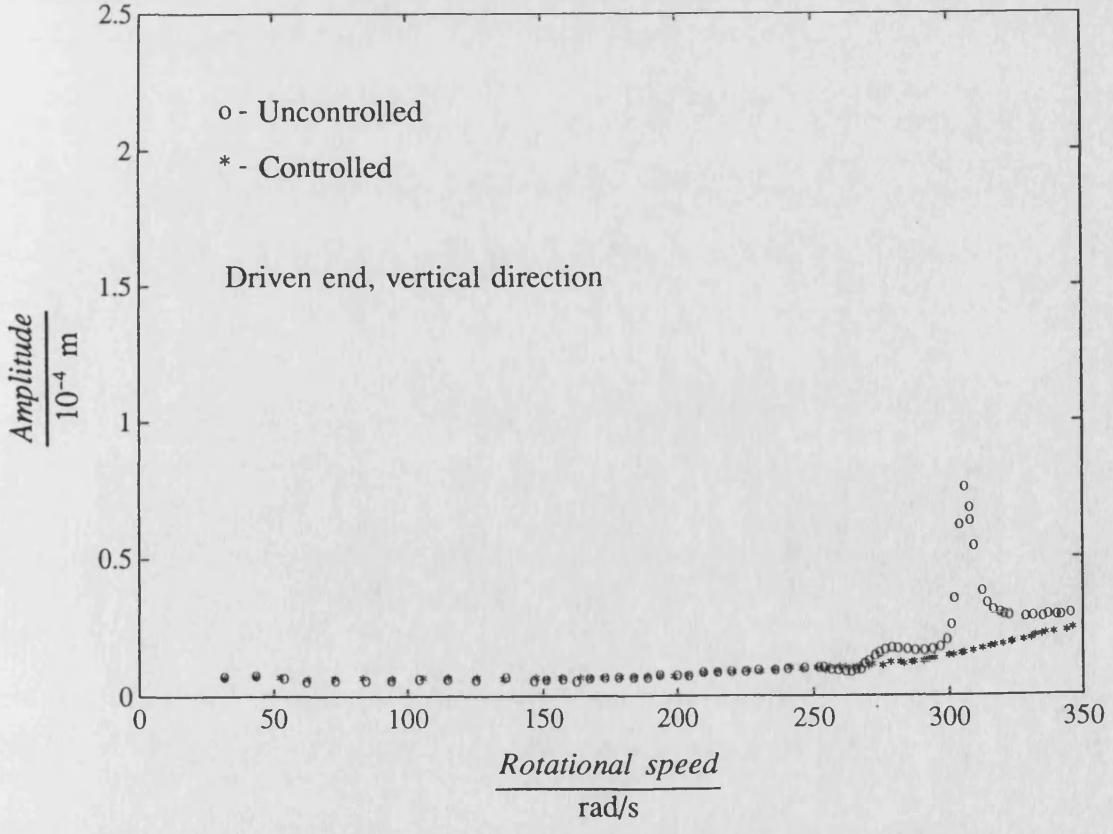

Fig. 7.6 Two speed H_∞ controlled measured synchronous responses with design based on inaccurate model

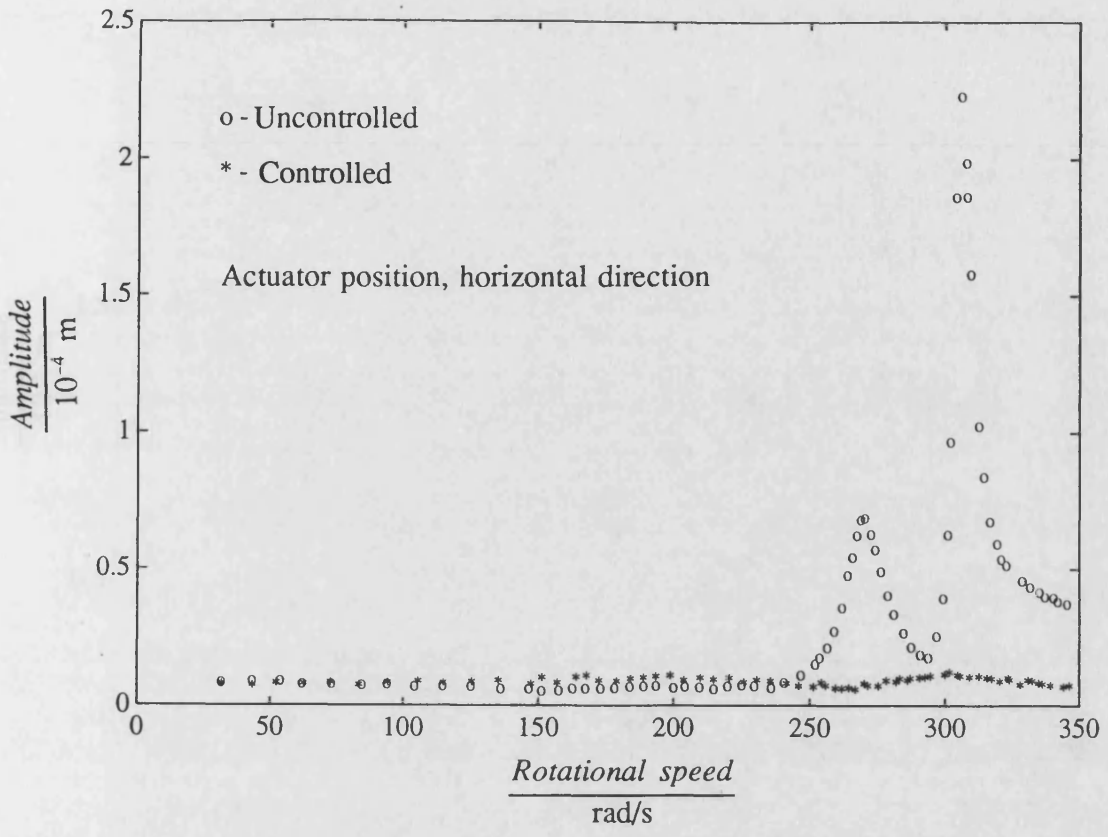

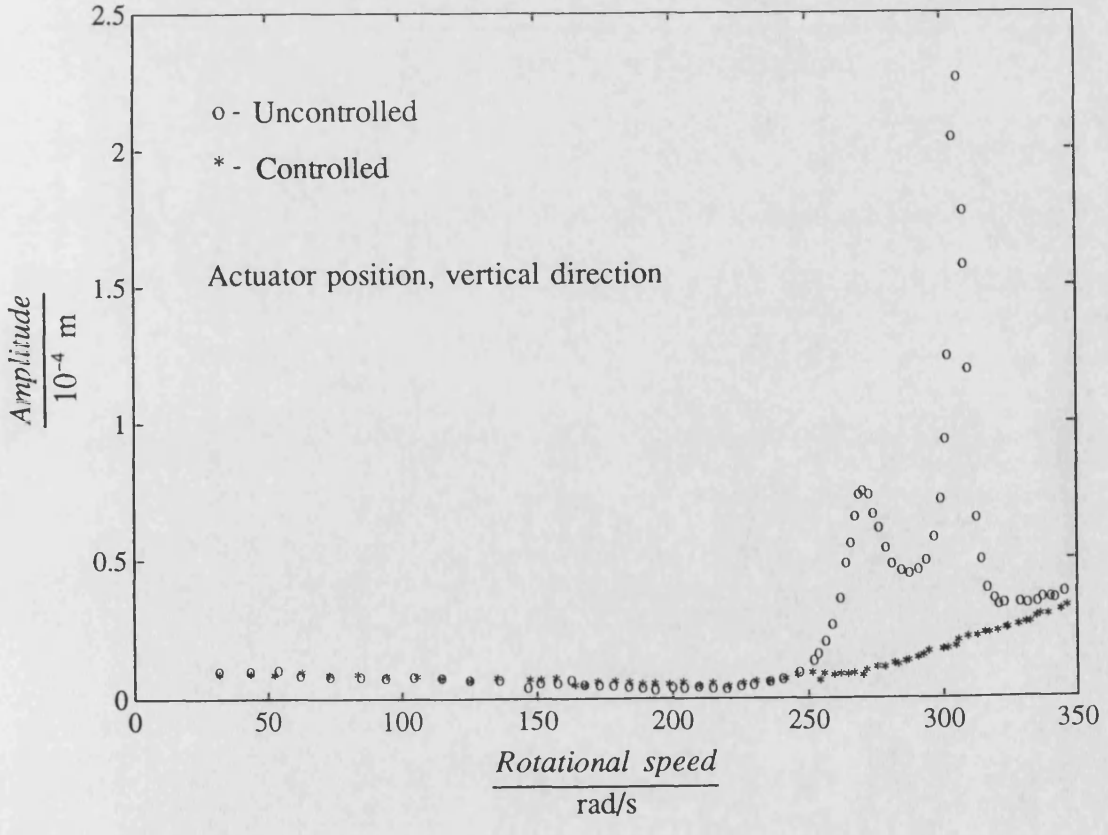

Fig. 7.6 (continued)

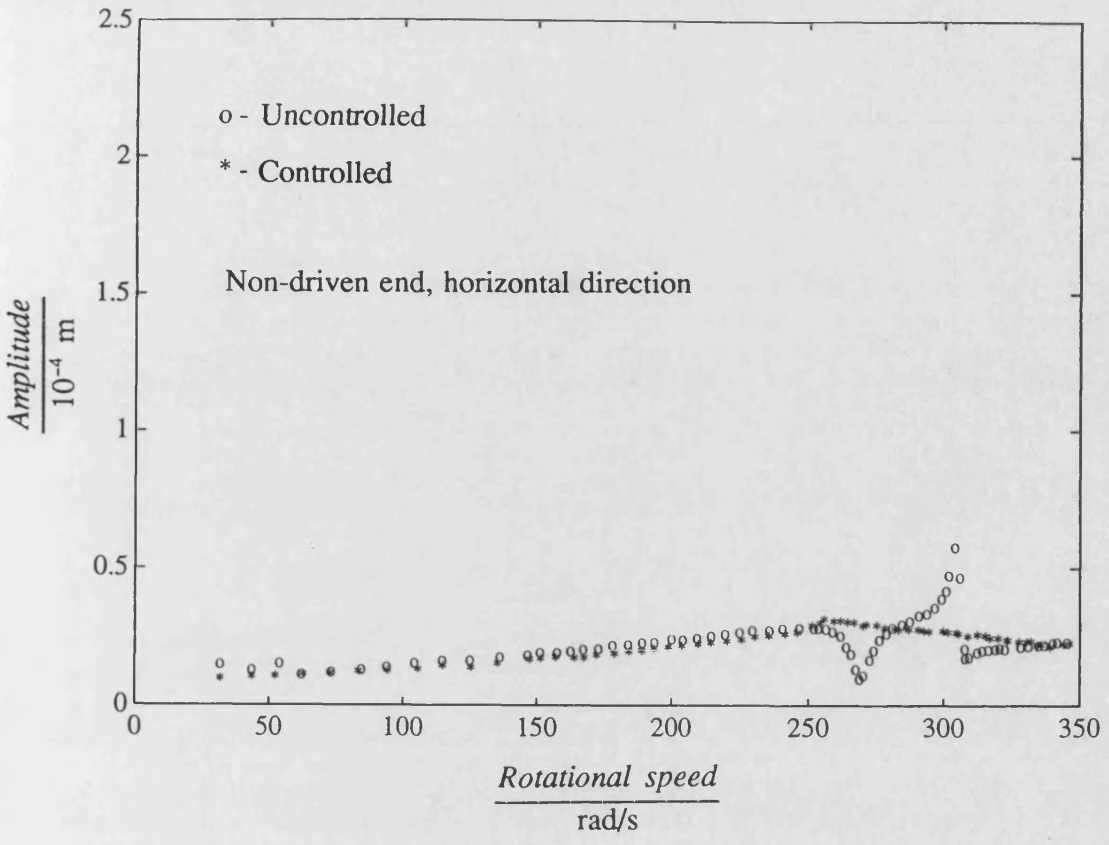

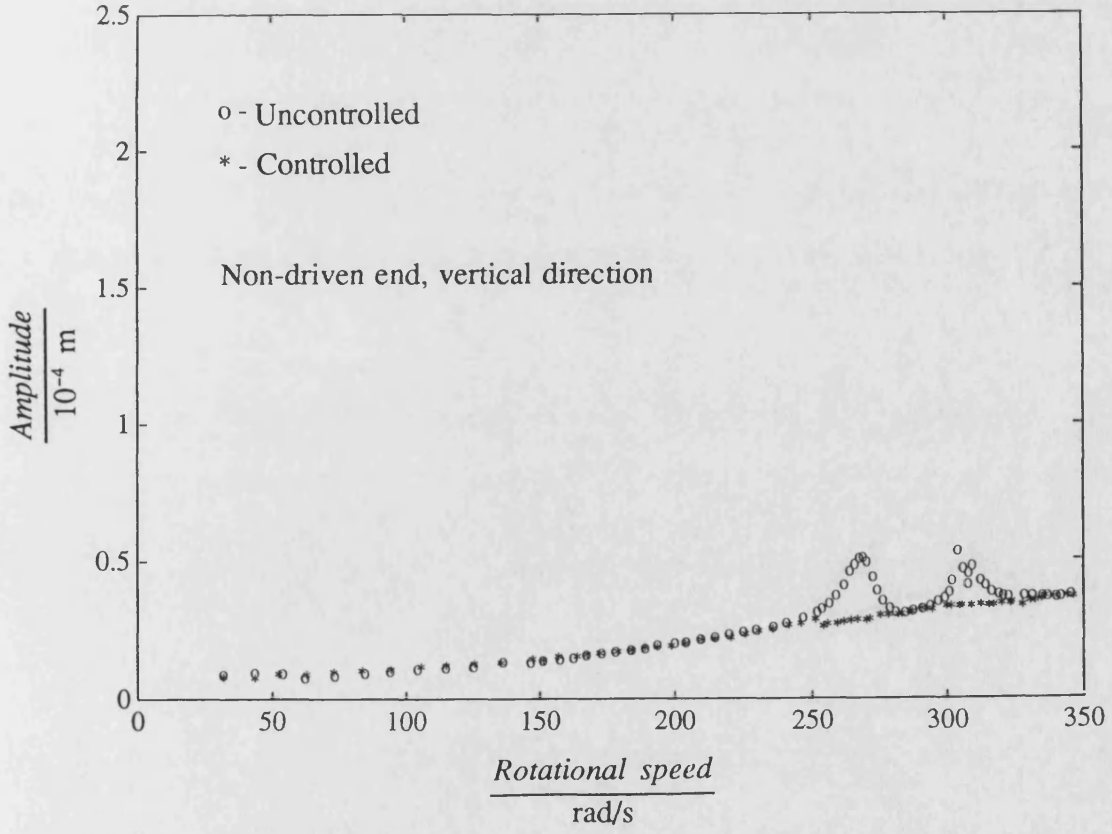

Fig. 7.6 (continued)

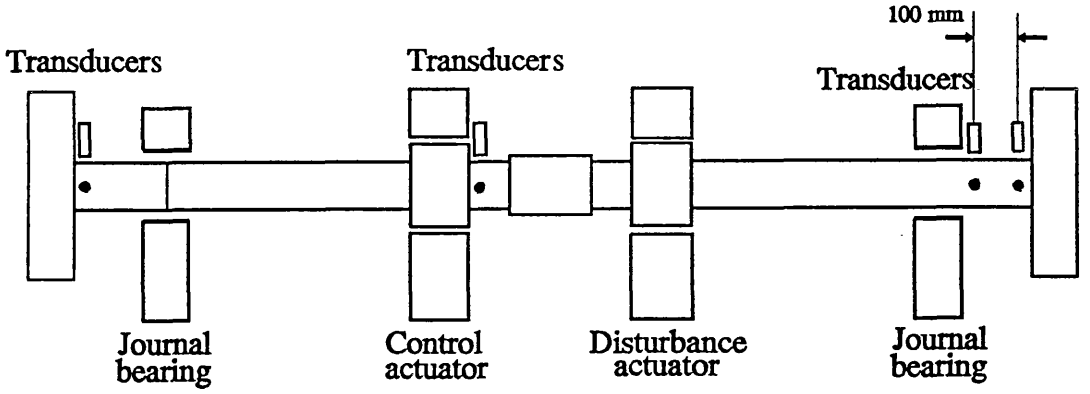

Fig. 7.7 Rotor with non-driven end transducers moved

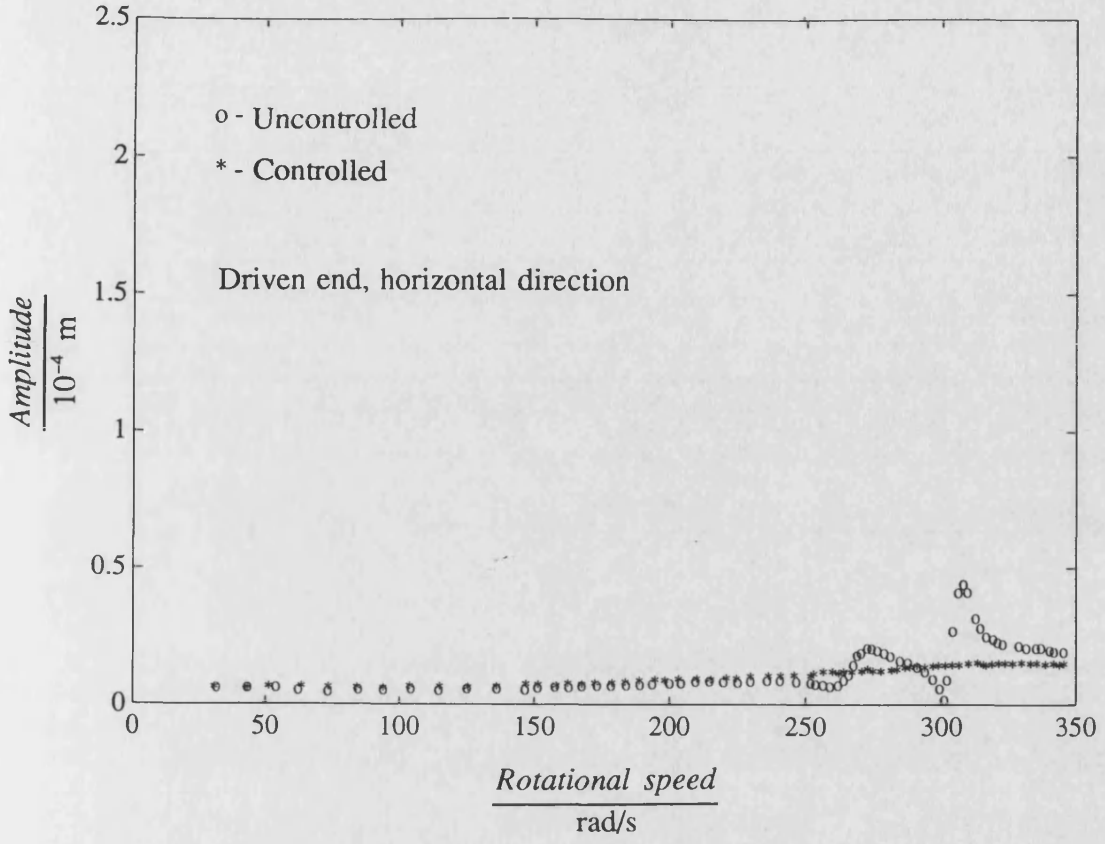

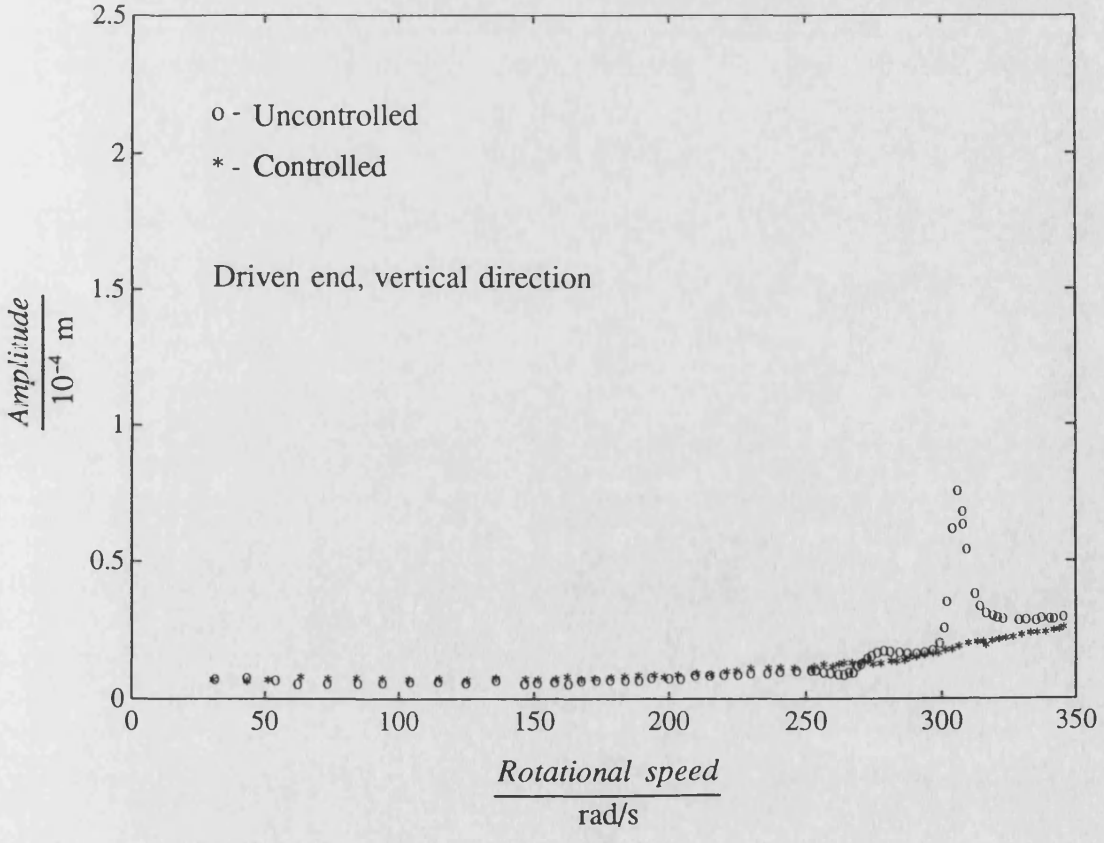

Fig. 7.8 Two speed H_∞ controlled measured synchronous responses with non-driven end transducers moved as in figure 7.7

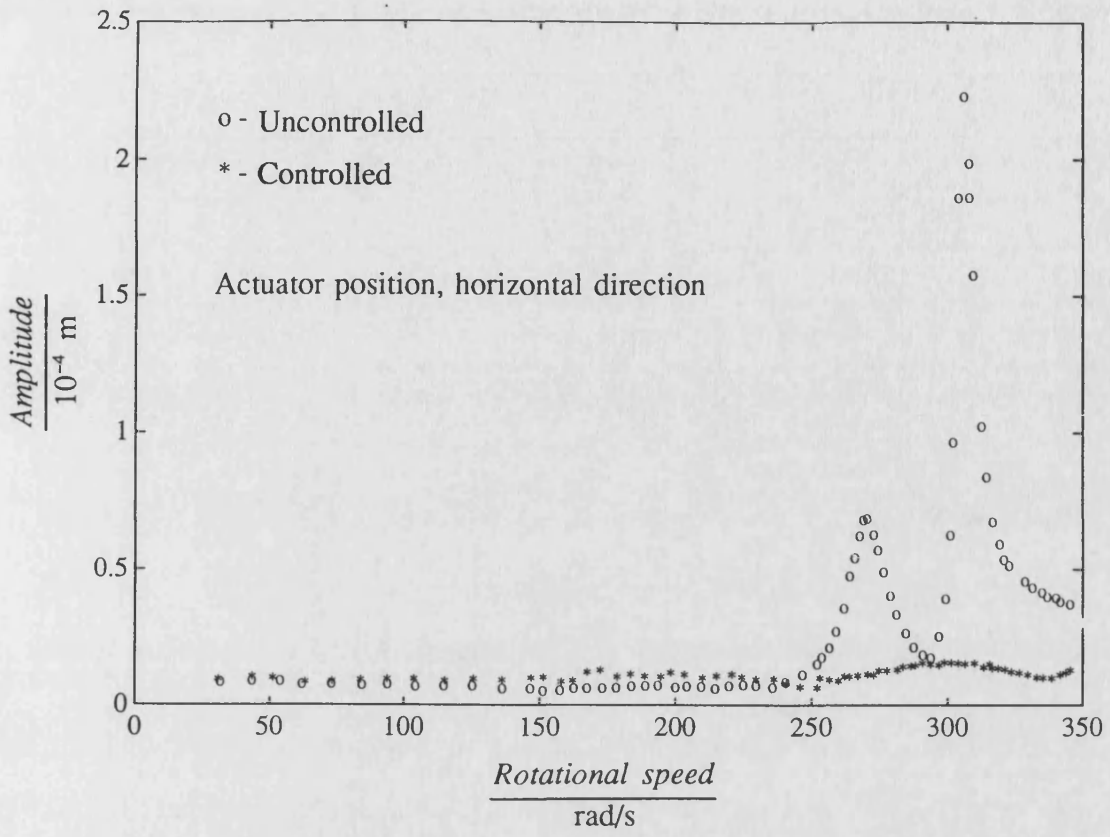

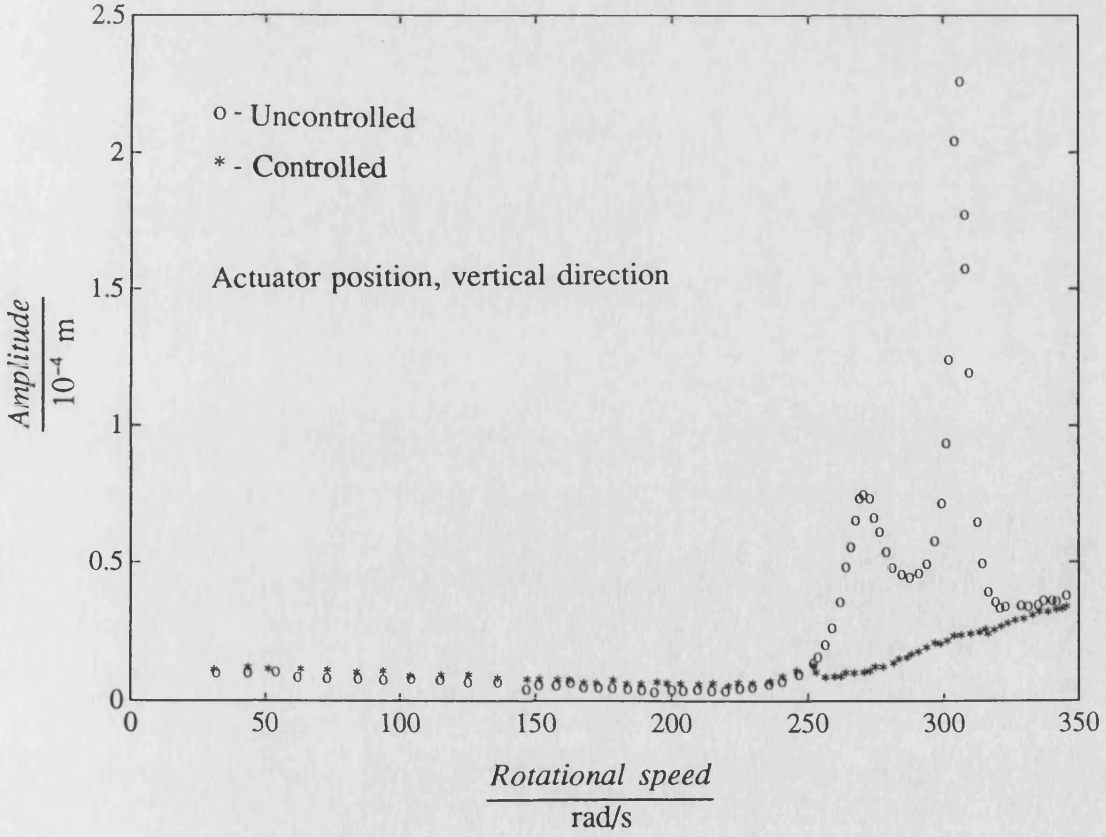

Fig. 7.8 (continued)

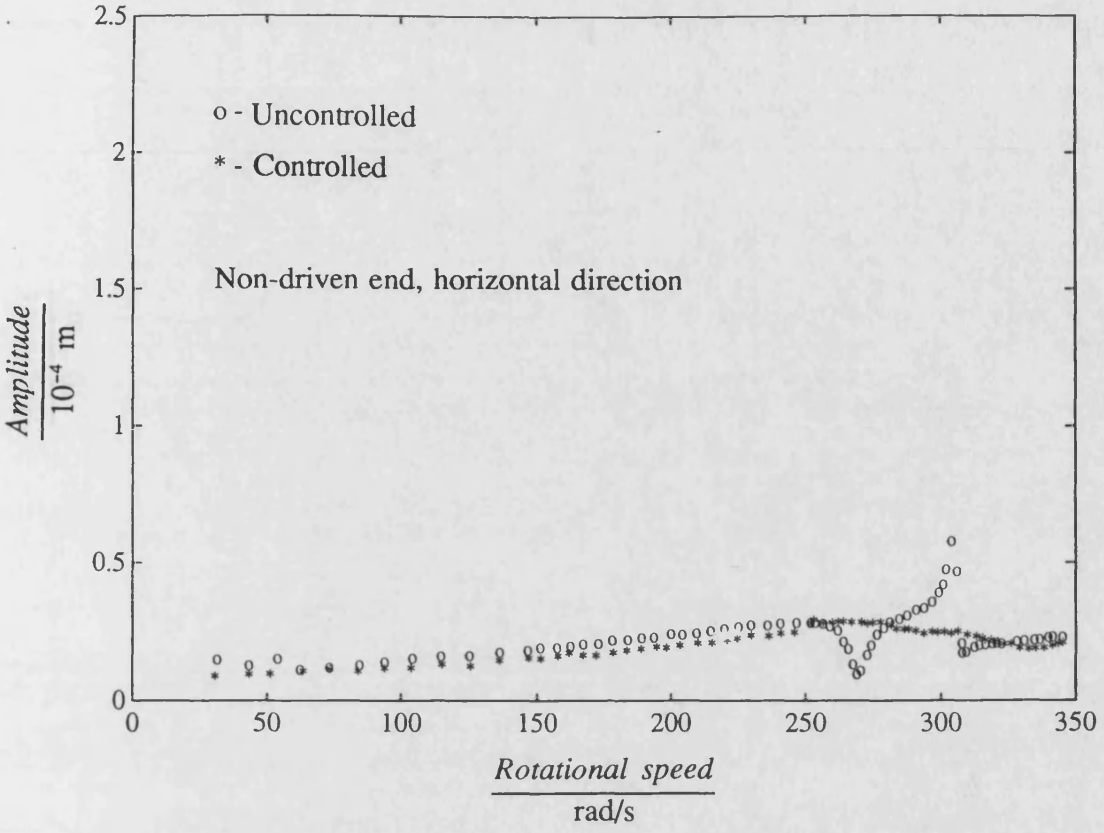

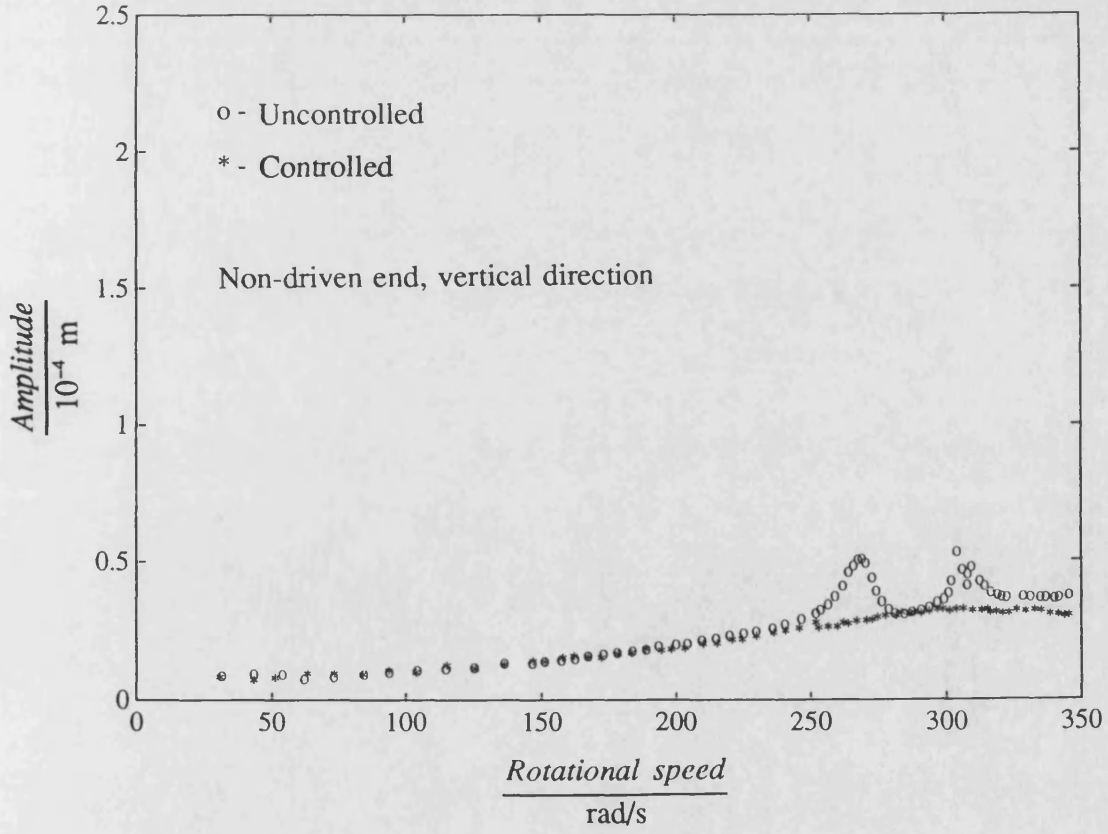

Fig. 7.8 (continued)

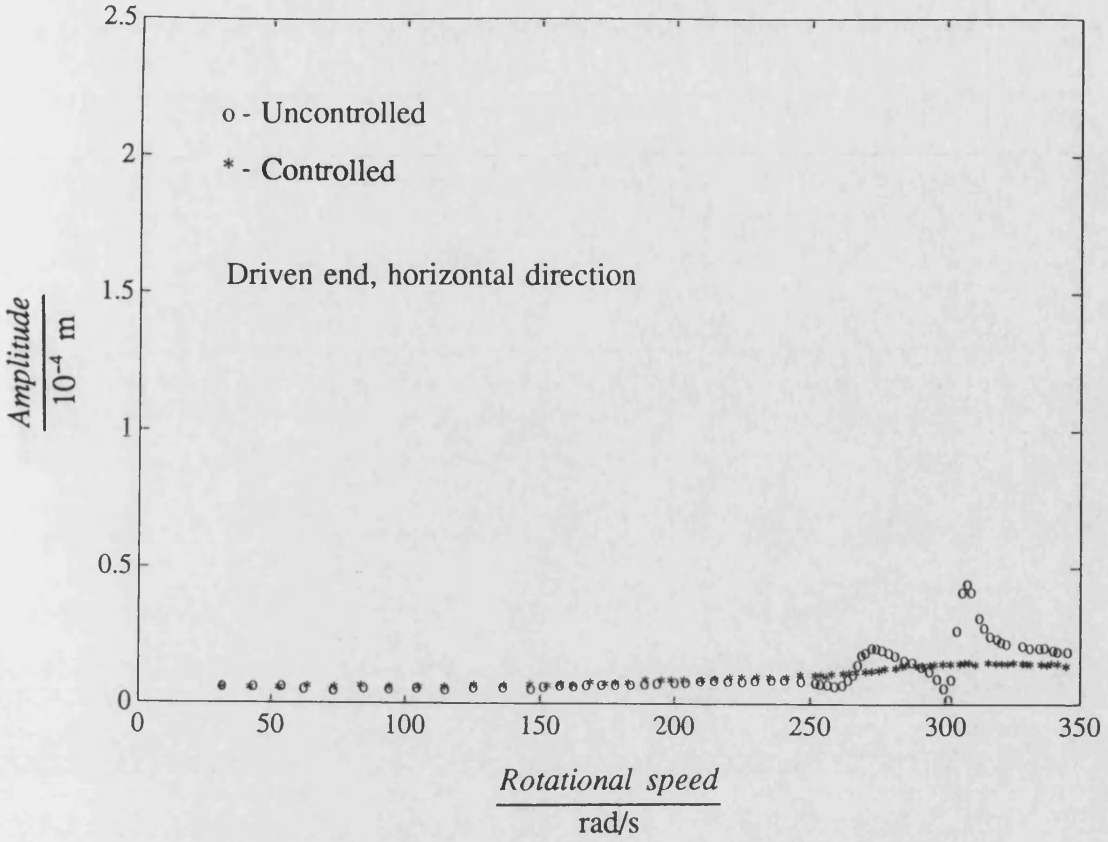

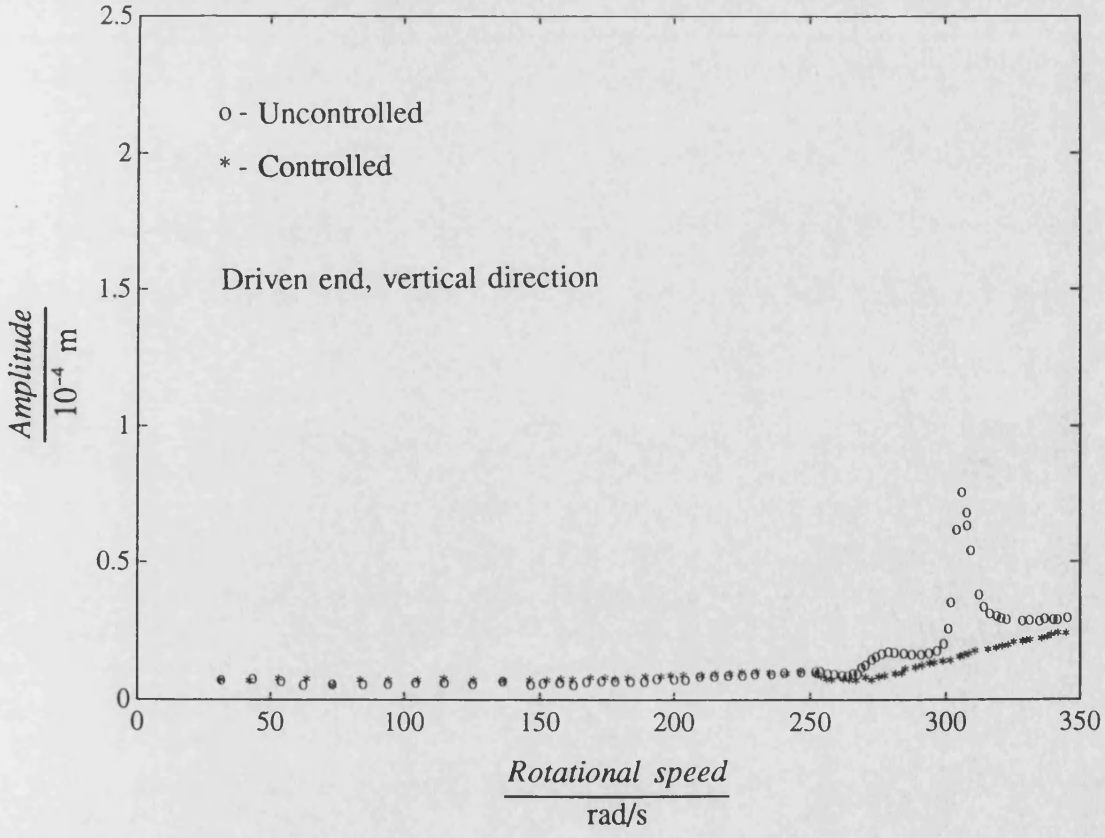

Fig. 7.9 Two speed H_∞ controlled measured synchronous responses with non-driven end horizontal transducer removed

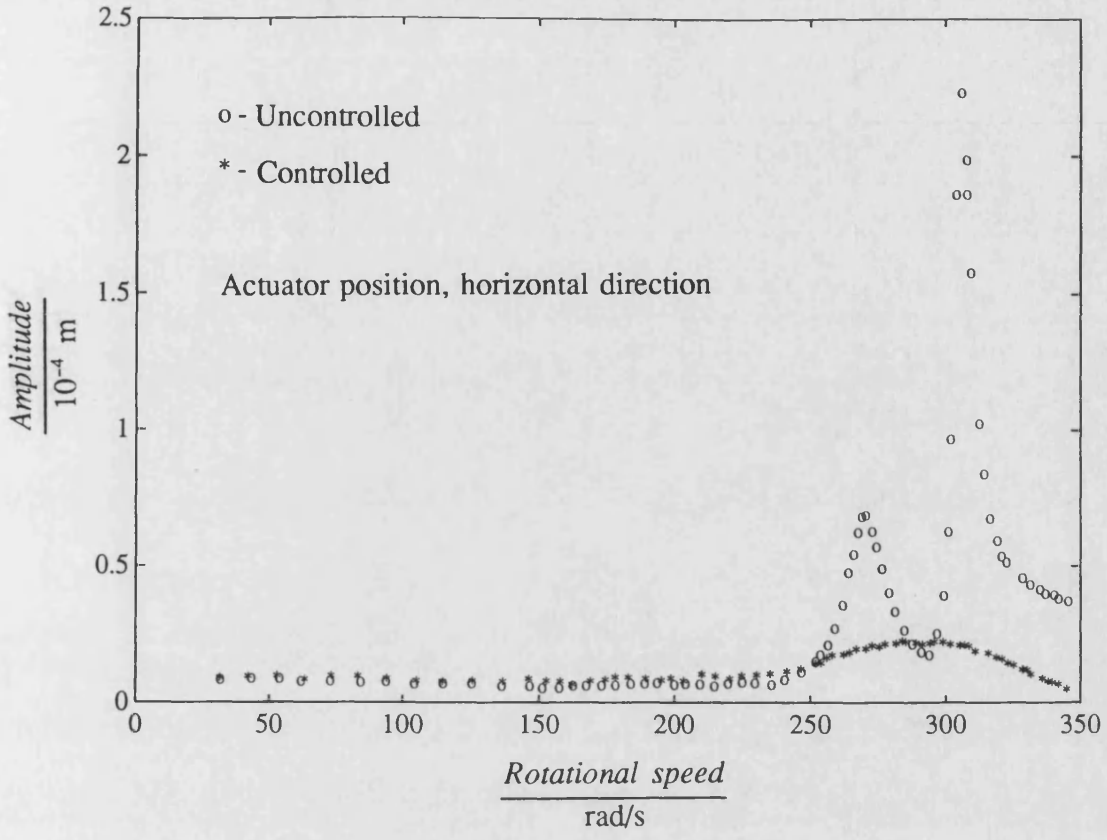

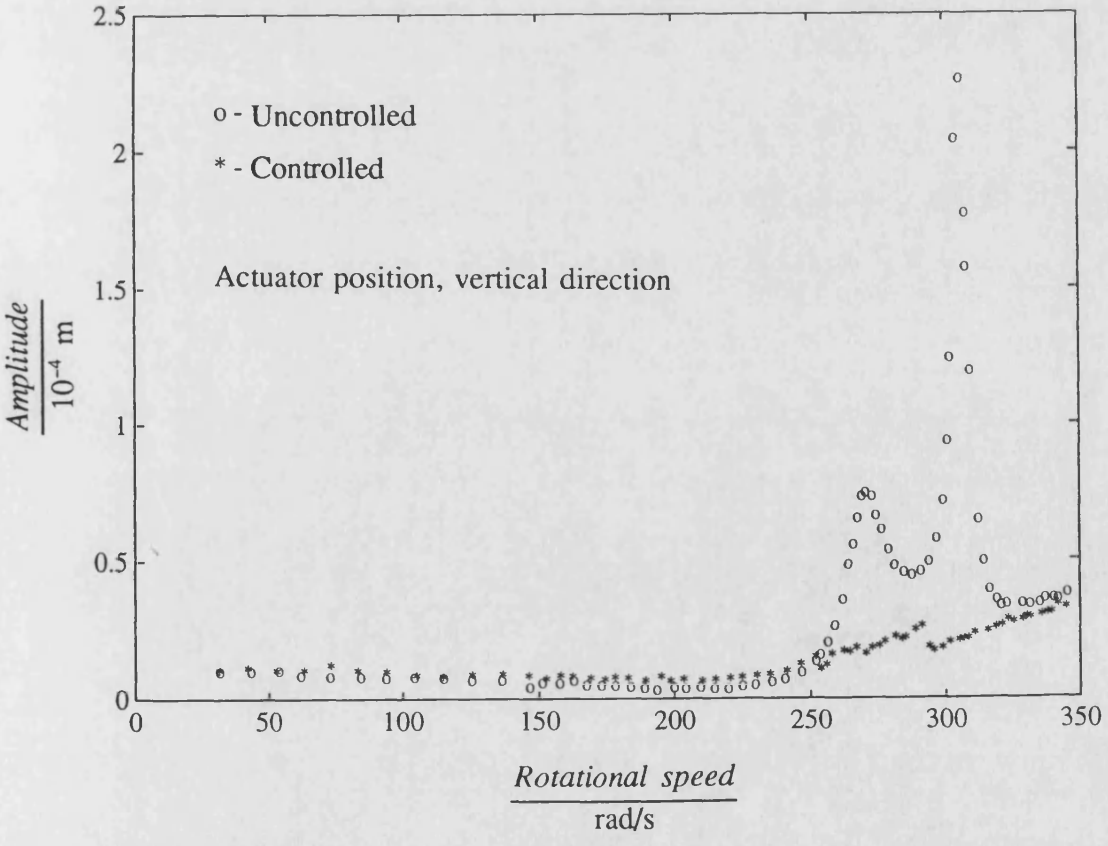

Fig. 7.9 (continued)

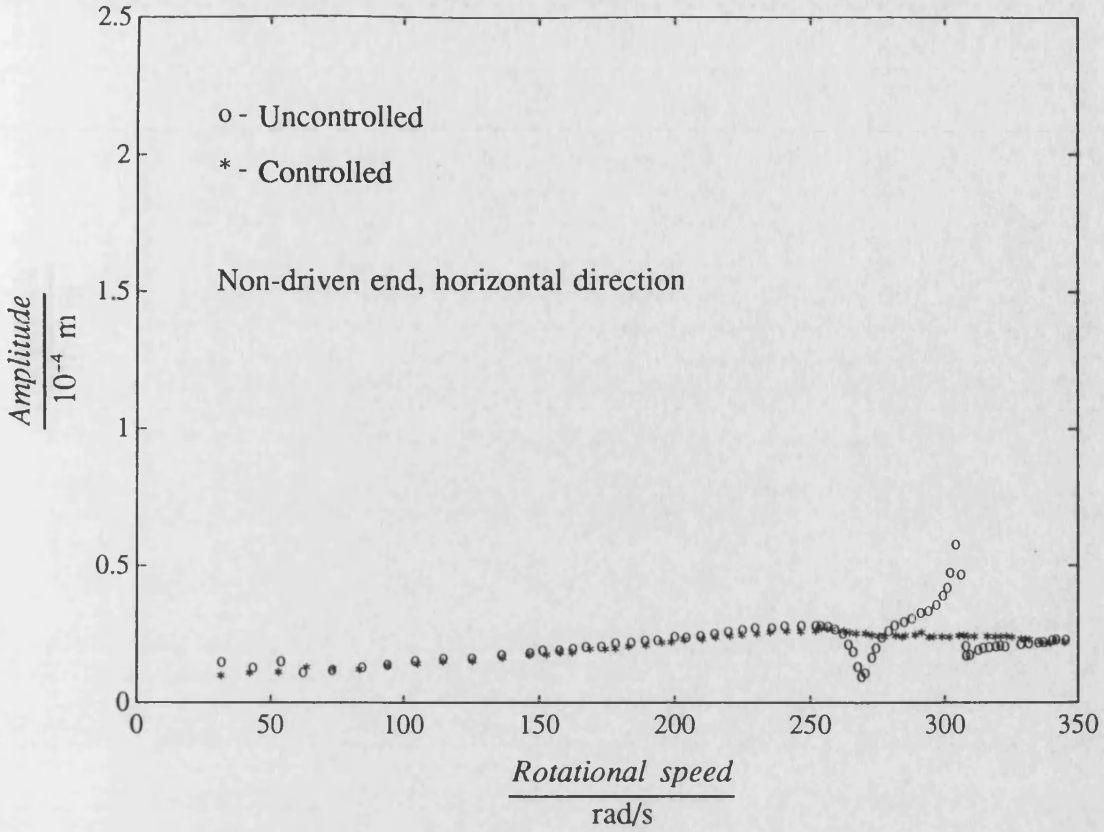

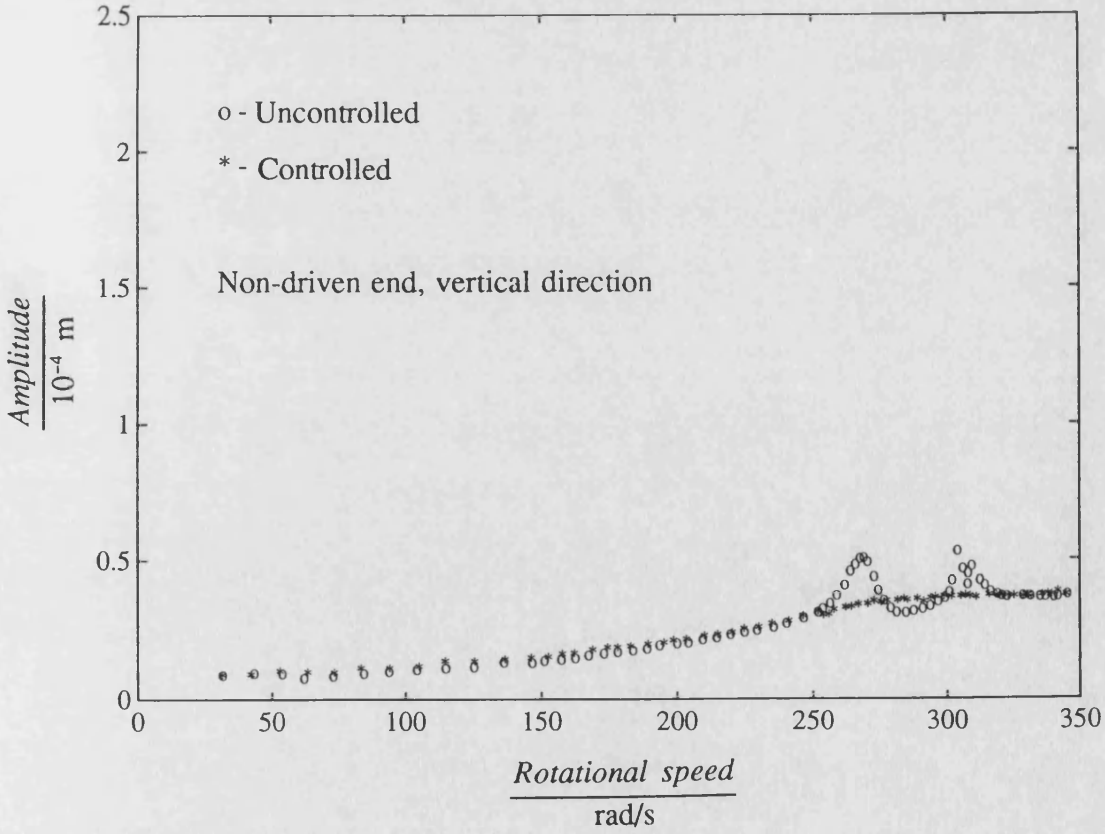

Fig. 7.9 (continued)

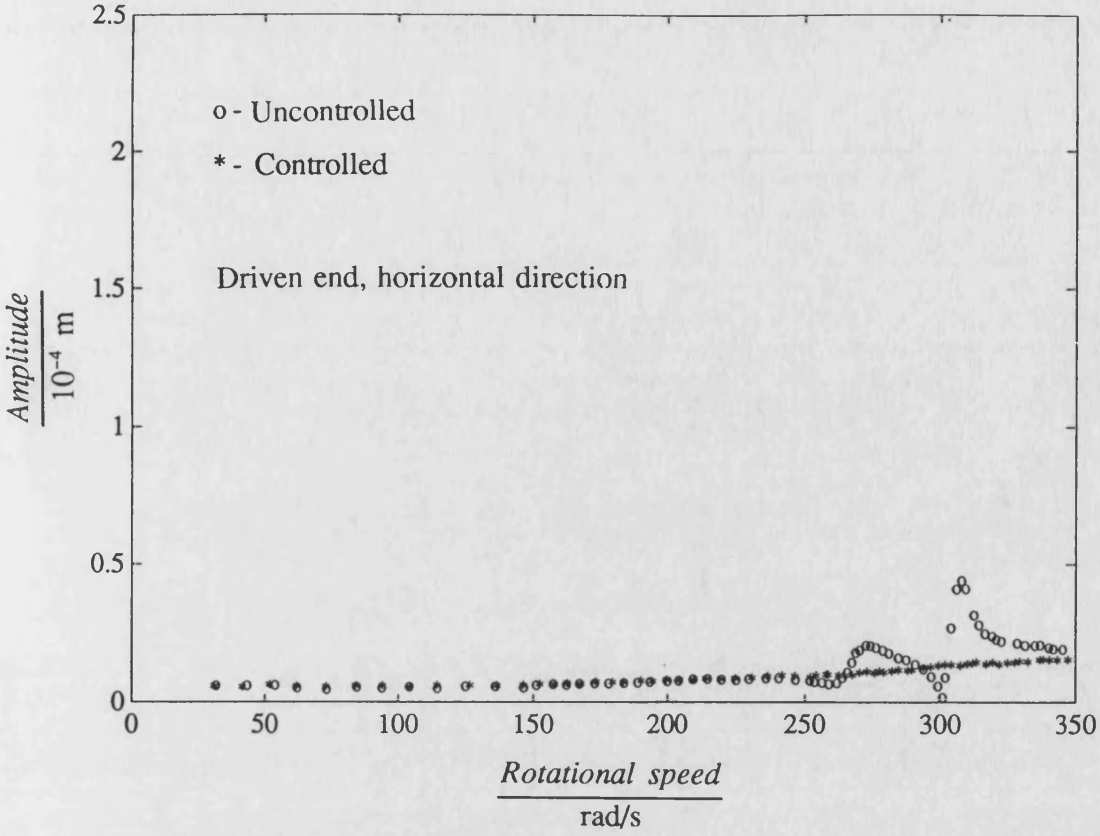

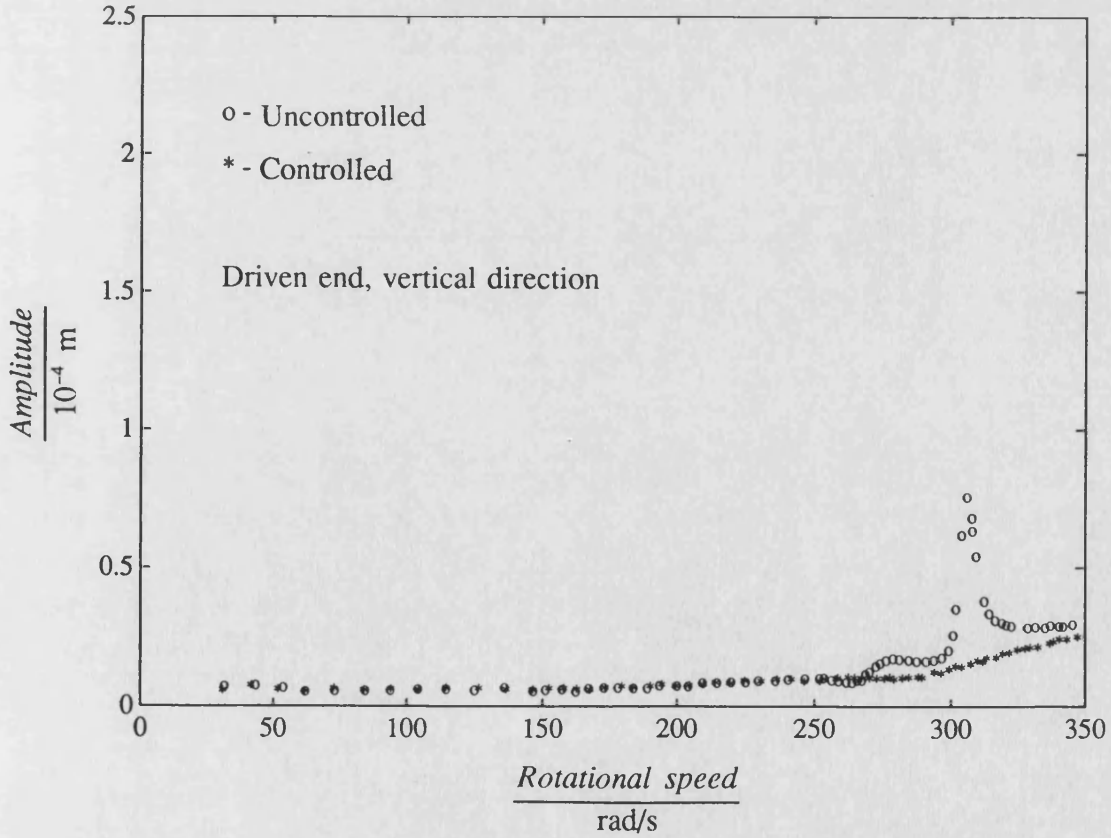

Fig. 7.10 Two speed H_∞ controlled measured synchronous responses with non-driven end pair of transducers removed

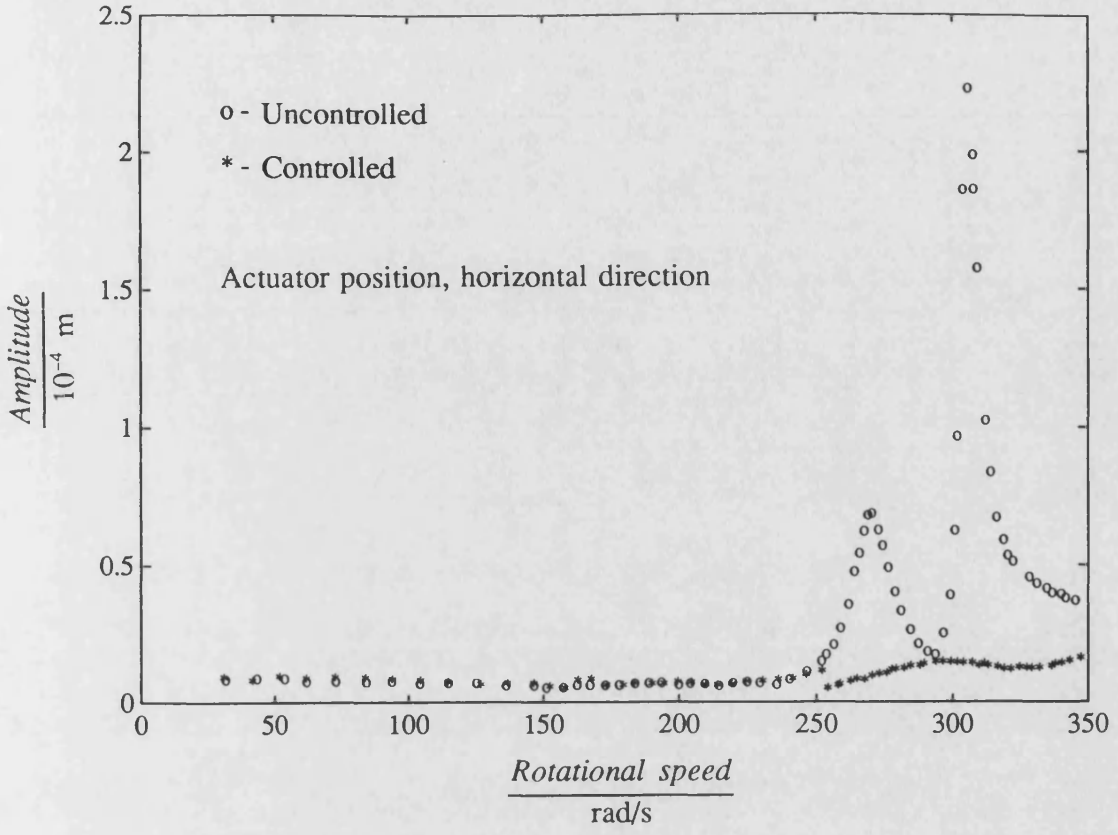

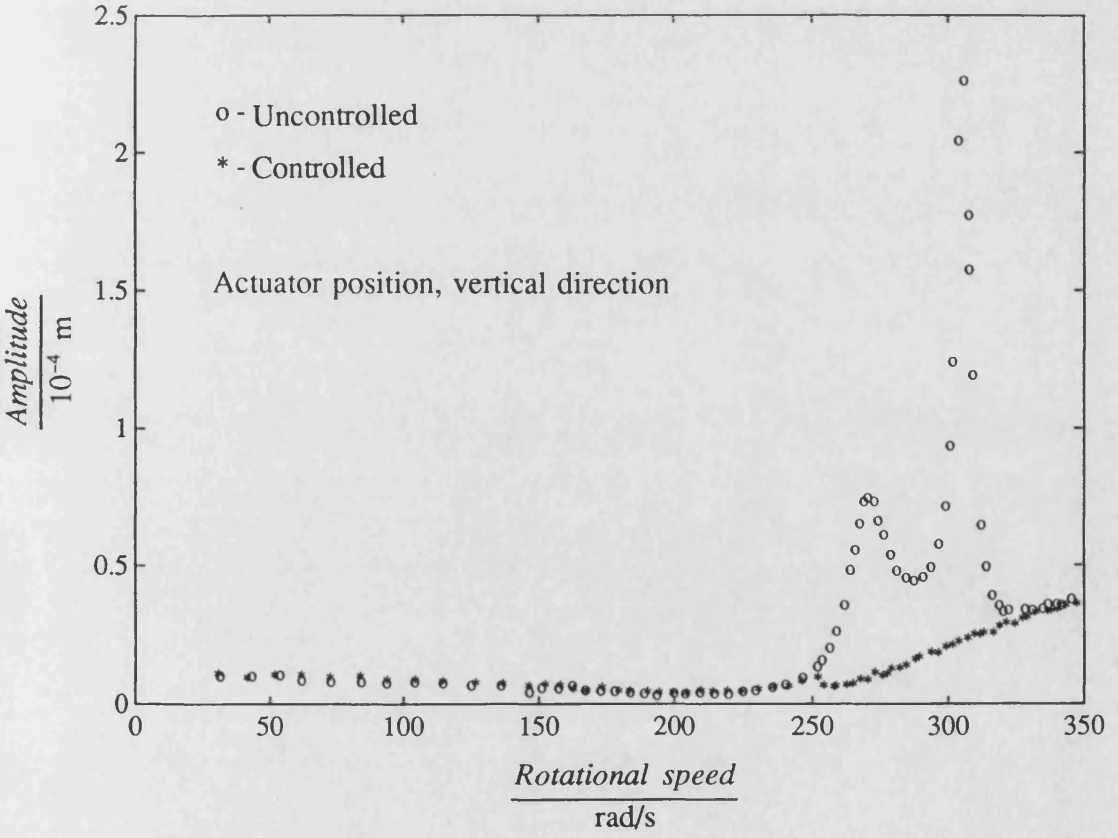

Fig. 7.10 (continued)

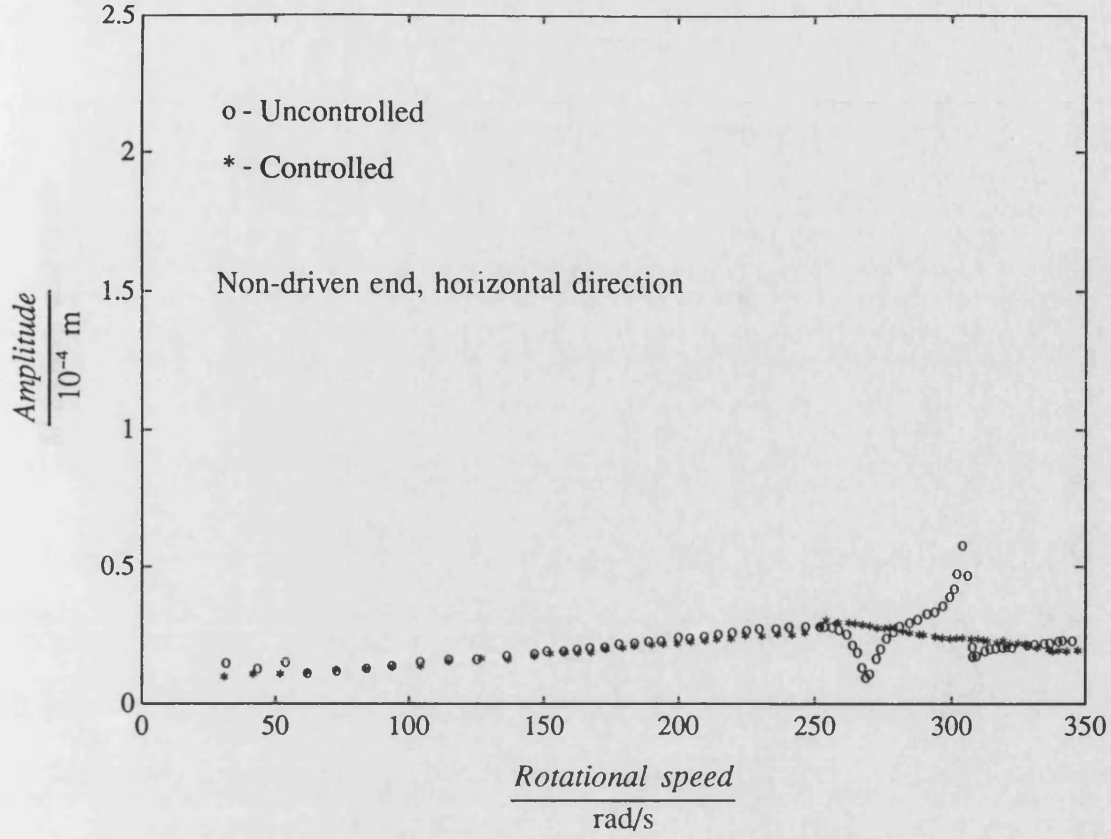

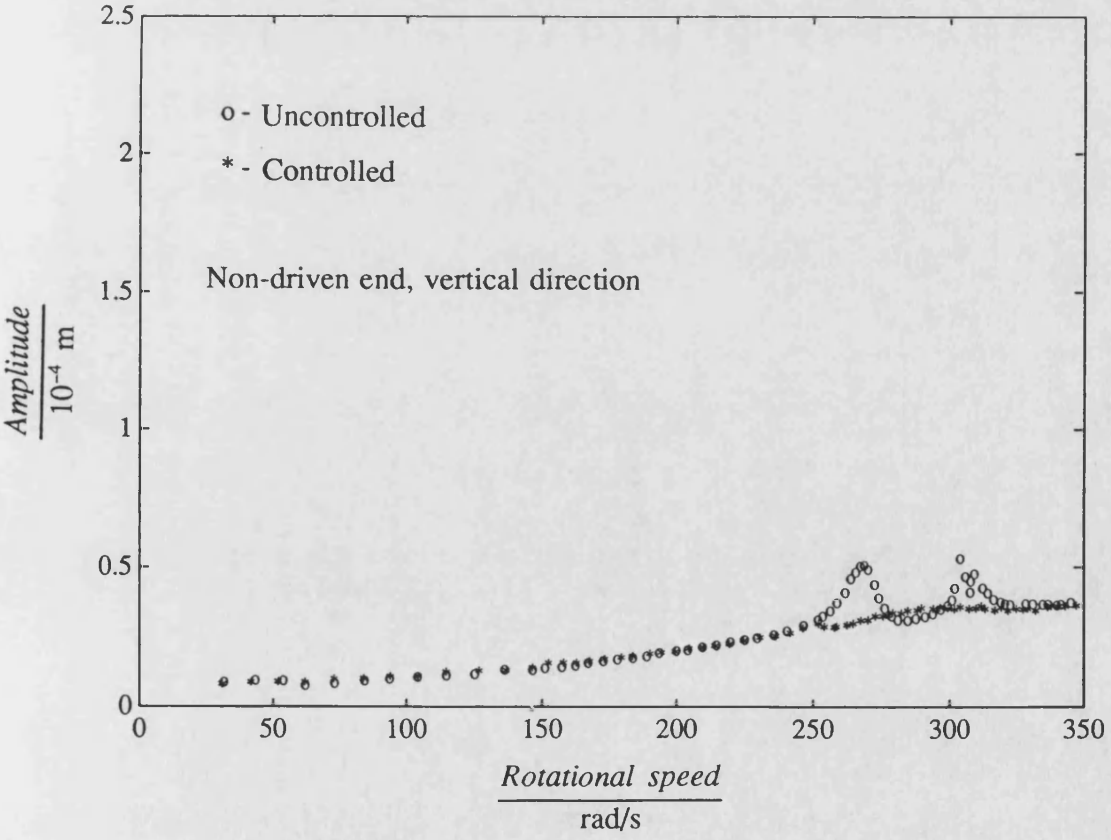

Fig. 7.10 (continued)

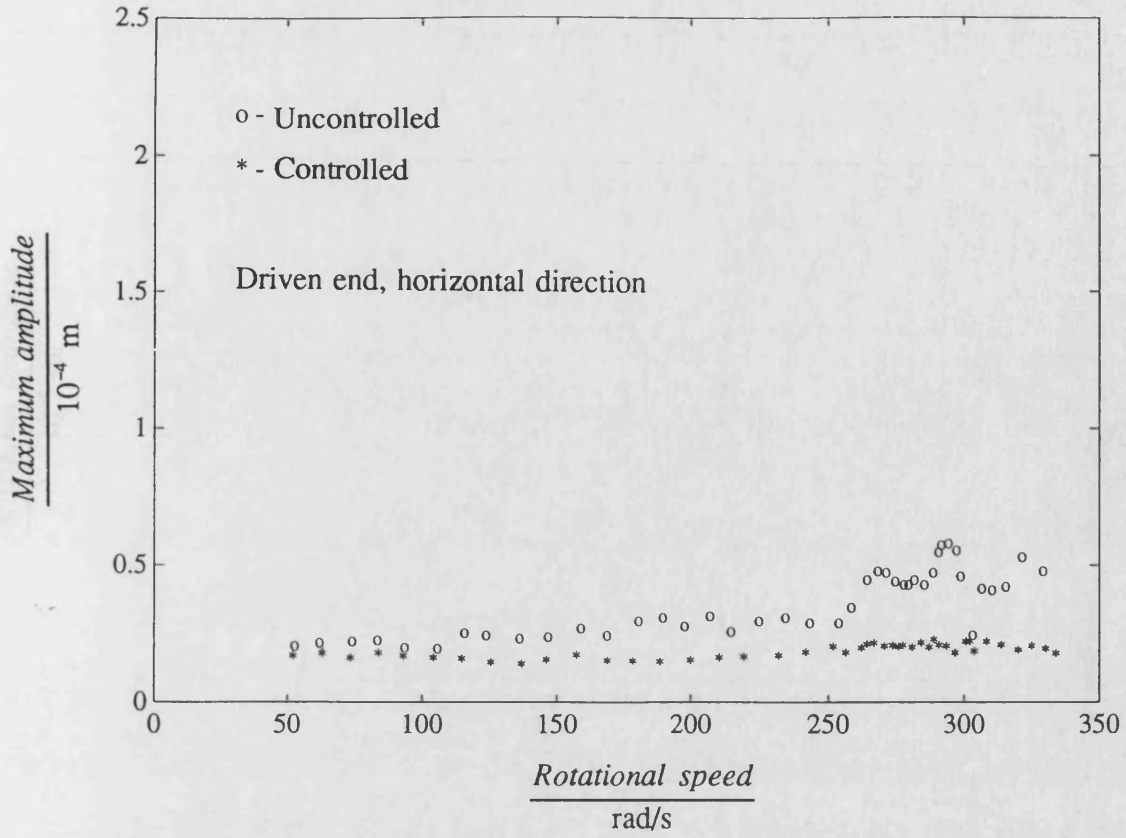

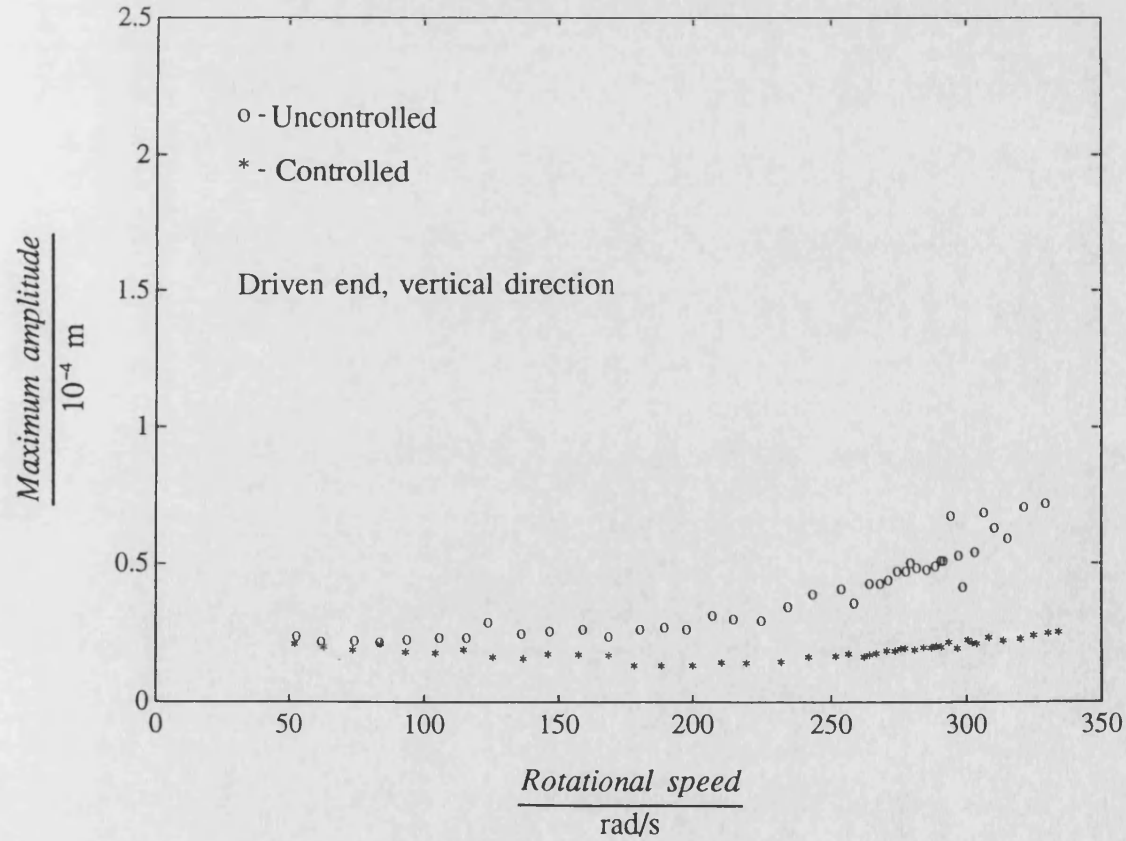

Fig. 7.11 Comparison of uncontrolled and two speed H_∞ controlled measured non-synchronous responses with 302 rad/s disturbance force in horizontal direction

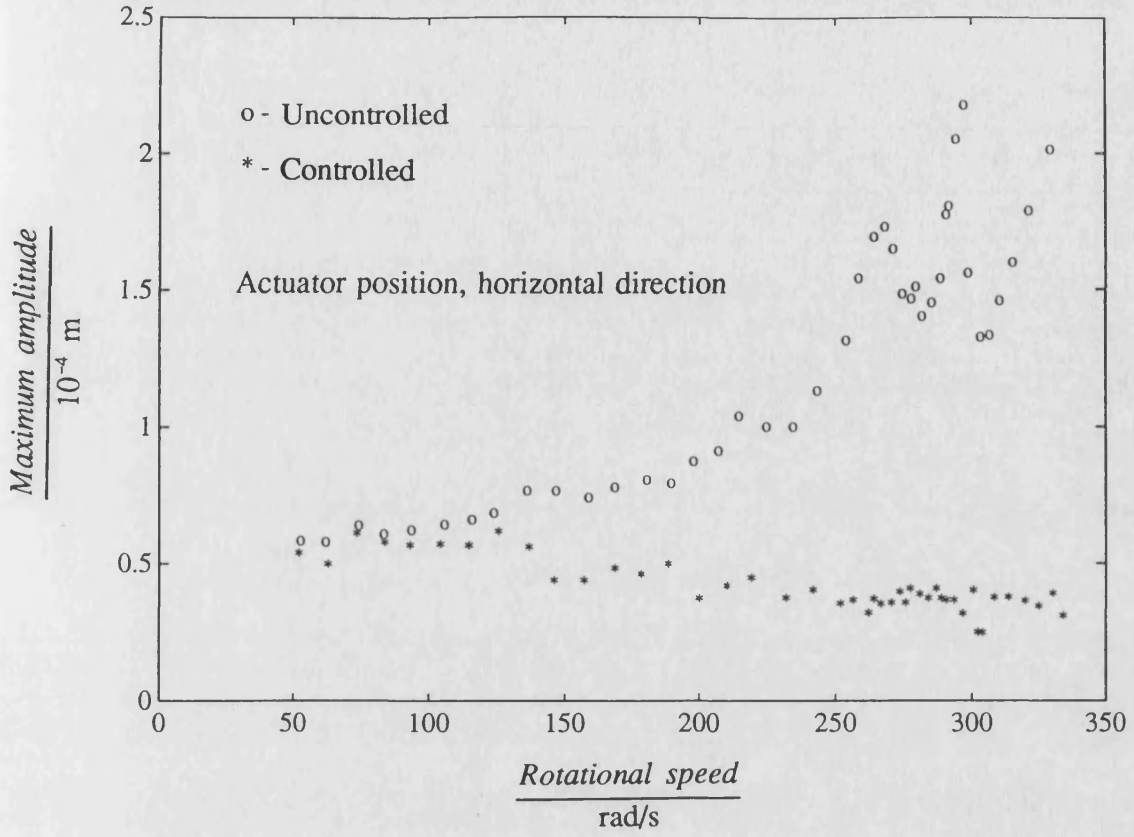

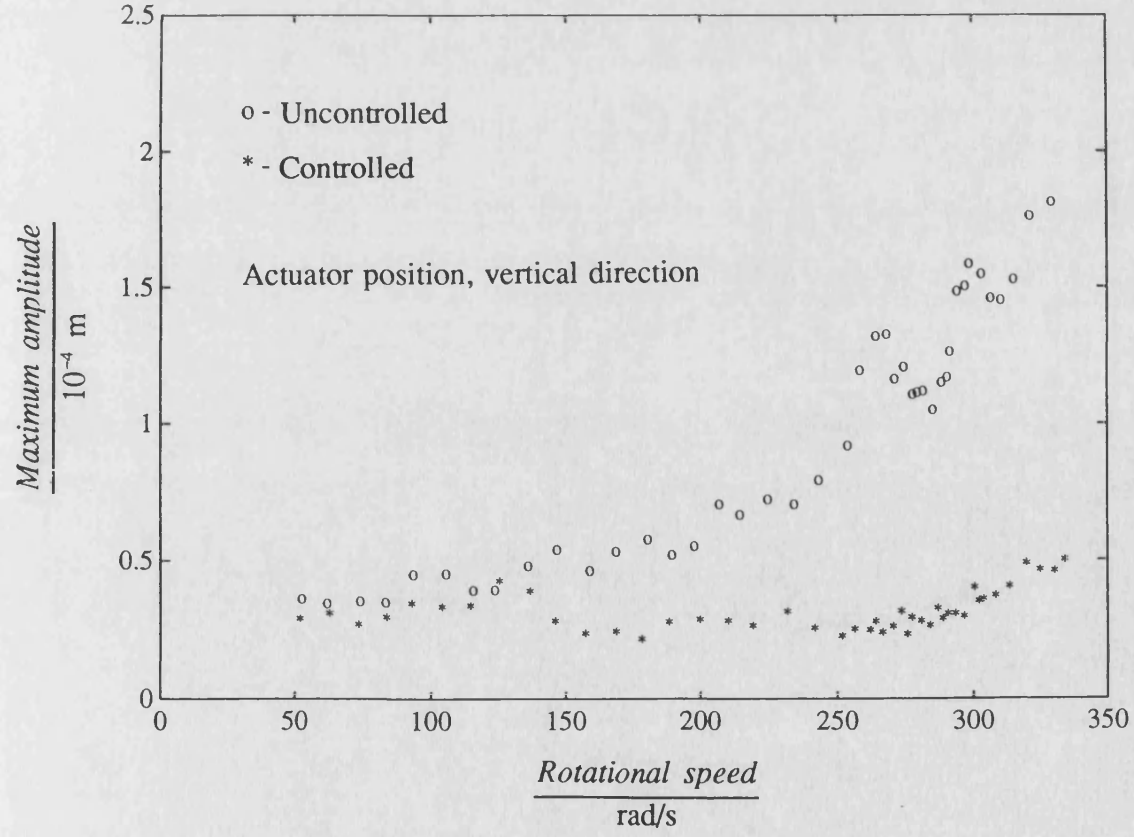

Fig. 7.11 (continued)

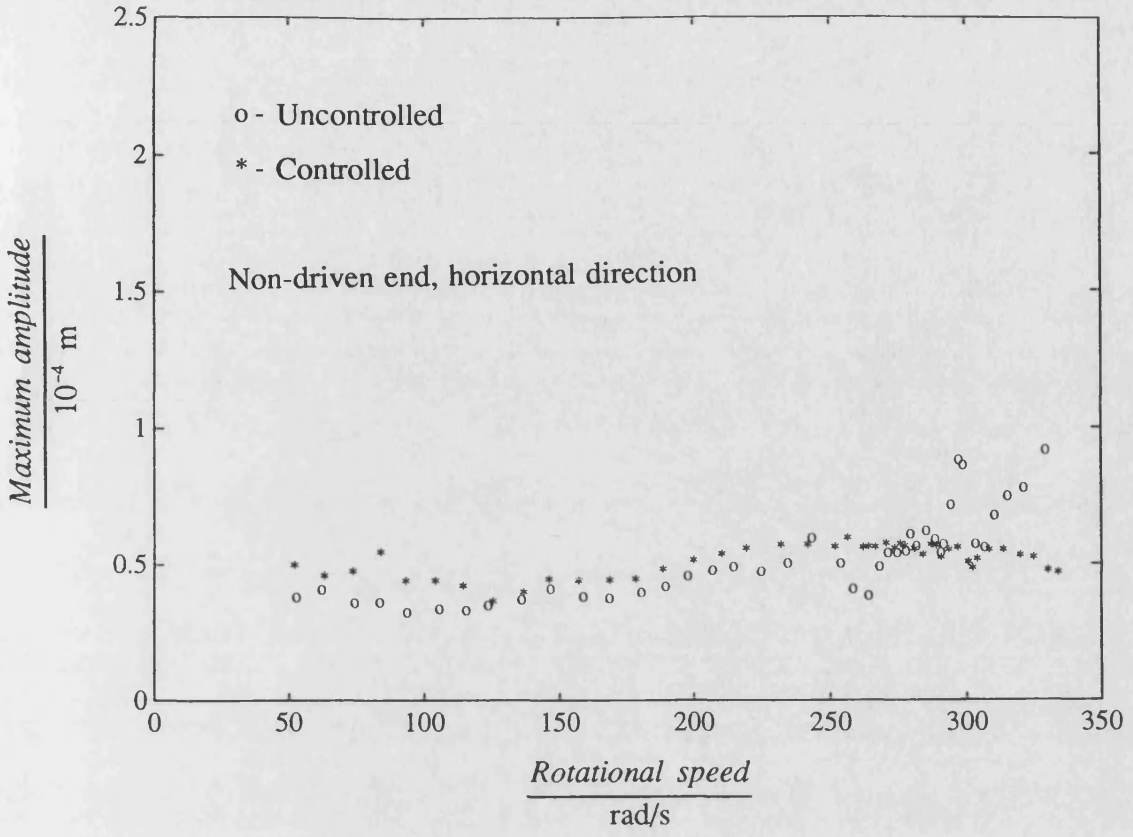

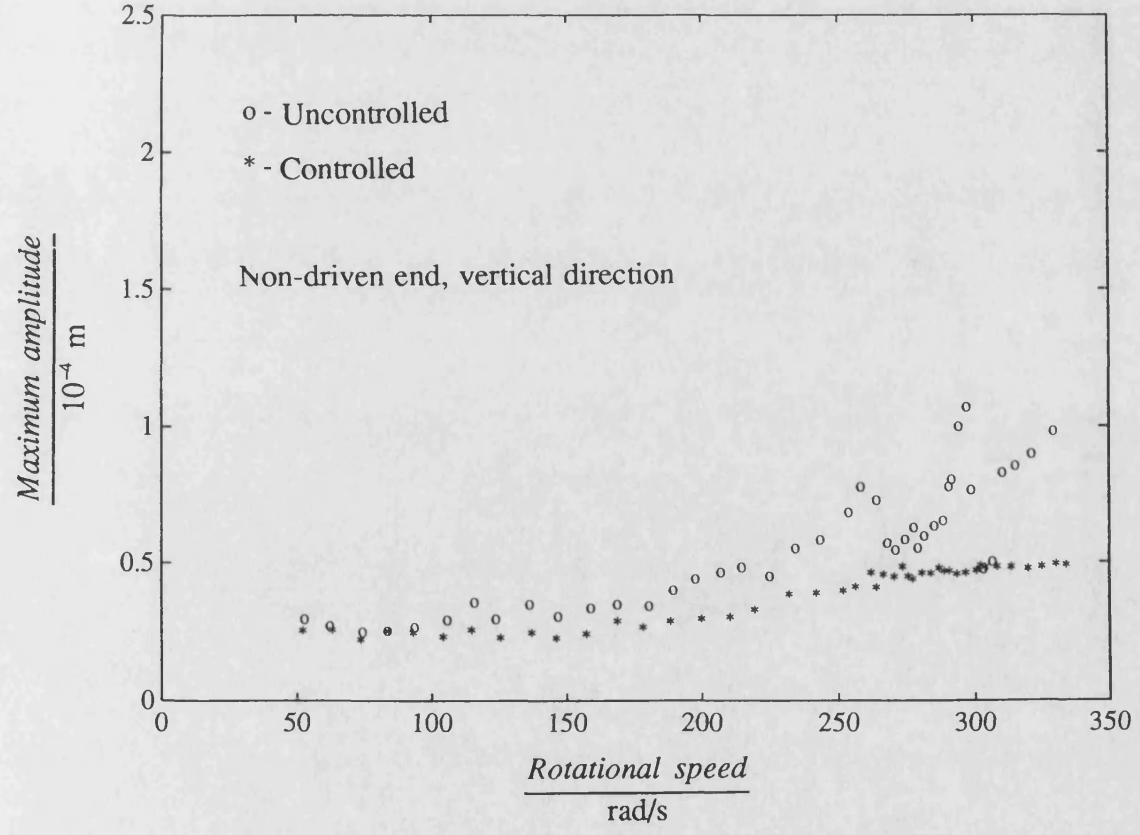

Fig. 7.11 (continued)

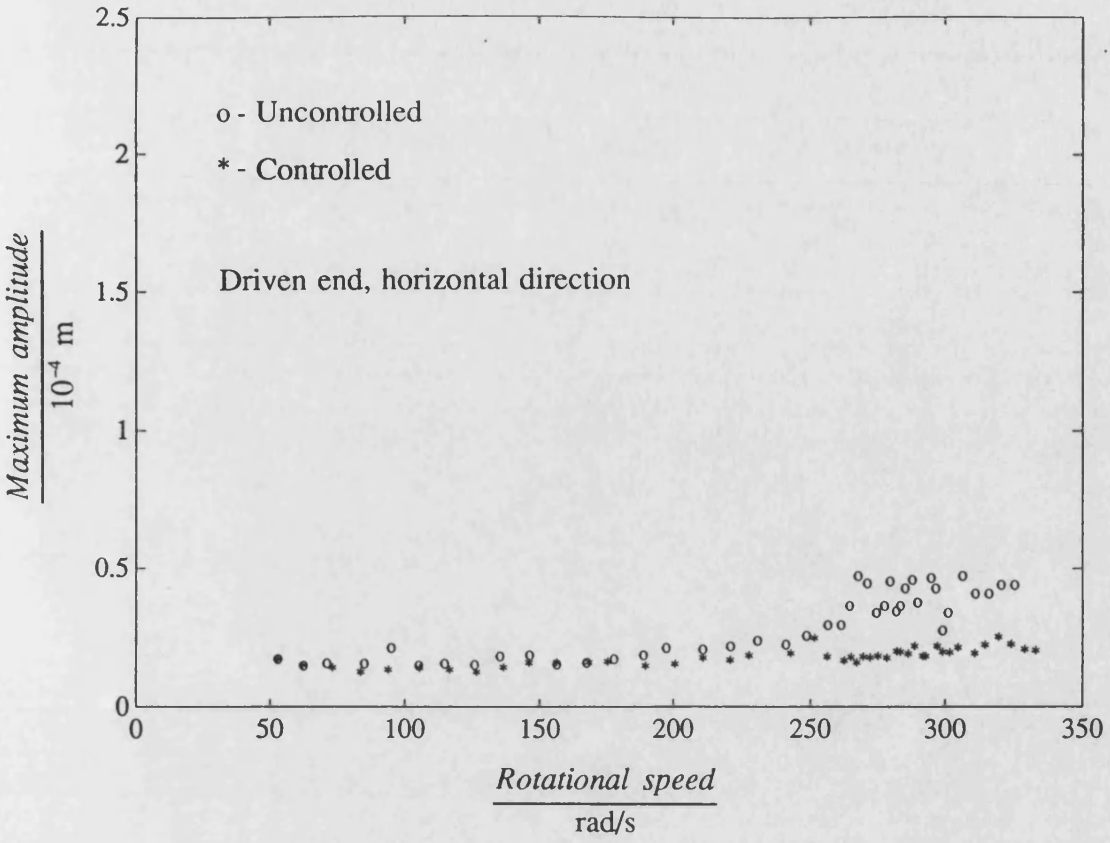

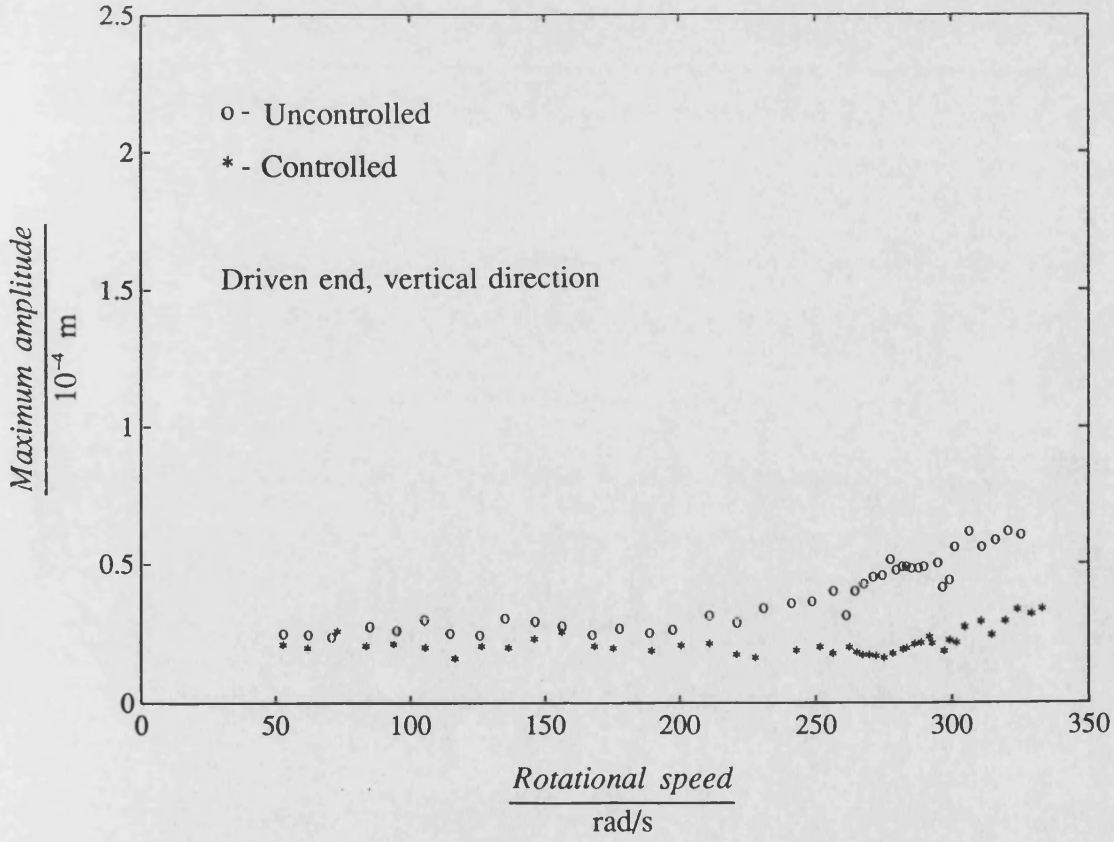

Fig. 7.12 Comparison of uncontrolled and two speed H_∞ controlled measured non-synchronous responses with 302 rad/s disturbance force in vertical direction

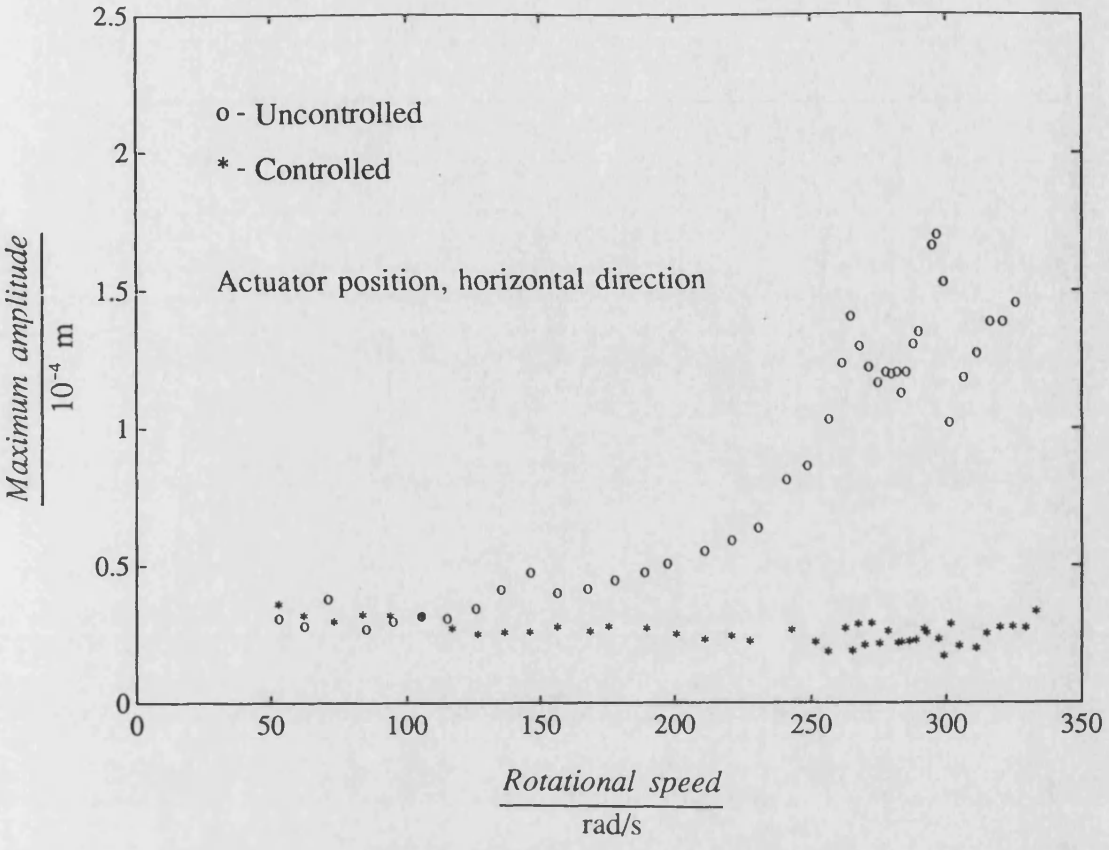

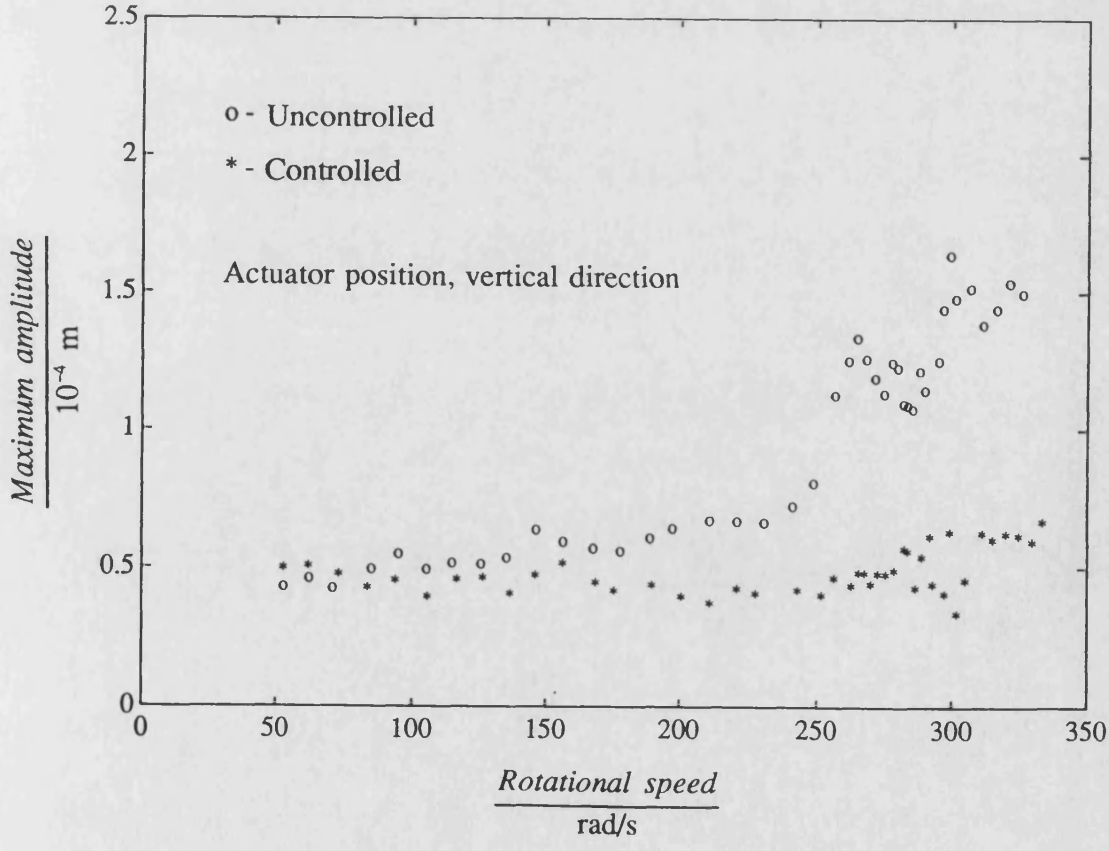

Fig. 7.12 (continued)

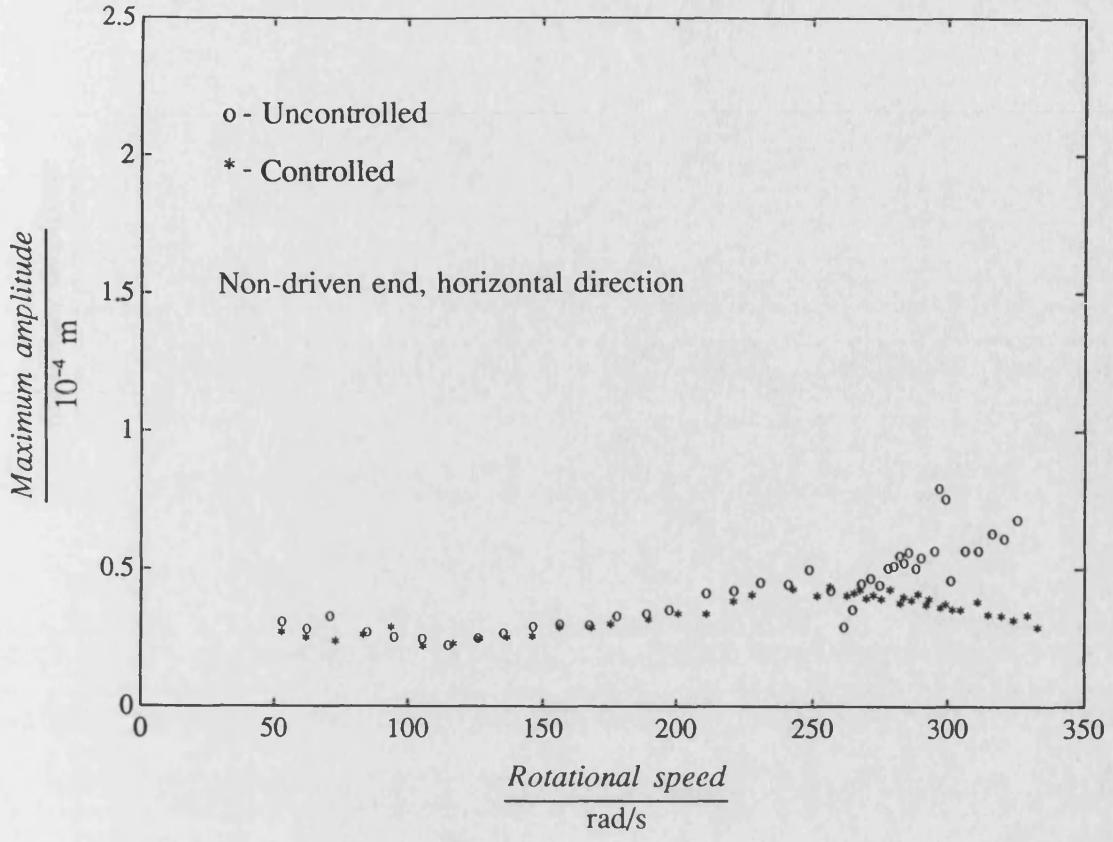

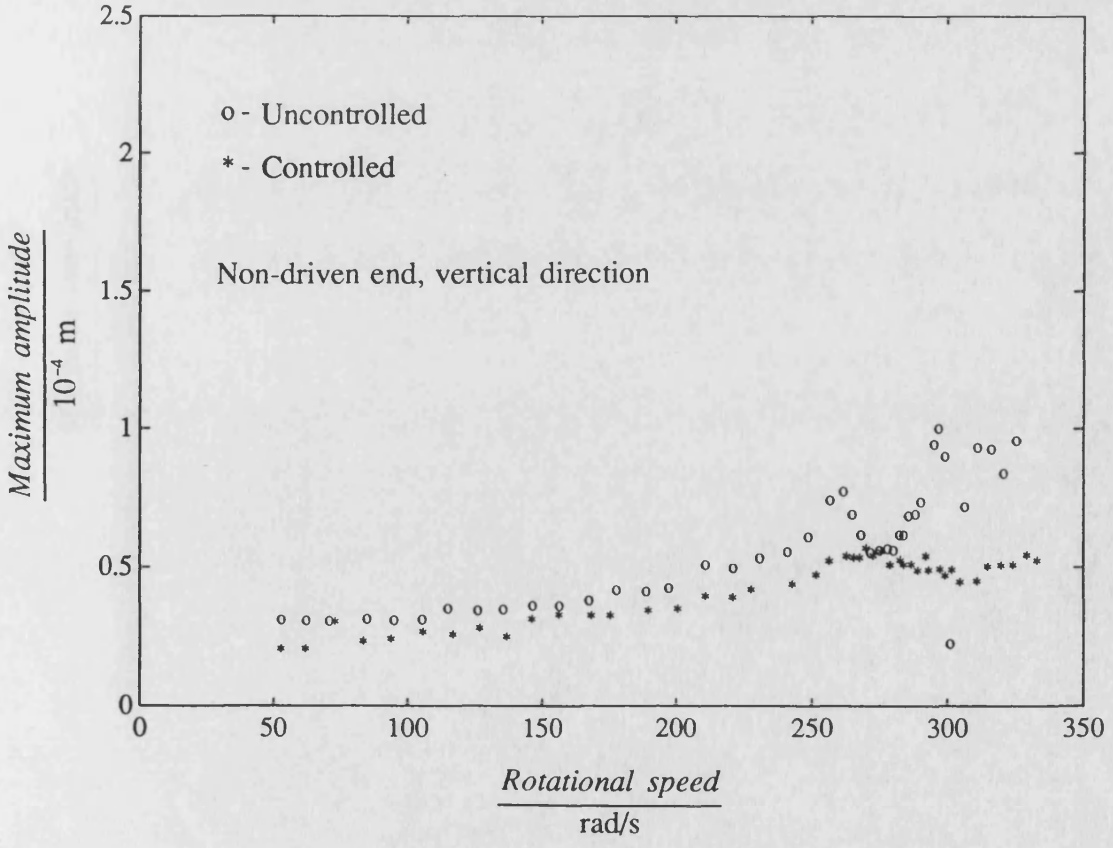

Fig. 7.12 (continued)

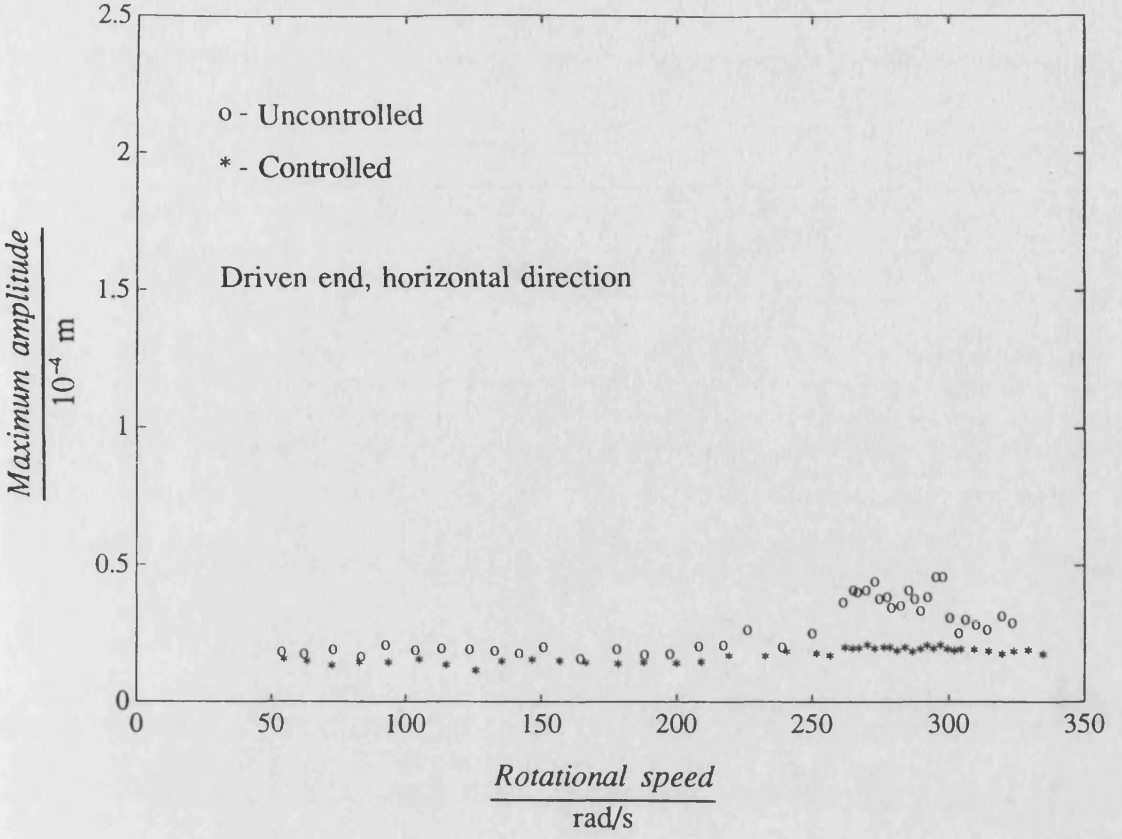

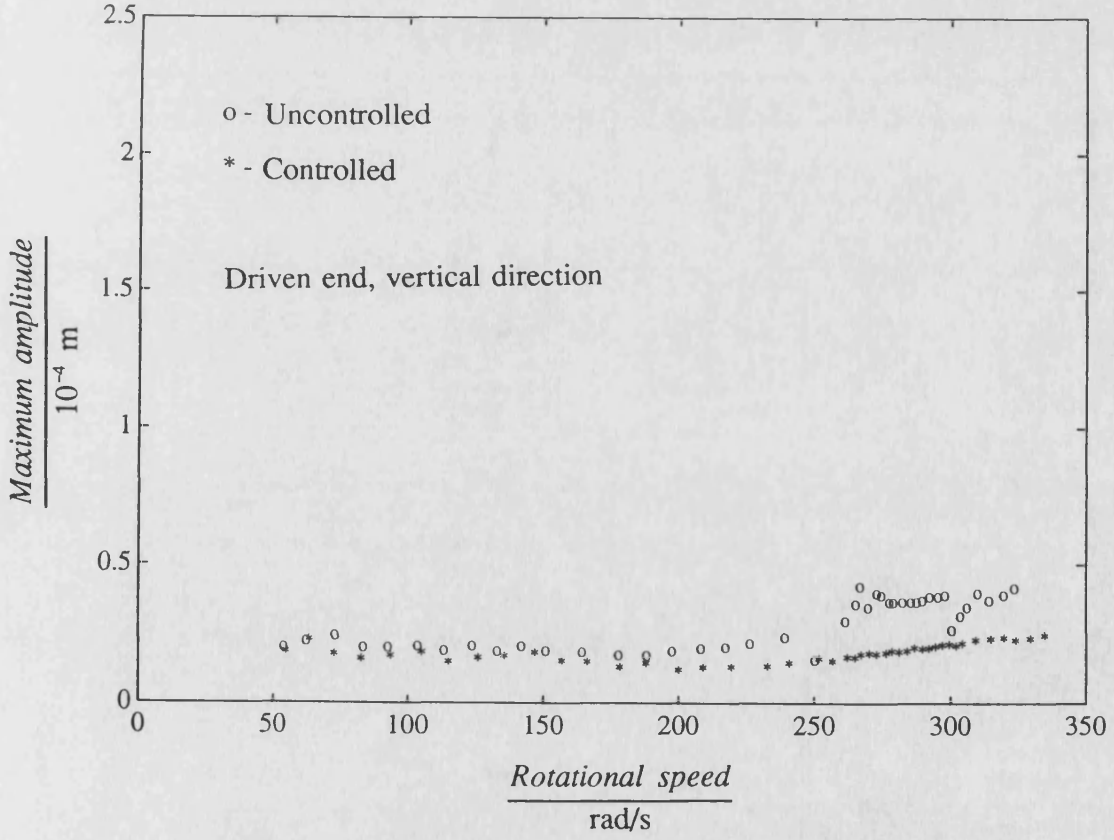

Fig. 7.13 Comparison of uncontrolled and two speed H_∞ controlled measured non-synchronous responses with 251 rad/s disturbance force in horizontal direction

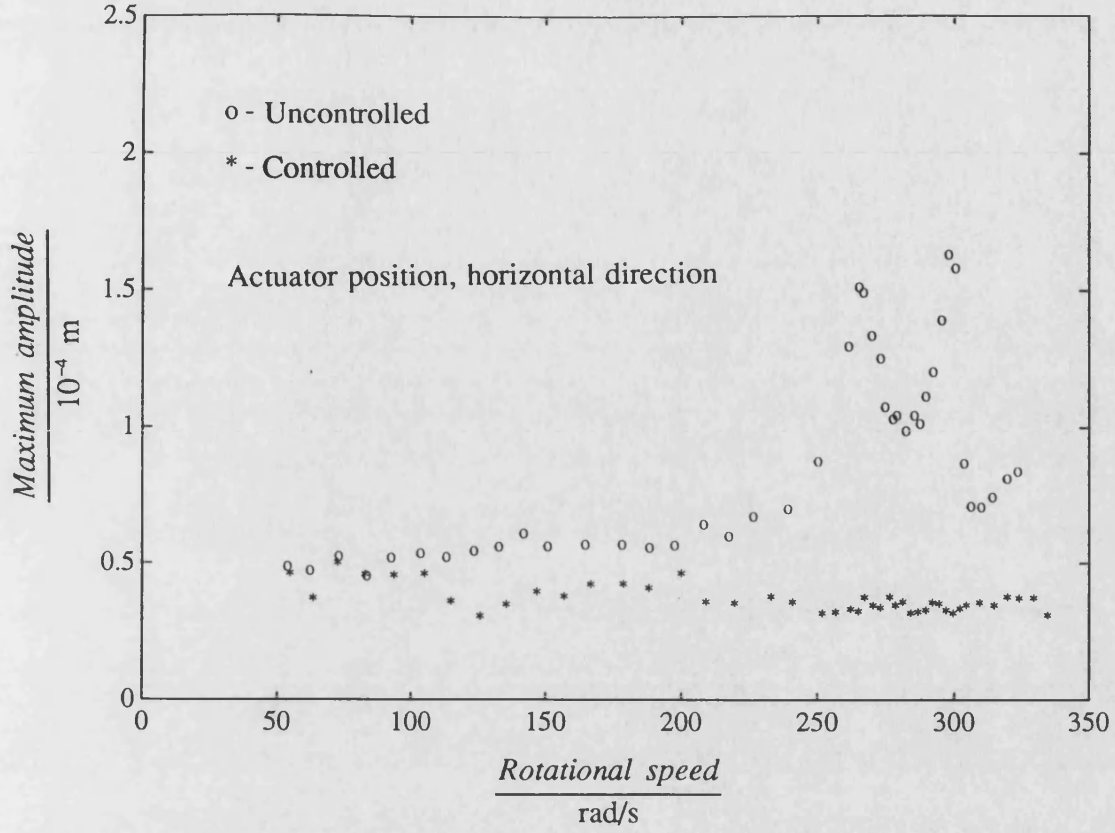

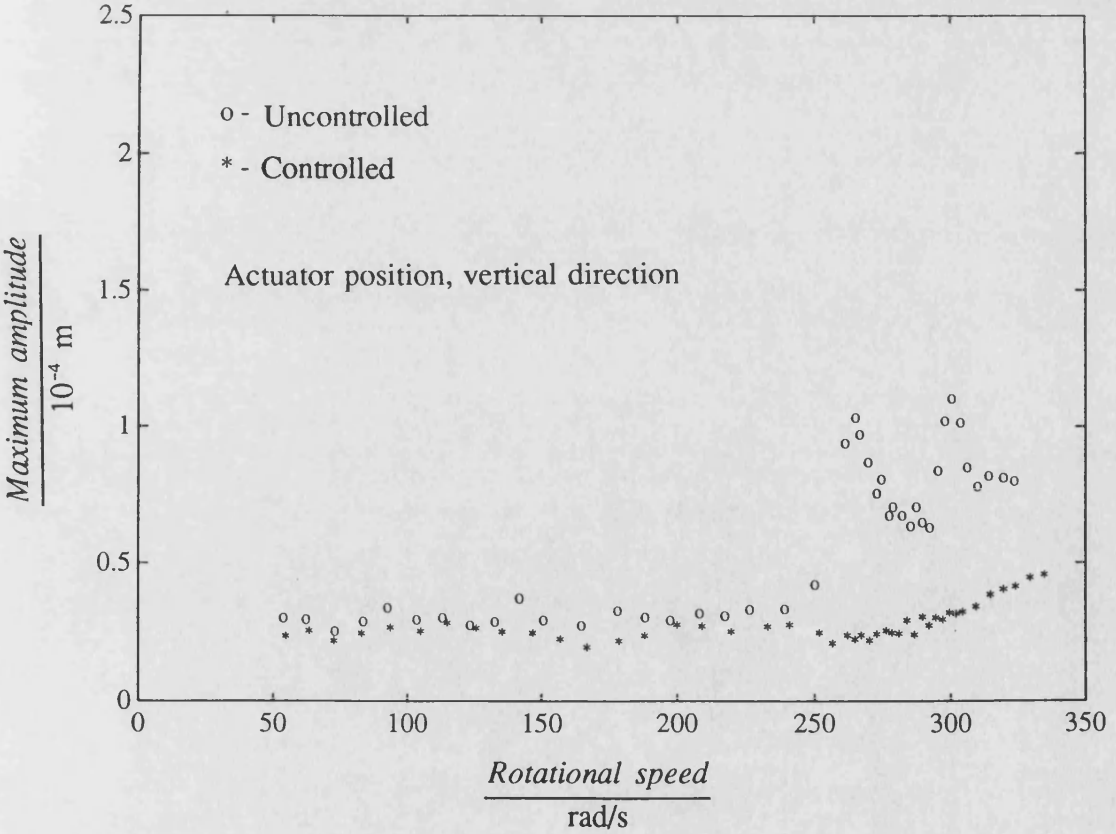

Fig. 7.13 (continued)

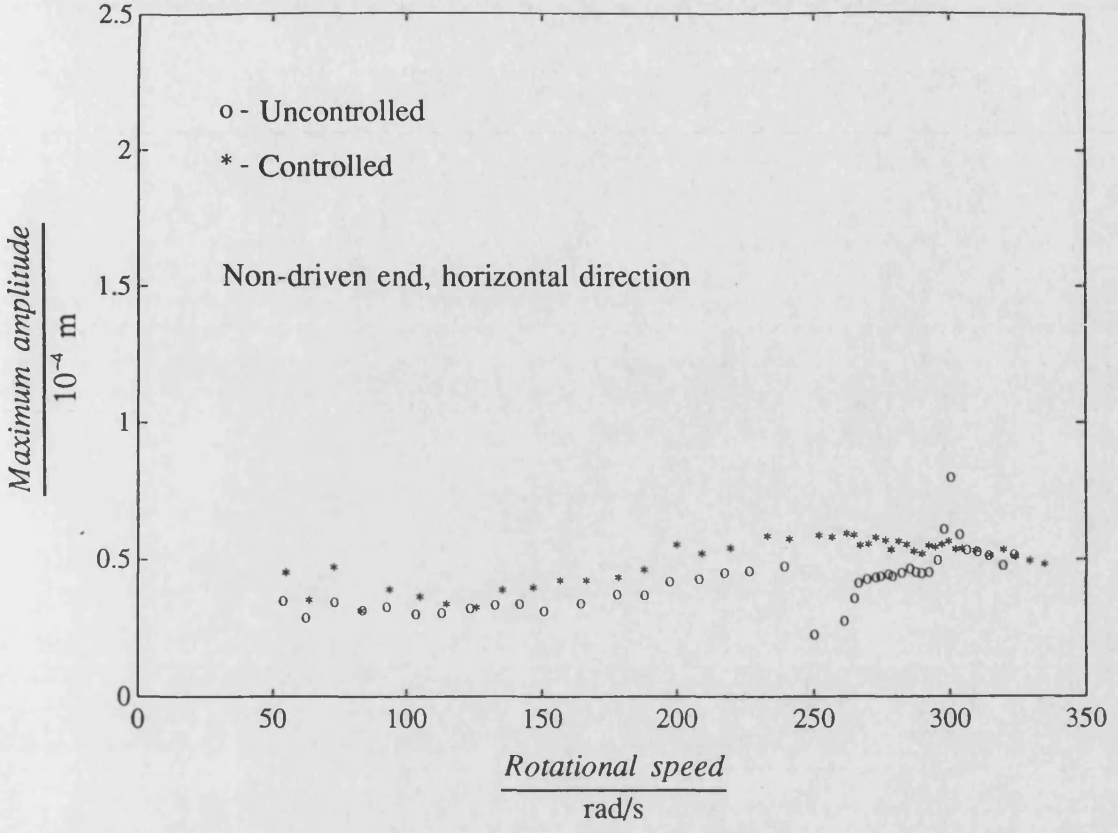

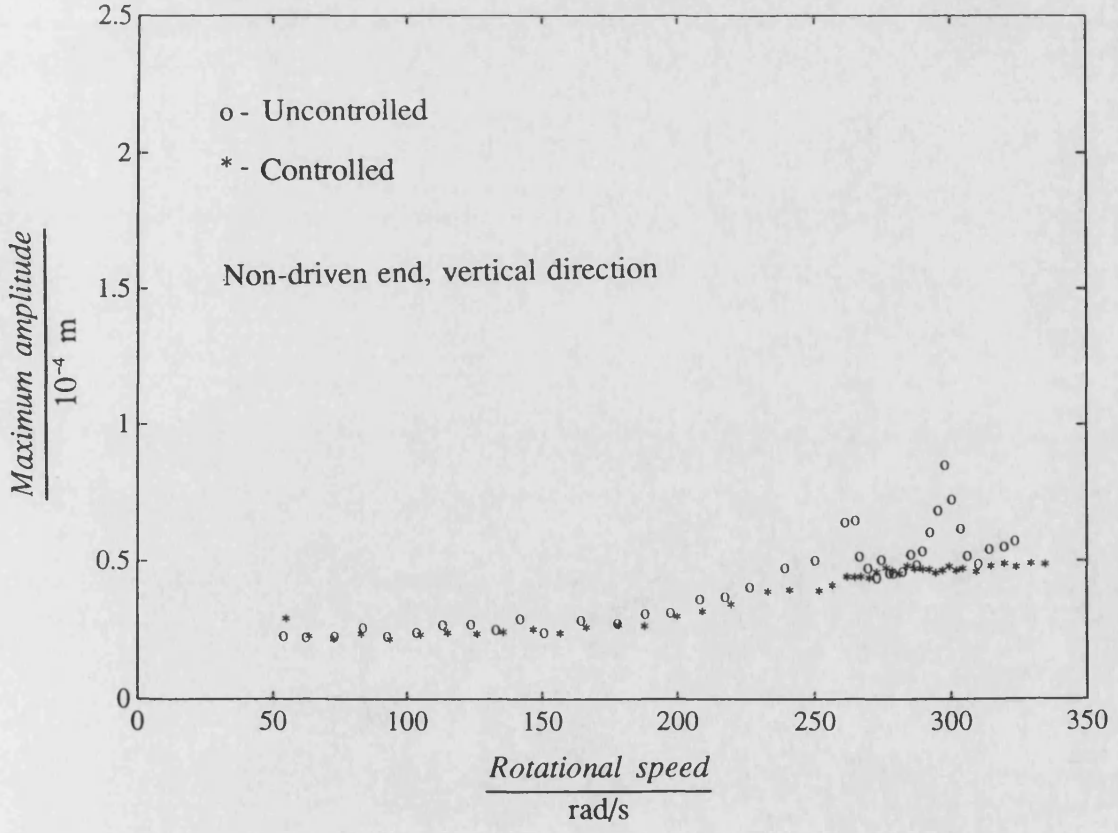

Fig. 7.13 (continued)

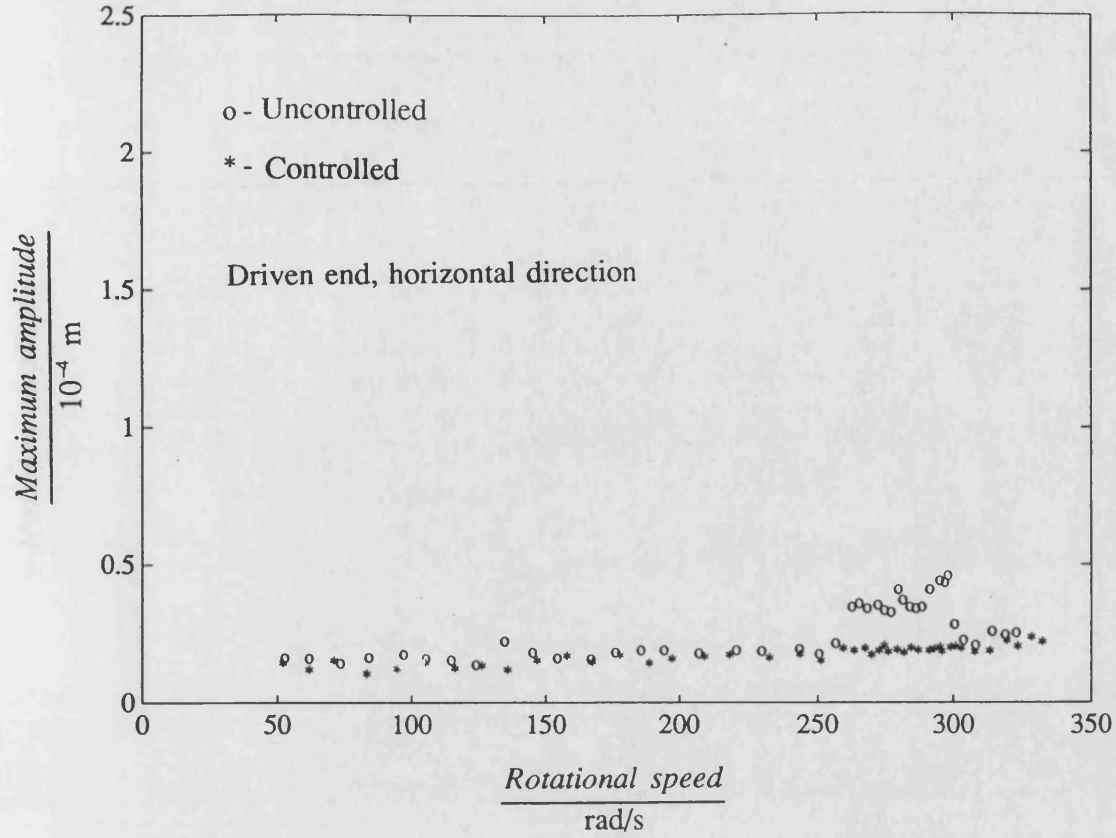

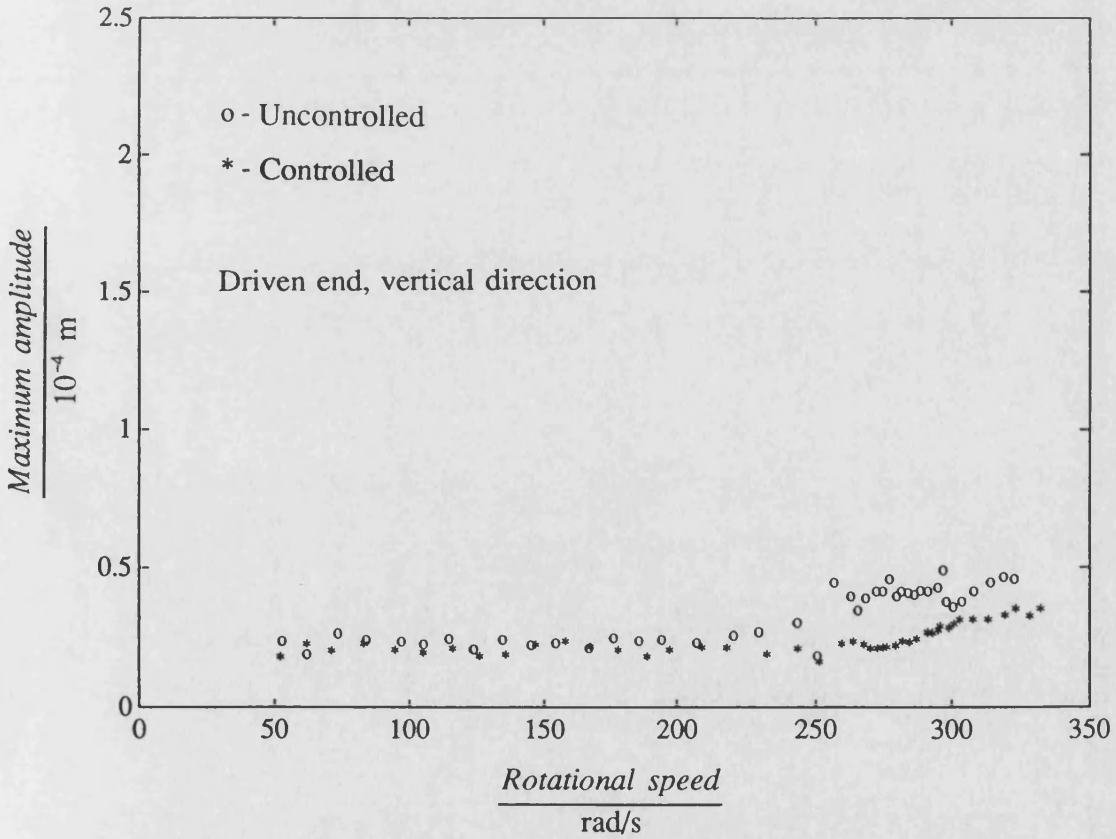

Fig. 7.14 Comparison of uncontrolled and two speed H_∞ controlled measured non-synchronous responses with 251 rad/s disturbance force in vertical direction

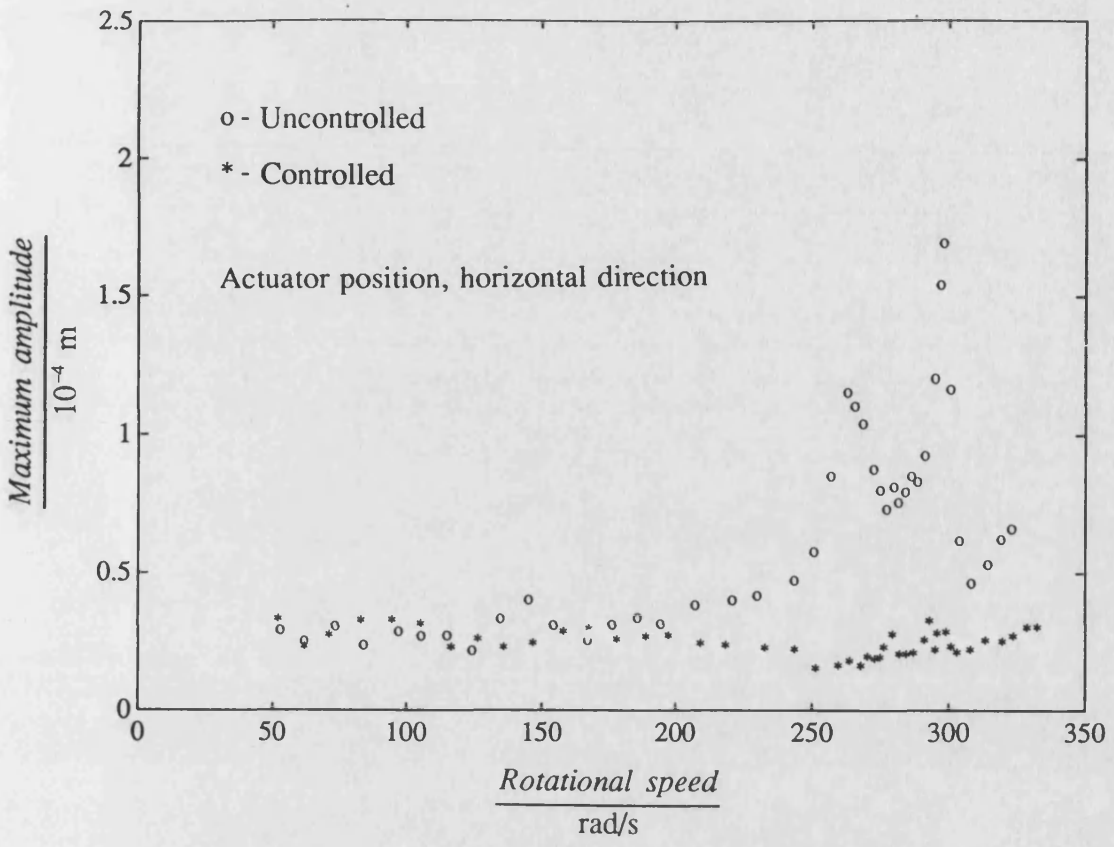

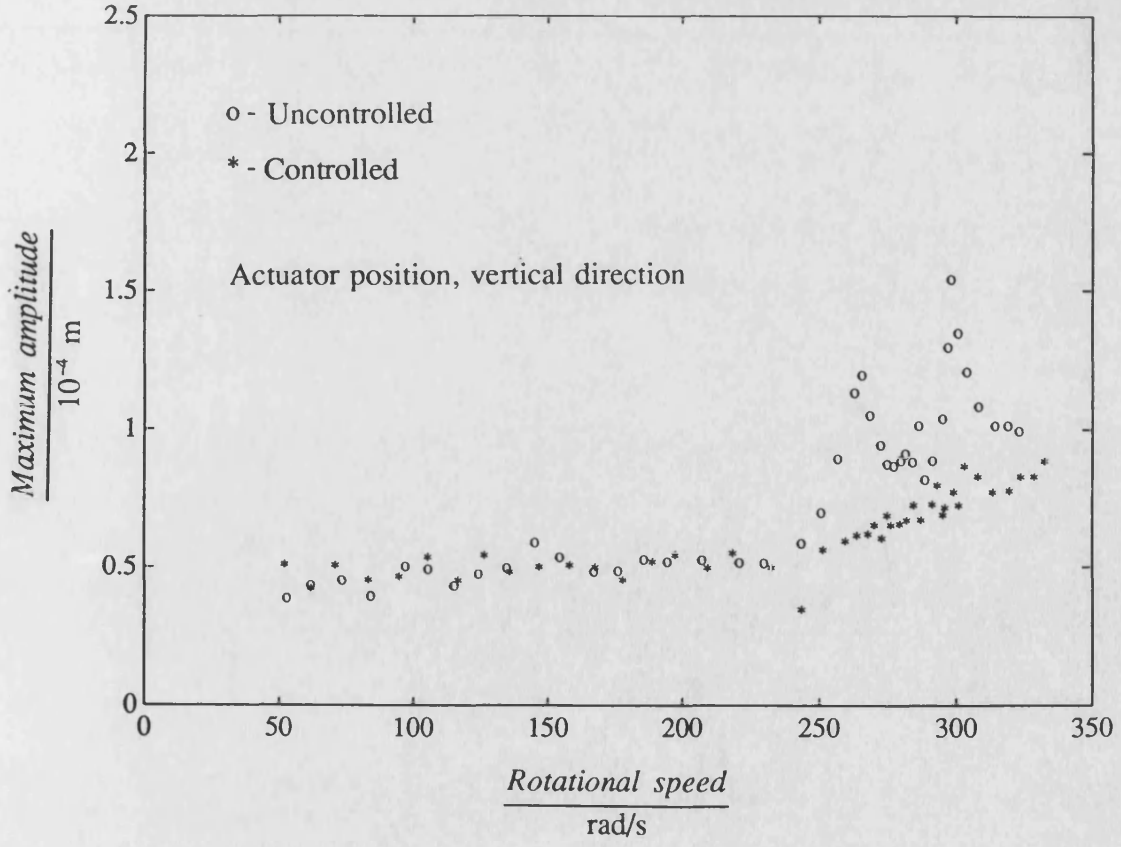

Fig. 7.14 (continued)

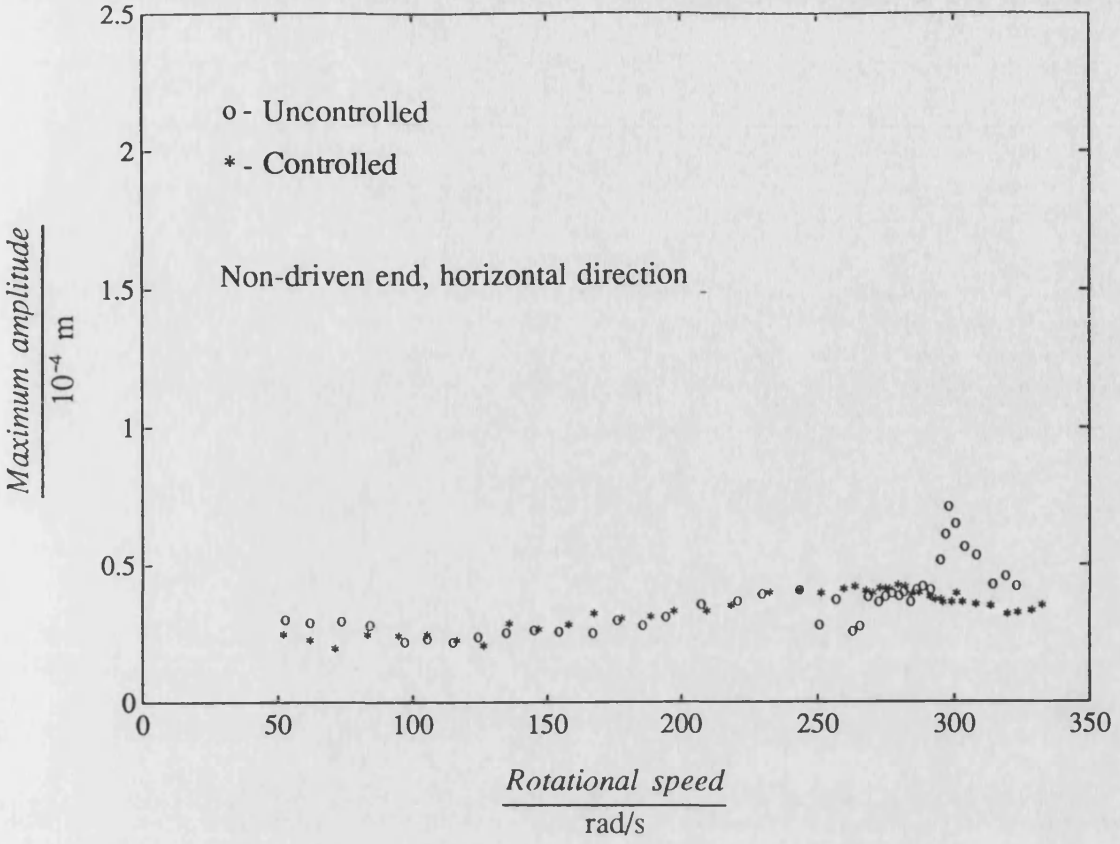

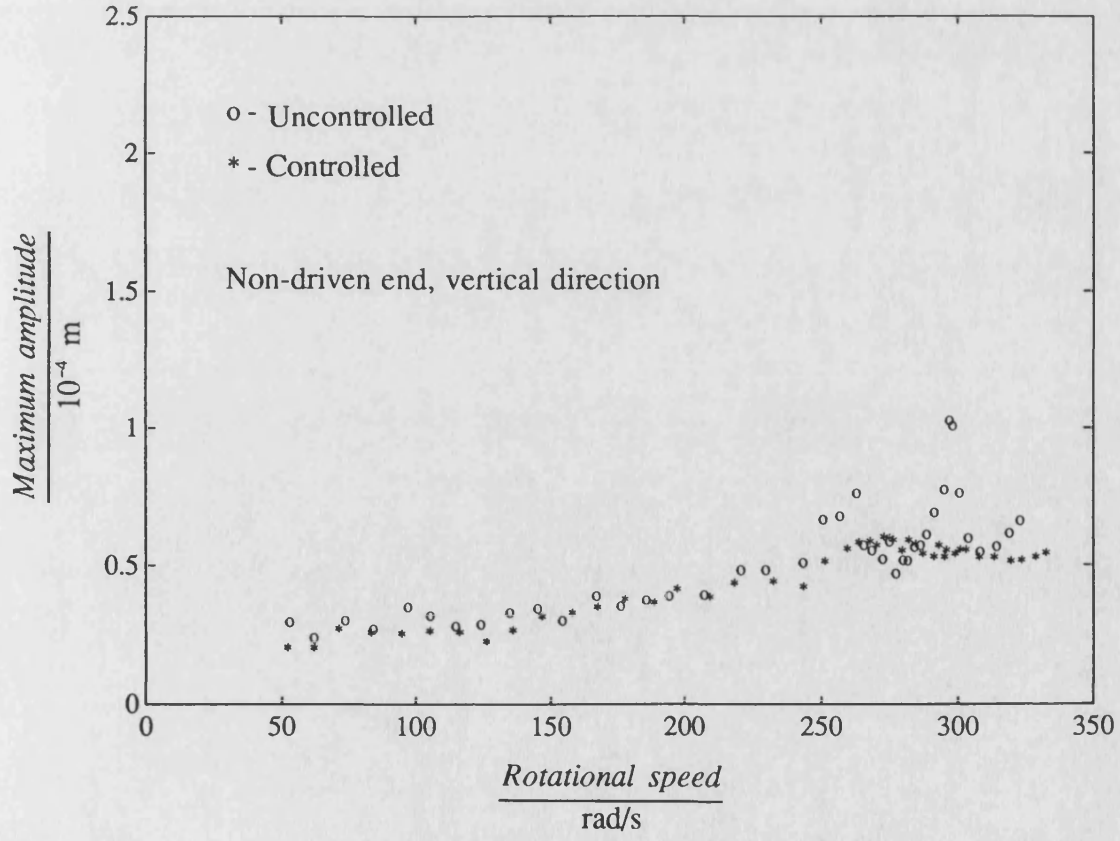

Fig. 7.14 (continued)

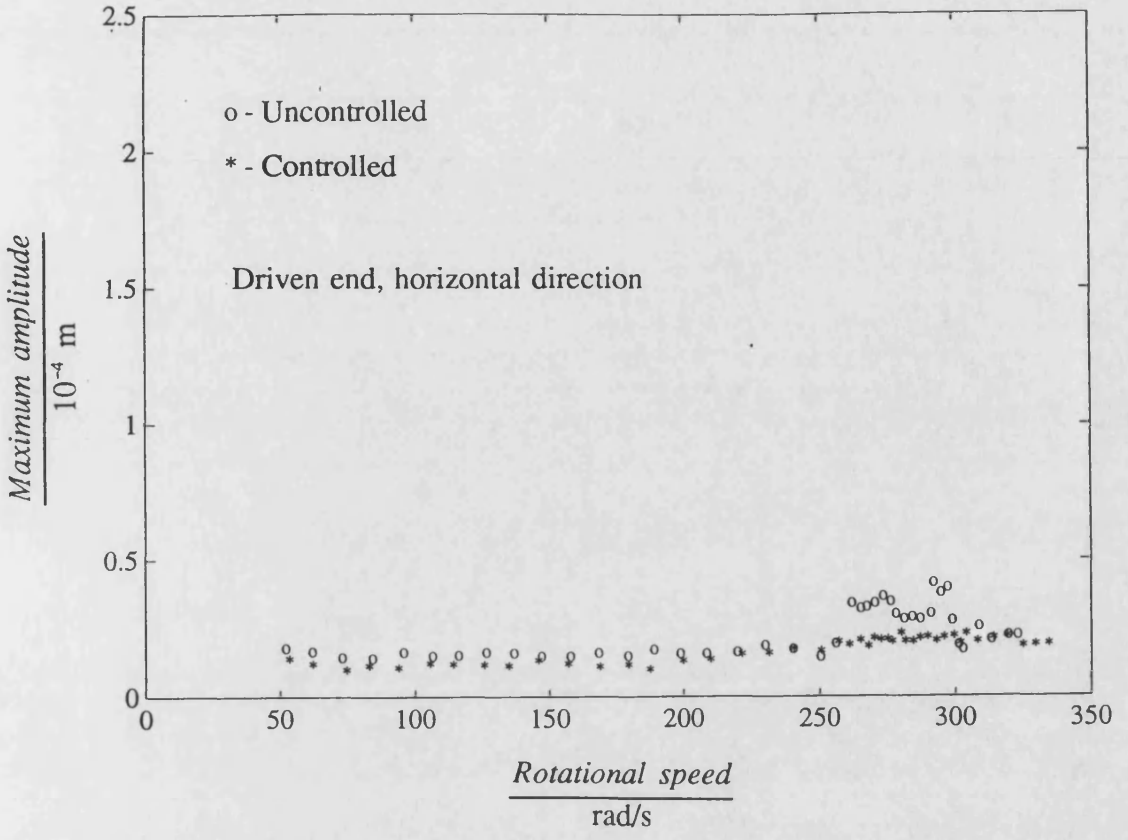

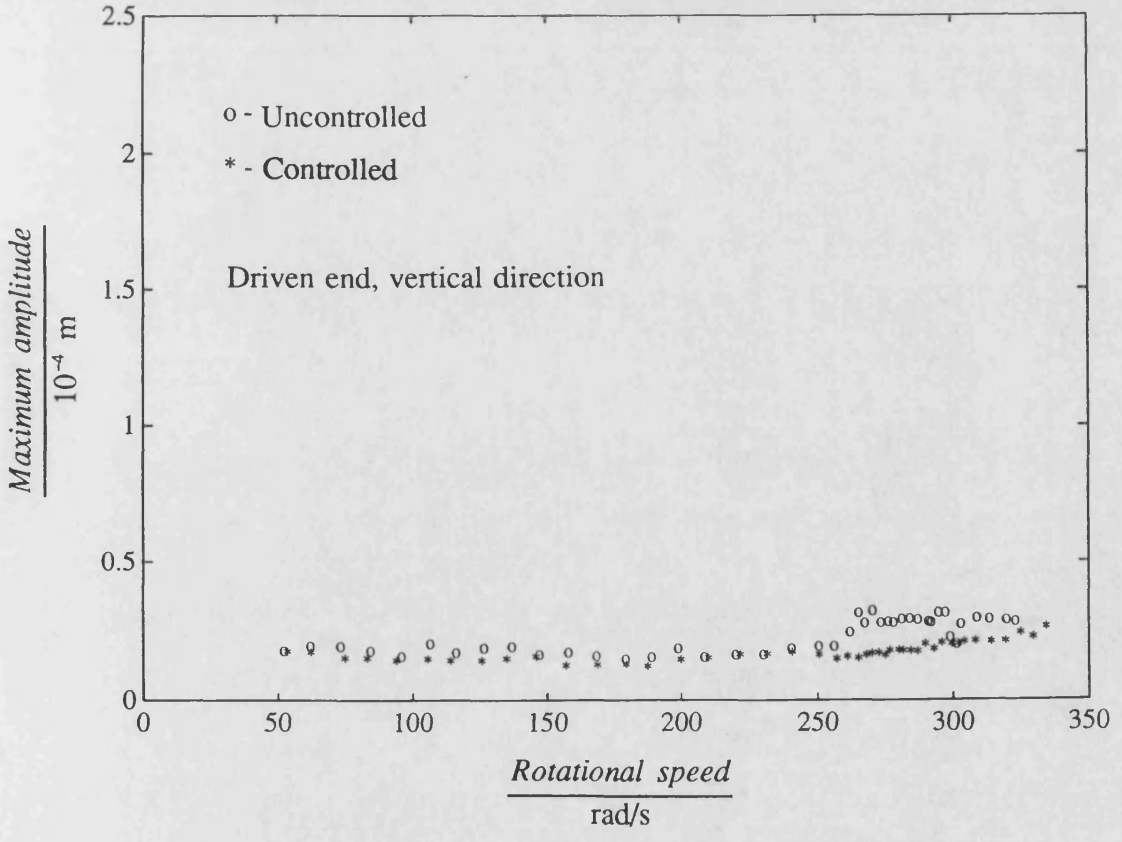

Fig. 7.15 Comparison of uncontrolled and two speed H_∞ controlled measured non-synchronous responses with 377 rad/s disturbance force in horizontal direction

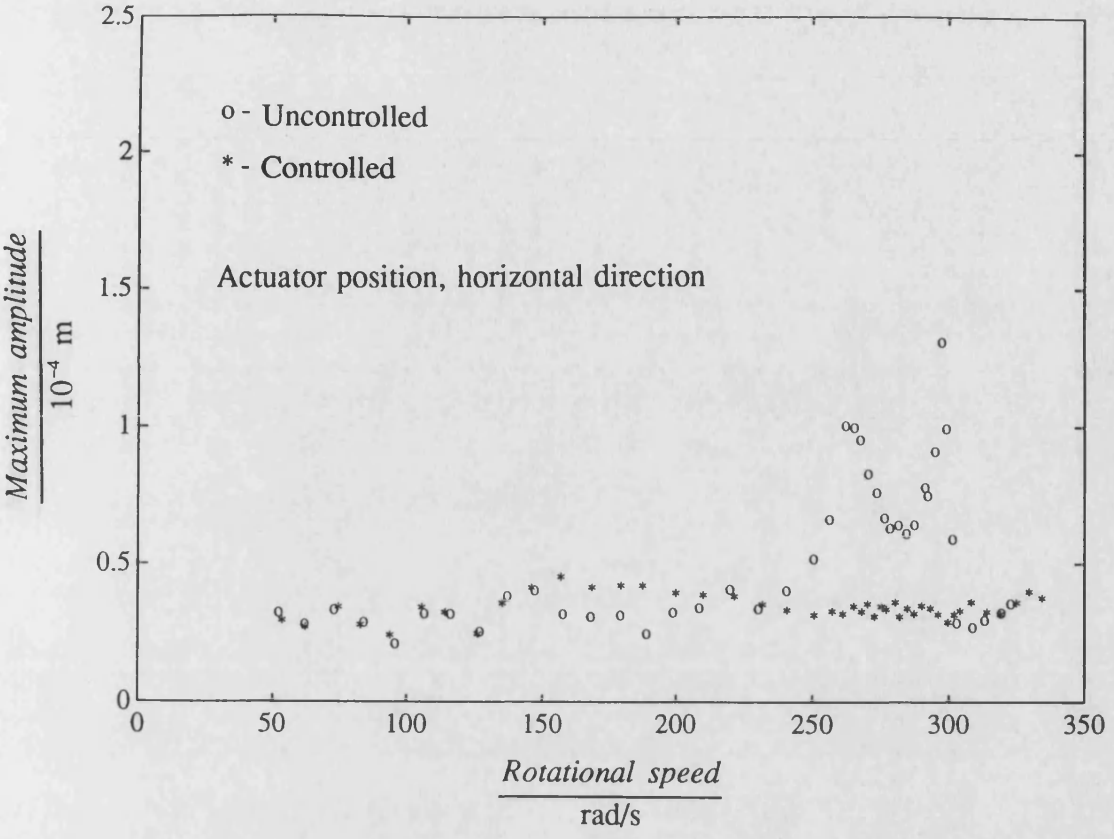

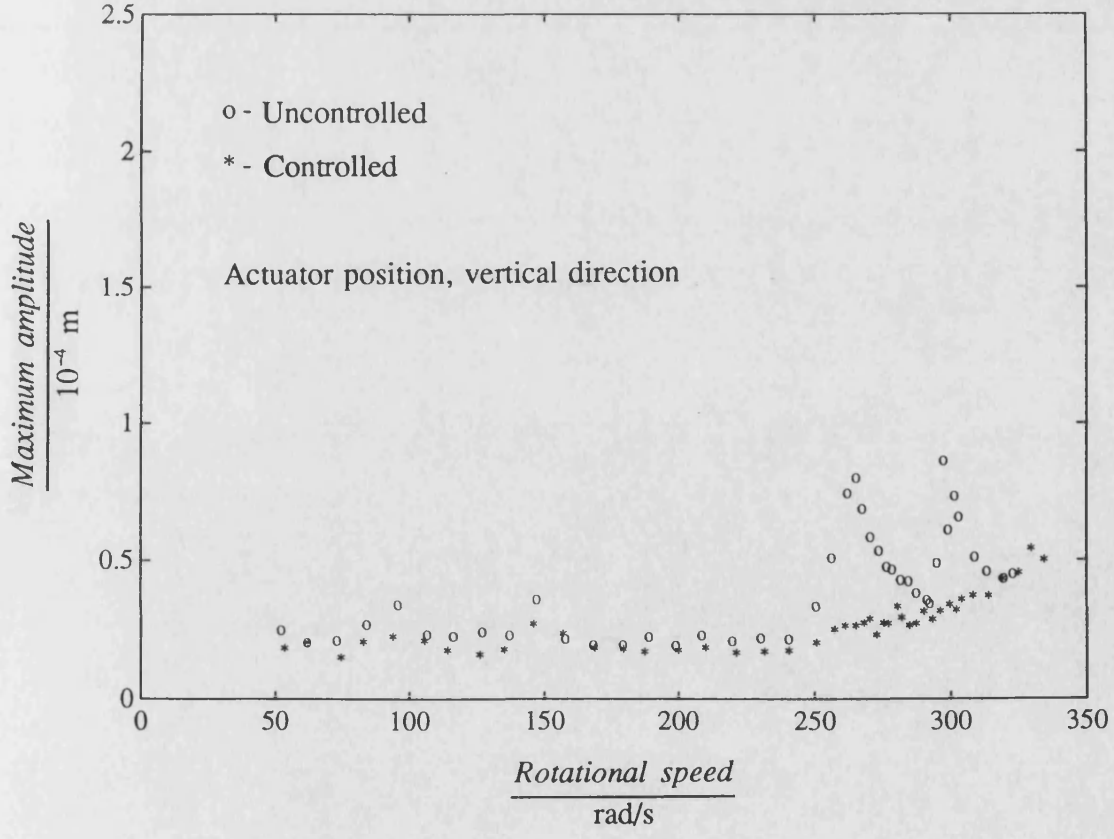

Fig. 7.15 (continued)

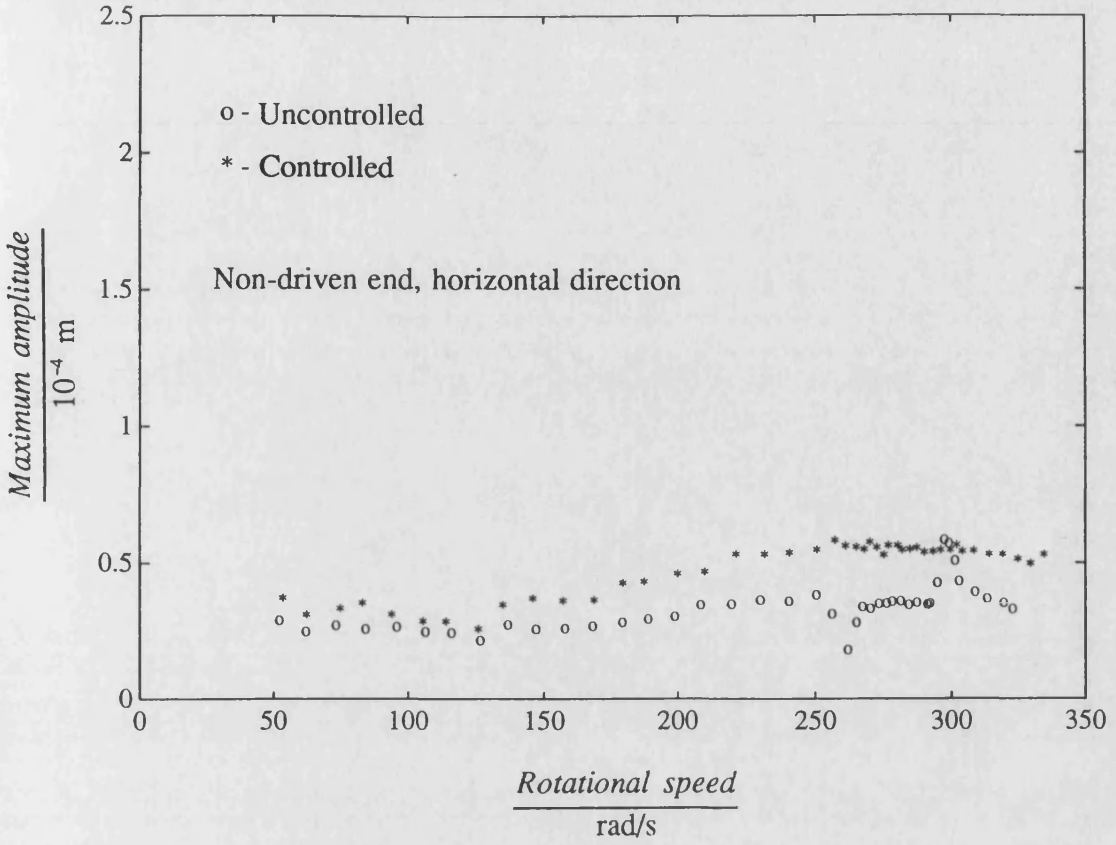

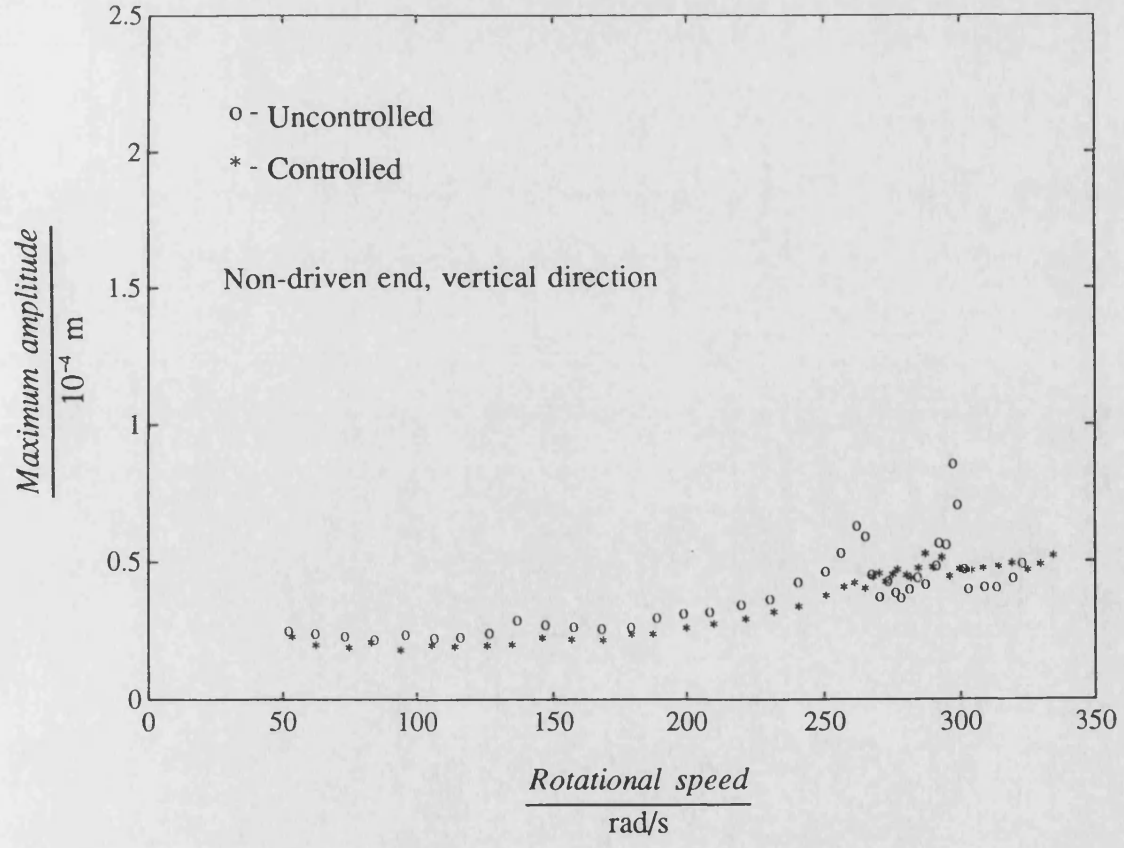

Fig. 7.15 (continued)

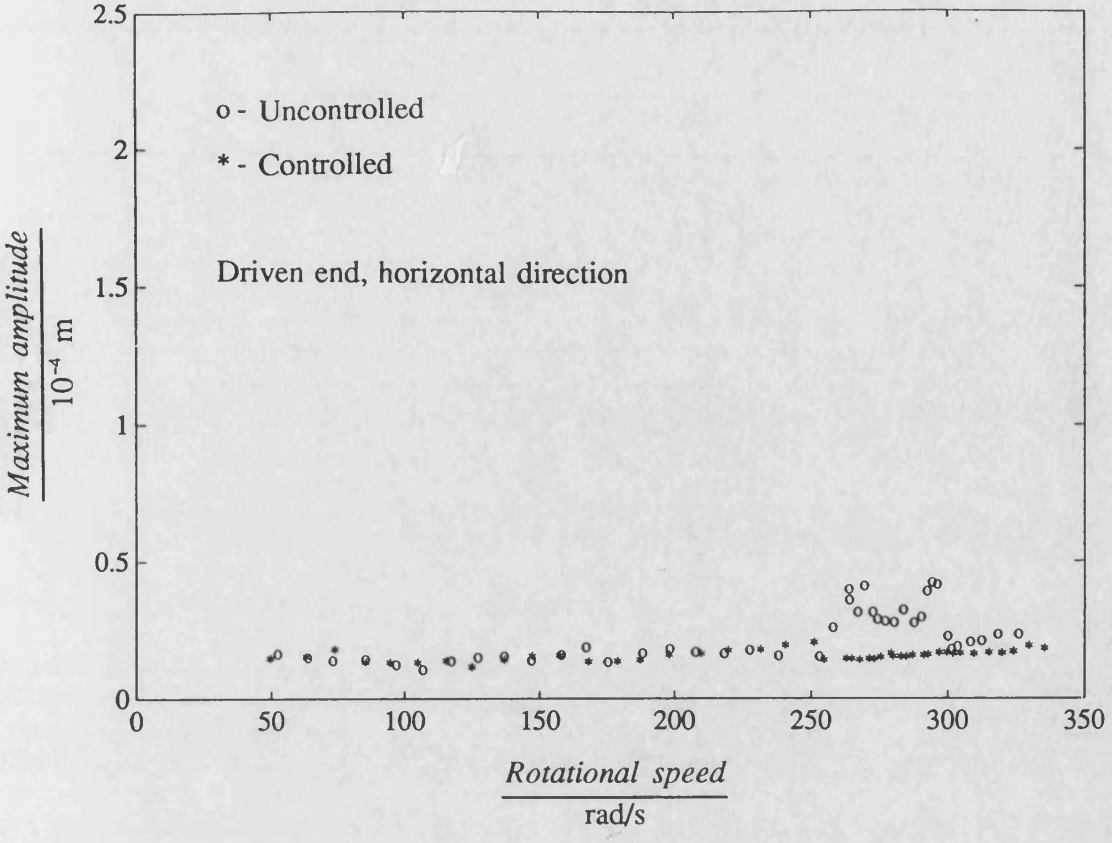

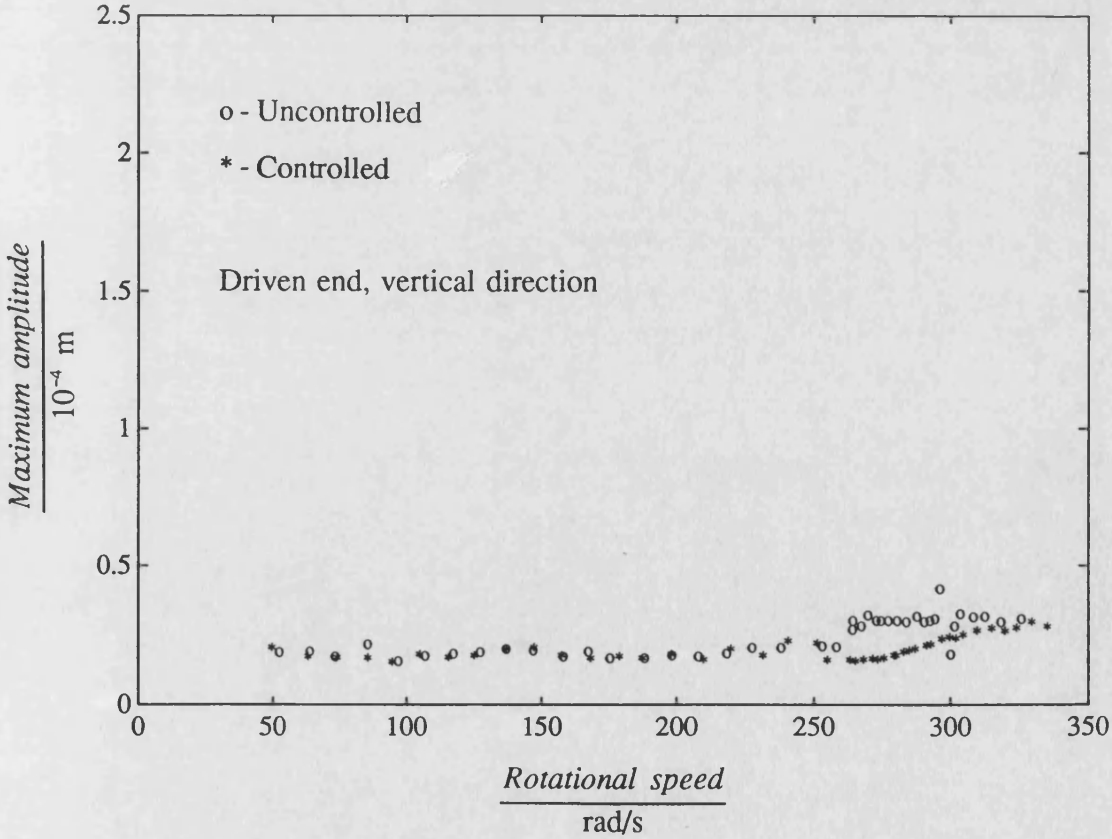

Fig. 7.16 Comparison of uncontrolled and two speed H_∞ controlled measured non-synchronous responses with 377 rad/s disturbance force in vertical direction

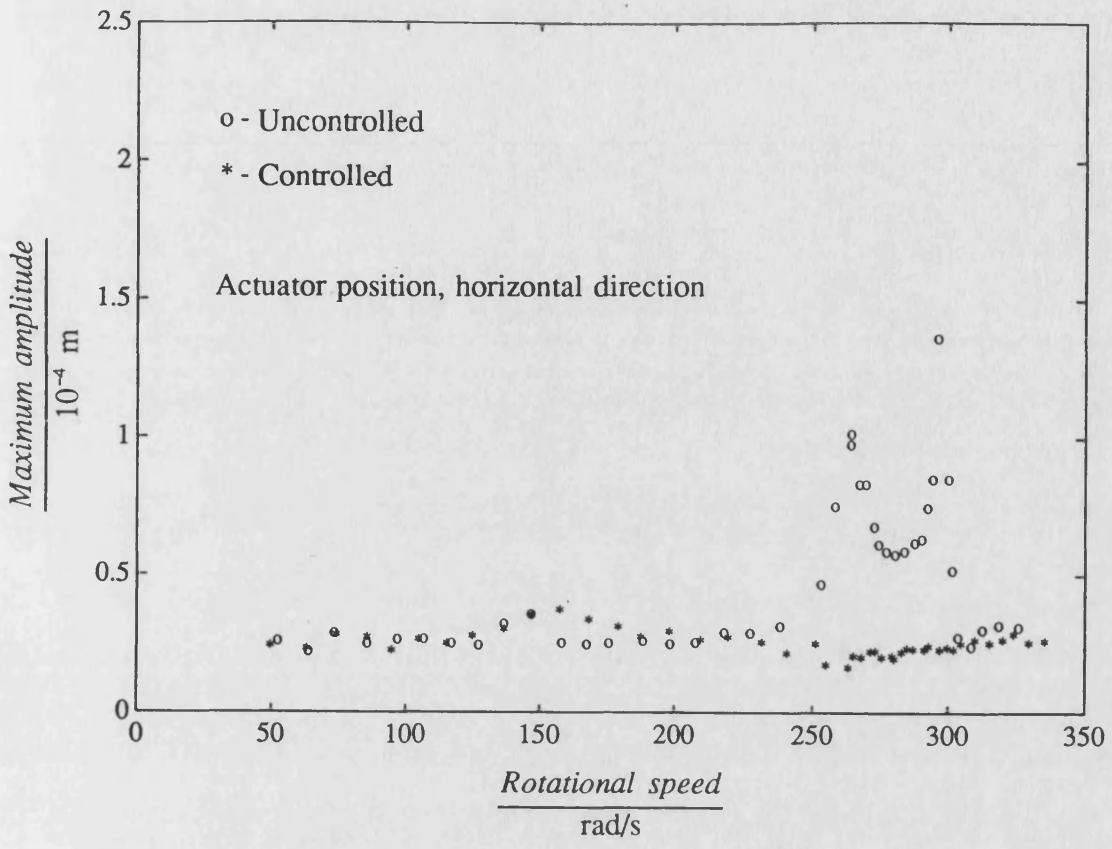

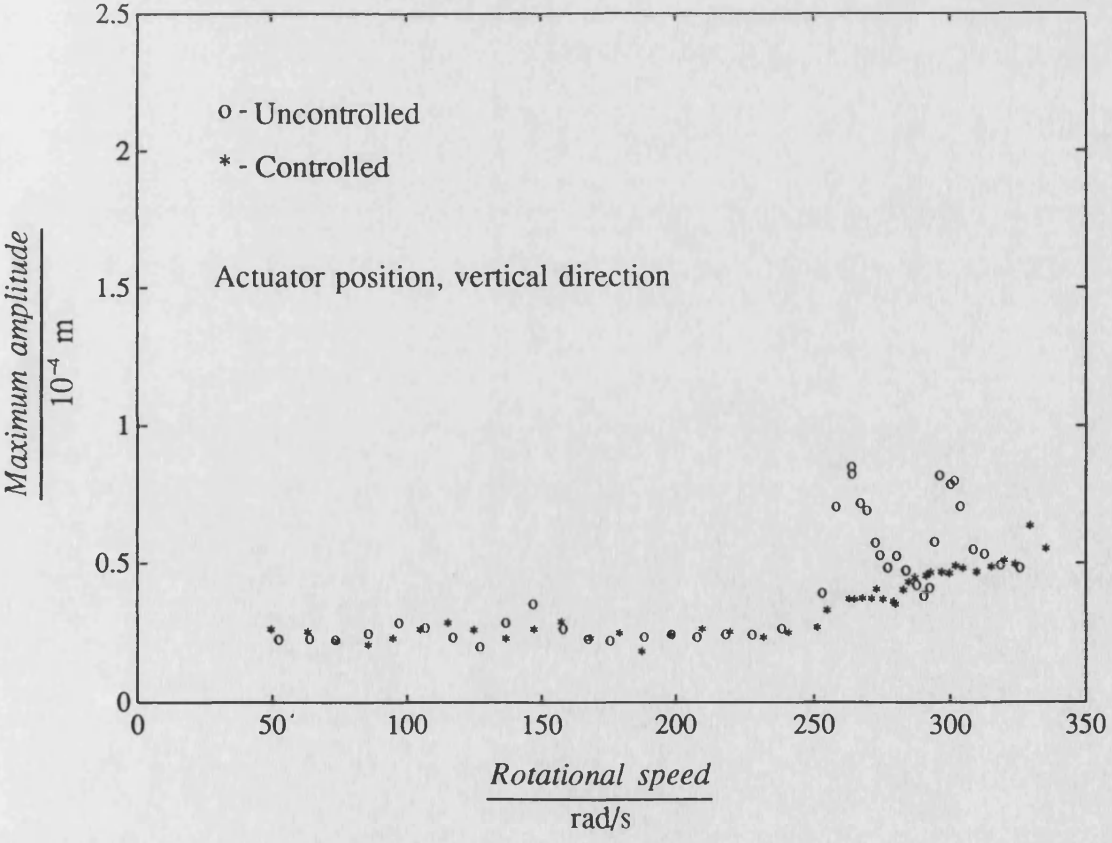

Fig. 7.16 (continued)

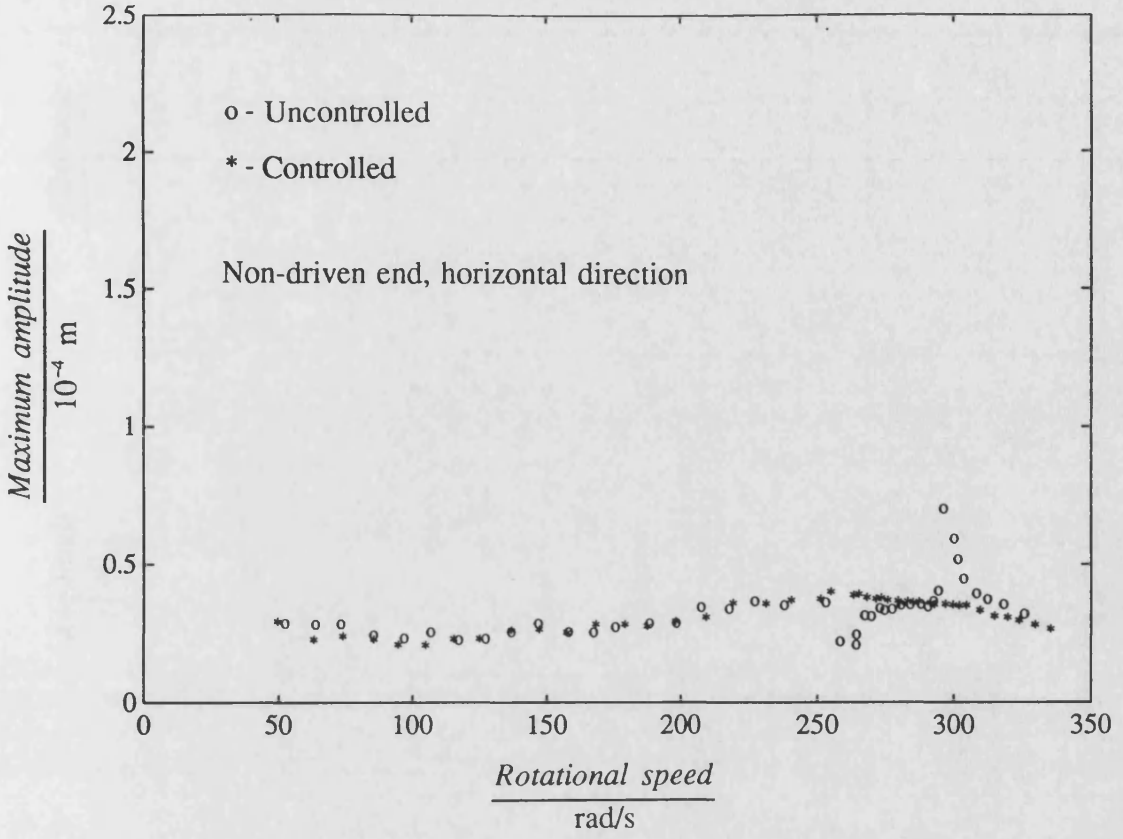

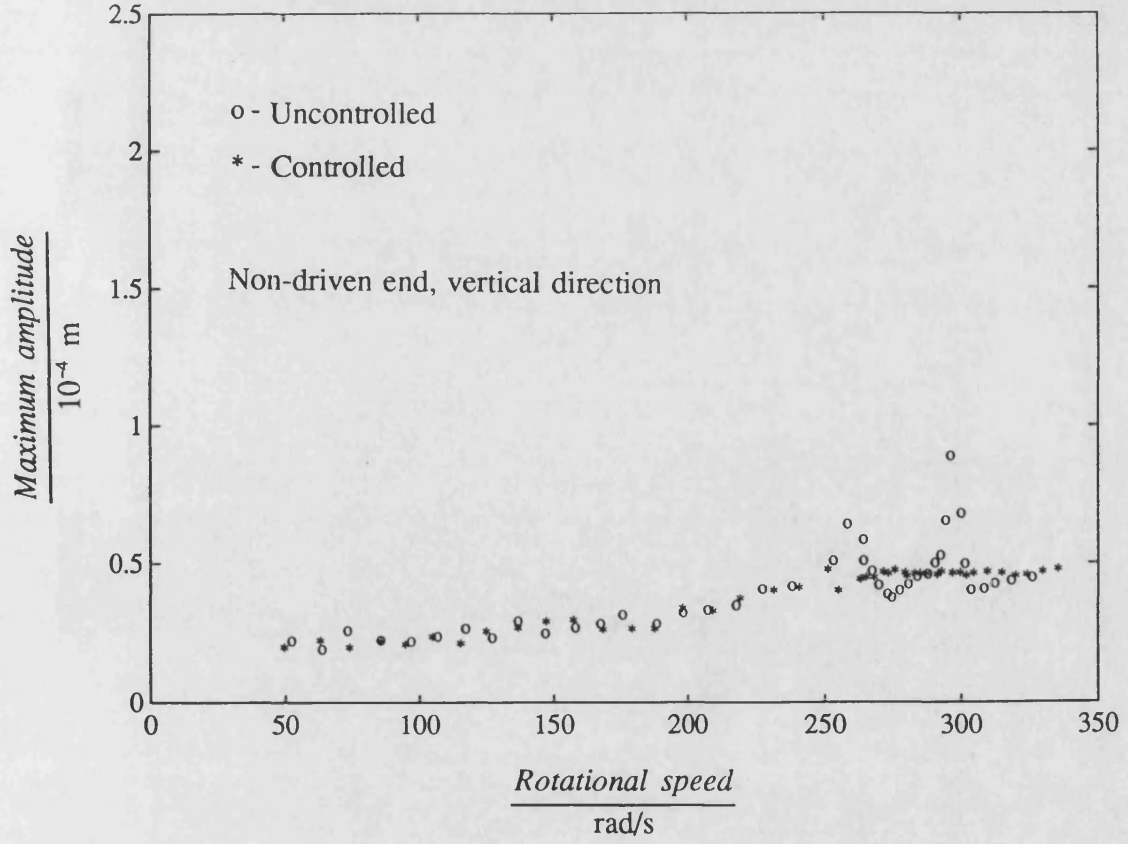

Fig. 7.16 (continued)

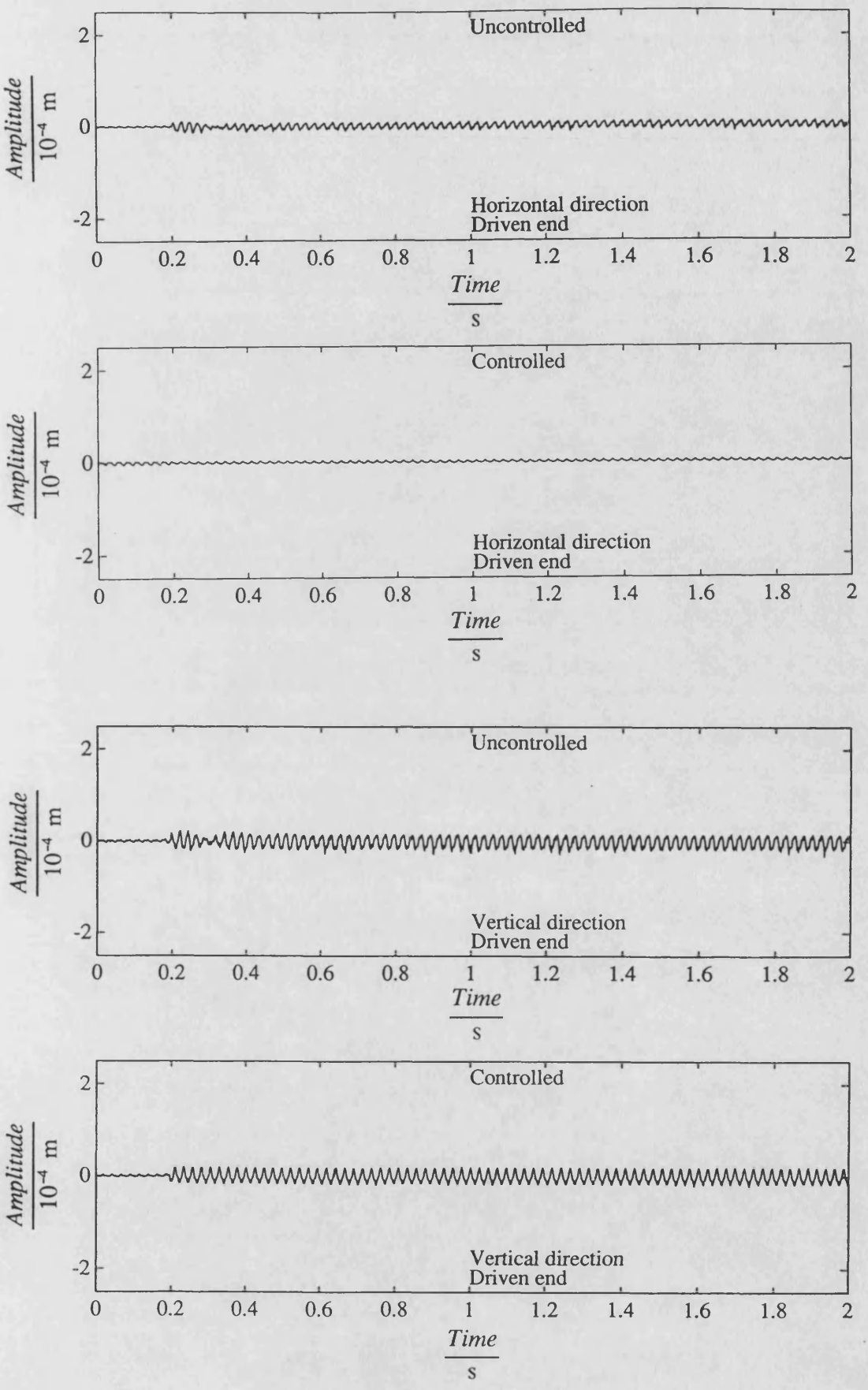

Fig. 7.17 Measured transient responses of uncontrolled and H_∞ controlled system due to sudden mass loss at speed 262 rad/s

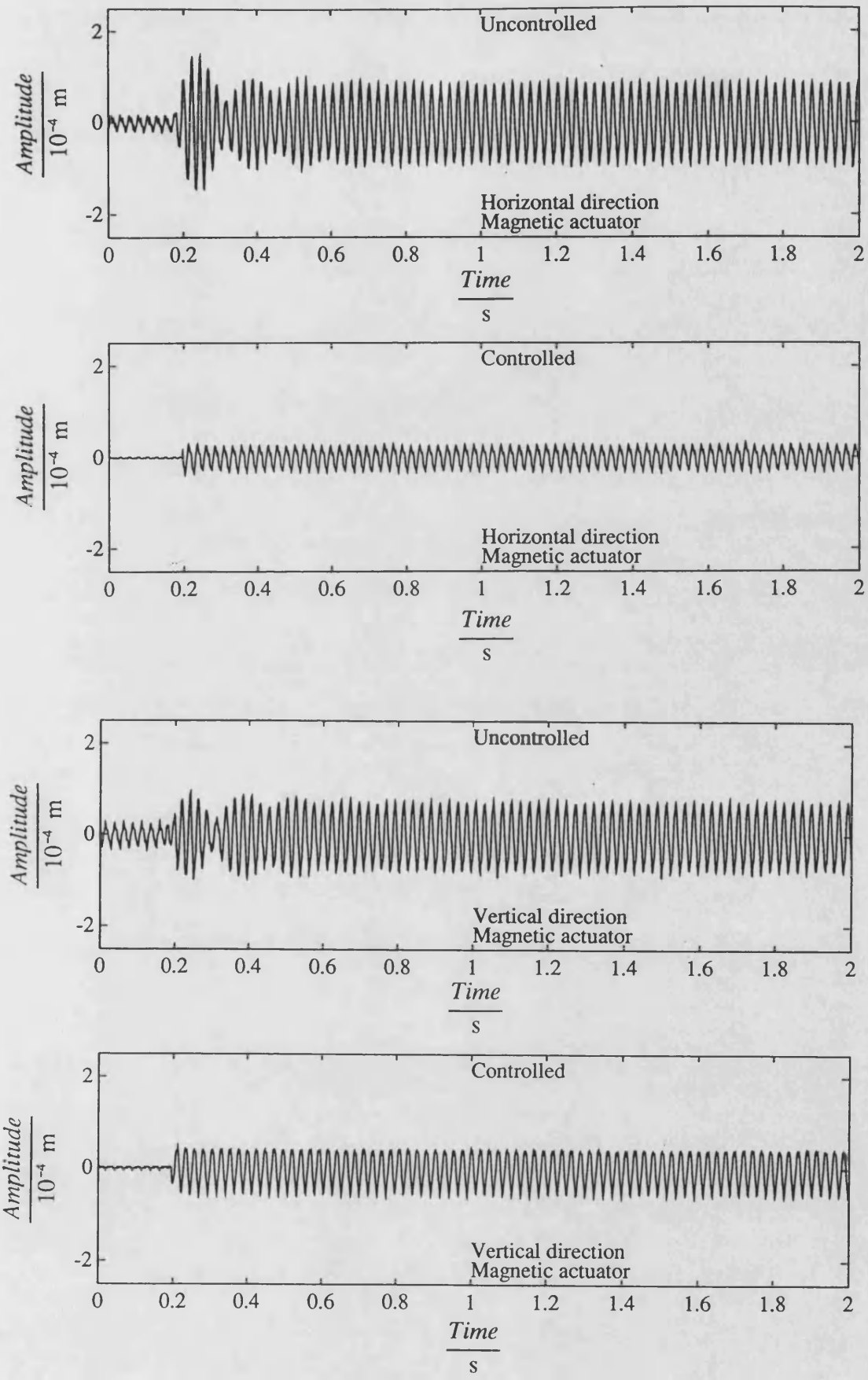

Fig. 7.17 (continued)

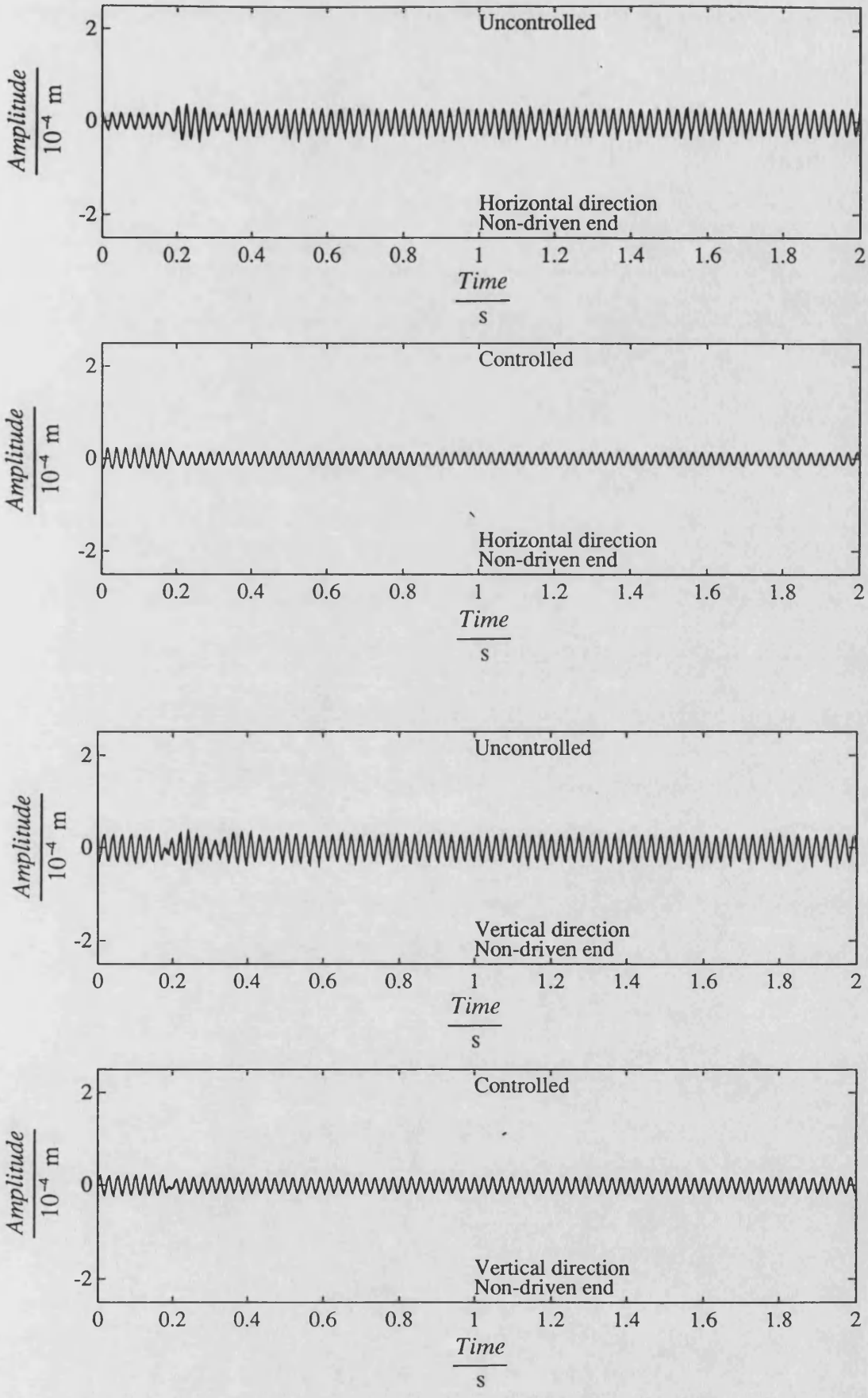

Fig. 7.17 (continued)

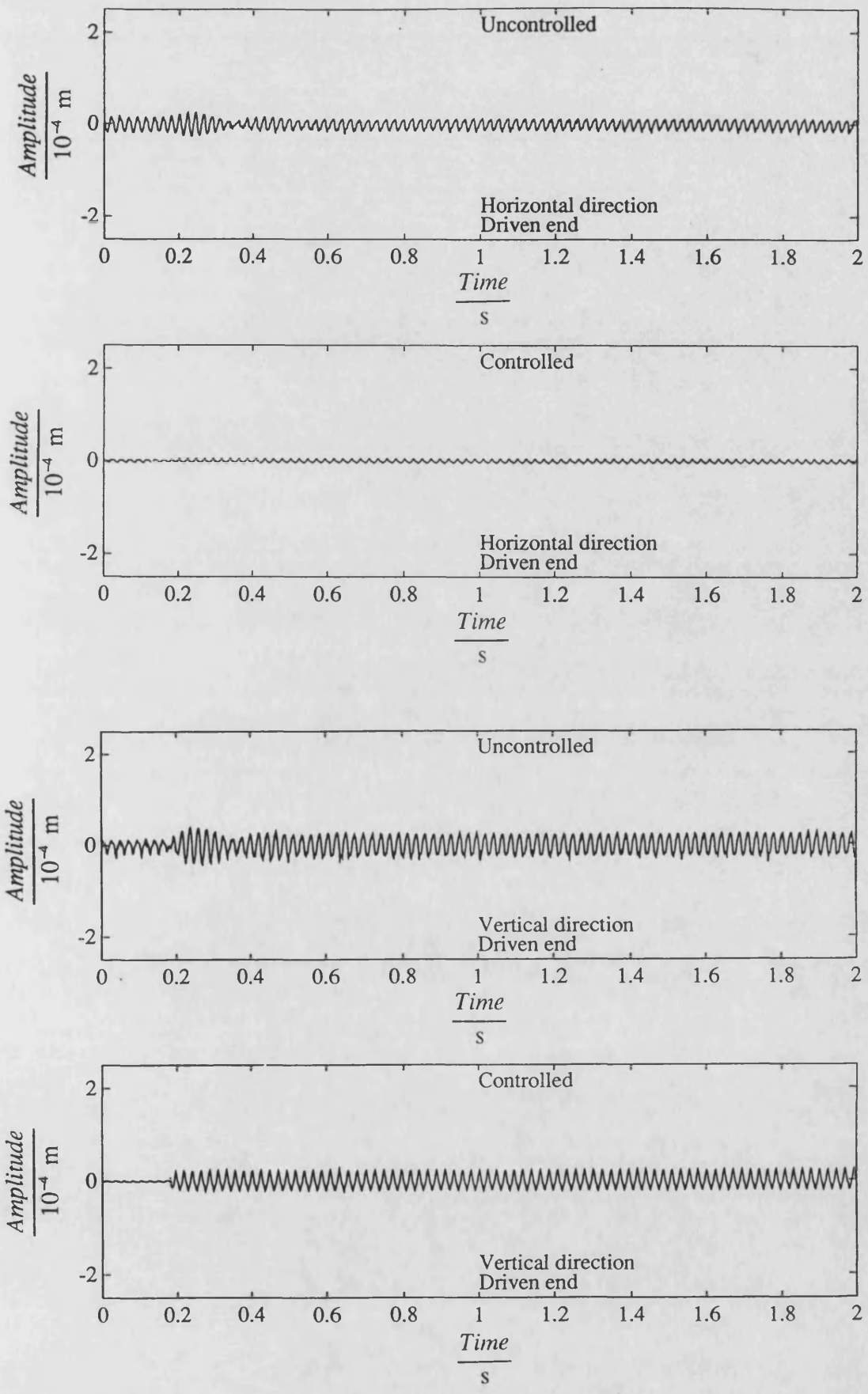

Fig. 7.18 Measured transient responses of uncontrolled and H_∞ controlled system due to sudden mass loss at speed 270 rad/s

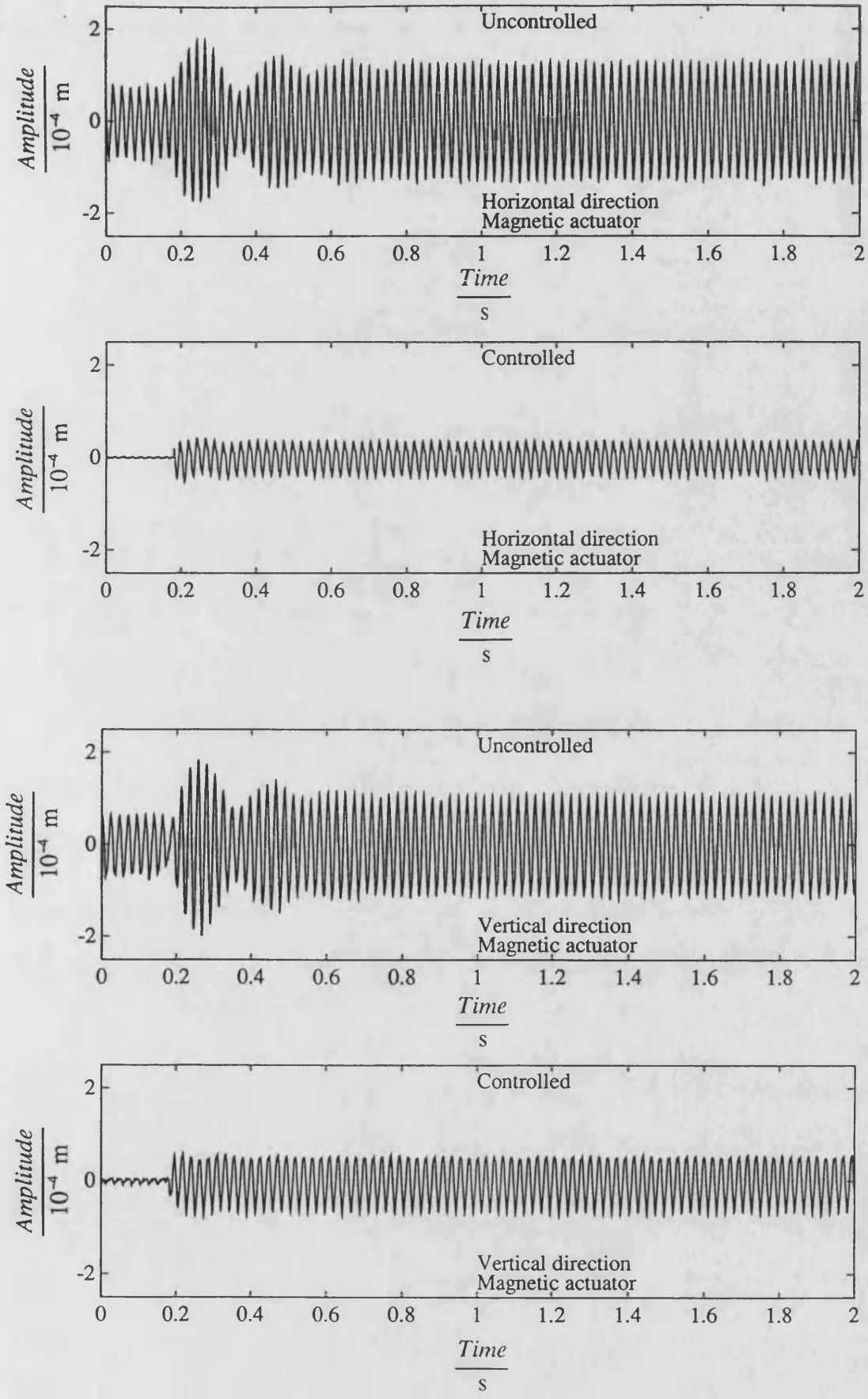

Fig. 7.18 (continued)

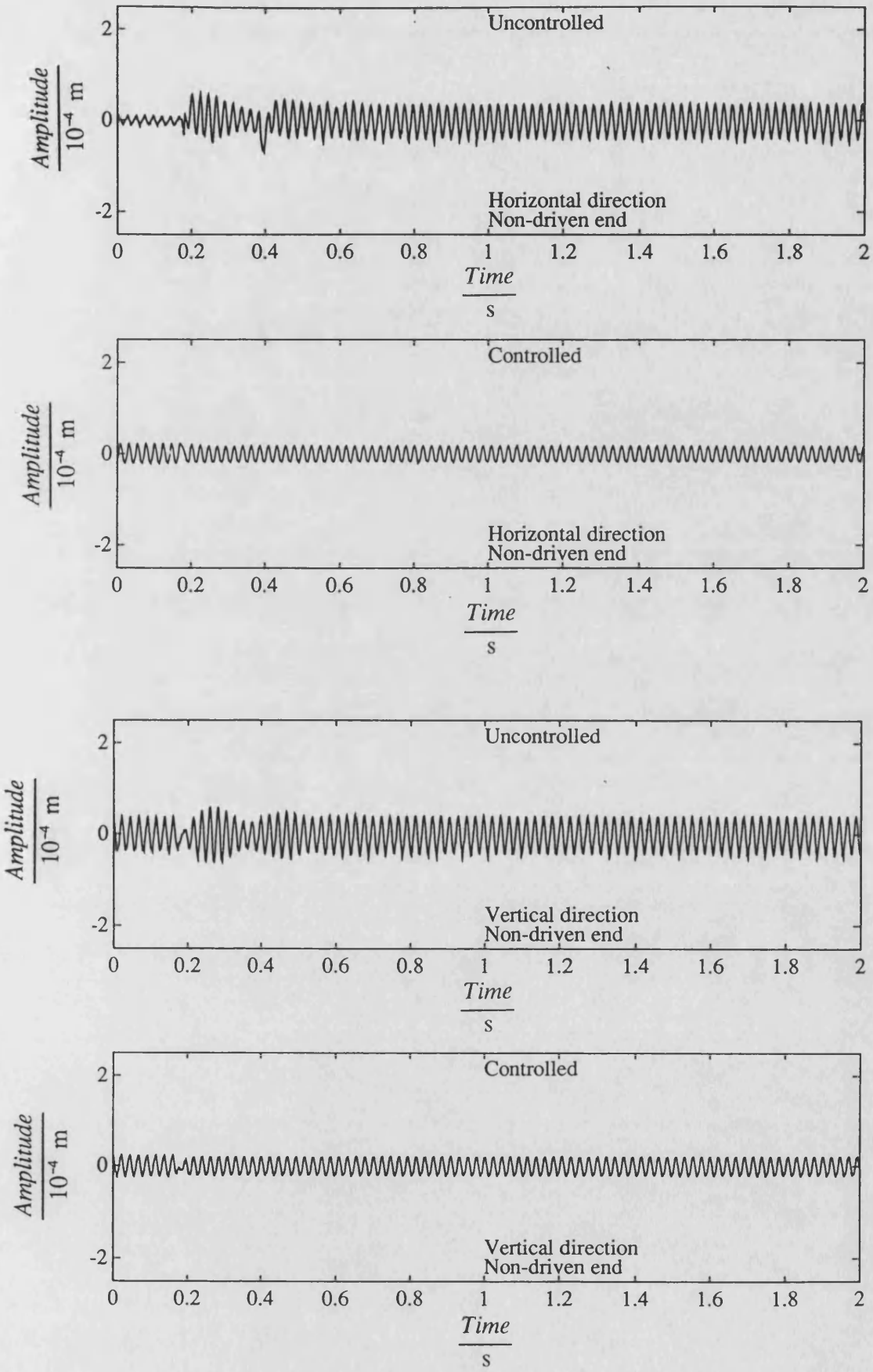

Fig. 7.18 (continued)

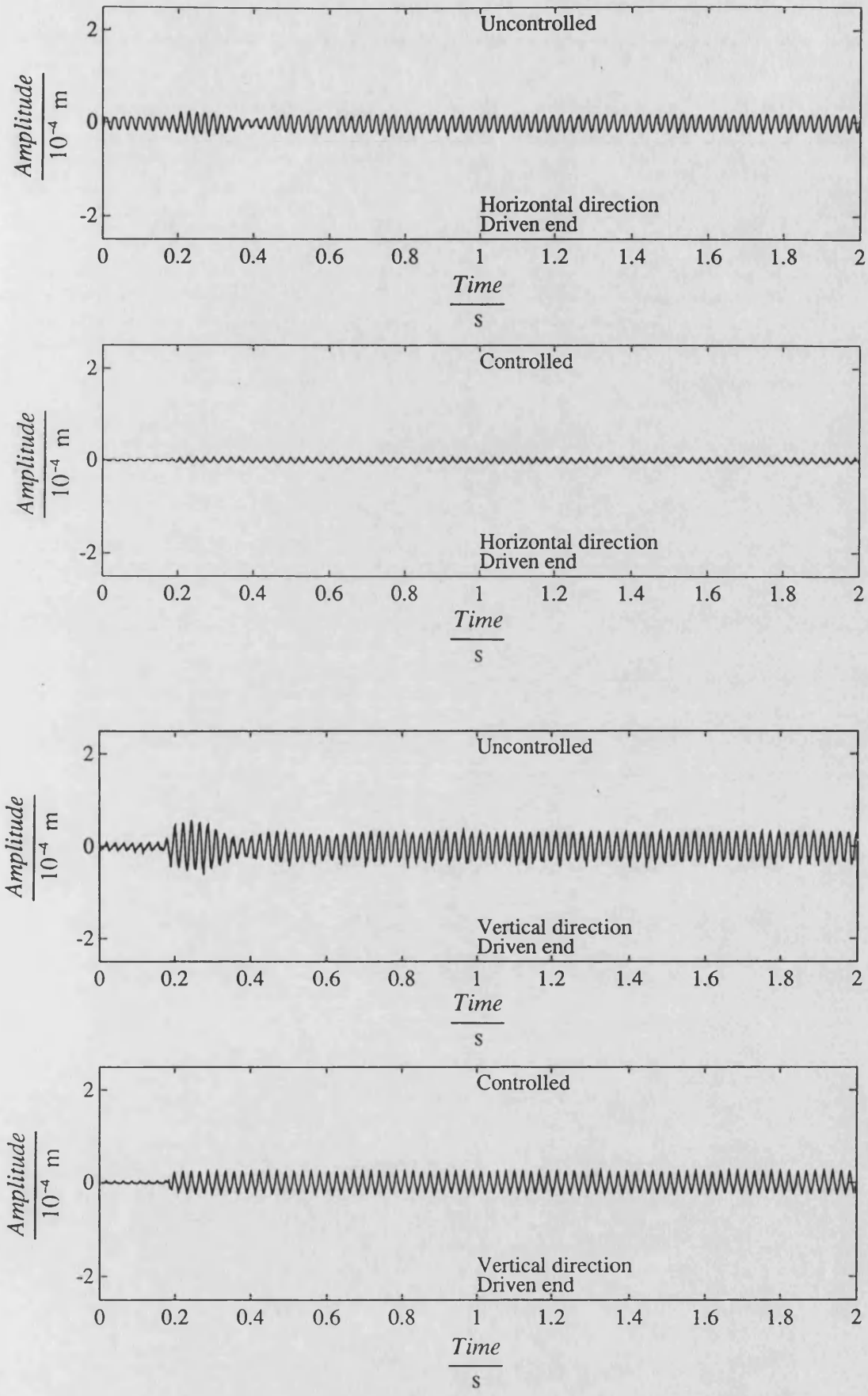

Fig. 7.19 Measured transient responses of uncontrolled and H_∞ controlled system due to sudden mass loss at speed 278 rad/s

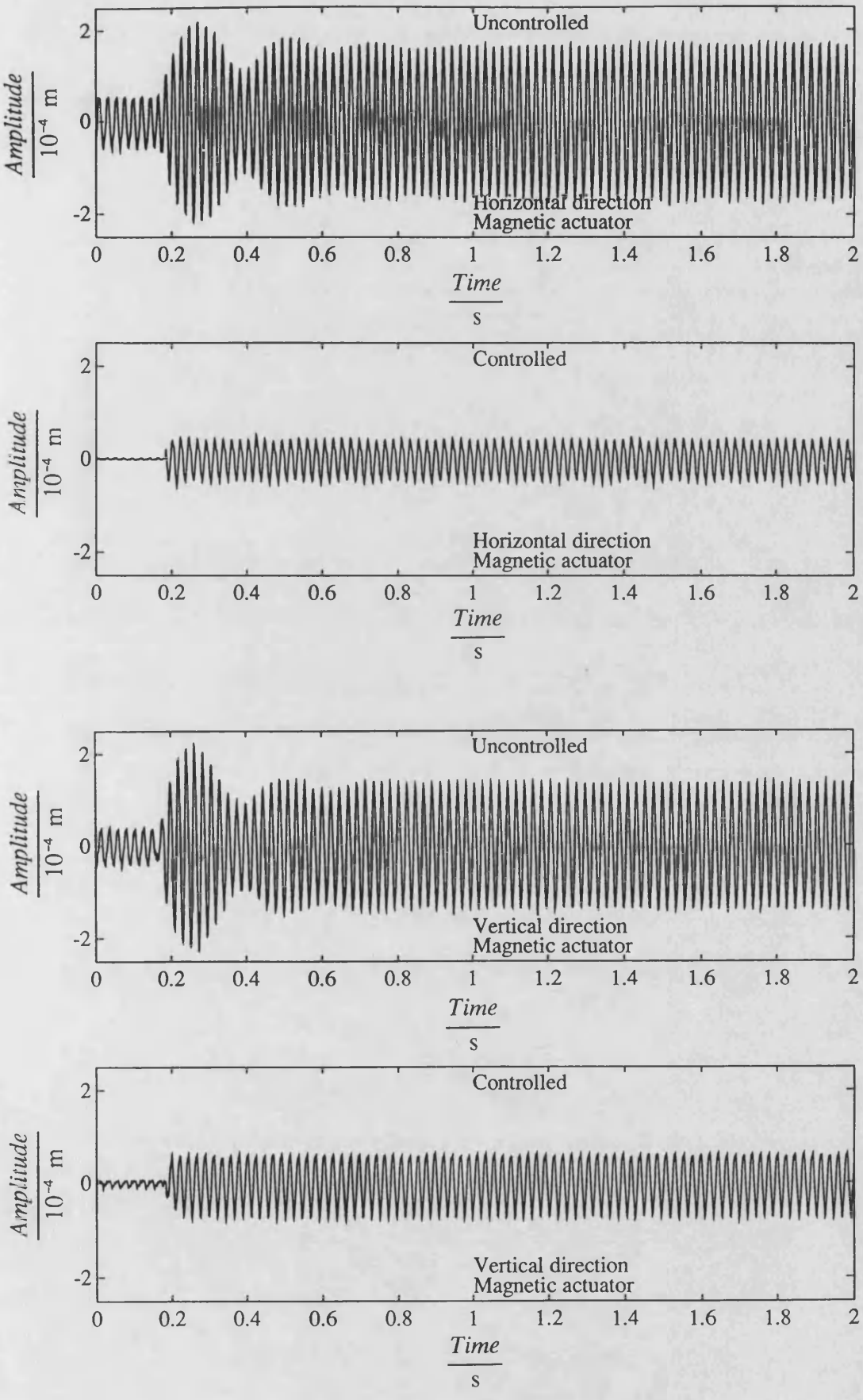

Fig. 7.19 (continued)

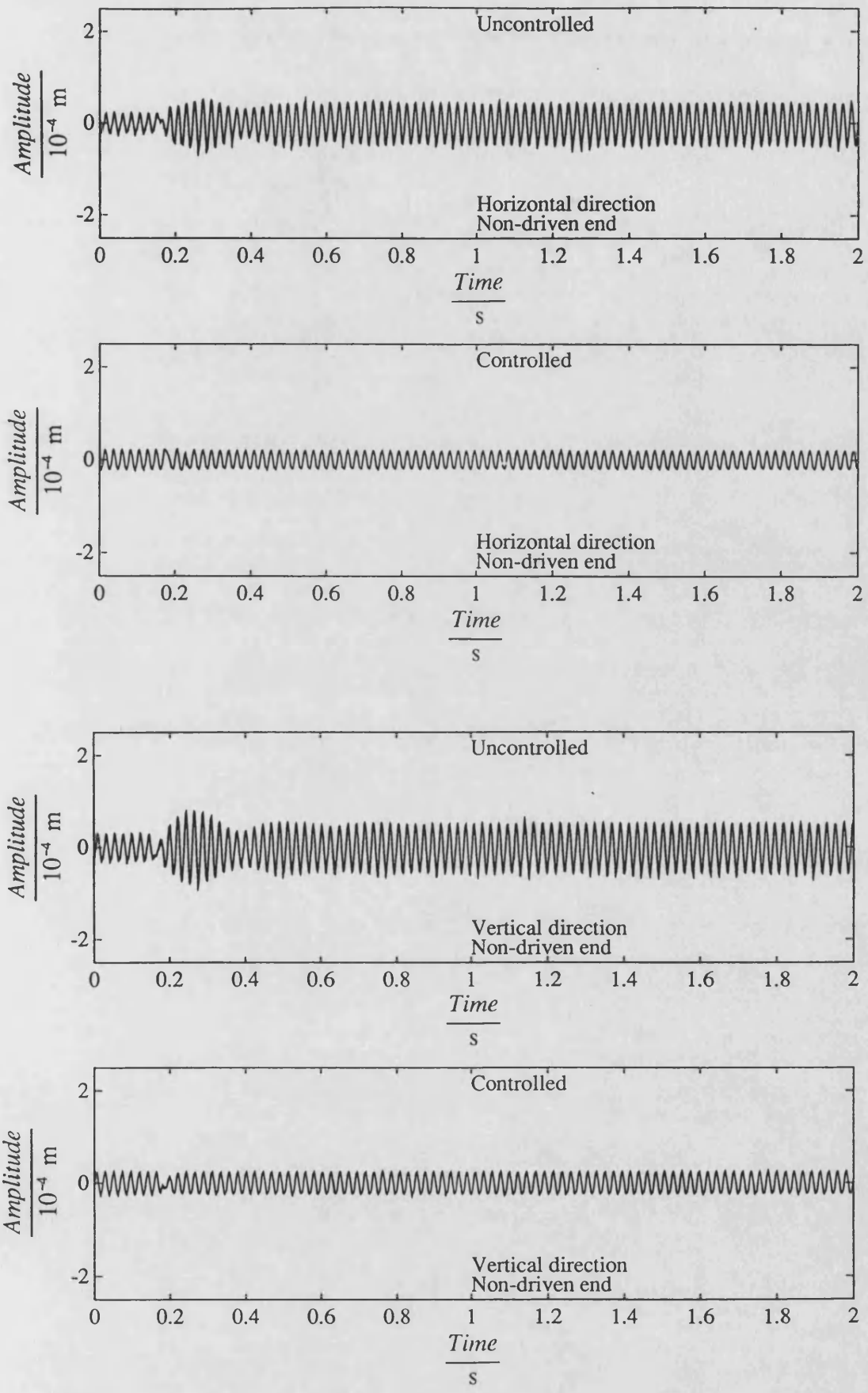

Fig. 7.19 (continued)

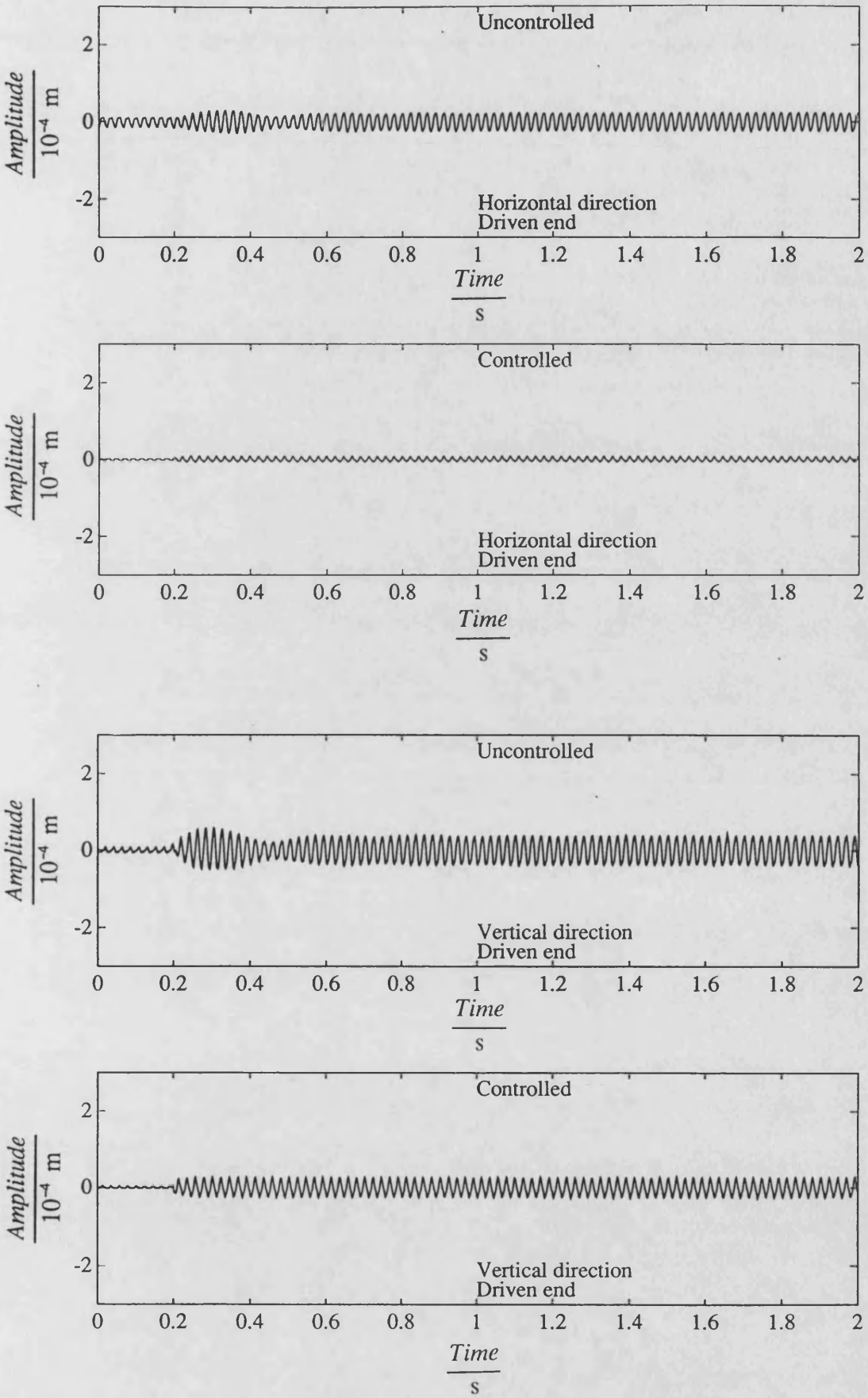

Fig. 7.20 Measured transient responses of uncontrolled and H_∞ controlled system due to sudden mass loss at speed 283 rad/s

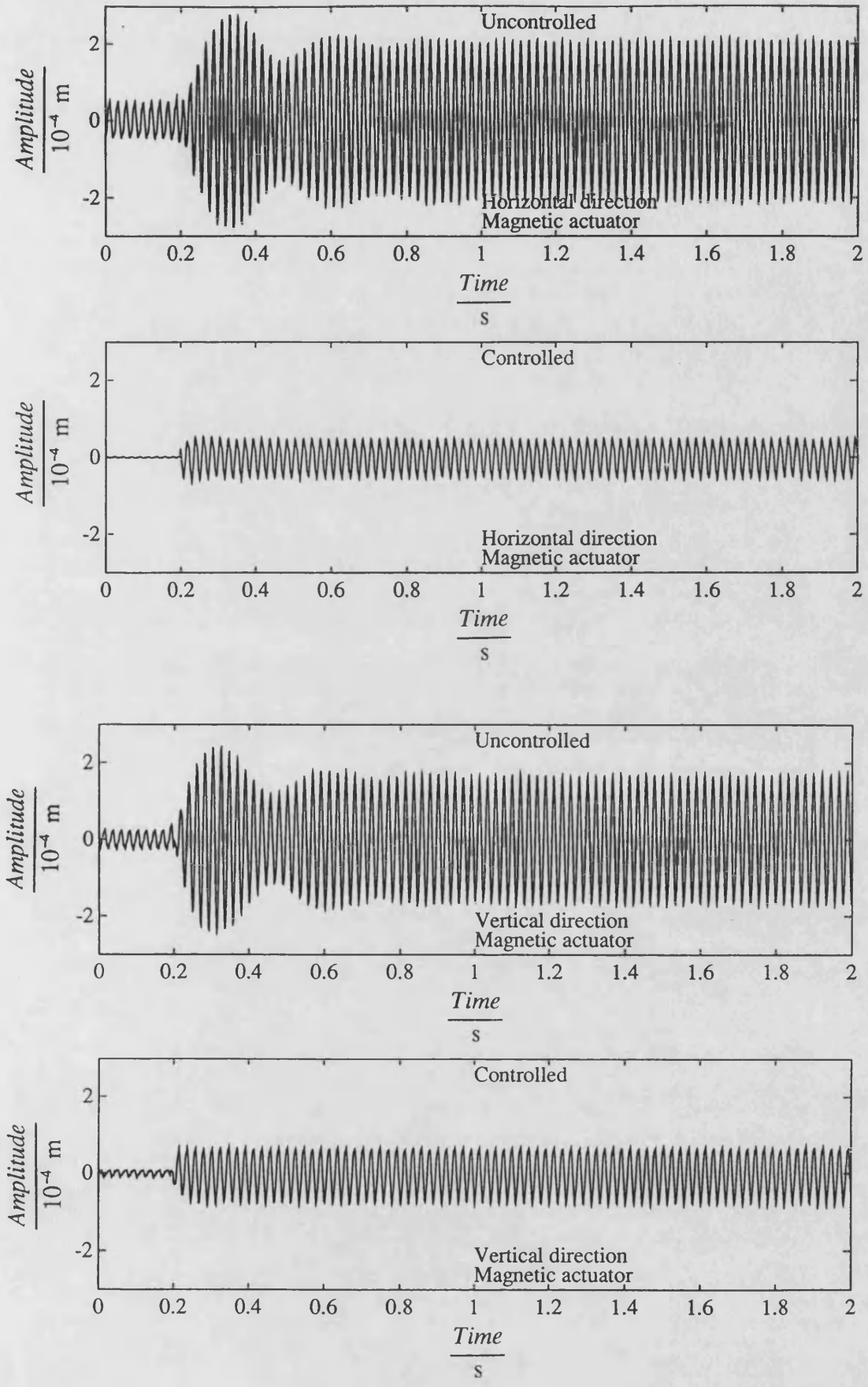

Fig. 7.20 (continued)

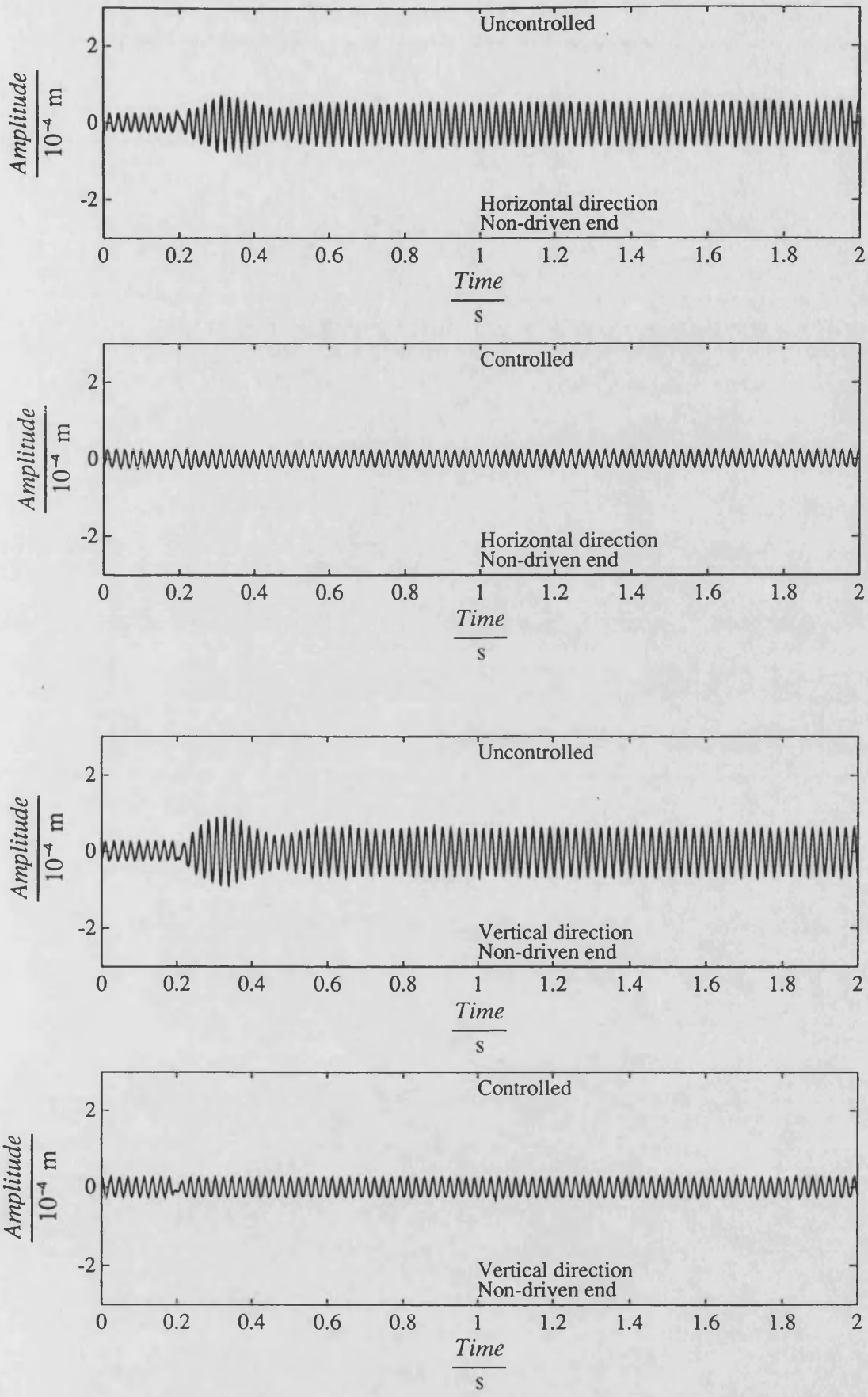

Fig. 7.20 (continued)

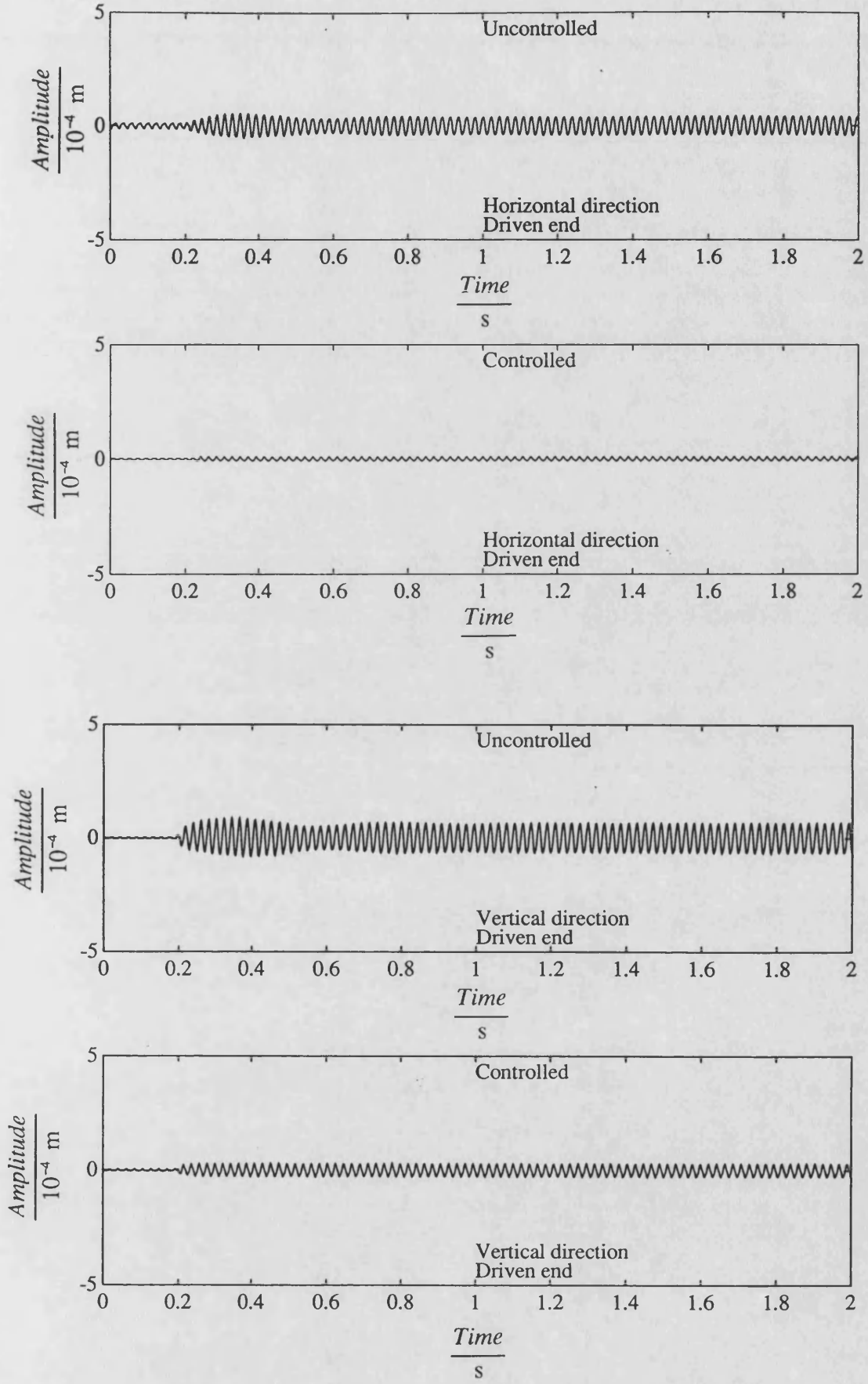

Fig. 7.21 Measured transient responses of uncontrolled and H_∞ controlled system due to sudden mass loss at speed 288 rad/s

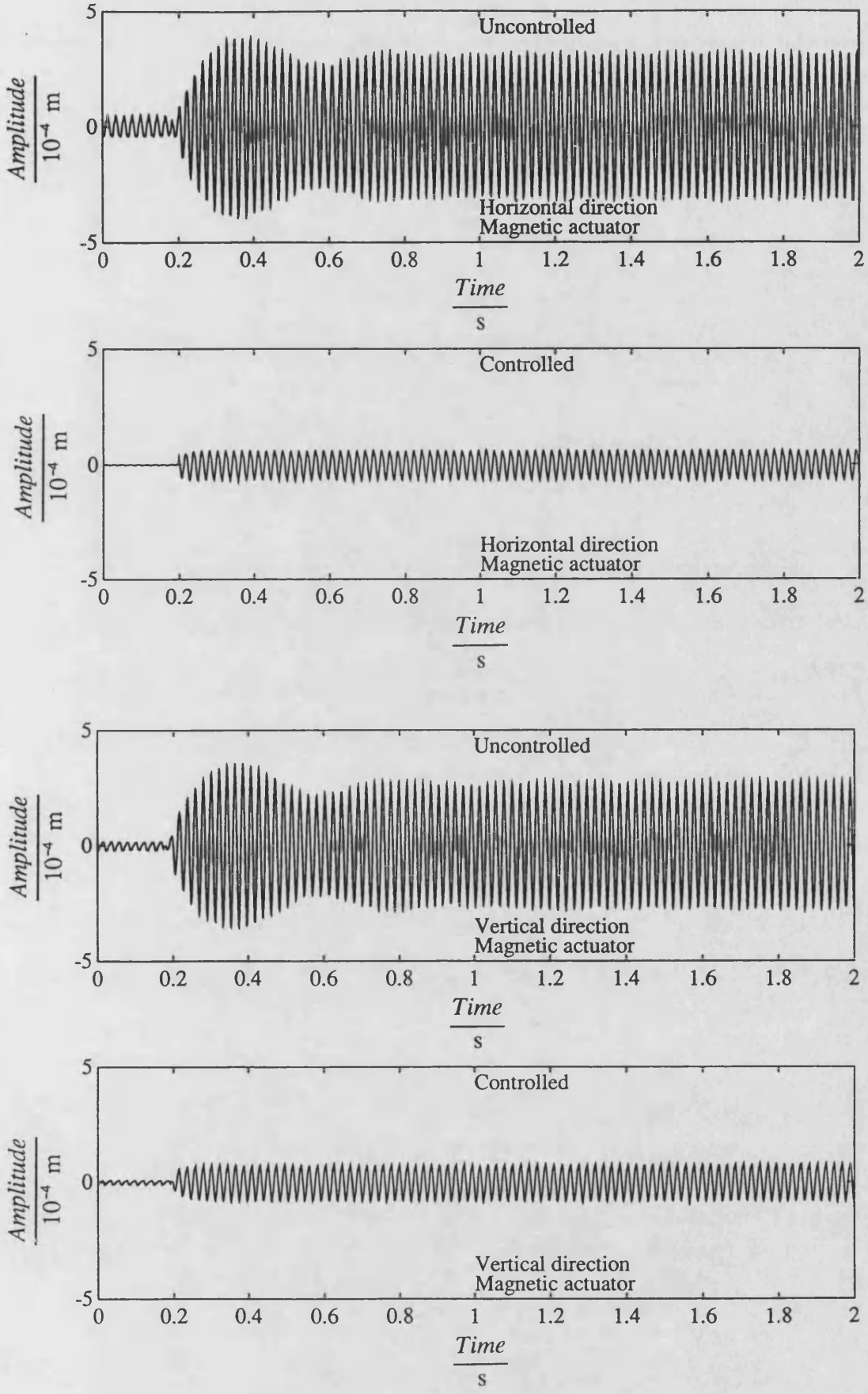

Fig. 7.21 (continued)

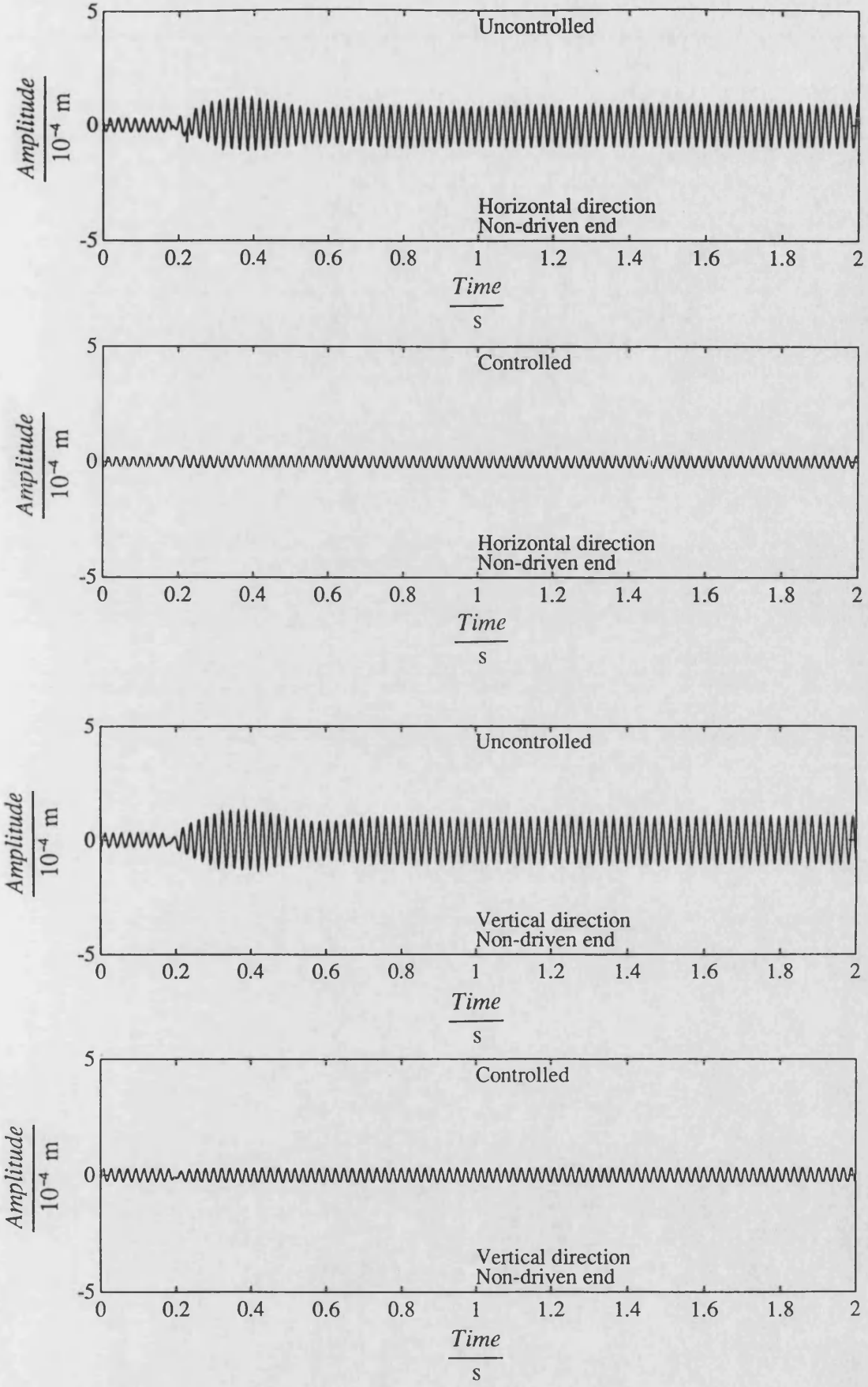

Fig. 7.21 (continued)

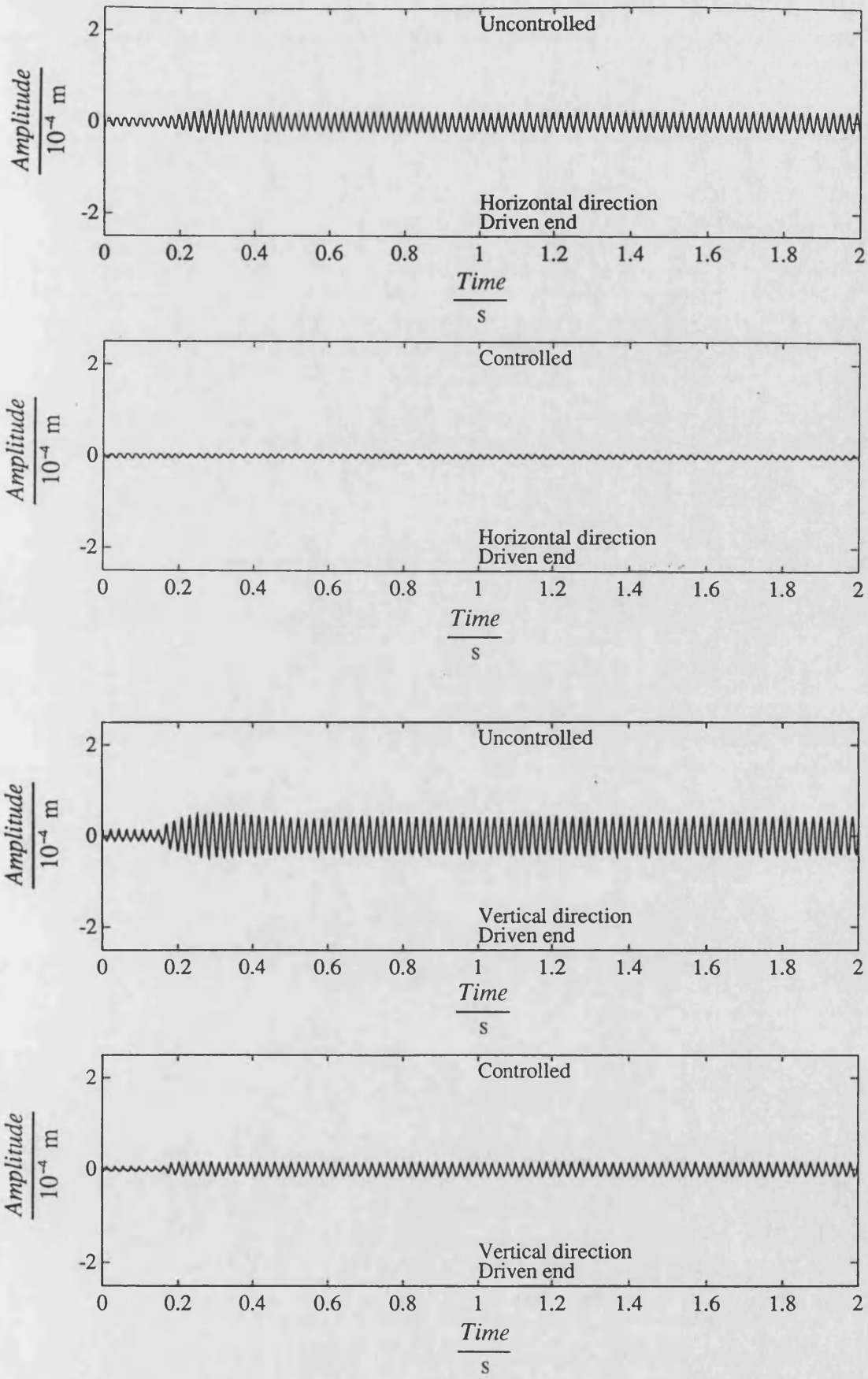

Fig. 7.22 Measured transient responses of uncontrolled and H_∞ controlled system due to sudden mass loss at speed 293 rad/s

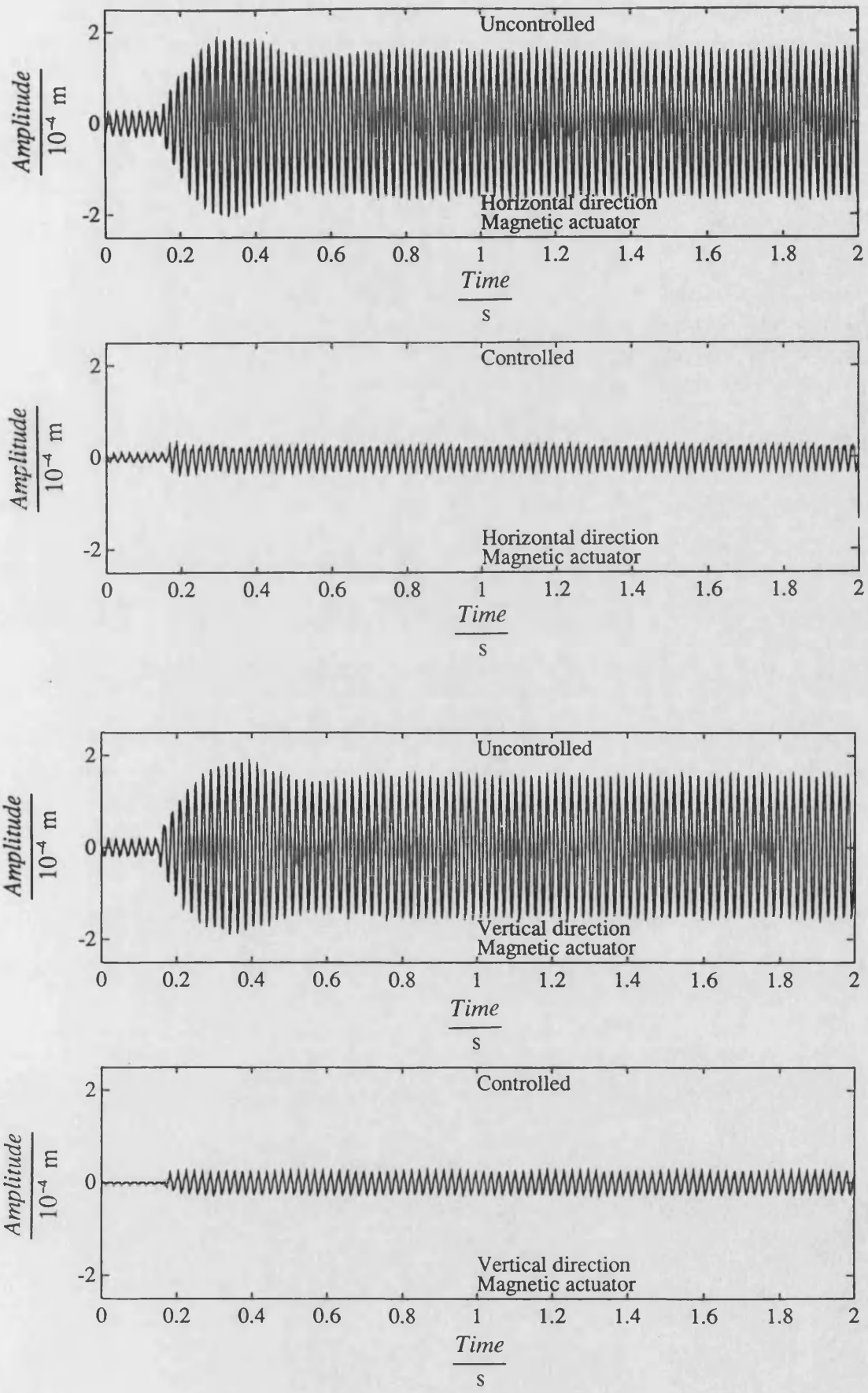

Fig. 7.22 (continued)

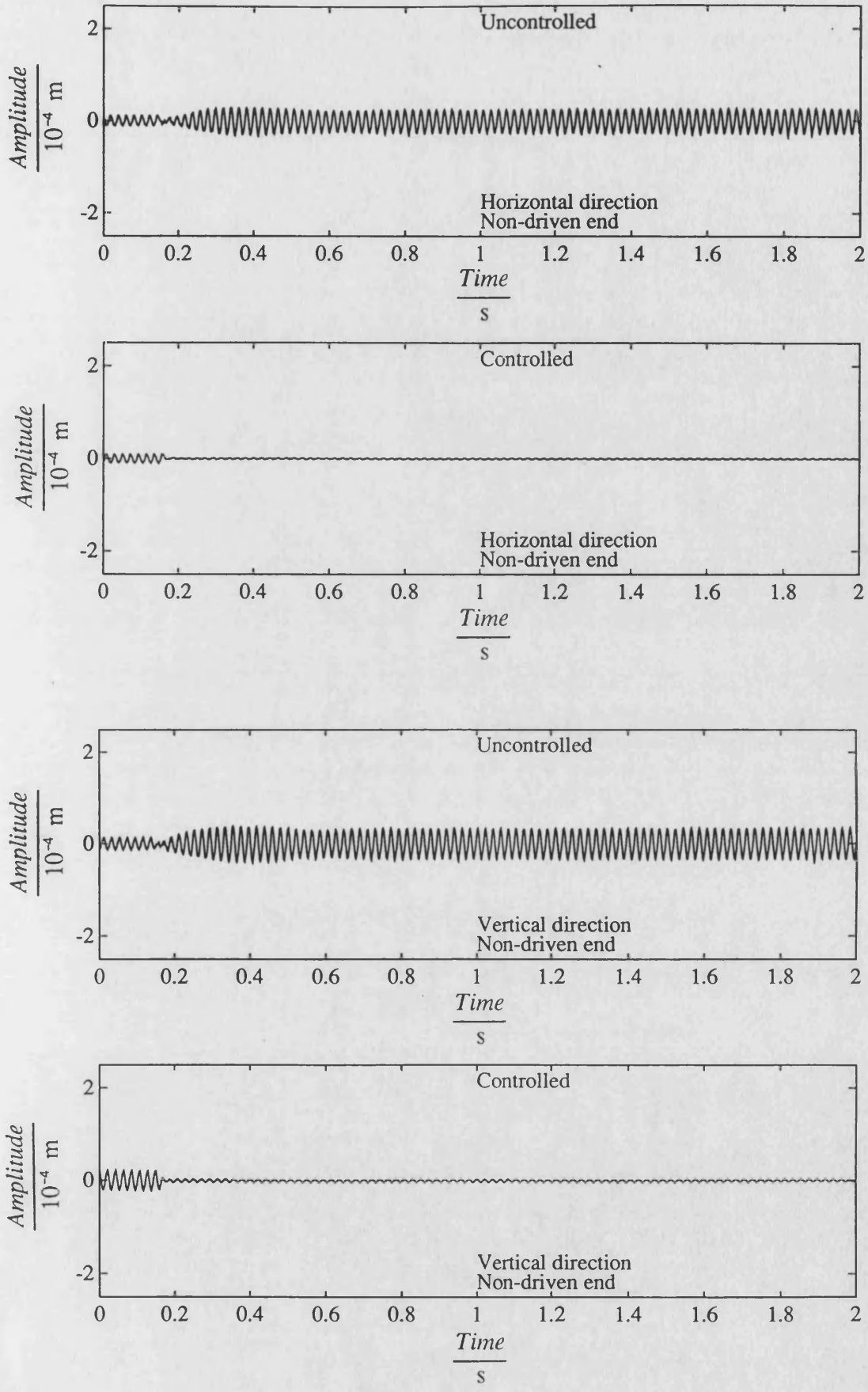

Fig. 7.22 (continued)

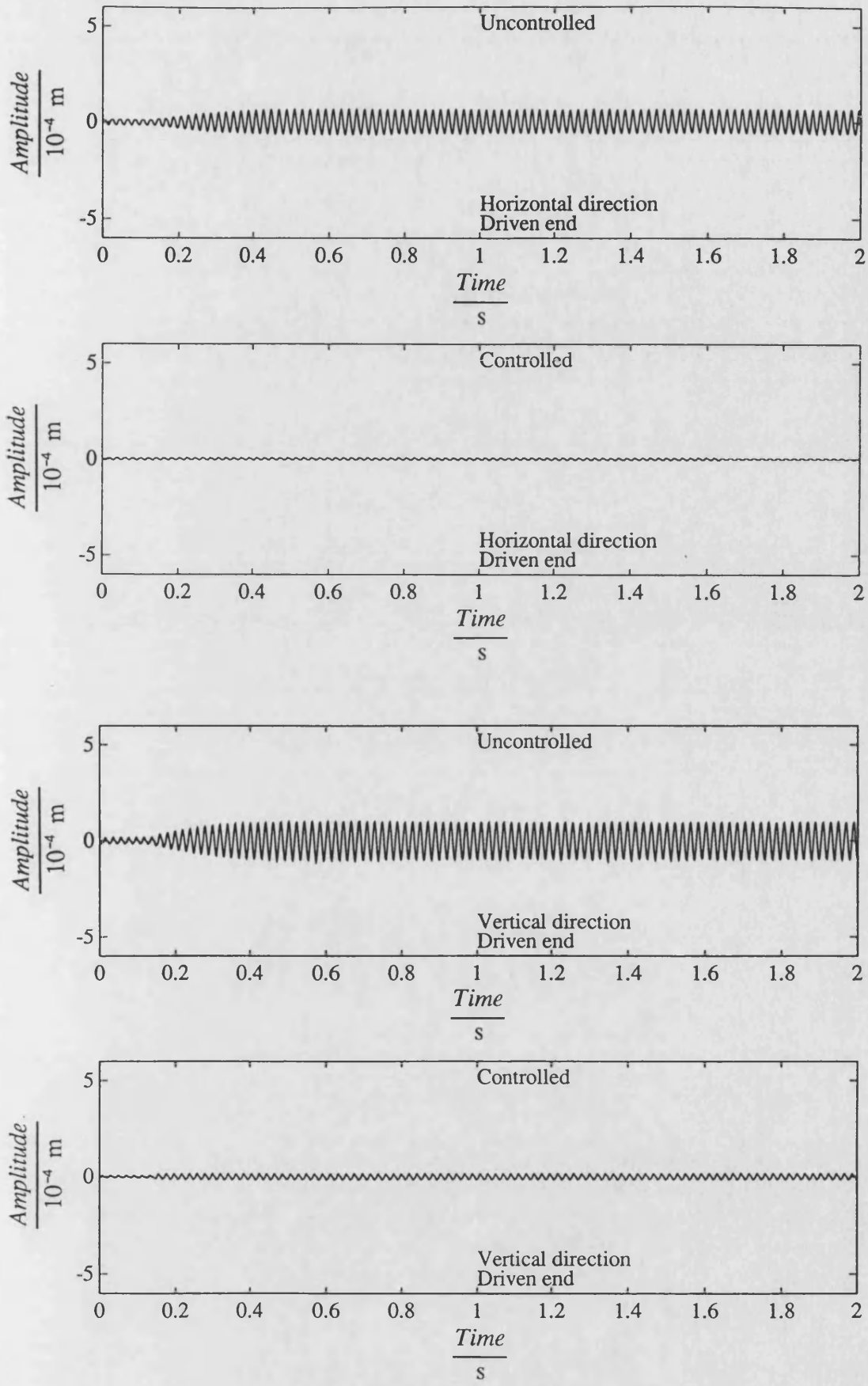

Fig. 7.23 Measured transient responses of uncontrolled and H_∞ controlled system due to sudden mass loss at speed 301 rad/s

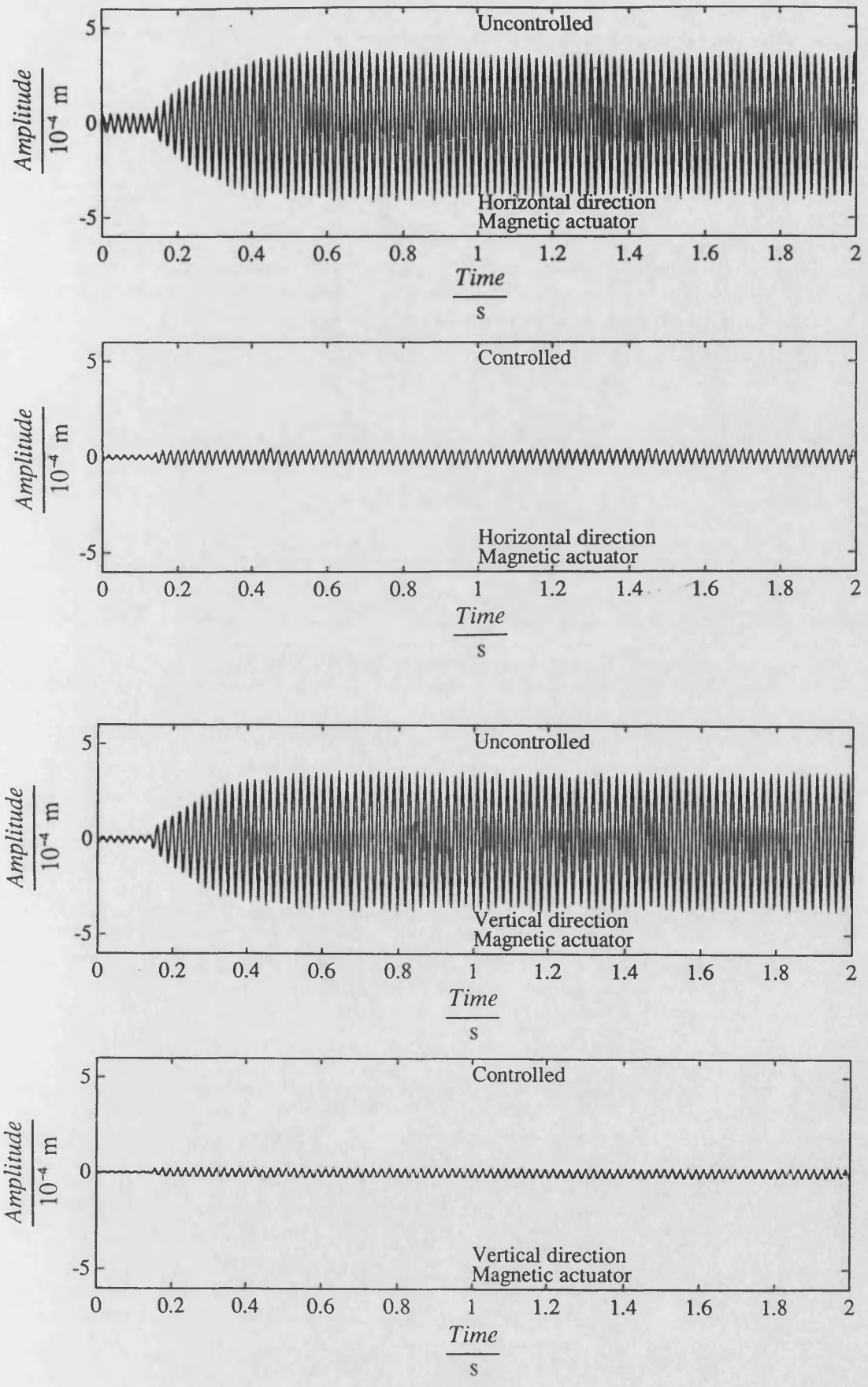

Fig. 7.23 (continued)

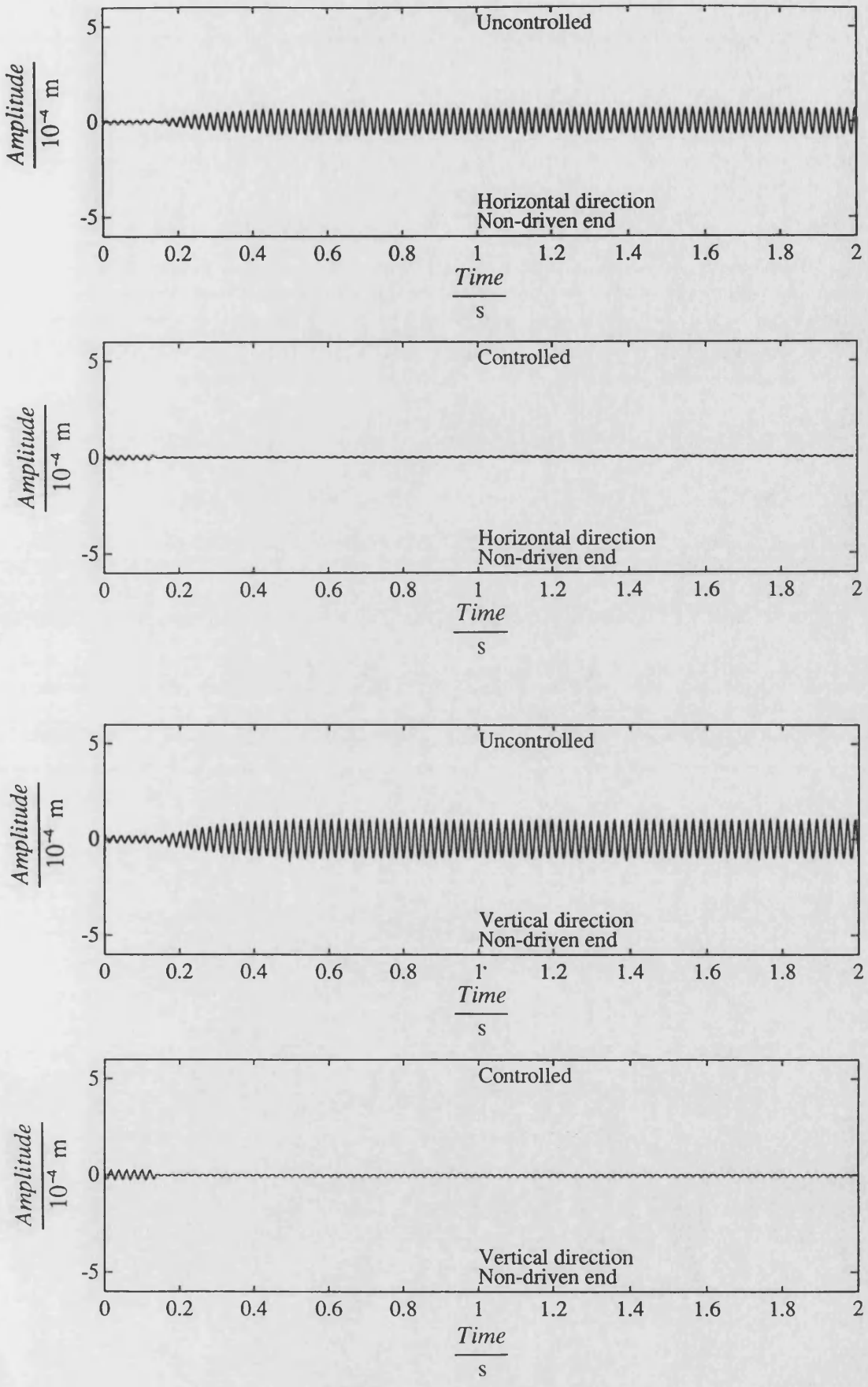

Fig. 7.23 (continued)

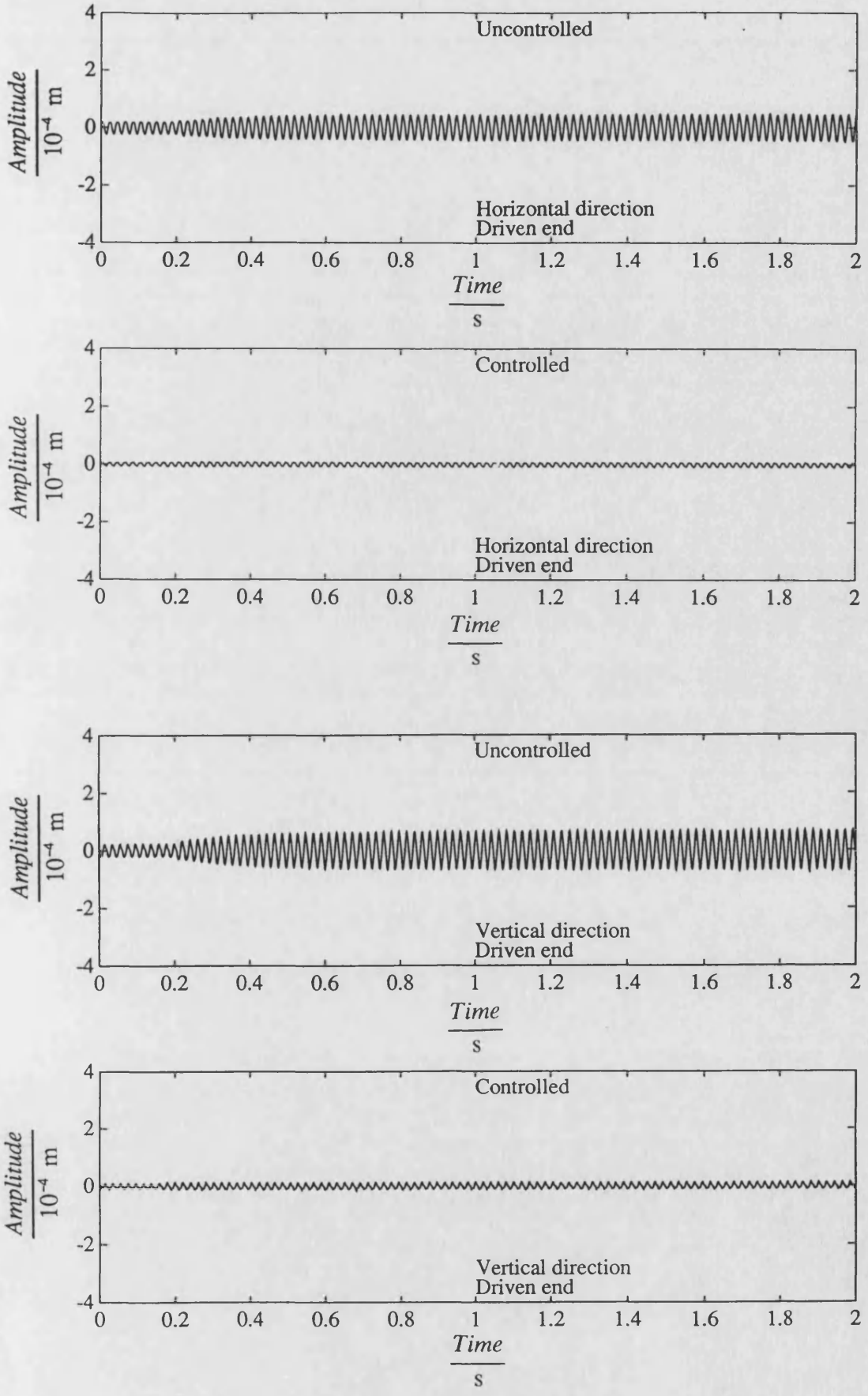

Fig. 7.24 Measured transient responses of uncontrolled and H_∞ controlled system due to sudden mass loss at speed 305 rad/s

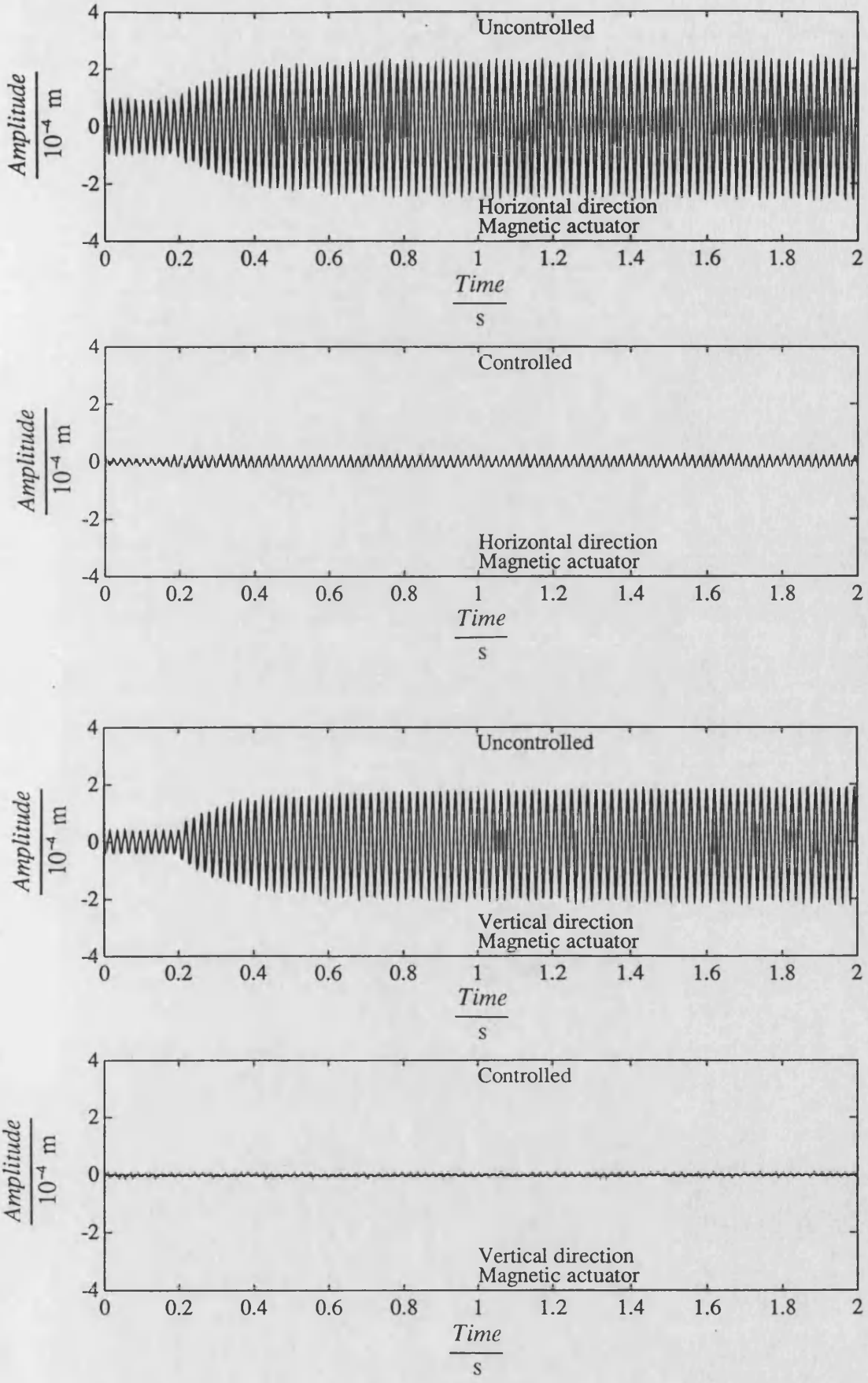

Fig. 7.24 (continued)

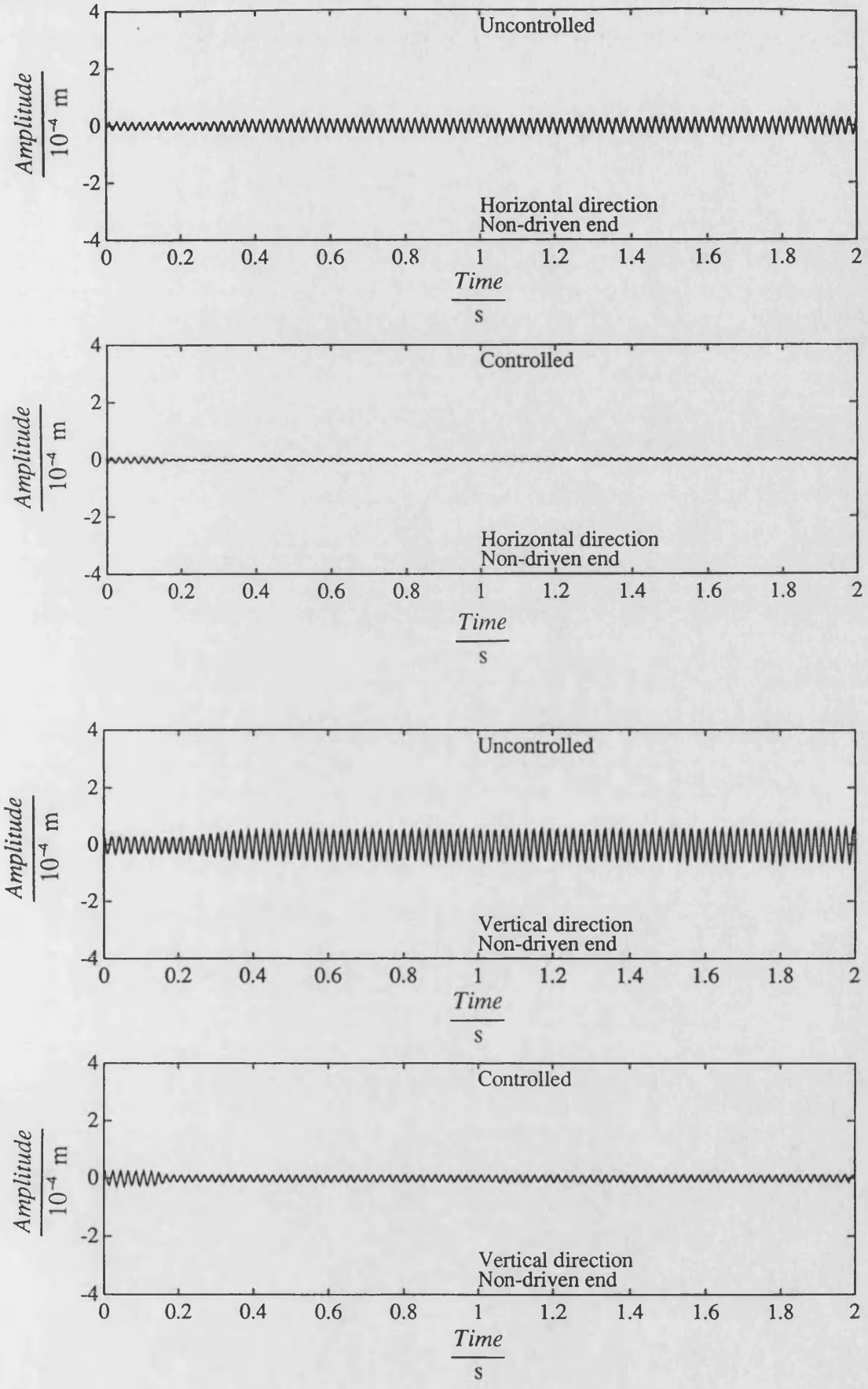

Fig. 7.24 (continued)

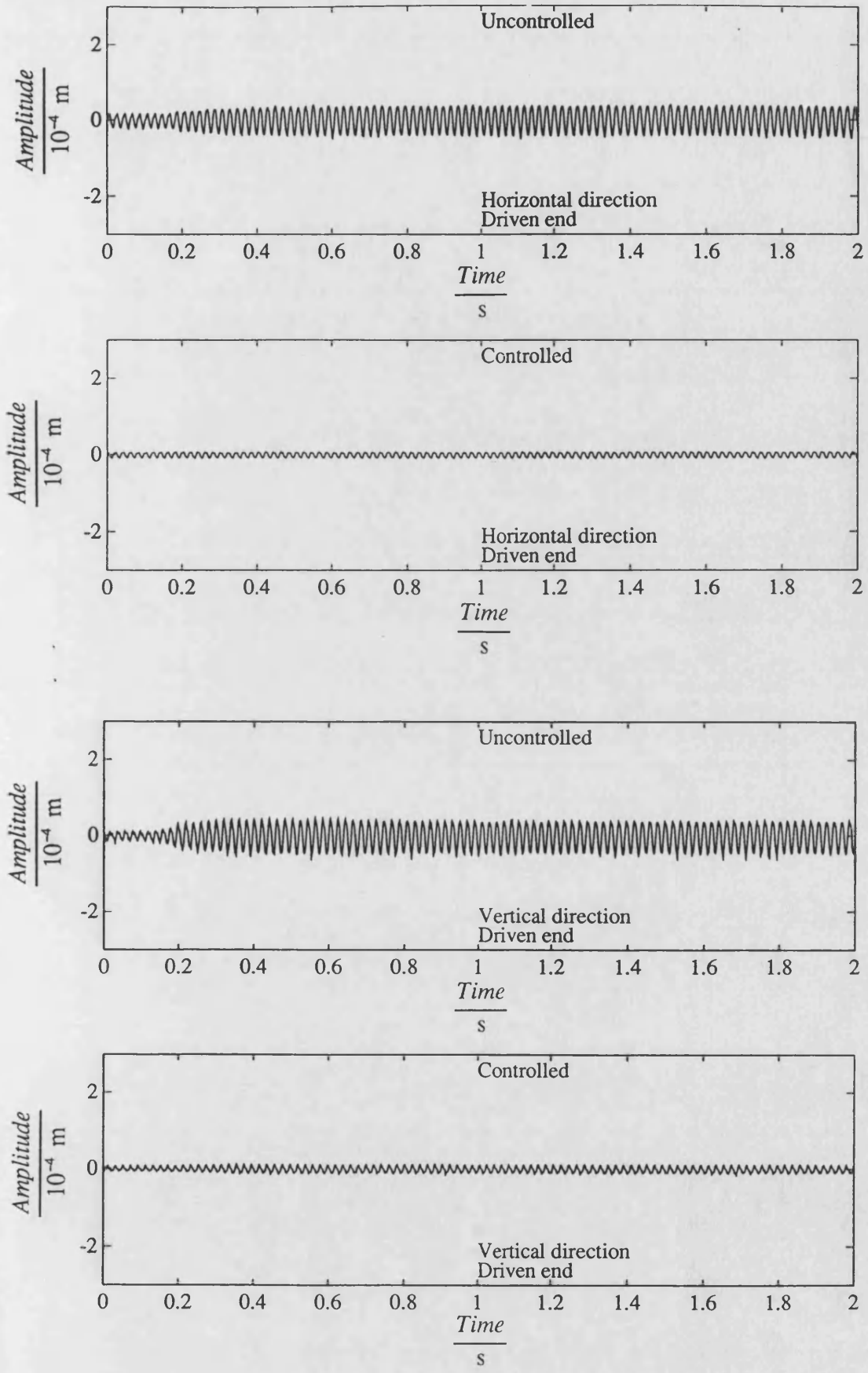

Fig. 7.25 Measured transient responses of uncontrolled and H_∞ controlled system due to sudden mass loss at speed 309 rad/s

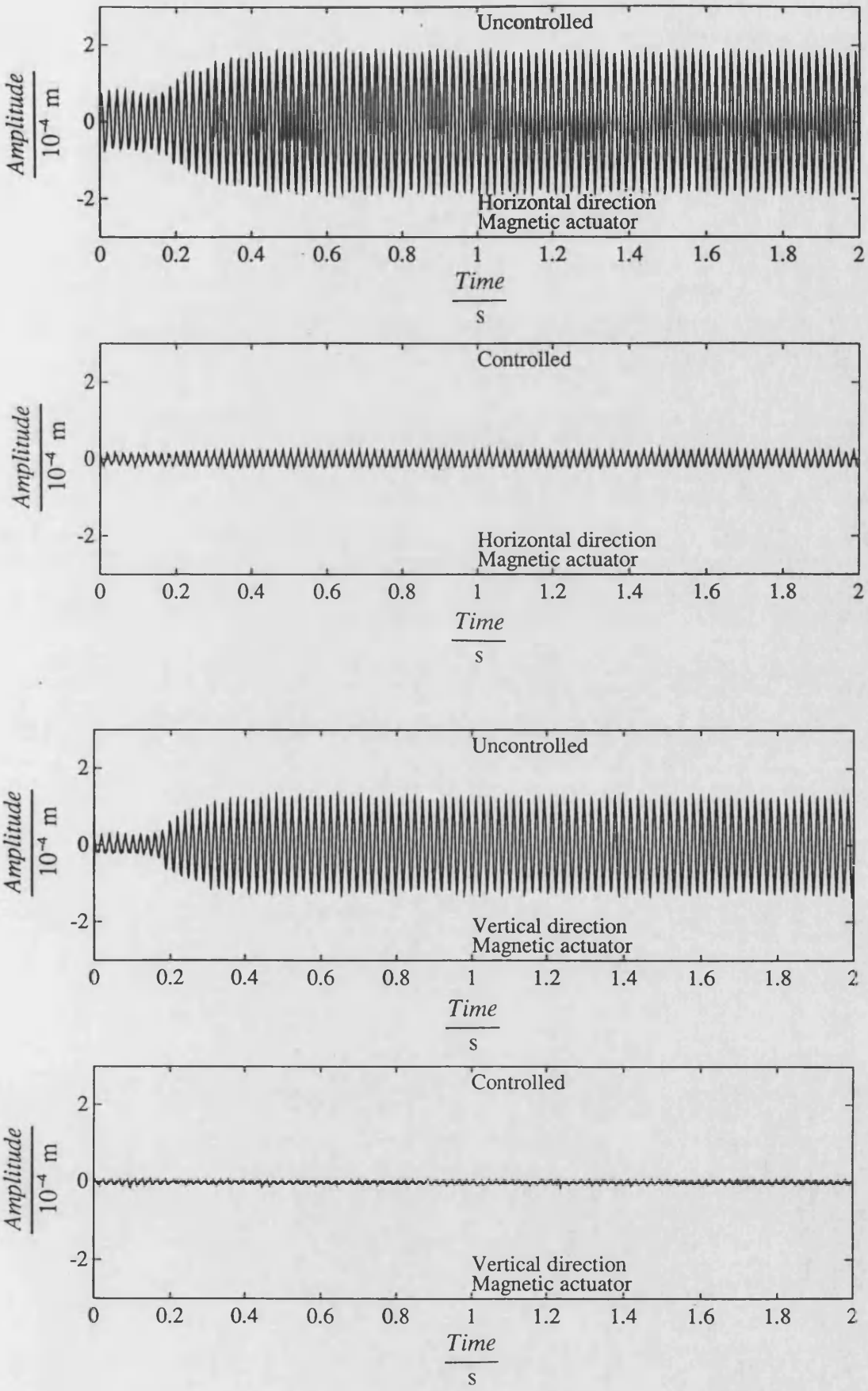

Fig. 7.25 (continued)

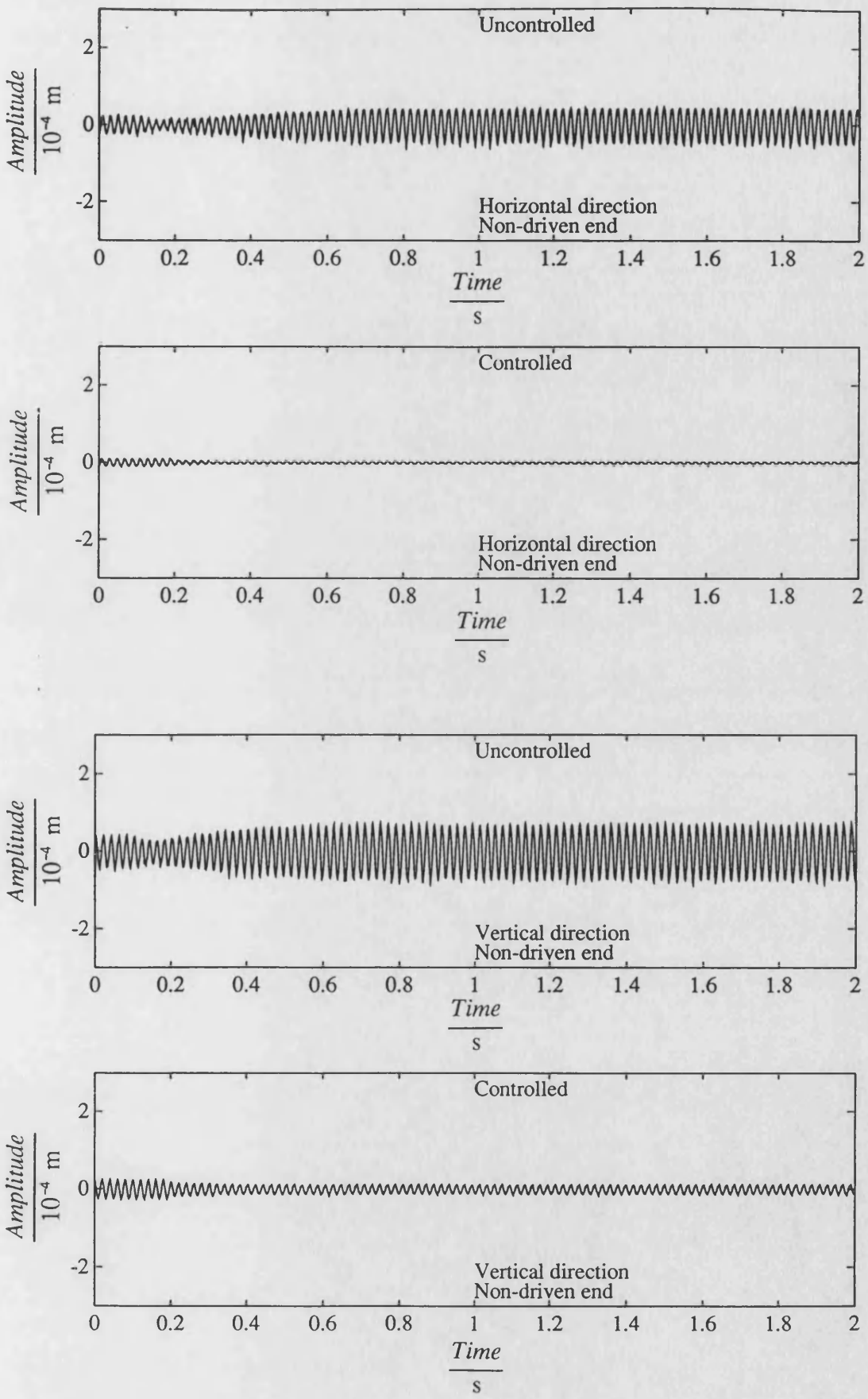

Fig. 7.25 (continued)

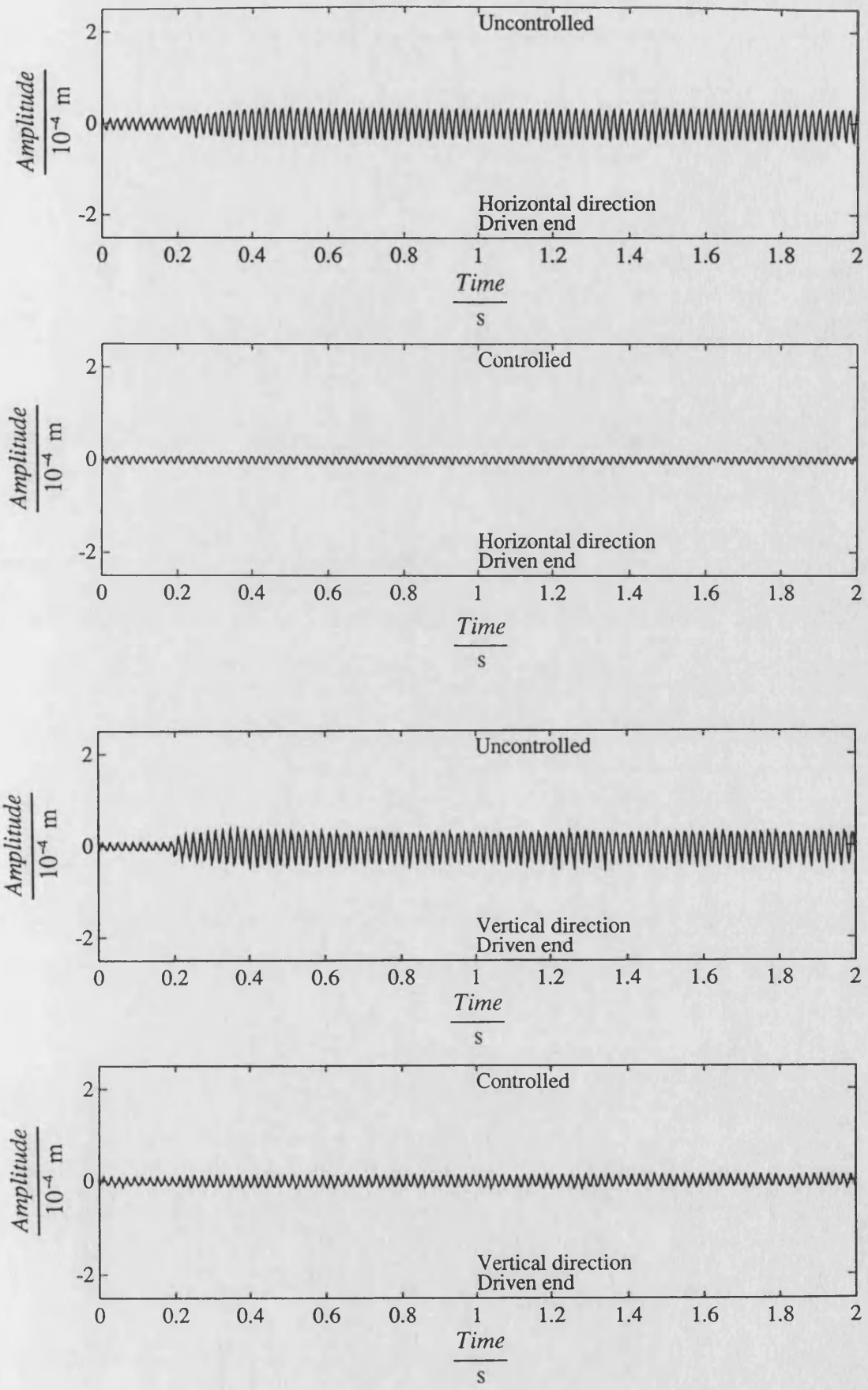

Fig. 7.26 Measured transient responses of uncontrolled and H_∞ controlled system due to sudden mass loss at speed 314 rad/s

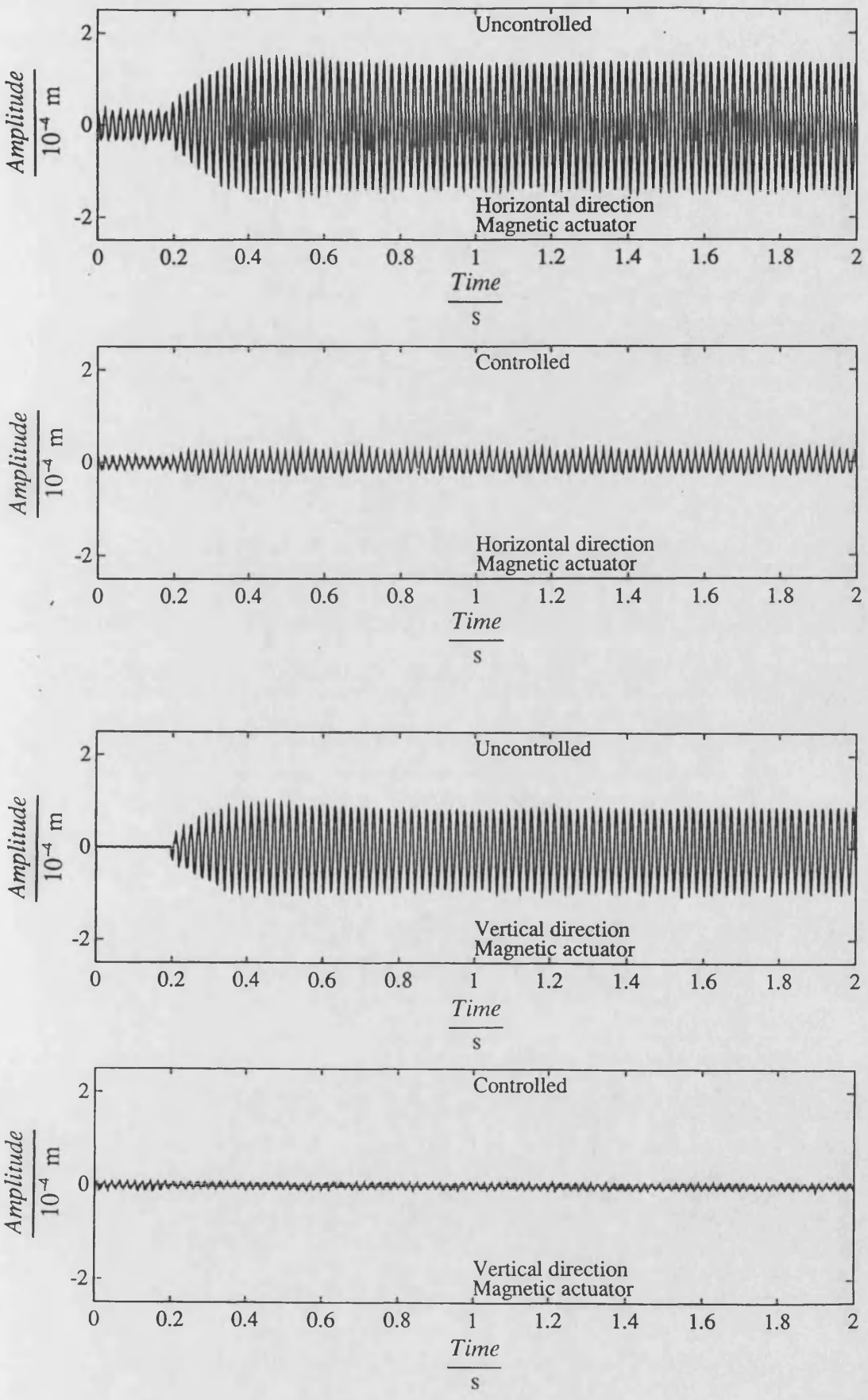

Fig. 7.26 (continued)

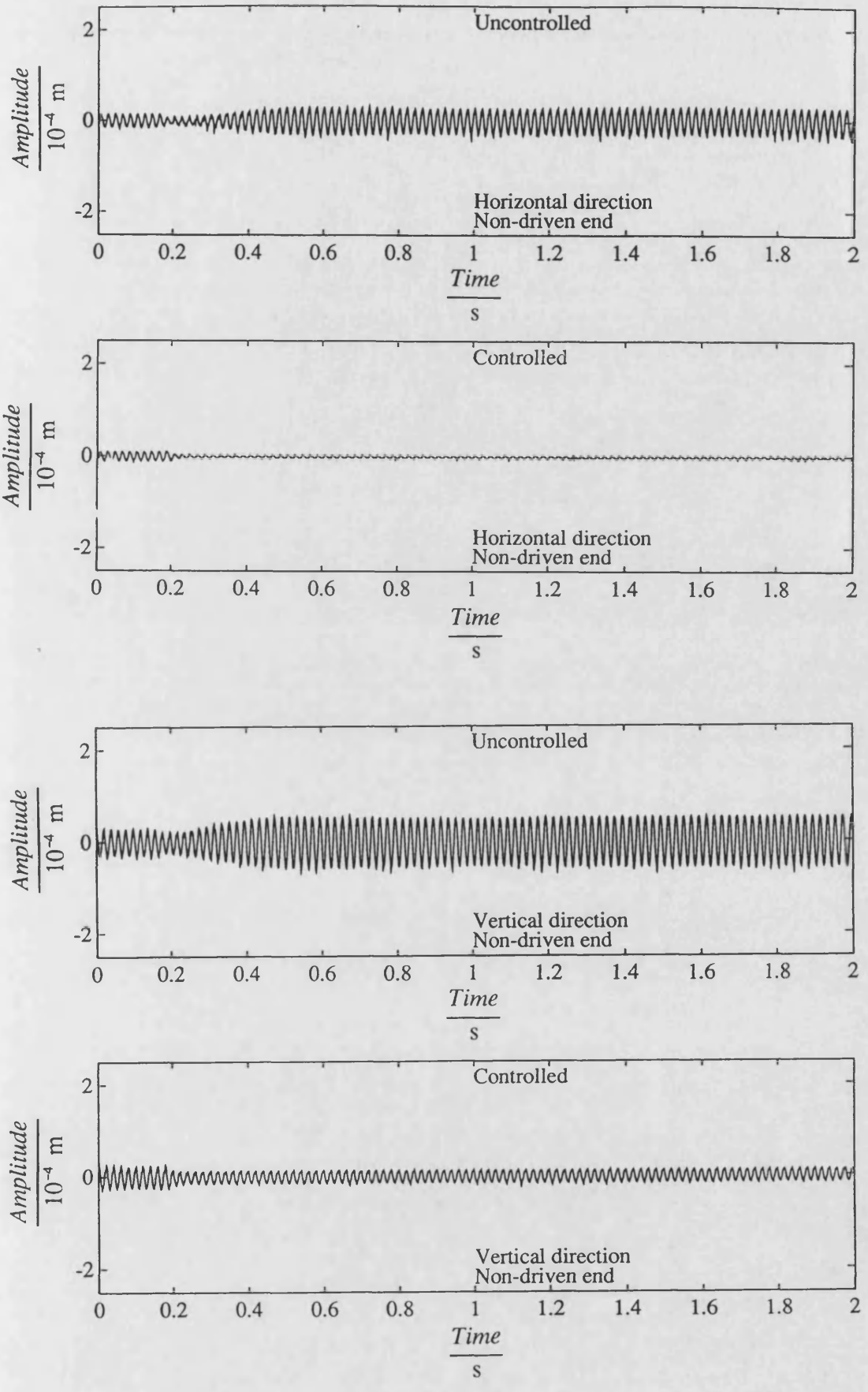

Fig. 7.26 (continued)

CHAPTER 8 CONCLUSIONS AND RECOMMENDATIONS

Theoretical and experimental research on the active vibration control of a flexible rotor-bearing system using H_∞ control strategies has been carried out. The control strategies were implemented in a rotor-bearing system using a magnetic actuator. Real time digital control was realized using transputer hardware. Both steady state and transient vibration reduction were considered and the control design was also carried out to achieve controller robustness and avoidance of spillover problems.

The H_∞ controller design procedure for rotor-bearing systems involved analysis of the open-loop system, model reduction, the control actuator, measurement noise, guidelines of choosing weighting functions, the formulation of the H_∞ problem, and derivation of the controller. The dynamic analysis of the open-loop system produced an overall view on how the system responses are distributed in the frequency domain. This information was used to determine the retained modes in the model reduction and the choice of a weighting function matrix. The results from the analysis of the actuator and measurement noise were used to determine two other weighting function matrices. Guidelines for weighting choices were presented. Computer simulation was used to predict the dynamic response of the system. The main characteristics and dynamic responses of both open loop and closed loop real system were then obtained. Errors were incurred since the unbalance mass distribution was unknown and the dynamic model of the journal bearings used was based on isoviscous theory.

Significant steady state synchronous vibration reduction was achieved by implementing the H_∞ controller on the experimental system with unknown unbalance forcing. In order to provide a performance case to compare with, the responses from

the open loop adaptive controlled system were measured. These responses were optimised in a least-squares sense. Similar performance for vibration reduction was achieved using H_∞ control.

Vibration reduction was also obtained in the non-synchronous response case, in which the rotor was excited by both the unbalance forcing and disturbance forces from a second magnetic actuator. The rotor vibration levels were brought down significantly using the H_∞ controller whenever the disturbance frequency was above, near, or below the system critical speeds. Exact forms of disturbance forcing were not required in the control design. This was the reason that the H_∞ controller could cope with a wide range of disturbances.

Transient vibration of the experimental system was excited by sudden loss of mass. Transient vibration levels were reduced significantly using the H_∞ controller together with the transition time from one steady state condition to another. Consequently, the responses of the controlled system could pass the transient period far more smoothly and quickly than those of the uncontrolled system. This demonstrates also that the H_∞ controller is well qualified to control transient vibration of rotor-bearing systems.

The robustness of the controller was also examined. It was found that the H_∞ controller was not sensitive to the variation of the system structure coefficients, which may be caused by the rotational speed variation and/or inaccurate modelling. Furthermore, inaccurate modelling of the rotor and bearings could be compensated by the controller. It was also found that the controller was not sensitive to the variation of the measurement positions. Of course, the above conclusions may not be valid if

the changes are large. In the case where a displacement transducer away from the actuator failed (zero signal), it was found that the controller still worked well. However, this is not true for the transducers at the actuator position, since system instability may result.

The dynamic analysis of the H_∞ controller showed that it had a low pass characteristic, which prevented high frequency signals leaving the controller. Hence, the neglected high frequency modes were not excited by the control forces. This was used to avoid spillover. Although model reduction method was used in the control design process, the formulation of H_∞ problem required that the neglected high frequency modes should remain as a disturbance to the system. The minimization of the influence from the disturbance to the system output constitutes a basis for the H_∞ control design. The results obtained from the experimental tests confirmed this. Whenever tests were carried out either in steady state or transient cases, no spillover problem was observed.

Other advantages also exist in applying the H_∞ controller. In some applications, where a direct output feedback control is used, differential circuitry is required to obtain the velocities of the rotor lateral motion. Not only is extra hardware needed, but the velocity signals, obtained by differentiating displacement signals, can be contaminated easily by high frequency noise. Moreover, spillover may occur. However, these weaknesses could be avoided by using the H_∞ controller. Open loop adaptive control is effective in both vibration reduction and spillover avoidance, but is not robust to the variation of the system structure and on-line estimation must be carried out at different rotational speeds. In contrast, the H_∞ controller could cope with a large

rotational speed range.

The effect of shaft surface roughness on the control design was introduced to improve the controlled system response. Without considering it, the controller may make the responses of the controlled system worse at low rotational speeds where the measurement signals are due mainly to the roughness. If the rotor surface is not very smooth, it may be incorporated into the controller design.

The work in this thesis has, for the first time, successfully developed H_∞ controllers for a flexible rotor-bearing system. Also steady state and transient vibration control was demonstrated experimentally. Another feature, not considered in other published work, was the inclusion of shaft surface roughness spectra in the controller designs. As a result the designed controllers did not suffer from the usual problem associated with closed loop instability. Controller tuning was not required. The work has therefore highlighted an improved approach to rotor vibration control.

Further investigation exists for the application of the H_∞ control strategy to a fully magnetically suspended rotor system. In the present project, the journal bearings provided support for the rotor and suppressed instability. The potential of the H_∞ strategy has not been fully evaluated. Thus, the application of the design to a fully magnetically suspended rotor system may give a deeper insight into the effectiveness of this method.

REFERENCES

[1] Beams, J. W., "Magnetic bearings", Soci. of Auto. Engr, Auto. Engineering Congress, Detroit, Paper 810A, Jan 1964, pp.13-17.

[2] Berry, T. and Keogh, P. S., "Modal analysis of a rotor system", Internal Report of School of Mech. Eng., University of Bath, No.2067, 1991.

[3] Berry, T., Burrows, C. R., and Keogh, P, "Active control of synchronous and transient rotor vibration with minimal system modelling", ASME paper 93-WA/DSC-4, 1993.

[4] Bleuler, H, and Schweitzer, G., "Dynamics of a magnetically suspended rotor with decentralized control", Applied Control and Identification Symposium, IASTED, Copenhagen, 1983.

[5] Bleuler, H., "Decentralized control of magnetic rotor bearing systems", Dissertation No. 7573, ETH, Zurich, 1984.

[6] Bleuler, H. and Salm, J., "Active electromagnetic suspension and vibration control of an elastic rotor with a signal processor", Proc. IMechE 4th Intl. Conf. on Vibration in Rotating Machinery, Paper C287/88, 1988, pp.101-108.

[7] Bornstein, K. R., "Dynamic load capabilities of active electromagnetic bearings", Trans. ASME J. of Tribology, Vol.113, July 1991, pp.589-603.

[8] Burrows, C. R. and Sahinkaya, M. N., "Vibration control of multi-mode rotor-

bearing systems", Proc. Royal Soci. Lond., A-386, 1983, pp.77-94.

[9] Burrows, C. R., Sahinkaya, M. N., and Turkay, O. S., "An adaptive squeeze film bearing", Trans. ASME J. Tribology, Vol.106, Jan. 1984, pp.145-151.

[10] Burrows, C. R. and Sahinkaya, M. N., "Control of stability and the synchronous vibration of a flexible rotor supported on oil film bearings", Trans. ASME J. of Dynamic Systems, Measurement, and Control, Vol.107, 1985, pp.139-144.

[11] Burrows, C. R. and Sahinkaya, M. N., "Control strategies for use with magnetic bearings", Proc. of IMechE 4th Intl. Conf. on Vibrations in Rotating Machinery, Edinburgh, Paper C273/88, 1988, pp.23-32.

[12] Burrows, C. R. and Sahinkaya, M. N., Traxler, A. and Schweitzer, G., "Design and application of a magnetic bearing for vibration control and stabilization of a flexible rotor", Proc. of 1st Intl. Symp. on Magnetic Bearings, Zurich, 1988, pp.159-168.

[13] Burrows, C. R., Sahinkaya, M. N., and Clements, S., "Electromagnetic control of oil film supported rotors using sparse measurements", Trans. ASME J. of Vibration, Acoustics, Stress, and Reliability in Design, Vol.110, July 1988, pp.295-299.

[14] Burrows, C. R., Sahinkaya, M. N., Kucuk, N. C., and Tong, M. L., "In situ estimation of the dynamic characteristics of an uncavitated squeeze film damper", Trans. ASME J. Tribology, Vol.110, Jan. 1988, pp.162-166.

[15] Burrows, C. R., Sahinkaya, M. N., and Clements, S., "Active vibration control of flexible rotors: an experimental and theoretical study", Proc. R. Soc. Lond., A422, 1989, pp.123-146.

[16] Burrows, C. R., Keogh, P. S., and Tasaltin, R, " Closed-loop vibration control of flexible rotors - an experimental study ", Proc. IMechE J. Mech. Eng. Sci., Vol. 207, No.C1, 1993, pp.1-17.

[17] Chen, H. M. and Darlow, M. S., "Magnetic bearing with rotating force control", Trans. ASME J. of Tribology, Vol.110, Jan. 1988, pp.100-105.

[18] Clements, S., "On-line vibration control of a flexible rotor bearing system", Ph.D Thesis, University of Stathclyde, 1987.

[19] Cooper, S., "Preliminary investigation of oil films for the control of vibration", Imeche Lubrication and Wear Conf., 1963, Paper 28, pp.305-315.

[20] Cunningham, R. E., Fleming, D. P., and Gunter, E. J., " Design of a squeeze-film damper for a multi-mass flexible rotor", Trans. ASME J. Eng. for Industry, 1975, pp.1383-1389.

[21] Den Hartog, J. P., Mechanical Vibrations, McGraw-Hill Book Company, New York, 1947.

[22] Dostal, M., Robert, J. B. and Holmes, R., "The effect of external damping on the vibration of flexible shafts supported in oil file bearings", J. of Sound and Vibration, 51(1), 1977, pp.69-87.

[23] Doyle, J. C., "Guaranteed margins for LQG regulators", IEEE Trans Auto. Cont., Ac-23, 1978, p756.

[24] Doyle, J. C., Glover, K., Khargonekar, P., and Francis, B. A., "State space solution to standard H_2 and H_infinity control problems", IEEE Trans. Auto. Cont., Vol.34, No.8, 1989, pp.831-847.

[25] Edney, S. L., Fox, C. H. J., and Williams, E. J., "Tapered Timoshenko finite elements for rotor dynamics analysis", J. of Sound and Vibration, 137(3), 1990, pp.463-481.

[26] Francis, B. A., A Course in H_∞ Control Theory, Springer Verlag, Berlin.

[27] Fujita, M., Matsumura, F., and Shimizu, M., "H-infinity robust control design for a magnetic suspension system", Proc. of 2nd Intl. Symp. on Magnetic Bearing, July 1990, Tokyo, pp.349-356.

[28] Furst, S. and Ulbrich, H., "An active support system for rotors with oil film bearings", Proc. of IMechE 4th Intl. Conf. on Vibration in Rotating Machinery, Paper C261/88, pp.61-68.

[29] Glover, K. and Doyle, J., "State space formulae for all stabilizing controllers that satisfy an H_infinity norm bound and relations to risk sensitivity", System & Control Letters, 11, 1988, pp.167-172.

[30] Goodwin, M. J., Roach, M. P., and Penny, J. E. T., "An analysis of combined squeeze film and variable stiffness hydrostatic bearings, and their use in

aircraft engine vibration control", Proc. IMechE 4th Intl. Conf. on Vibration in Rotating Machinery, 1988, pp.85-91.

[31] Herzog, R. and Bleuler, H., "Stiff AMB control using an H-infinity approach", Proc. of 2nd Intl. Symp. on Magnetic Bearing, July 1990, Tokyo, pp.343-348.

[32] Higuchi, T., Mizuno, T., and Tsukamoto, M., "Digital control system for magnetic bearings with automatic balancing", Proc. 2nd Intl. Symp. on Magnetic Bearing, July 1990, pp.27-32.

[33] Hisatani, M., Inami, S., Ohtsuka, T. and Fujita, M., "Design and testing of a flexible rotor bearing system", Proc. of 2nd Intl. Conf. on Magnetic Bearings, Tokyo, July 1990, pp.131-138.

[34] Holmes, R., "The vibration of a rigid shaft on short sleeve bearings", J. of Mech. Eng. Sci., Vol2, 1960, pp.337-341.

[35] Holmes, R., "The non-linear performance of squeeze film bearings", J. of Mech. Eng. Sci., Vol.14, No.1, 1972, pp.74-77.

[36] Imlach, J., Allaire, P. E., Humphris, R. R. and Barrett, L. E., "Magnetic bearing design optimization", Proc. IMechE 4th Intl. Conf. on Vibration in Rotating Machinery, Paper C277/88, pp.53-60.

[37] Imlach, J., Blair, B. J., and Allaire, P. E., "Measured and predicted force and stiffness characteristics of industrial magnetic bearings", Trans. ASME Paper 90-Trib-70, 1990.

[38] IMS T800 Data Sheet, Inmos, 1987.

[39] Jeffcott, H. H., "The lateral vibration of loaded shafts in the neighbourhood of a whirling speed - the effect of want of balance", Philosophical Magazine, Series 6, Vol.37, 1919, p.304.

[40] Kailath, T., Linear Systems, Prentice-Hall, 1980.

[41] Kanemitsu, Y., Ohsawa, M., and Watanabe, K., " Active control of a flexible rotor by an active magnetic bearing ", Proc. 1st Intl. Symp. on Magnetic Bearing, 1988, pp.367-380.

[42] Kanemitsu, Y., Ohsawa, M., and Watanabe, K., " Real time balancing of a flexible rotor supported by magnetic bearing", Proc. 2nd Intl. Symp. on Magnetic bearing, July 1990, Tokyo, pp.265-272.

[43] Kaya, F. and Roberts, J. B., "Optimum vibration control of flexible transmission shafts", Proc. of IMechE 3rd Intl. Conf. on Vibration in Rotating Machinery, York, 1984, pp.525-534.

[44] Keith, F. J., Williams, R. D.,Allaire, P. E., Schafer, R. M., "Digital control of magnetic bearings supporting a multimass flexible rotor", Tribology Trans., Vol.33, No.3, 1990, pp.307-314.

[45] Kirk, R. G., Hustak, J. F., and Schoeneck, K. A., "Analysis and test results of two centrifugal compressors using active magnetic bearings", Proc. IMechE 4th Intl. Conf. on Vibration in Rotating Mach., Paper C278/88, 1988, pp.93-100.

[46] Larsonneur, R., Siegwart, R., and Traxler, A., " Active magnetic bearing control strategies for solving vibration problem in industrial rotor system", Proc. IMechE 5th Intl. Conf. on Vibration in Rotating Machinery, Bath, 1992, pp.83-90.

[47] Lee, C. W. and Kim, J. S., "Modal testing and suboptimal vibration control of flexible rotor bearing system by using a magnetic bearing", Trans. ASME J. Dynamic Systems, Measurement, and Control, Vol.114, June 1992, pp.244-252.

[48] Li, S., " Decentralised control schemes for minimizing vibration in a multi-axis rotor isolation system", Proc. IMechE 5th Intl. Conf. on Vibration in Rotating Machinery, Bath, 1992, pp.115-124.

[49] Madiwale, A., Haddad, W., and Bernstein, D., "Robust H-infinity control design for systems with structured parameter uncertainty", System & Control Letters, 12(1989), pp.393-407.

[50] Maslen, E. H. and Allaire, P. E., "Active bearing load capacity requirements for rotating shaft", Proc IMechE 5th Intl. Conf. on Vibration in Rotating Machinery, Bath, 1992, pp.91-97.

[51] Moore, B. C., "Principal component analysis in linear system: controllability, observability, and model reduction", IEEE Trans. on Auto. Cont., AC-26, 1981, pp.17-31.

[52] Morishita, S. and Mitsui, J., "Controllable squeeze film damper (an application of electro-rheological fluid)", Trans ASME J of Vibration and Acoustics, Vol.114, July 1992, pp.354-357.

[53] Mu, C., Darling, J., and Burrows, C. R., "An appraisal of a proposed active squeeze film damper", Trans. ASME J. Tribology, 1991, Vol.113, pp.550-554.

[54] Mu, C., Keogh, P. S., and Burrows, C. R., " H_infinity controller design for active vibration control of a flexible rotor", Proc. IMechE 5th Intl. Conf. on Vibration in Rotating Machinery, Bath, 1992, pp.131-140.

[55] Muszynska, A., Franklin, W. D., and Bently, D. E., "Rotor active "Anti-Swirl" control", Trans. ASME J. Vibr., Acous., Stress, and Relia. in Design, Vol.110, April 1988, pp.143-150.

[56] Nelson, H. D., "A finite rotating shaft element using Timoshenko beam theory", Trans. ASME J. of Mech. Design, Vol.102, Oct 1980, pp.793-803.

[57] Newkirk, B. L. and Taylor, H. D., "Shaft whipping due to oil action in journal bearings", General Electric Review, Vol.28, No.8, August 1925, pp.559-568.

[58] Nonami, K., Yamanaka, T., and Tominaga, M., "Vibration and control of a flexible rotor supported by magnetic bearings _ control system analysis and experiments without gyroscopic effects", JSME Intl. Journal, Series 3, Vol.33, No.4, 1990, pp.475-482.

[59] Ormondroyd, J. and Den Hartog, J. P., "Theory of dynamic vibration absorber", Trans, ASME, Vol.50, 1928, APM-50-7.

[60] Palazzolo, A. B., Kascak, A. F., Montague, G. T., and Kiraly, L. J., "Hybrid active vibration control of retorbearing systems using piezoelectic actuators",

Proc. ASME Conf. Modal Analysis, Modelling, Diagnostics, and Control, DE-Vol. 38, pp.227-240.

[61] Perihelion Software Ltd, The Helios Parallel Operating Systems, Prentice Hall, 1991.

[62] Pinkus, O. and Sternlicht, B., Theory of Hydrodynamic Lubrication, McGraw-Hill Book Company, New York, 1961.

[63] Prohl, M. A., " A general method for calculating critical speeds of flexible rotors", Trans ASME, Vol 66, Sept 1945, p A-142.

[64] Rankine, W. A., "On the centrifugal force of rotating shafts", Engineer, Lond., Vol.27, 1869, p.249.

[65] Redmond, I., "Vibration reduction of flexible rotors", Ph.D. Thesis, University of strathclyde, 1985.

[66] RTI-800/815 User's Manual, Analog Devices, Inc.

[67] Salm, J. and Schweitzer, G., "Modelling and control of a flexible rotor with magnetic bearing", Proc. of 3rd IMechE Conf. on vibrations in Rotating Machinery, York, 1984, pp.553-561.

[68] Salm, J., "Active electromagnetic suspension of an elastic rotor: modelling, control, and experimental results", Rotating Machinery Dynamics, ASME Design Technology Conf., Boston, 1987, pp.187-191.

[69] Sandler, B., "Adaptive mechanisms - Automatic vibration control", J. Sound & Vibration, Vol.73 No.2, 1980, pp.166-175.

[70] Scherer, C., "H_infinity control by state feedback: An iterative algorithm and characterization of high gain occurrence", System & Control Letter, 12(1989), pp.383-391.

[71] Schmied, J., "Experience with magnetic bearings supporting a pipeline compressor", Proc. 2nd Intl. Symp. on Magnetic bearing, July 1990, Tokyo, pp.47-53.

[72] Schweitzer, G., "Stabilization of self-excited rotor vibrations by an active damper", Dynamics of Rotors, Ed. F. I. Niordson, Springer Verlag, New York, 1975.

[73] Schweitzer, G. and Lange, R., "Characteristics of a magnetic rotor bearing for active vibration control", Proc. IMechE Conf. on Vibrations in Rotating Machinery, Cambridge, August 1976, pp.1-6.

[74] Schweitzer, G. and Ulbrich, H., "Magnetic bearings - a novel type of suspension", IMechE Conf. on Vibrations in Rotating Machinery, Paper C273/80, 1980, pp.151-156.

[75] Software Manual for the RTI 800, 802, 815, 817, 820, Analog Devices, Inc.

[76] Tasaltin, R.," Active vibration control strategies for a flexible rotor-bearing system", PhD Thesis, University of Bath, 1991.

[77] Thomas, D. L., Wilson, J. M., and Wilson, R. R., "Timoshenko beam finite elements", J. of Sound and Vibration, 31(1), 1973, pp.315-330.

[78] Vernon, J. B., Linear Vibration Theory, John Wiley and Sons, 1967.

[79] Viggiano, F. and Schweitzer, G., "Blade loss dynamics of a magnetically supported rotor", Rotating Machinery: Dynamics. Proc. 3rd Intl. Sym. Transport Phenomena & Dynamics of Rotating Machinery, 1992, Ed. J. H. Kim & W. J. Yang, Hemisphere Publishing Company, Washington.

[80] Williams, R. D., Keith, F. J., and Allaire, P. E., "A comparison of analog and digital controls for rotor dynamics vibration reduction through active magnetic bearings", Trans. ASME J. of Eng. for Gas Turbines and Power, Vol.113, Oct 1991, pp.535-543.

[81] Zames, G., "Feedback and optimal sensitivity: model reference transformation, multiplicative seminorms, and approximate inverses", IEEE Trans. Auto. Cont., Vol.126, 1981, pp.301-320.

[82] Zhou, K. and Khargonekar, P. P., "An algebraic Riccati equation approach to H_infinity optimization", System & Control Letters, 11(1988), pp.85-91.

APPENDIX A FINITE ELEMENT MATRICES

Finite element stiffness matrix

$$K^e = \frac{EI}{l^3(1+\Phi)}(K_0^e + \Phi K_1^e)$$

$$K_0^e = \begin{bmatrix} 12 & & & & & & & \\ 0 & 12 & & & & & sym & \\ 0 & -6l & 4l^2 & & & & & \\ 6l & 0 & 0 & 4l^2 & & & & \\ -12 & 0 & 0 & -6l & 12 & & & \\ 0 & -12 & 6l & 0 & 0 & 12 & & \\ 0 & -6l & 2l^2 & 0 & 0 & 6l & 4l^2 & \\ 6l & 0 & 0 & 2l^2 & -6l & 0 & 0 & 4l^2 \end{bmatrix}$$

$$K_1^e = \begin{bmatrix} 0 & & & & & & & \\ 0 & 0 & & & & & sym & \\ 0 & 0 & l^2 & & & & & \\ 0 & 0 & 0 & l^2 & & & & \\ 0 & 0 & 0 & 0 & 0 & & & \\ 0 & 0 & 0 & 0 & 0 & 0 & & \\ 0 & 0 & -l^2 & 0 & 0 & 0 & l^2 & \\ 0 & 0 & 0 & -l^2 & 0 & 0 & 0 & l^2 \end{bmatrix}$$

Finite element translational mass matrix

$$\boldsymbol{M}_t^{\,e} = \frac{m_\rho l}{420(1+\Phi)^2}(\boldsymbol{M}_{t0}^{\,e} + \Phi \boldsymbol{M}_{t1}^{\,e} + \Phi^2 \boldsymbol{M}_{t2}^{\,e})$$

$$\boldsymbol{M}_{t0}^{\,e} = \begin{bmatrix} 156 & & & & & & & \\ 0 & 156 & & & & & sym & \\ 0 & -22l & 4l^2 & & & & & \\ 22l & 0 & 0 & 4l^2 & & & & \\ 54 & 0 & 0 & 13l & 156 & & & \\ 0 & 54 & -13l & 0 & 0 & 156 & & \\ 0 & 13l & -3l^2 & 0 & 0 & 22l & 4l^2 & \\ -13l & 0 & 0 & -3l^2 & -22l & 0 & 0 & 4l^2 \end{bmatrix}$$

$$\boldsymbol{M}_{t1}^{\,e} = \begin{bmatrix} 294 & & & & & & & \\ 0 & 294 & & & & & sym & \\ 0 & -38.5l & 7l^2 & & & & & \\ 38.5l & 0 & 0 & 7l^2 & & & & \\ 126 & 0 & 0 & 31.5l & 294 & & & \\ 0 & 126 & -31.5l & 0 & 0 & 294 & & \\ 0 & 31.5l & -7l^2 & 0 & 0 & 38.5l & 7l^2 & \\ -31.5l & 0 & 0 & -7l^2 & -38.5l & 0 & 0 & 7l^2 \end{bmatrix}$$

$$\boldsymbol{M}_{t2}^{\,e} = \begin{bmatrix} 140 & & & & & & & \\ 0 & 140 & & & & & sym & \\ 0 & -17.5l & 3.5l^2 & & & & & \\ 17.5l & 0 & 0 & 3.5l^2 & & & & \\ 70 & 0 & 0 & 17.5l & 140 & & & \\ 0 & 70 & -17.5l & 0 & 0 & 140 & & \\ 0 & 17.5l & -3.5l^2 & 0 & 0 & 17.5l & 3.5l^2 & \\ -17.5l & 0 & 0 & -3.5l^2 & -17.5l & 0 & 0 & 3.5l^2 \end{bmatrix}$$

Finite element rotational mass matrix

$$M_r^e = \frac{m_\rho d^2}{480l(1+\Phi)^2}(M_{r0}^e + \Phi M_{r1}^e + \Phi^2 M_{r2}^e)$$

$$M_{r0}^e = \begin{bmatrix} 36 & & & & & & & \\ 0 & 36 & & & & & sym & \\ 0 & -3l & 4l^2 & & & & & \\ 3l & 0 & 0 & 4l^2 & & & & \\ -36 & 0 & 0 & -3l & 36 & & & \\ 0 & -36 & 3l & 0 & 0 & 36 & & \\ 0 & -3l & -l^2 & 0 & 0 & 3l & 4l^2 & \\ 3l & 0 & 0 & -l^2 & -3l & 0 & 0 & 4l^2 \end{bmatrix}$$

$$M_{r1}^e = \begin{bmatrix} 0 & & & & & & & \\ 0 & 0 & & & & & sym & \\ 0 & 15l & 5l^2 & & & & & \\ -15l & 0 & 0 & 5l^2 & & & & \\ 0 & 0 & 0 & 15l & 0 & & & \\ 0 & 0 & -15l & 0 & 0 & 0 & & \\ 0 & 15l & -5l^2 & 0 & 0 & -15l & 5l^2 & \\ -15l & 0 & 0 & -5l^2 & 15l & 0 & 0 & 5l^2 \end{bmatrix}$$

$$M_{r2}^e = \begin{bmatrix} 0 & & & & & & & \\ 0 & 0 & & & & & sym & \\ 0 & 0 & 10l^2 & & & & & \\ 0 & 0 & 0 & 10l^2 & & & & \\ 0 & 0 & 0 & 0 & 0 & & & \\ 0 & 0 & 0 & 0 & 0 & 0 & & \\ 0 & 0 & 5l^2 & 0 & 0 & 0 & 10l^2 & \\ 0 & 0 & 0 & 5l^2 & 0 & 0 & 0 & 10l^2 \end{bmatrix}$$

Finite element gyroscopic matrix

$$\boldsymbol{G}^{e} = \frac{m_{\rho} d^{2}}{240l(1+\Phi)^{2}}(\boldsymbol{G}_{0}^{e} + \Phi \boldsymbol{G}_{1}^{e} + \Phi^{2}\boldsymbol{G}_{2}^{e})$$

$$\boldsymbol{G}_{0}^{e} = \begin{bmatrix} 0 & & & & & & & \\ 36 & 0 & & & & skew & sym & \\ -3l & 0 & 0 & & & & & \\ 0 & -3l & 4l^{2} & 0 & & & & \\ 0 & 36 & -3l & 0 & 0 & & & \\ -36 & 0 & 0 & -3l & 36 & 0 & & \\ -3l & 0 & 0 & l^{2} & 3l & 0 & 0 & \\ 0 & -3l & -l^{2} & 0 & 0 & 3l & 4l^{2} & 0 \end{bmatrix}$$

$$\boldsymbol{G}_{1}^{e} = \begin{bmatrix} 0 & & & & & & & \\ 0 & 0 & & & & skew & sym & \\ 15l & 0 & 0 & & & & & \\ 0 & 15l & 5l^{2} & 0 & & & & \\ 0 & 0 & 15l & 0 & 0 & & & \\ 0 & 0 & 0 & 15l & 0 & 0 & & \\ 15l & 0 & 0 & 5l^{2} & -15l & 0 & 0 & \\ 0 & 15l & -5l^{2} & 0 & 0 & -15l & 5l^{2} & 0 \end{bmatrix}$$

$$\boldsymbol{G}_{2}^{e} = \begin{bmatrix} 0 & & & & & & & \\ 0 & 0 & & & & skew & sym & \\ 0 & 0 & 0 & & & & & \\ 0 & 0 & 10l^{2} & 0 & & & & \\ 0 & 0 & 0 & 0 & 0 & & & \\ 0 & 0 & 0 & 0 & 0 & 0 & & \\ 0 & 0 & 0 & -5l^{2} & 0 & 0 & 0 & \\ 0 & 0 & 5l^{2} & 0 & 0 & 0 & 10l^{2} & 0 \end{bmatrix}$$

APPENDIX B JOURNAL BEARING STIFFNESS AND DAMPING COEFFICIENTS

The oil film force expressions obtained by Holmes [33] are as follows:

$$F_r = -c_{rr}\dot{r} - k_{rr}r + c_{rs}\dot{s} - k_{rs}s - F_{ro}$$

$$F_s = c_{sr}\dot{r} + k_{sr}r - c_{ss}\dot{s} - k_{ss}s + F_{so}$$

where

$$k_{rr} = \frac{F_o}{c}\frac{8(1+\varepsilon_o^2)}{(1-\varepsilon_o^2)\left[\pi^2(1-\varepsilon_o^2)+16\varepsilon_o^2\right]^{1/2}}$$

$$k_{rs} = \frac{F_o}{c}\frac{\pi(1-\varepsilon_o^2)^{1/2}}{\varepsilon_o\left[\pi^2(1-\varepsilon_o^2)+16\varepsilon_o^2\right]^{1/2}}$$

$$k_{sr} = \frac{F_o}{c}\frac{\pi(1+2\varepsilon_o^2)}{\varepsilon_o(1-\varepsilon_o^2)^{1/2}\left[\pi^2(1-\varepsilon_o^2)+16\varepsilon_o^2\right]^{1/2}}$$

$$k_{ss} = \frac{F_o}{c}\frac{4}{\left[\pi^2(1-\varepsilon_o^2)+16\varepsilon_o^2\right]^{1/2}}$$

$$c_{rs} = c_{sr} = \frac{2k_{ss}}{\Omega}\ , \qquad c_{ss} = \frac{2k_{rs}}{\Omega}\ , \qquad c_{rr} = \frac{2k_{sr}}{\Omega}$$

$$F_{ro} = \frac{\Omega\varepsilon_o^2\mu L^3 R}{c^2(1-\varepsilon_o^2)^2}\ , \qquad F_{so} = \frac{\Omega\pi\varepsilon_o\mu L^3 R}{4c^2(1-\varepsilon_o^2)^{3/2}}$$

The corresponding dynamic force expression in the fixed x-y coordinate system is of the form

$$F_x = -c_{xx}\dot{x} - c_{xy}\dot{y} - k_{xx}x - k_{xy}y + F_{xo}$$

$$F_y = -c_{yx}\dot{x} - c_{yy}\dot{y} - k_{yx}y - k_{yy}y + F_{yo}$$

where the stiffness and damping coefficients in the fixed x-y coordinate system can be obtained by the following transformation

$$\begin{bmatrix} c_{xx} \\ c_{xy} \\ c_{yx} \\ c_{yy} \\ k_{xx} \\ k_{xy} \\ k_{yx} \\ k_{yy} \end{bmatrix} = \begin{bmatrix} c_{rr} & c_{ss} & (c_{rs}+c_{sr}) \\ -c_{rs} & c_{sr} & (c_{rr}-c_{ss}) \\ -c_{sr} & c_{rs} & (c_{rr}-c_{ss}) \\ c_{ss} & c_{rr} & -(c_{rs}+c_{sr}) \\ k_{rr} & k_{ss} & (k_{sr}-k_{rs}) \\ k_{rs} & k_{sr} & (k_{rr}-k_{ss}) \\ -k_{sr} & -k_{rs} & (k_{rr}-k_{ss}) \\ k_{ss} & k_{rr} & (k_{rs}-k_{sr}) \end{bmatrix} \times \begin{bmatrix} \cos^2\phi_o \\ \sin^2\phi_o \\ \cos\phi_o \sin\phi_o \end{bmatrix}$$

$$\begin{bmatrix} F_{xo} \\ F_{yo} \end{bmatrix} = \begin{bmatrix} \cos\phi_o & -\sin\phi_o \\ \sin\phi_o & \cos\phi_o \end{bmatrix} \begin{bmatrix} -F_{ro} \\ F_{so} \end{bmatrix}$$

If the static load is known, the static eccentricity and angular position can be derived by solving the following algebraic equation

$$F_o = \sqrt{F_{ro}^{\,2} + F_{so}^{\,2}}$$

$$\tan\phi_o = \frac{|F_{ro}|}{|F_{so}|}$$

APPENDIX C WEIGHTING FUNCTION MATRICES

C.1 Weighting Function Matrix W_u

$$W_u(s) = \begin{bmatrix} \dfrac{0.0067s+1}{0.0001s+1} & 0 \\ 0 & \dfrac{0.0067s+1}{0.0001s+1} \end{bmatrix}$$

C.2 Weighting Function Matrices At 309 rad/s Controller Design

W_z band pass:

$$W_z(s) = \begin{bmatrix} \ddots & & \\ & \dfrac{0.748s^2+1.5\times10^4 s+5.99\times10^4}{s^2+6\times10^2 s+8\times10^4} & \\ & & \ddots \end{bmatrix}_{16\times16}$$

W_z low pass:

$$W_z(s) = \begin{bmatrix} \ddots & & \\ & \dfrac{2\times10^{-5}s+1}{2\times10^{-5}s+4\times10^{-2}} & \\ & & \ddots \end{bmatrix}_{16\times16}$$

W_z constant:

$$W_z(s) = \begin{bmatrix} \ddots & & \\ & 25.0 & \\ & & \ddots \end{bmatrix}_{16\times16}$$

W_y:

$$W_y(s) = \begin{bmatrix} \ddots & & \\ & \dfrac{9.923\times10^{-4}s+1}{9.923\times10^{-4}s+0.1} & \\ & & \ddots \end{bmatrix}_{6\times6}$$

C.3 Weighting Function Matrices At 100, 150, 200, 250 rad/s Controller Design

Ω = 100 rad/s:

$$W_y(s) = \begin{bmatrix} \ddots & & \\ & \dfrac{8.27\times10^{-4}s+1}{8.27\times10^{-4}s+0.4} & \\ & & \ddots \end{bmatrix}_{6\times6} \qquad W_z(s) = \begin{bmatrix} \ddots & & \\ & 50.0 & \\ & & \ddots \end{bmatrix}_{16\times16}$$

Ω = 150 rad/s:

$$W_y(s) = \begin{bmatrix} \ddots & & \\ & \dfrac{8.84\times10^{-4}s+1}{8.84\times10^{-4}s+0.333} & \\ & & \ddots \end{bmatrix}_{6\times6} \qquad W_z(s) = \begin{bmatrix} \ddots & & \\ & 40.0 & \\ & & \ddots \end{bmatrix}_{16\times16}$$

Ω = 200 rad/s:

$$W_y(s) = \begin{bmatrix} \ddots & & \\ & \dfrac{9.38\times10^{-4}s+1}{9.38\times10^{-4}s+0.25} & \\ & & \ddots \end{bmatrix}_{6\times6} \qquad W_z(s) = \begin{bmatrix} \ddots & & \\ & 35.0 & \\ & & \ddots \end{bmatrix}_{16\times16}$$

Ω = 250 rad/s:

$$W_y(s) = \begin{bmatrix} \ddots & & \\ & \dfrac{9.62\times10^{-4}s+1}{9.62\times10^{-4}s+0.2} & \\ & & \ddots \end{bmatrix}_{6\times6} \qquad W_z(s) = \begin{bmatrix} \ddots & & \\ & 30.0 & \\ & & \ddots \end{bmatrix}_{16\times16}$$

C.4 Weighting Function Matrices At Transient Controller Design

$$W_y(s) = \begin{bmatrix} \ddots & & \\ & \dfrac{10^{-3}s+1}{10^{-3}s+4\times10^{-2}} & \\ & & \ddots \end{bmatrix}_{6\times6} \qquad W_z(s) = \begin{bmatrix} \ddots & & \\ & 62.0 & \\ & & \ddots \end{bmatrix}_{16\times16}$$

C.5 Transfer Function Matrix W_{fm}

Transfer function matrix W_{fm} consists of three parts, i.e. high pass part

$$\frac{T_a s}{1+T_a s}$$

low pass part

$$\frac{1+10^{-2}T_b s}{1+T_b s}$$

and the part due to measurement time delay which can equivalently be modelled as

$$\frac{1-\frac{T_s}{2}s}{1+\frac{T_s}{2}s}$$

where T_a=94 ms, T_b=0.398 ms, and T_s=1.344 ms. The resulting W_{fm} is of the form

$$W_{fm}(s) = \begin{bmatrix} \ddots & & \\ & \dfrac{-5.03\times10^{-10}s^3-6.28\times10^{-5}s^2+9.4\times10^{-2}s}{2.51\times10^{-8}s^3+1.01\times10^{-4}s^2+9.51\times10^{-2}s+1} & \\ & & \ddots \end{bmatrix}_{6\times6}$$